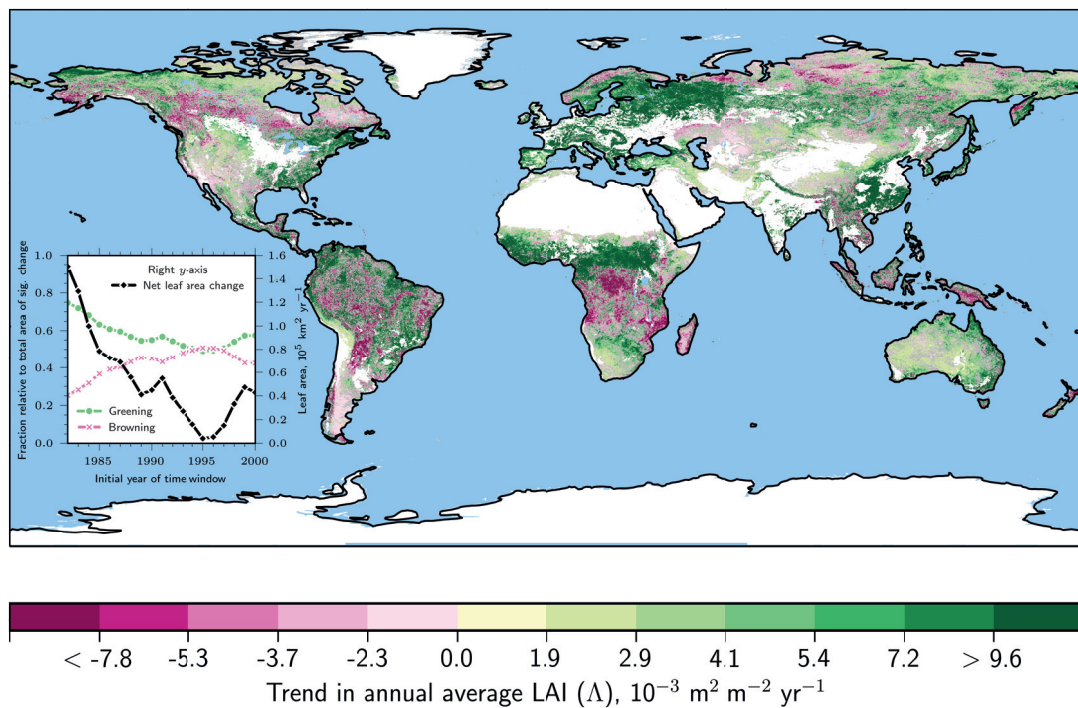




The Response of Global Terrestrial Photosynthesis to Rising CO₂

A Synthesis of Models and Observations



Alexander Josef Winkler

Hamburg 2020

Hinweis

Die Berichte zur Erdsystemforschung werden vom Max-Planck-Institut für Meteorologie in Hamburg in unregelmäßiger Abfolge herausgegeben.

Sie enthalten wissenschaftliche und technische Beiträge, inklusive Dissertationen.

Die Beiträge geben nicht notwendigerweise die Auffassung des Instituts wieder.

Die "Berichte zur Erdsystemforschung" führen die vorherigen Reihen "Reports" und "Examensarbeiten" weiter.

Anschrift / Address

Max-Planck-Institut für Meteorologie
Bundesstrasse 53
20146 Hamburg
Deutschland

Tel./Phone: +49 (0)40 4 11 73 - 0
Fax: +49 (0)40 4 11 73 - 298

name.surname@mpimet.mpg.de
www.mpimet.mpg.de

Notice

The Reports on Earth System Science are published by the Max Planck Institute for Meteorology in Hamburg. They appear in irregular intervals.

They contain scientific and technical contributions, including Ph. D. theses.

The Reports do not necessarily reflect the opinion of the Institute.

The "Reports on Earth System Science" continue the former "Reports" and "Examensarbeiten" of the Max Planck Institute.

Layout

Bettina Diallo and Norbert P. Noreiks
Communication

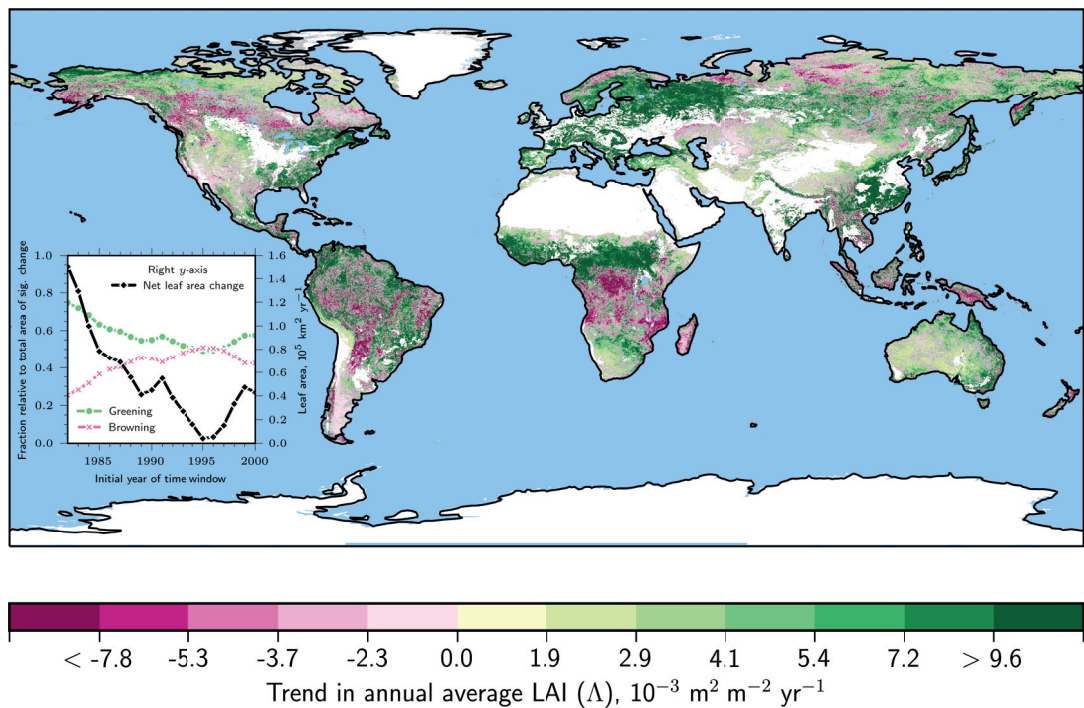
Copyright

Photos below: ©MPI-M
Photos on the back from left to right:
Christian Klepp, Jochem Marotzke,
Christian Klepp, Clotilde Dubois,
Christian Klepp, Katsumasa Tanaka



The Response of Global Terrestrial Photosynthesis to Rising CO₂

A Synthesis of Models and Observations



Alexander Josef Winkler

Hamburg 2020

Alexander Josef Winkler

from Trostberg, Germany

Max-Planck-Institut für Meteorologie
The International Max Planck Research School on Earth System Modelling
(IMPRS-ESM)
Bundesstrasse 53
20146 Hamburg

Universität Hamburg
Geowissenschaften
Meteorologisches Institut
Bundesstr. 55
20146 Hamburg

Tag der Disputation: 28. Oktober 2019

Folgende Gutachter empfehlen die Annahme der Dissertation:

Prof. Dr. Victor Brovkin

Prof. Dr. Martin Claussen

Vorsitzender des Promotionsausschusses:

Prof. Dr. Dirk Gajewski

Dekan der MIN-Fakultät:

Prof. Dr. Heinrich Graener

The figure on the front page depicts satellite observations of long-term changes in global leaf area for natural vegetation and for the period 1982–2017.

Für meine Eltern
Theresa
und
Johann Winkler (1950 – 1995)

ABSTRACT

In this dissertation I examine how photosynthesis on land has responded to rising CO₂ concentration in recent decades, and how we can use this knowledge to better predict the evolution of the climate-carbon system throughout the 21st century.

More than three decades of satellite data reveal widespread and persistent changes in Earth's ecosystems. The drivers underlying these changes and the implications for the terrestrial sink of anthropogenic carbon emissions are controversial.

In the first part of this thesis, I examine a long-term satellite record of global leaf area observations (1981–2017) and identify clusters of significant change on the biome level. Using process-based models and a framework relying on causal theory, I disentangle and attribute vegetation changes to CO₂-induced climatic changes and the CO₂ fertilization effect. I show that 40% of Earth's naturally vegetated surface is greening, predominately in the extratropics, and 14% is browning, mostly in the tropics. Although previous studies attributed the greening to CO₂ fertilization, I show that only some biomes show a marked response to this effect, whereas many biomes bear the signature of climatic changes, i.e. warming and rainfall anomalies. The leaf area loss in the tropical forests due to increased droughts and long-term drying could be an early indicator of a slow-down in the terrestrial carbon sink.

In the second part, I examine if the observed vegetation response to rising CO₂ can be used to reduce uncertainty in the evolution of the carbon cycle. Using an approach called Emergent Constraint (EC), I combine satellite observations and multi-model simulations to derive an estimate for the increase in photosynthetic carbon fixation of northern ecosystems for 2×CO₂ ($3.4 \pm 0.2 \text{ Pg C yr}^{-1}$). Three comparable independent estimates from CO₂ measurements and atmospheric inversions corroborate this result. The EC estimate is considerably larger than most model projections which suggests that the effect of rising CO₂ concentration on photosynthesis in northern terrestrial ecosystems is underestimated.

In the third part, I investigate the applicability of the EC method in a broader context of Earth system sciences. More and more EC estimates are being reported, however their robustness is controversial. By means of a thought experiment and analyses of a multi-model ensemble, I address the main caveats and highlight limitations as well as potential sources of uncertainty in the application of the EC method. All parts in this thesis highlight how the variety of observational data

and the strength of process-based models in conjunction with new methods advance the understanding of the terrestrial biosphere.

ZUSAMMENFASSUNG

In dieser Dissertation untersuche ich, wie die terrestrische Photosynthese auf die steigende CO₂-Konzentration der letzten Jahrzehnte reagiert hat und wie wir dieses Wissen nutzen können, um die Entwicklung des Klima-Kohlenstoff-Systems im 21. Jahrhundert besser vorherzusagen.

Satellitendaten aus mehr als drei Jahrzehnten zeigen, dass sich die Ökosysteme der Erde in großem Maßstab verändert haben. Die Treiber, die diesen Veränderungen zugrunde liegen und die damit verbundenen Auswirkungen auf die Landsenke von anthropogenen Kohlenstoffemissionen, sind umstritten.

Im ersten Teil dieser Arbeit untersuche ich Langzeit-Satellitenbeobachtungen der globalen Vegetation (Blattfläche, 1981–2017). Unter Berücksichtigung verschiedener Biome identifiziere ich Regionen, die sich signifikant verändert haben. Mit Hilfe von prozessbasierten Modellen und Kausaltheorie trenne ich die Auswirkungen des CO₂-verursachten Düngungs- und Treibhauseffekts auf die Vegetation auf. Ich zeige, dass 40% der natürlich bewachsenen Erdoberfläche ergrünt, vornehmlich in den Extratropen, und 14% erbraunen, hauptsächlich in den Tropen. Frühere Studien haben den CO₂-Düngungseffekt als Haupttreiber der Ergrünung identifiziert. Meine Analyse zeigt, dass nur einige Biome eine deutliche Reaktion auf diesen Effekt zeigen und dass Klimaveränderungen (Erwärmung und Niederschlagsanomalien) in vielen Ökosystemen eine stärkere Auswirkung haben. Der Verlust von Blattfläche in den Tropenwäldern durch häufiger auftretender Dürren und/oder stetigen Niederschlagsrückgang könnte ein Vorbote einer Abschwächung der terrestrischen Kohlenstoffsенke sein.

Im zweiten Teil untersuche ich, ob die beobachteten Veränderungen in der Vegetation als Folge der steigenden CO₂ Konzentration herangezogen werden können, um die Entwicklung des globalen Kohlenstoffkreislaufs besser abschätzen zu können. Unter der Zuhilfenahme von Emergent Constraints (EC) kombiniere ich Satellitenbeobachtungen und Multi-Modell-Simulationen, um die Zunahme der photosynthetischen Kohlenstoffaufnahme der Ökosysteme in den hohen Breiten für 2×CO₂ vorherzusagen ($3.4 \pm 0.2 \text{ Pg C yr}^{-1}$). Drei unabhängige, vergleichbare Schätzungen, die auf CO₂-Messungen und atmosphärischen Inversionen basieren, untermauern dieses Ergebnis. Die EC-basierte Schätzung ist wesentlich höher als die meisten Modellvorhersagen, was darauf hindeutet, dass der Einfluss der steigenden CO₂-Konzentration auf die Photosynthese der nördlichen terrestrischen Ökosysteme unterschätzt werden könnte.

Im dritten Teil untersuche ich die Anwendbarkeit der EC-Methode im

allgemeinen Kontext der Erdsystemwissenschaften. Es werden mehr und mehr EC-Studien durchgeführt, die Ergebnisse sind jedoch kontrovers. Anhand eines Gedankenexperiments und der Analyse eines Multi-Modell-Ensembles untersuche ich die wichtigsten Kritikpunkte und zeige mögliche Unsicherheitsquellen in der Anwendung der EC-Methode auf.

Die vorliegende Dissertation zeigt, wie die Vielzahl an Beobachtungsdatensätzen und prozessbasierten Modellen mit neuen Methoden zum besseren Verständnis der terrestrischen Biosphäre verknüpft werden kann.

PUBLICATIONS RELATED TO THIS DISSERTATION
Teilveröffentlichungen dieser Dissertation

Winkler, A. J., R. B. Myneni, G. A. Alexandrov, and V. Brovkin (2019a). "Earth System Models Underestimate Carbon Fixation by Plants in the High Latitudes." *Nature Communications* 10.1, p. 885. DOI: [10.1038/S41467-019-08633-Z](https://doi.org/10.1038/S41467-019-08633-Z)

Winkler, A. J., R. B. Myneni, and V. Brovkin (2019b). "Investigating the Applicability of Emergent Constraints." *Earth System Dynamics* 10.3, pp. 501–523. DOI: [10.5194/esd-10-501-2019](https://doi.org/10.5194/esd-10-501-2019)

Winkler, A. J., R. B. Myneni, A. Hannart, S. Sitch, V. Haverd, D. Lombardozzi, V. K. Arora, J. Pongratz, J. E. M. S. Nabel, D. S. Goll, E. Kato, H. Tian, A. Arneth, P. Friedlingstein, A. K. Jain, S. Zaehle, and V. Brovkin (submitted). "Slow-down of the Greening Trend in Natural Vegetation with Further Rise in Atmospheric CO₂." *Proceedings of the National Academy of Sciences*, pp. 1–14

CONTENTS

Unifying Essay

1	PLANTS UNDER RISING CO ₂ – AN ESSAY ON THE GLOBAL CHANGE OF VEGETATION	3
1.1	Photosynthesis and Earth’s History	4
1.2	Plants, CO ₂ and Climate	6
1.3	Observational evidence of a globally changing vegetation	8
1.4	Paper 1: Effects of rising CO ₂ on global natural vegetation	11
1.5	Uncertainty in the Terrestrial Carbon Sink	15
1.6	Paper 2: Emergent Constraint on projected photosynthetic carbon fixation	16
1.7	Paper 3: Investigating the Applicability of Emergent Constraints	20
1.8	Outlook	24

	BIBLIOGRAPHY	27
--	--------------	----

I THE EFFECTS OF RISING CO₂ ON GLOBAL NATURAL VEGETATION

II EARTH SYSTEM MODELS UNDERESTIMATE CARBON FIXATION BY PLANTS IN THE HIGH LATITUDES

III INVESTIGATING THE APPLICABILITY OF EMERGENT CONSTRAINTS

LIST OF FIGURES

- Figure 1 Probabilities of sufficient and necessary causation (PNS) of LAI changes in response to CO₂ for eleven clusters. 14
- Figure 2 CMIP5 ensemble mean considerably underestimates absolute increase of GPP for a doubling of pre-industrial atmospheric CO₂ concentration (2×CO₂). 19
- Figure 3 Schematic depiction of the *Emergent Constraint* (EC) method and factors affecting the uncertainty of the constrained estimate. 23

ACRONYMS

AVHRR	Advanced Very High Resolution Radiometer
CMIP	Coupled Model Intercomparison Project
ESM	Earth System Model
EC	Emergent Constraints
GPP	Gross Primary Production
IV	Internal Variability
LSM	Land Surface Model
LAI	Leaf Area Index
MODIS	Moderate Resolution Imaging Spectroradiometer
NHL	Northern High Latitudes
PNS	Probability of Necessary and Sufficient Causation
PE	Physiological Effect of CO ₂
RE	Radiative Effect of CO ₂

UNIFYING ESSAY

PLANTS UNDER RISING CO₂ – AN ESSAY ON THE GLOBAL CHANGE OF VEGETATION

How can the events in space and time which take place within the spatial boundary of a living organism be accounted for by physics and chemistry?

— Erwin Schrödinger, *What Is Life?*, 1943

This dissertation is about how terrestrial photosynthesis responds to rising atmospheric carbon dioxide concentrations, and what this response tells us about the future land sink of anthropogenic carbon. In my analyses I employ novel methods which combine multiple Earth system model simulations, satellite observations, and ground measurements. This cumulative thesis is structured into three individual articles attached in Part [i](#), [ii](#) and [iii](#). In the first paper, I analyze long-term satellite observations of global natural vegetation, identify clusters of significant change, and determine the underlying drivers using models and a attribution framework based on causal theory (Winkler et al., [submitted](#)). In the second paper, I apply the obtained knowledge of historical vegetation changes to reduce uncertainty in projections of the future terrestrial carbon sink using an approach called *Emergent Constraints* (Winkler et al., [2019a](#)). In the third paper, I scrutinize the applicability of the Emergent Constraints method for different settings and illustrate sources of uncertainty (Winkler et al., [2019b](#)).

I will summarize the three articles in the form of this essay and show how my findings contribute to a wider body of research into global vegetation changes under rising CO₂ and their implications for the terrestrial carbon sink. In order to help the reader understand the broader research context, I will first describe the role of plants in the Earth system and start at the very beginning: with an exploration into the emergence of photosynthesis on Earth.

1.1 PHOTOSYNTHESIS AND EARTH'S HISTORY

Overall
photosynthesis
reaction equation:
 $\text{CO}_2 + \text{H}_2\text{O} \rightarrow$
 $\text{CH}_2\text{O} + \text{O}_2$

The process of photosynthesis converts carbon dioxide (CO₂) and water (H₂O) into carbohydrates (CH₂O) and the by-product oxygen (O₂), using the energy of incoming sunlight. The continuous supply of both oxygen and carbohydrates lays the foundation of practically all life on Earth. But throughout Earth's history, photosynthesis and its products also irrevocably altered the inorganic surface of the planet.

Great Oxygenation
Event

Photosynthesis constitutes the only significant source of free oxygen on Earth's surface (Lyons et al., 2014). For the first half of Earth's history of 4.5 billion years, oxygen was merely a trace gas in the atmosphere (Holland, 2006; Lyons et al., 2014). The first appearance of photosynthesis is controversial (Holland, 2006; Lyons et al., 2014; Foster et al., 2017). The estimates range from 3.8 to 2.35 billion years, when cyanobacteria, the first photosynthesizing organisms, evolved and populated the oceans (Holland, 2006; Lyons et al., 2014). Slowly, oxygen started to rise in the oceans, and later in the atmosphere, initiating the Great Oxygenation Event approximately 2.45 billion years ago (Holland, 2006). The genesis of the highly reactive free oxygen left marked fingerprints in the geological rock record, for example, the emergence of oxidized red soils on land (Lyons et al., 2014). At first, the atmospheric oxygen concentration remained at a low level, until ~0.85 billion years ago, when photosynthesizing organisms also colonized the continents (Knauth and Kennedy, 2009). The explosion of photosynthesizing communities on the land surface caused a sharp increase in atmospheric oxygen and stabilized to the current level of ~21% (Holland, 2006; Knauth and Kennedy, 2009)

Snowball Earth

The continuous photosynthetic replenishment of oxygen sustains an oxidizing atmosphere with considerable consequences for the Earth system. For example, Kopp et al. (2005) suggested that the persistent inflow of oxygen depleted the concentration of methane, which was probably the most significant greenhouse gas in Earth's atmosphere around 2.2 – 2.3 billion years ago (Kasting and Catling, 2003). Photosynthetic oxygen nearly completely removed methane from the atmosphere, which induced a drastic climate shift to global glaciation, the so-called *Makganyene* Snowball Earth (Kopp et al., 2005).

The ability of photosynthesis to harvest energy directly from the incoming sunlight and store it in organic compounds generates chemical free energy on the planet (Kleidon, 2010). This free chemical energy can perform work in the Earth system, for example, by accelerating geochemical processes (Kleidon, 2010; Spohn and Breuer, 2010). Rosing et al. (2006) stated that photosynthesis contributes about three times more energy to geochemical cycles than Earth's internal heat engine at present day conditions. The authors suggested that this

source of energy fueled granite production, which led to the rise and stabilization of Earth's continents (Rosing et al., 2006). Höning et al. (2014) demonstrated that continents would cover only about 10% of Earth's surface in a hypothetical world in which life never had existed. Kleidon (2010) and others (Rosing et al., 2006; Spohn and Breuer, 2010; Dyke et al., 2011) go further, and speculate that photosynthetically generated energy and oxygen could even influence the Earth's interior, plate tectonics, mantle convection, and thus the geodynamo and Earth's magnetic field, where the latter prevents atmospheric escape and ozone depletion — essential conditions for multicellular life.

*The Rise of
Continents*

In this context, Lovelock and Margulis (1974) formulated the provocative *Gaia* hypothesis, which constitutes that Earth is a self-regulating system. They based their speculations on various processes induced by life to modify Earth to its net advantage. For instance, life introduced free oxygen in the atmosphere, which enabled the development of an effective ozone screen, which again shields organisms from harmful solar UV radiation (Kasting and Catling, 2003). Another example is the already described expansion of land plants and the associated draw-down of atmospheric CO₂ (mainly due to enhanced weathering rates), which helped to ensure Earth's long-term habitability (Foster et al., 2017). The *Gaia* hypothesis has been heavily criticized, but viewing Earth as an interconnected system of biological, chemical and physical processes has stimulated innovative research (Kleidon, 2010).

Gaia Hypothesis

In modern times, humans started to dominate Earth's surface and to change it on global and geological scales (Lewis and Maslin, 2015). Thus, Crutzen (2002) suggested the introduction of a new geological epoch, the *Anthropocene*. The discussion on the beginning of the Anthropocene is still ongoing. Lewis and Maslin (2015) proposed the arrival of Europeans in the Americas, which caused a catastrophic decline of the indigenous population by 95% (about 50 million deaths). The abandonment of agricultural areas facilitated the regrowth of forests, which resulted in a carbon sequestration of 5–40 Pg (Lewis and Maslin, 2015). It is thus speculated that this perturbation of the global carbon cycle significantly contributed to the decline of atmospheric CO₂ peaking between 1570 and 1620, which resulted in a subsequent cool period, known as the *Little Ice Age* (Dull et al., 2010; Lewis and Maslin, 2015).

Anthropocene

Zalasiewicz et al. (2008) suggested the onset of the industrial revolution as a starting point of the Anthropocene. The industrial revolution is characterized by the extraction and combustion of fossil fuels as source of energy — solar energy fixated by photosynthesis and stored in biomass over millions of years. Associated anthropogenic carbon emissions led to a sharp increase in atmospheric CO₂ concentration, unprecedented for at least 15–20 million years (Tripathi et al., 2009; Foster et al., 2017). This drastic human-induced perturbation of the

*Human Perturbation
of the Carbon Cycle*

global carbon cycle has significant consequences for the Earth system, the most prominent being climate change. The biosphere, particularly plants, play a central role in this, because they are getting more productive with rising CO₂ concentrations. This phenomenon is the topic I turn to next.

1.2 PLANTS, CO₂ AND CLIMATE

Carbon Cycle

Plants modulate land-atmosphere interactions through the exchange of energy, water and carbon. Stomata, microscopic pores on the surface of leaves, enable and regulate the gas exchange between the leaf interior and the atmosphere. In this way, plants absorb and fixate atmospheric carbon dioxide in sugars. This constitutes the largest flux in the global carbon cycle (~ 120 Pg C yr⁻¹; gross primary production, GPP; Beer et al., 2010; Schlesinger and Bernhardt, 2013). The assimilated sugars are allocated to grow leaves, stems, and roots, as well as to maintain the plant's metabolism (~ 60 Pg C yr⁻¹; autotrophic respiration; Schlesinger and Bernhardt, 2013). At equilibrium, the carbon fixed by plants reenters the atmosphere due to microbial respiration and decomposition processes (~ 60 Pg C yr⁻¹; heterotrophic respiration; Schlesinger and Bernhardt, 2013).

Hydrological Cycle

Through their root system, plants absorb water from soils. Especially trees are capable of pumping up groundwater from deeper soils. Due to the atmospheric demand for water (i.e. vapor pressure deficit), plants lose water vapor when opening their stomata (transpiration). Globally, the transpiration water flux is about 50% larger than the terrestrial evaporation flux (Schlesinger and Jasechko, 2014; Lian et al., 2018). As a consequence, transpiration constitutes a dominant force in the continental moisture recycling and accounts for about 40% of the precipitation over land (Schlesinger and Jasechko, 2014).

Surface Energy Fluxes

In addition to the exchange of moisture and carbon, plants influence Earth's surface properties through their persistent structures of leaves and stems (Kleidon, 2010). Foremost, photosynthetic absorption of solar radiation decreases the surface albedo. Further, vegetation's physical presence increases the surface roughness, which modulates the near-surface air flow (McPherson, 2007). Both processes affect the surface energy balance and thus have an impact on prevailing environmental conditions, such as the surface temperature (Kleidon, 2010; Schlesinger and Bernhardt, 2013).

The strength of these processes strongly depends on the vegetation type, which is determined by the regional climatological boundary conditions. Through interspecific (i.e. between species) competition an optimized plant functional type evolved for different environmental

conditions comprising the seasonal variations of temperature, incoming radiation, and large scale precipitation patterns. Köppen (1884) used the tight link between climate and vegetation in the definition and classification of Earth's climate zones (Köppen, 1884; Köppen, 1923).

Climate Zones

In the climate context, changes of vegetation are expressed in changes in leaf area index (LAI), defined as leaf area per unit ground area ($\text{m}^2 \text{m}^{-2}$). A persistent increase in LAI is referred to as vegetation greening, whereas a decline characterizes browning. Land use and land cover changes are characterized as direct anthropogenic drivers of vegetation changes (Chen et al., 2019), and mainly have local climatic effects due to changes of surface properties (neglecting associated carbon fluxes). Humans also indirectly affect global natural vegetation through carbon emissions from fossil fuel and biomass burning (indirect anthropogenic drivers). The enrichment of atmospheric CO₂ induces climate changes and the CO₂ fertilization effect of plants.

*Direct and Indirect
Vegetation Changes*

The term "CO₂ fertilization" conflates two effects of increased ambient CO₂ on the physiology of plants. Foremost, photosynthesis is generally CO₂-limited (Lemon, 1983). In the leaf interior, carbon assimilation is preformed by the macromolecule Ribulose 1,5-Bisphosphat Carboxylase/Oxygenase (RuBisCO), the most abundant enzyme on Earth (Foyer et al., 2009). However, RuBisCO also preforms photorespiration, a light-dependent reaction in which CO₂ is released and oxygen is consumed, similar to respiration. The relative rates of carbon assimilation and photorespiration are determined by the partial pressures of CO₂ and O₂ in the leaf interior, hence, CO₂ and O₂ compete for RuBisCO (Sharkey, 1988; Foyer et al., 2009). The physiological functions of photorespiration remain controversial (Foyer et al., 2009). The RuBisCO machinery evolved under a CO₂-rich and oxygen-poor atmosphere (Section 1.1), hence photorespiration was an insignificant process under these conditions (Foyer et al., 2009). At present-day conditions, roughly 25% of the incoming solar energy is used up by photorespiration, which classifies it to be among the most wasteful processes on the planet (Sharkey, 1988; Foyer et al., 2009). A back-of-the-envelope calculation based on the numbers for energy fluxes provided by Kleidon (2010), indicates that the energy loss due to photorespiration is about four times as high as the current primary energy consumption by humans. Overall, elevated CO₂ concentration in the interior of leaves stimulates higher rates of carbon and energy fixation (Leakey et al., 2009; Fatichi et al., 2016).

CO₂ Fertilization

Photorespiration

Simultaneously, the CO₂ enrichment in the atmosphere, and thus, in the leaf interior, decreases the demand of gas exchange between plants and atmosphere. As a consequence, plants adapt in lowering their stomatal conductance and thereby save soil moisture. The decrease in water loss through reduced plant transpiration results

Water-Use Efficiency in an enhanced water-use efficiency (ratio of carbon assimilation to transpiration rate; Ukkola et al., 2016; Fatichi et al., 2016). In theory, both effects – increased carbon assimilation and increased water-use efficiency – should result in an expansion of leaf area, especially in environments where plant growth is constrained by water availability (Donohue et al., 2009; Donohue et al., 2013; Ukkola et al., 2016).

Effects of Climatic Changes

The radiative effect of CO₂, namely the absorption and emission of infrared radiation in the atmosphere (greenhouse effect), induces climatic changes (temperature, precipitation, and radiation), which can affect ecosystems in either way. Temperature-limited biomes are expected to green due to warming and a prolongation of the growing season (Myneni et al., 1997; Nemani et al., 2003; Park et al., 2016). Persistent changes in rainfall, the most significant modulator of plant growth on global scale, can induce vegetation greening in water-limited ecosystems (Fensholt et al., 2012). On the other hand, long-term drying (Zhou et al., 2014) as well as increased intensity and frequency of disturbances (Seidl et al., 2017) such as droughts (Bonafant et al., 2016) and wildfires (Goetz et al., 2005; Verbyla, 2011) can induce regional vegetation browning trends. Changes in cloudiness determine the amount of radiation that reaches the surface, thus, changes in cloud cover can trigger or weaken plant growth (Nemani et al., 2003).

Other Factors

Other factors of greening and browning patterns can be associated to increased nitrogen deposition (in consequence of rising concentration of nitrogen oxides due to fossil fuel, biomass burning and application of agricultural synthetic fertilizer; Houlton and Morford, 2014), or ecosystem stress induced by insect outbreaks favored by climatic changes (Verbyla, 2011). However, these drivers are considered to be of minor importance on global scale (Zhu et al., 2016).

Carbon-Climate Feedbacks

The terrestrial biosphere and climate interact through a web of feedbacks (Ciais et al., 2013; Prentice et al., 2015). The most prominent example are the carbon-climate feedbacks (Friedlingstein et al., 2003; Schimel et al., 2015). Climate change is expected to reduce the terrestrial carbon fixation, especially in the tropics, resulting in a positive feedback in the climate-carbon system (Friedlingstein et al., 2003). On the other hand, rising CO₂ stimulates enhanced terrestrial carbon fixation through the physiological effects, inducing a negative feedback in the climate-carbon system (Friedlingstein et al., 2003).

1.3 OBSERVATIONAL EVIDENCE OF A GLOBALLY CHANGING VEGETATION

Over the last decades, several studies reported large-scale changes of the terrestrial biosphere. In 1996, a team led by David Charles Keeling demonstrated that plant productivity in the Northern Hemisphere

has increased since the 1960s analyzing the seasonal cycle of atmospheric CO₂ concentration (Keeling et al., 1996). More pronounced seasonal swings of atmospheric CO₂ concentration reflect an increased productivity of land vegetation. Based on the observational records from the Mauna Loa Observatory, Hawaii, and stations in the Arctic, the authors showed that northern hemispheric vegetation activity increased by 20%, and 40% in the Arctic. Moreover, they reported that phase changes in the seasonal cycle indicate a lengthening of the growing seasons by about seven days. They argued that increased surface temperatures are the main driver of the enhancement in northern vegetation activity – an early responder to global warming.

*Seasonal Cycle of
Atmospheric CO₂*

In the following year, Myneni et al. (1997) corroborated these findings using the first spaceborne measurements of Earth's spectral reflectances. Photosynthesizing organisms absorb solar radiation in the spectrum of visible light (wavelength of $\sim 0.4 - 0.7 \mu\text{m}$). So, changes in the measured reflectances are indicative of changes in the photosynthetic activity of Earth's surface. Myneni et al. (1997) demonstrated that the biospheric activity in the mid and high northern latitudes increased substantially throughout the 1980s. The satellite observations also confirmed the evidence of a prolongation of the growing season. The authors attributed the observed greening trend of the temperature-limited ecosystems to warming and the reduction in snow cover.

Greening North

In 2003, Nemani et al. (2003) demonstrated that the vegetation greening trend is a global phenomenon. Analyzing almost two decades of satellite observation, they report that especially the tropical forests exhibit intensified photosynthetic carbon fixation associated to climatic changes, mainly due to cloud cover. Several studies followed examining the detection of persistent declining trends in leaf area in the Earth's forests on regional scale (Goetz et al., 2005; Verbyla, 2011; Zhou et al., 2014). Zhu et al. (2016) presented the first global driver attribution of observed vegetation changes, focusing on the greening areas. On the basis of Earth system model simulations and the rich methodology of the Detection and Attribution discipline (e.g. Hasselmann, 1993; Ribes et al., 2013), they reported that 70% of the observed increase in vegetation can be tied to the CO₂ fertilization effect.

Greening Earth

Recent results by Chen et al. (2019) are challenging previous studies which identified the effects of CO₂ as main drivers of observed greening. The authors reported that more than one third of the vegetated area is greening in consequence of human land management, i.e. artificial irrigation, multiple cropping, and the application of fertilizers and pesticides (direct drivers). In general, the greening of anthropogenic vegetation has practically no long-term effect on the carbon

*Anthropogenic
Vegetation*

cycle, because CO₂ absorbed by agricultural plants quickly reenters the atmosphere through food consumption.

Natural Vegetation

Natural ecosystems, on the contrary, act as a strong carbon sink of anthropogenic emissions (Quéré et al., 2018b) and mitigate man-made climate change (Sitch et al., 2015; Bonan, 2008). A mechanistic understanding of natural vegetation dynamics in a CO₂-enriched atmosphere is thus critical and helps to answer one of the key question in current climate research, *where does the anthropogenic carbon go* (Marotzke et al., 2017)?

1.4 PAPER 1: EFFECTS OF RISING CO₂ ON GLOBAL NATURAL VEGETATION*Paper 1*

Several decades of satellite observations reveal widespread and persistent changes of the terrestrial vegetation across the globe. The controversial debate on the mechanisms underlying these changes is ongoing (Section 1.3). A detailed assessment of regionally dominating drivers on biome scale, but integrated in the global picture, is lacking. In light of nearly forty years of continuous satellite observations and the new generation of Earth system models, I conduct a driver attribution of global vegetation changes and challenge previous findings. I focus my analyses on the response of natural vegetation to the two main indirect drivers: the physiological and radiative effect of rising CO₂. In particular, I formulate the following guiding research questions:

1. **How is global natural vegetation changing in response to increasing CO₂ concentration?**
2. **What is causing vegetation greening and browning on biome level?**

*Research questions
in Paper 1*

In this study, I analyze 37 years of global LAI satellite observations (1982–2017) based on the Advanced Very High Resolution Radiometer (AVHRR) sensors (Zhu et al., 2013). Although these sensors have their limitations (Chen et al., 2019), the AVHRR record is unique in terms of its temporal coverage and opens up the opportunity to investigate the evolution of Earth’s vegetation while atmospheric CO₂ concentration increased by 65 ppm (341 to 406 ppm). Vegetation changes, i.e. greening or browning, are defined as annual averaged LAI sensitivity to rising CO₂ relative to the initial years of the record (1982–1984, denoted Δ). I develop a detailed biome map and identify spatial clusters of significant greening and browning trends in natural vegetation.

Further, I conduct a series of historical and factorial simulations with the latest version of the fully-coupled Max Planck Institute Earth system model (MPI-ESM, multiple realizations) and make use of a collection of 13 land surface models (LSMs) driven with observed climatic conditions (Quéré et al., 2018b, TRENDYv7 ensemble). As a first step, I examine if the historical simulations capture the observed behavior of natural vegetation under rising CO₂. Next, I analyze factorial simulations to disentangle and quantify the different effects of rising CO₂ on LAI. Each factorial experiment includes all historical forcings except one, which is retained at its pre-industrial conditions. The conventional approach in the field of Detection and Attribution is the optimal fingerprinting method (Hasselmann, 1993; Ribes et al.,

2013; Zhu et al., 2016). However, this framework is based on assumptions which are not suitable for the problem formulated in this study (Winkler et al., *submitted*). To overcome these limitations, I propose to apply the recently introduced approach of Causal Counterfactual Theory (Pearl, 2009; Hannart et al., 2016; Hannart and Naveau, 2018). This technique is anchored in a formal theory of event causation developed in computer science (Pearl, 2009; Marotzke, 2019). The method allows us to test if long-term greening/browning trends can be attributed to the effects of rising CO₂ in a probabilistic setting combining necessary and sufficient causation (PNS). More precisely, I address the question, what is the probability (i.e. PNS) that a given forcing (e.g. radiative effect of CO₂) has caused an observed long-term change in the system (e.g. greening of the Arctic).

Results

This is the first study that addresses vegetation browning as well as greening patterns across biomes on global scale. My analysis suggests, that greening is dominating in terms of area fraction, but browning clusters are beginning to emerge. Particularly, throughout the recent two decades, the Earth's greening trend is slowing down and clusters of browning are intensifying. I find that leaf area is primarily decreasing in the pan-tropical green belt of dense and biodiverse vegetation. Leaf area gain occurs mostly in sparsely vegetated regions in cold and/or arid climatic zones, and in the temperate forests. Taken together, vegetation greening occurs mainly in regions of low LAI, whereas browning happens primarily in regions of high LAI. In a global comparison, the greening of low LAI and the browning of high LAI induces a convergence of Earth's natural vegetation.

I identify clusters of greening and browning across all continents and conduct a regional driver attribution based on factorial model simulations. Figure 1 illustrates PNS for all greening and browning clusters, comparing the radiative, physiological, and the overall effect of CO₂. These results suggest that the physiological effect of CO₂ (i.e. "CO₂ fertilization") is merely the dominant driver of increasing leaf area in the temperate forests, cool arid grasslands and likely the Australian shrublands, but might only contribute slightly in other biomes. This finding questions the study by Zhu et al. (2016), who reported that CO₂ fertilization accounts for ~70% of the Earth's greening trend. My analysis suggests that many clusters of greening and browning bear the signature of climatic changes. For example, the greening of Sub-Saharan grasslands and savannas can be explained by increased rainfall, however, a robust attribution remains inconclusive. Climate changes, primarily warming and drying, also determine the patterns of vegetation changes in the northern ecosystems, i.e. greening of Eurasian boreal forests and North American tundra, but also emerging browning in Eurasian tundra. Models fail to capture the browning of the North American boreal forests. In the tropics, models suggest that rising CO₂ has compensatory effects on LAI. Climatic changes

induce browning, which is outbalanced by greening due to a strong CO₂ fertilization effect in models. Hence, if the physiological effect of CO₂ is neglected, models simulate browning patterns in the tropics comparable to observations.

The current generation of land surface models lack and/or misrepresent essential processes of the terrestrial biosphere. They mainly fail to capture the full extent of detrimental effects of rising CO₂ in natural ecosystems. Especially, the deficiency of reproducing the observed leaf area loss in the highly productive tropics has considerable implications on climate-carbon system projections. For the 21st century, estimates range from a stable CO₂ fertilization-driven carbon sink to a warming-induced collapse of the system at a certain CO₂ concentration (Cox et al., 2000). Hence, the tropical forests have the potential to crucially influence the evolution of climate in the next decades, and thus, should be a vital issue in model development and future research.

- 1. The Earth is predominantly greening in the extratropics, but browning clusters are emerging, mainly in the tropics.**
- 2. CO₂ fertilization is not the globally prevalent driver of greening as previously suggested. Many patterns of greening and browning can be attributed to climatic changes.**

*Key findings in
Paper 1*

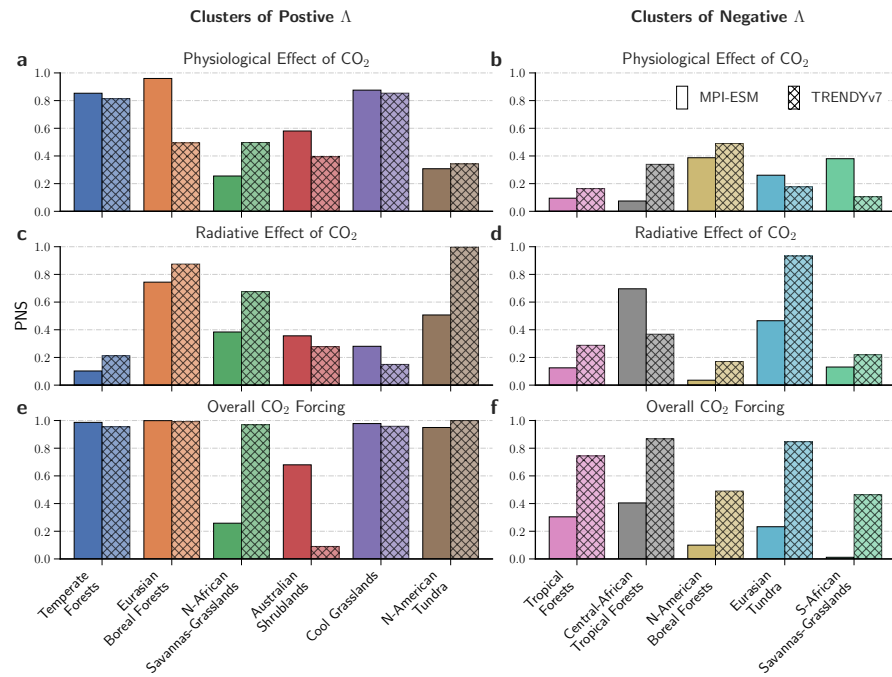


Figure 1 | Probabilities of sufficient and necessary causation (PNS) of LAI changes in response to CO₂ for eleven clusters. Bar charts represent PNS of LAI changes in response to the physiological effect (a, b), radiative effect of CO₂ (c, d) and all anthropogenic forcings (e, f). Different colors represent the identified clusters of substantial change in LAI. Panels on the left comprise clusters that show consistent greening, panels on the right represent emerging browning cluster (defined as observed net leaf area loss in the period 2000–2017). The two types of bar illustrate the two different ensembles of model simulations (left: MPI-ESM, right: TRENDYv7).

1.5 UNCERTAINTY IN THE TERRESTRIAL CARBON SINK

Next, I demonstrate how the obtained knowledge about historical vegetation changes can be used to reduce the uncertainty of a key unknown in current climate research – the future terrestrial carbon sink. But first, I explore the origins of this uncertainty.

Predicting climate change requires knowing where the emitted CO₂ (currently ~ 40 Pg CO₂ yr⁻¹; Quéré et al., 2018a) goes. The Global Carbon Project (GCP; Quéré et al., 2018a) regularly reports the updated global budget of carbon fluxes. The oceanic ($\sim 24\%$), and particularly, the airborne ($\sim 46\%$) fraction are considered to be robust estimates. Determining the increased carbon uptake by the terrestrial biosphere is more challenging. As a consequence, GCP did not estimate the land carbon sink independently, but rather considered it as the residual from the other terms ($\sim 30\%$) in the global budget, until recently (Quéré et al., 2018a). Given that the estimate of the current terrestrial carbon sink is uncertain, despite the variety of global observations, naturally, predicting the future terrestrial carbon sink is a complex endeavor.

The main source of uncertainty arises from the divergence of top-down (e.g. atmospheric CO₂ inversions, satellite observations) and bottom-up approaches (e.g. ecological *in-situ* studies). CO₂ fertilization and warming in temperature-limited ecosystems are expected to cause enhanced plant growth based on our physiological understanding (Section 1.2). From an atmospheric perspective, many studies find evidence for an increased plant productivity. For instance, the seasonal cycle of atmospheric CO₂ from multi-decadal measurements (Section 1.3; Keeling et al., 1996; Graven et al., 2013; Wenzel et al., 2016; Forkel et al., 2016) as well as global atmospheric CO₂ transport models clearly point at an increased carbon uptake by the terrestrial biosphere (Schimel et al., 2015; Fernández-Martínez et al., 2019). Several field studies, however, suggest that no significant carbon uptake can be determined. For instance, a number of free-air CO₂ enrichment (FACE) experiments revealed that biomass and/or leaf area are not significantly increasing in response to elevated CO₂ (Norby et al., 2003; Körner et al., 2005; Körner, 2006). However, other *in-situ* studies found evidence for increased vegetation productivity resulting from elevated atmospheric CO₂ levels (Leakey et al., 2009). These inconsistent findings and underlying mechanisms are matter of debate (Leakey et al., 2009; Norby and Zak, 2011). Norby et al. (2010) demonstrated that nutrient limitation, primarily nitrogen, suppresses or weakens the effect of CO₂ fertilization. Others suggested that the presence of mycorrhiza (i.e. symbiosis between fungi and plants) controls the strength of CO₂ fertilization (Terrer et al., 2016). Körner (2006) reviewed findings of FACE experiments across various biomes and concluded that photo-

synthetic carbon fixation in response to elevated CO₂ is by far not as high as anticipated.

But where does the residual term of ~ 3.2 Pg (GCP; Quéré et al., 2018b) of anthropogenic carbon emissions go every year, if plants do not absorb considerably more carbon with rising CO₂? In my second study, I employ a new method that combines observations and process-based model predictions to shed light upon the uncertainty in the terrestrial carbon sink.

1.6 PAPER 2: EMERGENT CONSTRAINT ON PROJECTED PHOTOSYNTHETIC CARBON FIXATION

Paper 2

Emergent Constraints

Pronounced uncertainty in the terrestrial carbon sink results in divergent trajectories of the evolution of the 21st century carbon cycle (Friedlingstein et al., 2013; Anav et al., 2013; Arora et al., 2013). In recent years, the concept of *Emergent Constraints* (EC) arose in this context, namely, a method to reduce uncertainty in ESM projections relying on the synergy of observations and historical simulations (Hall and Qu, 2006; Cox et al., 2013; Klein and Hall, 2015; Wenzel et al., 2016). The EC method consists of two parts, a linear relationship arising from the collective behavior of a multi-model ensemble and an observational estimate for imposing a constraint on the projections. The linear relationship is a physically (or physiologically) based correlation between inter-model variations in an observable entity of the contemporary climate system (*predictor*) and a projected variable (*predictand*). Combining the emergent linear relationship with observations of the predictor sets a constraint on the predictand (Knutti et al., 2017; Klein and Hall, 2015; Cox et al., 2013; Flato et al., 2013).

In my second paper, I apply the EC concept to reduce uncertainty in multi-model projections of terrestrial photosynthetic carbon fixation (gross primary production, GPP) using historical simulations and satellite observations of LAI. I focus my analysis on the northern high latitudes (NHL, north of 60° N), because of two reasons. First, the direct human impact (i.e. land management) can be neglected in this region, thus, I can assume that the observed changes reflect the response of natural ecosystems. Second, the observational evidence of an increased plant productivity in the recent decades is well established (e.g. Keeling et al., 1996; Myneni et al., 1997; Graven et al., 2013; Forkel et al., 2016; Wenzel et al., 2016; Winkler et al., submitted) – an important requisite in defining a robust predictor.

The enhanced GPP due to the radiative and physiological effects of CO₂ becomes evident in large scale increase in summer time green leaf area (Myneni et al., 1997; Zhu et al., 2016; Mao et al., 2016; Winkler et al., submitted). Satellite observations over the last three decades

reveal that 52% of the vegetated lands in the NHL show statistically significant greening trends, while only 12% show browning trends, mostly in the North American boreal forests due to disturbances (Goetz et al., 2005; Winkler et al., [submitted](#)). I therefore hypothesize that the LAI changes in response to increased CO₂ inferred from the historical period can be used to obtain a constrained estimate of future GPP enhancement from both the radiative and physiological effects. In particular, I pursue the following research questions in this study:

1. **Can we use the observed greening trends to constrain projections of photosynthetic carbon fixation under rising CO₂?**
2. **If so, is the *Emergent Constraint* in agreement with other observational estimates?**

*Research questions
in Paper 2*

I use two sets of simulations available from seven ESMs from the Coupled Model Intercomparison Project Phase 5 (CMIP5; Taylor et al., 2012) – one with historical forcings including anthropogenic CO₂ emissions for the period 1850–2005, and the second with idealized forcing (1% CO₂ increase per year, compounded annually, starting from a pre-industrial value of 284 ppm until quadrupling). Leaf area changes are represented as changes in annual maximum LAI (LAI_{max}), a good measure in the comparison of observations and models (Cook and Pau, 2013). The magnitude of the physiological effect is represented by the CO₂ concentration and the radiative effect by growing degree days (GDDo, > 0° C) as plant growth in NHL is principally limited by the growing season temperature (Nemani et al., 2003). To avoid redundancy from co-linearity between the two driver variables, but retain their underlying time-trend and interannual variability, I use the dominant mode from a principal component analysis of CO₂ and GDDo as the proxy driver (denoted ω). For models and observations alike, I derive the LAI_{max} sensitivity to the forcing signal ω (m² m⁻² per unit ω , hereafter greening sensitivity), which constitutes the predictor in the EC analysis (Figure 2a). The predictand is defined as the absolute increase in GPP (Δ GPP) arising from the combined radiative and physiological effects for a doubling of the atmospheric CO₂ concentration (2×CO₂).

The CMIP5 models show a large spread in both modeled historical greening sensitivities (predictor, Figure 2a and 2b) and Δ GPP at 2×CO₂ (predictand, Figure 2c). The inter-model variation in the predictor maps linearly to variation in the predictand (Figure 2c). More precisely, models with low LAI_{max} sensitivity (Figure 2b) project lower Δ GPP for a given increment of CO₂ concentration, and *vice versa*. This linear relation in inter-model variation together with the observed estimate of the predictor renders the application of an EC on

Results

Δ GPP at $2\times$ CO₂ possible. Moreover, the probability contours about the best linear fit across the ensemble together with the uncertainty in the observed predictor (blue and grey shadings in 2c) allow a robust characterization of the constrained estimate, namely 3.4 ± 0.2 Pg C yr⁻¹ for $2\times$ CO₂ in NHL (Figure 2d). This EC estimate is $\sim 60\%$ larger than the conventionally used multi-model mean value (2.1 ± 1.91 Pg C yr⁻¹ for $2\times$ CO₂ in NHL). To imbue confidence in the EC estimate, I derive three independent comparable estimates from long-term *in-situ* atmospheric CO₂ measurements and atmospheric inversions (details in Winkler et al., 2019a).

The presented LAI-based analyses corroborate the findings of a substantial increase of plant carbon fixation in the NHL (Keeling et al., 1996; Forkel et al., 2016; Ciais et al., 2019). These results challenge the field studies, which could not detect a considerable increase in carbon fixation under elevated CO₂ (Körner, 2006). I argue, that FACE experiments due to their design of a sharp increase of CO₂ concentration (quasi-instant forcing of >100 ppm) are not representative for the real-world response (annual forcing of 2-3 ppm). In this study, I demonstrated how the synthesis of observations and models through the EC concept can help to reduce uncertainty of the future terrestrial carbon sink. The EC method also has its limitations which is the topic I turn to next.

*Key findings in
Paper 2*

1. **The greening sensitivity can be used as an Emergent Constraint on projections of photosynthesis enhancement in a $2\times$ CO₂ world (3.4 ± 0.2 Pg C yr⁻¹ in NHL).**
2. **Independent lines of evidence corroborate the Emergent Constraint estimate indicating that most models underestimate the effect of rising CO₂ on photosynthesis.**

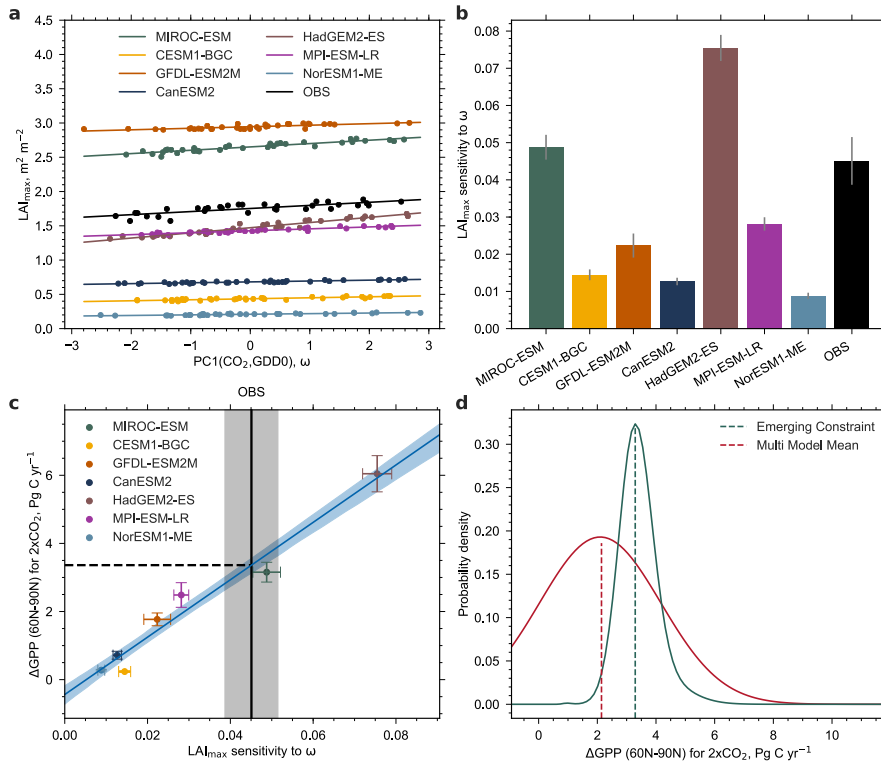


Figure 2 | CMIP5 ensemble mean considerably underestimates absolute increase of GPP for a doubling of pre-industrial atmospheric CO₂ concentration ($2\times\text{CO}_2$). **a**, Observations (black) and CMIP5 historical simulations (colors) of the first principal component of annual mean atmospheric CO₂ and annual growing degree days above 0 °C (ω) versus the annual LAI_{max}. All quantities are area weighted and spatially averaged for NHL (60°N - 90°N). **b**, Bar chart showing the corresponding slopes of the best linear fits, where the grey bar at the top indicates the standard error. Linear trends are derived for the period 1982-2016 for observations and 1971-2005 for model simulations, maximizing the overlap and sample size. **c**, Linear relationship between the sensitivity of annual LAI_{max} to ω (x axis) and the absolute increase of high-latitude GPP at $2\times\text{CO}_2$. Each model is represented by an individually colored marker with error bars indicating one standard deviation (y axis) and standard error (x axis). The black solid line shows observed sensitivity, where the grey shading indicates the respective standard error. The blue line shows the best linear fit across the CMIP5 ensemble including the 68% confidence interval estimated by bootstrapping (blue shading; Methods). The intersection of the blue and black line gives the Emerging Constraint on ΔGPP at $2\times\text{CO}_2$ (dashed black line). **d**, Probability density functions resulting from Emerging Constraint (blue) and CMIP5 ensemble mean estimates (red, assuming Gaussian distribution).

1.7 PAPER 3: INVESTIGATING THE APPLICABILITY OF EMERGENT CONSTRAINTS

Paper 3 The concept of EC constitutes a pivotal method in reducing uncertainty in climate and carbon cycle projections and becomes evermore popular (e.g. Mystakidis et al., 2016; Wenzel et al., 2016; Cox et al., 2018; Lian et al., 2018; Hall et al., 2019). However, a detailed analysis of its applicability and limitations is lacking.

The robustness of the reported EC estimates is still controversially debated. For example, Cox et al. (2013), Wang et al. (2014), and Wenzel et al. (2015) investigated on constraining future terrestrial tropical carbon storage using the same set of models and observations. However, they arrived at different EC estimates and divergent conclusions. Some reasons for the failure and essential criteria required for successful application of the EC approach were described previously (Bracegirdle and Stephenson, 2012; Klein and Hall, 2015), but this list is far from complete. Thus, a detailed investigation of potential sources of uncertainty and limitations of the EC method is needed. In particular, the guiding research questions of my third study read as follows:

*Research questions
in Paper 3*

1. **What are potential sources of uncertainty in the Emergent Constraint approach?**
2. **What are the limitations of the applicability of the Emergent Constraint method?**

In general terms, the EC method utilizes a measurable variable (i.e. predictor) from the recent historical past to obtain a constrained estimate of change in an entity (i.e. predictand) that is difficult-to-measure and/or at a potential future state (i.e. CO₂ forcing; Figure 3). This procedure critically depends on, first, accurate estimation of the predictor from observations and models, and second, on a robust relationship between inter-model variations in the predictor-predictand space. Here, I revisit the EC analysis presented in Section 1.6 (Winkler et al., 2019a) and elaborate on key issues related to these two themes.

First, I address potential uncertainties rooted in spatial aggregation of data and model simulations, as the EC method is applied on large areal values of predictor and predictand. This requires an investigation into uncertainties in the observational data source and an evaluation of the spatial and temporal variability of the predictor in both observations and model simulations. Second, the relationship between the predictor (here LAI_{max} sensitivity to ω) and the predictand (here Δ GPP) across the model ensemble depends on a strong

coupling among simultaneous changes in the entities. This coupling depends in a complex manner on the magnitude (level), time-rate of application (scenarios) and effects (e.g. radiative and/or physiological) of CO₂ forcing. I investigate how each one of these three aspects of forcing can impair the EC estimate of the predictand (ΔGPP).

The observational uncertainty, as in many statistical methods, is an important issue. The EC method, however, is particularly sensitive to observational uncertainty, because the single observational predictor essentially determines the constrained estimate. On the contrary, the emergent linear relationship, the second component of the EC approach, is established based on a collection of multi-model estimates, where each model gets 'one vote' (however, some models might be more influential than others; Bracegirdle and Stephenson, 2012). Thus, the observational uncertainty has a much larger bearing on the EC than the uncertainty of each individual model. To overcome this source of uncertainty, I argue, that various meaningful observations, if applicable, should be taken into consideration.

Results

A large source of uncertainty is associated with temporal variability and model-observations comparability of the predictor. The evaluation of the predictor requires temporal window lengths of sufficient duration (high signal-to-noise ratio; ~ 30 years, dependent on the variable). Further, the estimation of modeled and observed predictor needs to be based on temporally matching window length and location along the forcing time line. In other words, it is important that all predictors describe the system for the same state of forcing. For example, some analyses (e.g. Wenzel et al., 2016) might have yielded different results and conclusions if model and observational predictors were temporally matched.

The EC method raises an obvious question – does it not implicitly assume that the key operative mechanisms underpinning the EC relation remain unchanged because a future system state is being predicted based on its past behavior (i.e. assumption of linearity)? To investigate this hypothesis, I perform a thought experiment combining linear and non-linear predictor-predictand relationships. I demonstrate that changes in predictor and predictand relate linearly within the model ensemble, given the models agree on the system dynamics under increasing forcing. For instance, the relationship underpinning the EC approach presented in Winkler et al. (2019a), namely, concurrent changes of ΔGPP and $\Delta\text{LAI}_{\text{max}}$, saturate at higher CO₂ concentration (i.e. non-linear response for e.g. $3\times\text{CO}_2$) I find that all CMIP5 models agree on the this saturation effect, and thus, the predictor-predictand linear relationship in the ensemble holds. However, at even higher CO₂ concentrations, the models diverge at which point the predictor-predictand relation breaks down and the EC method fails.

Another intriguing finding is that photosynthesis seems to exhibit a pathway-dependence (e.g. different RCP scenarios). This means, that the projections of enhanced plant productivity vary among different time rates of forcing, but fixed magnitude (i.e. same increment of CO₂). This aspect could be related to memory effects and/or non-linearities in the system, which require further investigation and should be taken into account when estimating the predictand.

In this study, I addressed various aspects of the EC method. My findings are illustrated by means of a carbon cycle example, however, they generally contribute to a more robust application of the EC method in Earth system sciences.

*Key findings in
Paper 3*

- 1. Potential sources of uncertainty in the EC method are associated to model-observation comparability, temporal variability, and observational data source of the predictor.**
- 2. Limitations of the EC method primarily originate from a disagreement between models on system dynamics.**

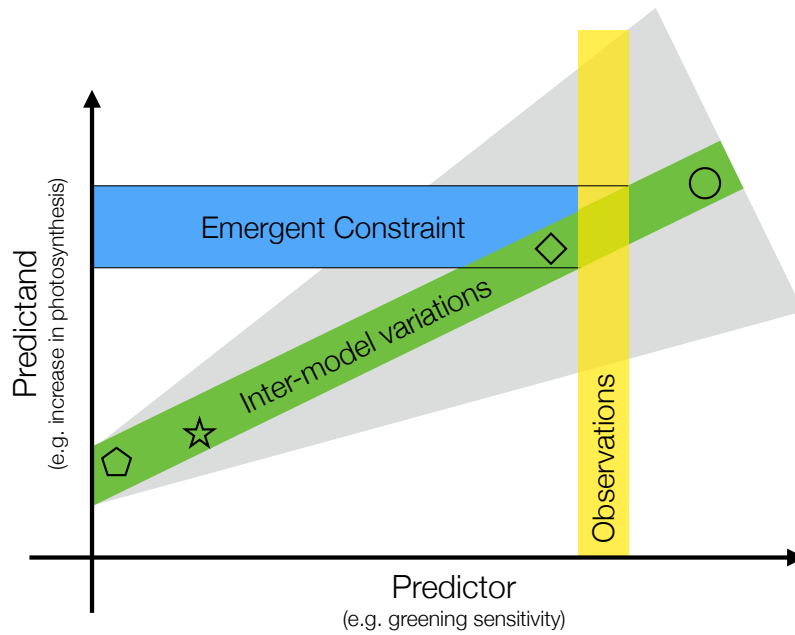


Figure 3 | Schematic depiction of the *Emergent Constraint* (EC) method and factors affecting the uncertainty of the constrained estimate. The predictor (x axis) is change in annual maximum of green leaf area index (LAI_{max}) due to unit forcing (CO_2 increase and associated climatic changes) during a representative historical period. It is termed greening sensitivity in this study. The predictand (y axis) is projected changes in Gross Primary Productivity (GPP) in response to rising CO_2 concentration (e.g. for a doubling of the pre-industrial level). Both the predictor and predictand refer to large area values, in this case, the entire Northern High Latitudes (NHL). Inter-model variations (each symbol represents a model) in matching pairs of predictor and predictand result in a linear relationship between the two (green band), i.e. the ratio (predictand/predictor) is approximately constant across the model ensemble. The slope depends on forcing attributes (gray shading), such as its level (CO_2 concentration), time rate of application (scenarios such as various RCPs) and different effects (i.e. fertilization, radiative, etc.). The observed sensitivity (yellow vertical bar) is used to find the constrained estimate of the predictand (i.e. change in GPP). The ability to accurately estimate the predictor depends on the source of observational data, and its spatial and temporal variability. Observed (yellow bar) and modeled predictor values (x coordinate of symbols) must be obtained from matching time periods, i.e. at the same level of historical forcing, to ensure comparability. All these factors, together with the goodness-of-fit of inter-model variations (width of green shading), finally define the uncertainty of the derived constrained estimate (blue horizontal bar with black solid lines depicting the upper and lower bound of uncertainty).

1.8 OUTLOOK

Erwin Schrödinger in his book *What Is Life?* (1943) questions whether life can be accounted for by physics and chemistry (see quotation at the beginning of this essay). Since Schrödinger wrote those lines, our scientific understanding of life has advanced considerably. However, we still are unable to formulate general laws describing the mechanics of life.

In the context of climate change, this means that the influence of organisms as well as their capability to adapt to a high-CO₂ world remain unknown. For example, some plant species already adjust and develop leaves with fewer stomata, because there is a lower demand for gas exchange with a CO₂-enriched atmosphere (Lammertsma et al., 2011; Boer et al., 2011). But why do some plant species pursue this strategy and others do not? Will the plants that pursue this strategy continue to do so? Such questions were already at the center of attention during the international conference on *CO₂ And Plants: The Response Of Plants To Rising Levels Of Atmospheric Carbon Dioxide* in 1982. Lemon (1983) stated in the proceedings of this conference, that the scientific community of plant physiologists is mainly retrospective, in that they explain observed changes, but they are not predictive. Almost four decades later we have access to an extensive collection of different observational datasets that reflect how plants respond to rising CO₂ concentrations. This not only enables us to explain the observed changes in a robust way (Winkler et al., submitted), but also to take the next step and use this knowledge to predict the response of plants to further rising CO₂ (Winkler et al., 2019a; Winkler et al., 2019b).

The profound changes of Earth's surface as observed from space reflect the human dominance on the planet. In the first part of this thesis, I demonstrate that the extratropical terrestrial biosphere is predominantly greening due to warming and the fertilization effect induced by anthropogenic CO₂ emissions. In the tropics, only the sub-Saharan area exhibits a profound increase in plant productivity, mainly due to enhanced rainfall, which is an important development for human livelihood in these semi-arid regions. However, these ecosystems and thus food security are also particularly susceptible to climatic changes and variability (Fensholt et al., 2012). This is a vital issue, because sub-Saharan Africa is expected to account for the majority of global population growth in the 21st century (Osborne, 2016). Future research should therefore focus on how precipitation and plant productivity develop in these regions with further rise in atmospheric CO₂ concentration.

Another central finding of my work is that greening trends across various biomes are slowing down and browning clusters are beginning

to emerge in consequence of climatic changes. This development is particularly prominent in the tropical forests. The Amazon, the largest rainforest, is afflicted by episodic droughts which increase in frequency (Cai et al., 2014) and intensity (Fasullo et al., 2018). In tropical Africa on the other hand, the browning of forests is driven by a persistent drying trend (Zhou et al., 2014). Declining leaf area in the tropical forests is particularly of concern, because these ecosystems harbor the most diverse flora and fauna of the planet. My analyses demonstrate that extratropical and tropical forests show opposed responses to rising CO₂. This asymmetric development should be studied in more detail to assess how long the extratropics can compensate for the losses in the tropics.

Since 1870, the terrestrial biosphere absorbed about ~190 Pg of carbon, which is approximately equivalent to the cumulative sum of all carbon emissions due to the combustion of coal (Quéré et al., 2018b). However, future predictions of the strength of the land carbon sink are uncertain. In the second and third part of my dissertation, I address this problem using the method of *Emergent Constraints*, which combines large-scale satellite observations, ground measurements and multiple model simulations. The observational-based constraints suggest that photosynthetic carbon fixation of northern ecosystems in a high-CO₂ world is more substantial than most models predict. I scrutinized the method of *Emergent Constraints* and examined independent sources of observations to imbue confidence in my findings. My conclusions are in line with the growing evidence that the extratropical ecosystems absorb most of the anthropogenic carbon (Peñuelas et al., 2017; Song et al., 2018; Ciais et al., 2019). This means that the tropics, which account for ~60% of the global gross primary production (Beer et al., 2010), remain the key uncertainty in the carbon cycle of the 21st century. In accordance with the findings of this thesis, several studies (e.g. Cox et al., 2013; Peñuelas et al., 2017; Baccini et al., 2017) suggest that CO₂-induced forest dieback is strengthening, which might cause the tropics to switch from a net carbon sink to a source. My analyses show that the current generation of models largely underestimate vegetation browning in the tropical rainforests. Hence, the latest climate projections do not account for the potential of a weakening terrestrial carbon sink, which could pose a further obstacle in achieving the international targets as defined by the Paris agreement (Rogelj et al., 2016). Model development must focus on a better representation of the response of tropical forests to rising CO₂ and associated effects in order to realize plausible climate projections for the coming decades.

At the time when it was still being discussed whether the CO₂ concentration was actually increasing, the Russian scientists Rusin and Flit (1966) had already recognized the potential of the terrestrial biosphere in shaping climate. The first lines of their book *Man Versus Climate* read as follows: "Plant life and climate are closely linked;

plants exert a major influence on the climate, but at the same time are greatly dependent on it" (Rusin and Flit, 1966). The results of my dissertation on the Earth's transition to a high CO₂ state show that this statement from half a century ago is even more relevant today.

BIBLIOGRAPHY

- Anav, A. et al. (2013). "Evaluating the Land and Ocean Components of the Global Carbon Cycle in the CMIP5 Earth System Models." *Journal of Climate* 26.18, pp. 6801–6843. DOI: [10.1175/JCLI-D-12-00417.1](https://doi.org/10.1175/JCLI-D-12-00417.1).
- Arora, V. K. et al. (2013). "Carbon–Concentration and Carbon–Climate Feedbacks in CMIP5 Earth System Models." *Journal of Climate* 26.15, pp. 5289–5314. DOI: [10.1175/JCLI-D-12-00494.1](https://doi.org/10.1175/JCLI-D-12-00494.1).
- Baccini, A. et al. (2017). "Tropical Forests Are a Net Carbon Source Based on Aboveground Measurements of Gain and Loss." *Science*, eaam5962. DOI: [10.1126/science.aam5962](https://doi.org/10.1126/science.aam5962).
- Beer, C. et al. (2010). "Terrestrial Gross Carbon Dioxide Uptake: Global Distribution and Covariation with Climate." *Science* 329.5993, pp. 834–838. DOI: [10.1126/SCIENCE.1184984](https://doi.org/10.1126/SCIENCE.1184984).
- Boer, H. J. de et al. (2011). "Climate Forcing Due to Optimization of Maximal Leaf Conductance in Subtropical Vegetation under Rising CO₂." *Proceedings of the National Academy of Sciences* 108.10, pp. 4041–4046. DOI: [10.1073/pnas.1100555108](https://doi.org/10.1073/pnas.1100555108).
- Bonal, D., B. Burban, C. Stahl, F. Wagner, and B. Hérault (2016). "The Response of Tropical Rainforests to Drought—Lessons from Recent Research and Future Prospects." *Annals of Forest Science* 73, pp. 27–44. DOI: [10.1007/S13595-015-0522-5](https://doi.org/10.1007/S13595-015-0522-5).
- Bonan, G. B. (2008). "Forests and Climate Change: Forcings, Feedbacks, and the Climate Benefits of Forests." *Science* 320.5882, pp. 1444–1449. DOI: [10.1126/science.1155121](https://doi.org/10.1126/science.1155121).
- Bracegirdle, T. J. and D. B. Stephenson (2012). "On the Robustness of Emergent Constraints Used in Multimodel Climate Change Projections of Arctic Warming." *Journal of Climate* 26.2, pp. 669–678. DOI: [10.1175/JCLI-D-12-00537.1](https://doi.org/10.1175/JCLI-D-12-00537.1).
- Cai, W. et al. (2014). "Increasing Frequency of Extreme El Niño Events Due to Greenhouse Warming." *Nature Climate Change* 4.2, pp. 111–116. DOI: [10.1038/NCLIMATE2100](https://doi.org/10.1038/NCLIMATE2100).
- Chen, C. et al. (2019). "China and India Lead in Greening of the World through Land-Use Management." *Nature Sustainability* 2.2, p. 122. DOI: [10.1038/s41893-019-0220-7](https://doi.org/10.1038/s41893-019-0220-7).
- Ciais, P. et al. (2013). "Carbon and Other Biogeochemical Cycles." In: *Climate Change 2013: The Physical Science Basis. Contribution of Working Group I to the Fifth Assessment Report of the Intergovernmental Panel on Climate Change*. Ed. by T. Stocker et al. Cambridge, United Kingdom and New York, NY, USA: Cambridge University Press, pp. 465–570. ISBN: ISBN 978-1-107-66182-0.

- Ciais, P. et al. (2019). "Five Decades of Northern Land Carbon Uptake Revealed by the Interhemispheric CO₂ Gradient." *Nature* 568.7751, p. 221. DOI: [10.1038/s41586-019-1078-6](https://doi.org/10.1038/s41586-019-1078-6).
- Cook, B. I. and S. Pau (2013). "A Global Assessment of Long-Term Greening and Browning Trends in Pasture Lands Using the GIMMS LAI3g Dataset." *Remote Sensing* 5.5, pp. 2492–2512. DOI: [10.3390/rs5052492](https://doi.org/10.3390/rs5052492).
- Cox, P. M., R. A. Betts, C. D. Jones, S. A. Spall, and I. J. Totterdell (2000). "Acceleration of Global Warming Due to Carbon-Cycle Feedbacks in a Coupled Climate Model." *Nature* 408.6809, pp. 184–187. DOI: [10.1038/35041539](https://doi.org/10.1038/35041539).
- Cox, P. M. et al. (2013). "Sensitivity of Tropical Carbon to Climate Change Constrained by Carbon Dioxide Variability." *Nature* 494.7437, pp. 341–344. DOI: [10.1038/nature11882](https://doi.org/10.1038/nature11882).
- Cox, P. M., C. Huntingford, and M. S. Williamson (2018). "Emergent Constraint on Equilibrium Climate Sensitivity from Global Temperature Variability." *Nature* 553.7688, pp. 319–322. DOI: [10.1038/nature25450](https://doi.org/10.1038/nature25450).
- Crutzen, P. J. (2002). "Geology of Mankind." *Nature* 415.6867, p. 23. DOI: [10.1038/415023a](https://doi.org/10.1038/415023a).
- Donohue, R. J., T. R. McVicar, and M. L. Roderick (2009). "Climate-Related Trends in Australian Vegetation Cover as Inferred from Satellite Observations, 1981–2006." *Global Change Biology* 15.4, pp. 1025–1039. DOI: [10.1111/j.1365-2486.2008.01746.x](https://doi.org/10.1111/j.1365-2486.2008.01746.x).
- Donohue, R. J., M. L. Roderick, T. R. McVicar, and G. D. Farquhar (2013). "Impact of CO₂ Fertilization on Maximum Foliage Cover across the Globe's Warm, Arid Environments." *Geophysical Research Letters* 40.12, pp. 3031–3035. DOI: [10.1002/grl.50563](https://doi.org/10.1002/grl.50563).
- Dull, R. A. et al. (2010). "The Columbian Encounter and the Little Ice Age: Abrupt Land Use Change, Fire, and Greenhouse Forcing." *Annals of the Association of American Geographers* 100.4, pp. 755–771. DOI: [10.1080/00045608.2010.502432](https://doi.org/10.1080/00045608.2010.502432).
- Dyke, J. G., F. Gans, and A. Kleidon (2011). "Towards Understanding How Surface Life Can Affect Interior Geological Processes: A Non-Equilibrium Thermodynamics Approach." *Earth System Dynamics* 2.1, pp. 139–160. DOI: <https://doi.org/10.5194/esd-2-139-2011>.
- Fasullo, J. T., B. L. Otto-Bliesner, and S. Stevenson (2018). "ENSO's Changing Influence on Temperature, Precipitation, and Wildfire in a Warming Climate." *Geophysical Research Letters* 45.17, pp. 9216–9225. DOI: [10.1029/2018GL079022](https://doi.org/10.1029/2018GL079022).
- Fatichi, S. et al. (2016). "Partitioning Direct and Indirect Effects Reveals the Response of Water-Limited Ecosystems to Elevated CO₂." *Proceedings of the National Academy of Sciences* 113.45, pp. 12757–12762. DOI: [10.1073/pnas.1605036113](https://doi.org/10.1073/pnas.1605036113).
- Fensholt, R. et al. (2012). "Greenness in Semi-Arid Areas across the Globe 1981–2007 — an Earth Observing Satellite Based Analysis of

- Trends and Drivers." *Remote Sensing of Environment* 121, pp. 144–158. DOI: [10.1016/j.rse.2012.01.017](https://doi.org/10.1016/j.rse.2012.01.017).
- Fernández-Martínez, M. et al. (2019). "Global Trends in Carbon Sinks and Their Relationships with CO₂ and Temperature." *Nature Climate Change* 9.1, p. 73. DOI: [10.1038/s41558-018-0367-7](https://doi.org/10.1038/s41558-018-0367-7).
- Flato, G. et al. (2013). "Evaluation of Climate Models." In: *Climate Change 2013: The Physical Science Basis. Contribution of Working Group I to the Fifth Assessment Report of the Intergovernmental Panel on Climate Change*. Ed. by T. Stocker et al. Cambridge, United Kingdom and New York, NY, USA: Cambridge University Press, pp. 741–866. ISBN: ISBN 978-1-107-66182-0.
- Forkel, M. et al. (2016). "Enhanced Seasonal CO₂ Exchange Caused by Amplified Plant Productivity in Northern Ecosystems." *Science* 351.6274, pp. 696–699. DOI: [10.1126/science.aac4971](https://doi.org/10.1126/science.aac4971).
- Foster, G. L., D. L. Royer, and D. J. Lunt (2017). "Future Climate Forcing Potentially without Precedent in the Last 420 Million Years." *Nature Communications* 8, p. 14845. DOI: [10.1038/ncomms14845](https://doi.org/10.1038/ncomms14845).
- Foyer, C. H., A. J. Bloom, G. Queval, and G. Noctor (2009). "Photorespiratory Metabolism: Genes, Mutants, Energetics, and Redox Signaling." *Annual Review of Plant Biology* 60.1, pp. 455–484. DOI: [10.1146/annurev.arplant.043008.091948](https://doi.org/10.1146/annurev.arplant.043008.091948).
- Friedlingstein, P., J.-L. Dufresne, P. M. Cox, and P. Rayner (2003). "How Positive Is the Feedback between Climate Change and the Carbon Cycle?" *Tellus B* 55.2, pp. 692–700. DOI: [10.1034/j.1600-0889.2003.01461.x](https://doi.org/10.1034/j.1600-0889.2003.01461.x).
- Friedlingstein, P. et al. (2013). "Uncertainties in CMIP5 Climate Projections Due to Carbon Cycle Feedbacks." *Journal of Climate* 27.2, pp. 511–526. DOI: [10.1175/JCLI-D-12-00579.1](https://doi.org/10.1175/JCLI-D-12-00579.1).
- Goetz, S. J., A. G. Bunn, G. J. Fiske, and R. A. Houghton (2005). "Satellite-Observed Photosynthetic Trends across Boreal North America Associated with Climate and Fire Disturbance." *Proceedings of the National Academy of Sciences of the United States of America* 102.38, pp. 13521–13525. DOI: [10.1073/pnas.0506179102](https://doi.org/10.1073/pnas.0506179102).
- Graven, H. D. et al. (2013). "Enhanced Seasonal Exchange of CO₂ by Northern Ecosystems Since 1960." *Science* 341.6150, pp. 1085–1089. DOI: [10.1126/science.1239207](https://doi.org/10.1126/science.1239207).
- Hall, A. and X. Qu (2006). "Using the Current Seasonal Cycle to Constrain Snow Albedo Feedback in Future Climate Change." *Geophysical Research Letters* 33.3, p. L03502. DOI: [10.1029/2005GL025127](https://doi.org/10.1029/2005GL025127).
- Hall, A., P. Cox, C. Huntingford, and S. Klein (2019). "Progressing Emergent Constraints on Future Climate Change." *Nature Climate Change* 9.4, pp. 269–278. DOI: [10.1038/s41558-019-0436-6](https://doi.org/10.1038/s41558-019-0436-6).
- Hannart, A., J. Pearl, F. E. L. Otto, P. Naveau, and M. Ghil (2016). "Causal Counterfactual Theory for the Attribution of Weather and Climate-Related Events." *Bulletin of the American Meteorological Society* 97.1, pp. 99–110. DOI: [10.1175/BAMS-D-14-00034.1](https://doi.org/10.1175/BAMS-D-14-00034.1).

- Hannart, A. and P. Naveau (2018). "Probabilities of Causation of Climate Changes." *Journal of Climate* 31.14, pp. 5507–5524. DOI: [10.1175/JCLI-D-17-0304.1](https://doi.org/10.1175/JCLI-D-17-0304.1).
- Hasselmann, K. (1993). "Optimal Fingerprints for the Detection of Time-Dependent Climate Change." *Journal of Climate* 6.10, pp. 1957–1971. DOI: [10.1175/1520-0442\(1993\)006<1957:OFFTDO>2.0.CO;2](https://doi.org/10.1175/1520-0442(1993)006<1957:OFFTDO>2.0.CO;2).
- Holland, H. D. (2006). "The Oxygenation of the Atmosphere and Oceans." *Philosophical Transactions of the Royal Society B: Biological Sciences* 361.1470, pp. 903–915. DOI: [10.1098/rstb.2006.1838](https://doi.org/10.1098/rstb.2006.1838).
- Höning, D., H. Hansen-Goos, A. Airo, and T. Spohn (2014). "Biotic vs. Abiotic Earth: A Model for Mantle Hydration and Continental Coverage." *Planetary and Space Science*. Planetary Evolution and Life 98, pp. 5–13. DOI: [10.1016/j.pss.2013.10.004](https://doi.org/10.1016/j.pss.2013.10.004).
- Houlton, B. Z. and S. L. Morford (2014). "A New Synthesis for Terrestrial Nitrogen Inputs." *SOIL Discussions* 1, pp. 497–540. DOI: [10.5194/soild-1-497-2014](https://doi.org/10.5194/soild-1-497-2014).
- Kasting, J. F. and D. Catling (2003). "Evolution of a Habitable Planet." *Annual Review of Astronomy and Astrophysics* 41.1, pp. 429–463. DOI: [10.1146/annurev.astro.41.071601.170049](https://doi.org/10.1146/annurev.astro.41.071601.170049).
- Keeling, C. D., J. F. S. Chin, and T. P. Whorf (1996). "Increased Activity of Northern Vegetation Inferred from Atmospheric CO₂ Measurements." *Nature* 382.6587, pp. 146–149. DOI: [10.1038/382146a0](https://doi.org/10.1038/382146a0).
- Kleidon, A. (2010). "Life, Hierarchy, and the Thermodynamic Machinery of Planet Earth." *Physics of Life Reviews* 7.4, pp. 424–460. DOI: [10.1016/j.plrev.2010.10.002](https://doi.org/10.1016/j.plrev.2010.10.002).
- Klein, S. A. and A. Hall (2015). "Emergent Constraints for Cloud Feedbacks." *Current Climate Change Reports* 1.4, pp. 276–287. DOI: [10.1007/s40641-015-0027-1](https://doi.org/10.1007/s40641-015-0027-1).
- Knauth, L. P. and M. J. Kennedy (2009). "The Late Precambrian Greening of the Earth." *Nature* 460.7256, pp. 728–732. DOI: [10.1038/nature08213](https://doi.org/10.1038/nature08213).
- Knutti, R. et al. (2017). "A Climate Model Projection Weighting Scheme Accounting for Performance and Interdependence." *Geophysical Research Letters* 44.4, pp. 1909–1918. DOI: [10.1002/2016GL072012](https://doi.org/10.1002/2016GL072012).
- Kopp, R. E., J. L. Kirschvink, I. A. Hilburn, and C. Z. Nash (2005). "The Paleoproterozoic Snowball Earth: A Climate Disaster Triggered by the Evolution of Oxygenic Photosynthesis." *Proceedings of the National Academy of Sciences of the United States of America* 102.32, pp. 11131–11136. DOI: [10.1073/pnas.0504878102](https://doi.org/10.1073/pnas.0504878102).
- Köppen, W. P. (1923). *Die Klimate Der Erde: Grundriss Der Klimakunde*. Berlin und Leipzig: Walter de Gruyter. 369 pp.
- Köppen, W. (1884). "Die Wärmezonen Der Erde, Nach Der Dauer Der Heissen, Gemässigten Und Kalten Zeit Und Nach Der Wirkung Der Wärme Auf Die Organische Welt Betrachtet." *Meteorologische Zeitschrift* 1, pp. 215–226.

- Körner, C. (2006). "Plant CO₂ Responses: An Issue of Definition, Time and Resource Supply." *New Phytologist* 172.3, pp. 393–411. DOI: [10.1111/j.1469-8137.2006.01886.x](https://doi.org/10.1111/j.1469-8137.2006.01886.x).
- Körner, C. et al. (2005). "Carbon Flux and Growth in Mature Deciduous Forest Trees Exposed to Elevated CO₂." *Science* 309.5739, pp. 1360–1362. DOI: [10.1126/SCIENCE.1113977](https://doi.org/10.1126/SCIENCE.1113977).
- Lammertsma, E. I. et al. (2011). "Global CO₂ Rise Leads to Reduced Maximum Stomatal Conductance in Florida Vegetation." *Proceedings of the National Academy of Sciences* 108.10, pp. 4035–4040. DOI: [10.1073/pnas.1100371108](https://doi.org/10.1073/pnas.1100371108).
- Leakey, A. D. B. et al. (2009). "Elevated CO₂ Effects on Plant Carbon, Nitrogen, and Water Relations: Six Important Lessons from FACE." *Journal of Experimental Botany* 60.10, pp. 2859–2876. DOI: [10.1093/jxb/erp096](https://doi.org/10.1093/jxb/erp096).
- Lemon, E. R. (1983). *CO₂ And Plants: The Response Of Plants To Rising Levels Of Atmospheric Carbon Dioxide*. Boulder, Colorado, USA: Westview Press. 280 pp. ISBN: 978-0-86531-597-6.
- Lewis, S. L. and M. A. Maslin (2015). "Defining the Anthropocene." *Nature* 519.7542, pp. 171–180. DOI: [10.1038/nature14258](https://doi.org/10.1038/nature14258).
- Lian, X. et al. (2018). "Partitioning Global Land Evapotranspiration Using CMIP5 Models Constrained by Observations." *Nature Climate Change* 8.7, pp. 640–646. DOI: [10.1038/s41558-018-0207-9](https://doi.org/10.1038/s41558-018-0207-9).
- Lovelock, J. E. and L. Margulis (1974). "Atmospheric Homeostasis by and for the Biosphere: The Gaia Hypothesis." *Tellus* 26.1-2, pp. 2–10. DOI: [10.3402/tellusa.v26i1-2.9731](https://doi.org/10.3402/tellusa.v26i1-2.9731).
- Lyons, T. W., C. T. Reinhard, and N. J. Planavsky (2014). "The Rise of Oxygen in Earth's Early Ocean and Atmosphere." *Nature* 506.7488, pp. 307–315. DOI: [10.1038/NATURE13068](https://doi.org/10.1038/NATURE13068).
- Mao, J. et al. (2016). "Human-Induced Greening of the Northern Extratropical Land Surface." *Nature Climate Change* 6.10, pp. 959–963. DOI: [10.1038/nclimate3056](https://doi.org/10.1038/nclimate3056).
- Marotzke, J. (2019). "Quantifying the Irreducible Uncertainty in Near-term Climate Projections." *Wiley Interdisciplinary Reviews: Climate Change* 10.1, e563. DOI: [10.1002/wcc.563](https://doi.org/10.1002/wcc.563).
- Marotzke, J. et al. (2017). "Climate Research Must Sharpen Its View." *Nature Climate Change* 7, pp. 89–91. DOI: [10.1038/nclimate3206](https://doi.org/10.1038/nclimate3206).
- McPherson, R. A. (2007). "A Review of Vegetation—Atmosphere Interactions and Their Influences on Mesoscale Phenomena." *Progress in Physical Geography: Earth and Environment* 31.3, pp. 261–285. DOI: [10.1177/0309133307079055](https://doi.org/10.1177/0309133307079055).
- Myneni, R. B., C. D. Keeling, C. J. Tucker, G. Asrar, and R. R. Nemani (1997). "Increased Plant Growth in the Northern High Latitudes from 1981 to 1991." *Nature* 386, pp. 698–702. DOI: [10.1038/386698a0](https://doi.org/10.1038/386698a0).
- Mystakidis, S., E. L. Davin, N. Gruber, and S. I. Seneviratne (2016). "Constraining Future Terrestrial Carbon Cycle Projections Using

- Observation-Based Water and Carbon Flux Estimates." *Global Change Biology* 22.6, pp. 2198–2215. DOI: [10.1111/gcb.13217](https://doi.org/10.1111/gcb.13217).
- Nemani, R. R. et al. (2003). "Climate-Driven Increases in Global Terrestrial Net Primary Production from 1982 to 1999." *Science* 300.5625, pp. 1560–1563. DOI: [10.1126/science.1082750](https://doi.org/10.1126/science.1082750).
- Norby, R. J. and D. R. Zak (2011). "Ecological Lessons from Free-Air CO₂ Enrichment (FACE) Experiments." *Annual Review of Ecology, Evolution, and Systematics* 42.1, pp. 181–203. DOI: [10.1146/annurev-ecolsys-102209-144647](https://doi.org/10.1146/annurev-ecolsys-102209-144647).
- Norby, R. J., J. D. Sholtis, C. A. Gunderson, and S. S. Jawdy (2003). "Leaf Dynamics of a Deciduous Forest Canopy: No Response to Elevated CO₂." *Oecologia* 136.4, pp. 574–584. DOI: [10.1007/s00442-003-1296-2](https://doi.org/10.1007/s00442-003-1296-2).
- Norby, R. J., J. M. Warren, C. M. Iversen, B. E. Medlyn, and R. E. McMurtrie (2010). "CO₂ Enhancement of Forest Productivity Constrained by Limited Nitrogen Availability." *Proceedings of the National Academy of Sciences* 107.45, pp. 19368–19373. DOI: [10.1073/pnas.1006463107](https://doi.org/10.1073/pnas.1006463107).
- Osborne, C. P. (2016). "Crop Yields: CO₂ Fertilization Dries Up." *Nature Plants* 2.9, p. 16138. DOI: [10.1038/nplants.2016.138](https://doi.org/10.1038/nplants.2016.138).
- Park, T. et al. (2016). "Changes in Growing Season Duration and Productivity of Northern Vegetation Inferred from Long-Term Remote Sensing Data." *Environmental Research Letters* 11.8, p. 084001. DOI: [10.1088/1748-9326/11/8/084001](https://doi.org/10.1088/1748-9326/11/8/084001).
- Peñuelas, J. et al. (2017). "Shifting from a Fertilization-Dominated to a Warming-Dominated Period." *Nature Ecology & Evolution* 1.10, p. 1438. DOI: [10.1038/S41559-017-0274-8](https://doi.org/10.1038/S41559-017-0274-8).
- Pearl, J. (2009). *Causality: Models, Reasoning and Inference*. 2nd ed. Cambridge: Cambridge University Press. ISBN: 978-0-521-89560-6. DOI: [10.1017/CB09780511803161](https://doi.org/10.1017/CB09780511803161).
- Prentice, I. C., S. Williams, and P. Friedlingstein (2015). "Biosphere Feedbacks and Climate Change." *Grantham Institute Briefing Paper* 12.
- Quéré, C. L. et al. (2018a). "Global Carbon Budget 2017." *Earth System Science Data* 10.1, pp. 405–448. DOI: [10.5194/essd-10-405-2018](https://doi.org/10.5194/essd-10-405-2018).
- Quéré, C. L. et al. (2018b). "Global Carbon Budget 2018." *Earth System Science Data* 10.4, pp. 2141–2194. DOI: [10.5194/ESSD-10-2141-2018](https://doi.org/10.5194/ESSD-10-2141-2018).
- Ribes, A., S. Planton, and L. Terray (2013). "Application of Regularised Optimal Fingerprinting to Attribution. Part I: Method, Properties and Idealised Analysis." *Climate Dynamics* 41.11-12, pp. 2817–2836. DOI: [10.1007/s00382-013-1735-7](https://doi.org/10.1007/s00382-013-1735-7).
- Rogelj, J. et al. (2016). "Paris Agreement Climate Proposals Need a Boost to Keep Warming Well below 2 °C." *Nature* 534.7609, pp. 631–639. DOI: [10.1038/nature18307](https://doi.org/10.1038/nature18307).
- Rosing, M. T., D. K. Bird, N. H. Sleep, W. Glassley, and F. Albarede (2006). "The Rise of Continents—An Essay on the Geologic Conse-

- quences of Photosynthesis." *Palaeogeography, Palaeoclimatology, Palaeocology* 232.2, pp. 99–113. DOI: [10.1016/J.PALAEO.2006.01.007](https://doi.org/10.1016/J.PALAEO.2006.01.007).
- Rusin, N. P. and L. Flit (1966). *Man Versus Climate*. Trans. by D. Rottenberg. London, UK: Central Books Ltd. 175 pp. ISBN: 978-0-7147-0087-8.
- Schimmel, D., B. B. Stephens, and J. B. Fisher (2015). "Effect of Increasing CO₂ on the Terrestrial Carbon Cycle." *Proceedings of the National Academy of Sciences* 112.2, pp. 436–441. DOI: [10.1073/pnas.1407302112](https://doi.org/10.1073/pnas.1407302112).
- Schlesinger, W. H. and E. S. Bernhardt (2013). *Biogeochemistry: An Analysis of Global Change*. Oxford, UK: Academic press. 672 pp. ISBN: 0-12-385874-7.
- Schlesinger, W. H. and S. Jasechko (2014). "Transpiration in the Global Water Cycle." *Agricultural and Forest Meteorology* 189-190, pp. 115–117. DOI: [10.1016/j.agrformet.2014.01.011](https://doi.org/10.1016/j.agrformet.2014.01.011).
- Schrödinger, E. (1943). *What Is Life?* Cambridge, UK: University Press: Cambridge. 33 pp.
- Seidl, R. et al. (2017). "Forest Disturbances under Climate Change." *Nature Climate Change* 7.6, pp. 395–402. DOI: [10.1038/NCLIMATE3303](https://doi.org/10.1038/NCLIMATE3303).
- Sharkey, T. D. (1988). "Estimating the Rate of Photorespiration in Leaves." *Physiologia Plantarum* 73.1, pp. 147–152. DOI: [10.1111/J.1399-3054.1988.TB09205.X](https://doi.org/10.1111/J.1399-3054.1988.TB09205.X).
- Sitch, S. et al. (2015). "Recent Trends and Drivers of Regional Sources and Sinks of Carbon Dioxide." *Biogeosciences* 12.3, pp. 653–679. DOI: [10.5194/BG-12-653-2015](https://doi.org/10.5194/BG-12-653-2015).
- Song, X.-P. et al. (2018). "Global Land Change from 1982 to 2016." *Nature*, p. 1. DOI: [10.1038/s41586-018-0411-9](https://doi.org/10.1038/s41586-018-0411-9).
- Spohn, T. and D. Breuer (2010). "How Would Life Factor in the Evolution of Planetary Interiors?: Comment on "Life, Hierarchy, and the Thermodynamic Machinery of Planet Earth" by A. Kleidon." *Physics of Life Reviews* 7.4, pp. 471–472. DOI: [10.1016/j.plrev.2010.11.002](https://doi.org/10.1016/j.plrev.2010.11.002).
- Taylor, K. E., R. J. Stouffer, and G. A. Meehl (2012). "An Overview of Cmp5 and the Experiment Design." *Bulletin of the American Meteorological Society* 93.4, pp. 485–498. DOI: [10.1175/BAMS-D-11-00094.1](https://doi.org/10.1175/BAMS-D-11-00094.1).
- Terrer, C., S. Vicca, B. A. Hungate, R. P. Phillips, and I. C. Prentice (2016). "Mycorrhizal Association as a Primary Control of the CO₂ Fertilization Effect." *Science* 353.6294, pp. 72–74. DOI: [10.1126/science.aaf4610](https://doi.org/10.1126/science.aaf4610).
- Tripati, A. K., C. D. Roberts, and R. A. Eagle (2009). "Coupling of CO₂ and Ice Sheet Stability Over Major Climate Transitions of the Last 20 Million Years." *Science* 326.5958, pp. 1394–1397. DOI: [10.1126/science.1178296](https://doi.org/10.1126/science.1178296).
- Ukkola, A. M. et al. (2016). "Reduced Streamflow in Water-Stressed Climates Consistent with CO₂ Effects on Vegetation." *Nature Climate Change* 6.1, pp. 75–78. DOI: [10.1038/nclimate2831](https://doi.org/10.1038/nclimate2831).

- Verbyla, D. (2011). "Browning Boreal Forests of Western North America." *Environmental Research Letters* 6.4, p. 041003. DOI: [10.1088/1748-9326/6/4/041003](https://doi.org/10.1088/1748-9326/6/4/041003).
- Wang, J., N. Zeng, Y. Liu, and Q. Bao (2014). "To What Extent Can Interannual CO₂ Variability Constrain Carbon Cycle Sensitivity to Climate Change in CMIP5 Earth System Models?" *Geophysical Research Letters* 41.10, pp. 3535–3544. DOI: [10.1002/2014GL060004](https://doi.org/10.1002/2014GL060004).
- Wenzel, S., V. Eyring, E. P. Gerber, and A. Y. Karpechko (2015). "Constraining Future Summer Austral Jet Stream Positions in the CMIP5 Ensemble by Process-Oriented Multiple Diagnostic Regression." *Journal of Climate* 29.2, pp. 673–687. DOI: [10.1175/JCLI-D-15-0412.1](https://doi.org/10.1175/JCLI-D-15-0412.1).
- Wenzel, S., P. M. Cox, V. Eyring, and P. Friedlingstein (2016). "Projected Land Photosynthesis Constrained by Changes in the Seasonal Cycle of Atmospheric CO₂." *Nature* 538.7626, pp. 499–501. DOI: [10.1038/nature19772](https://doi.org/10.1038/nature19772).
- Winkler, A. J., R. B. Myneni, G. A. Alexandrov, and V. Brovkin (2019a). "Earth System Models Underestimate Carbon Fixation by Plants in the High Latitudes." *Nature Communications* 10.1, p. 885. DOI: [10.1038/S41467-019-08633-Z](https://doi.org/10.1038/S41467-019-08633-Z).
- Winkler, A. J., R. B. Myneni, and V. Brovkin (2019b). "Investigating the Applicability of Emergent Constraints." *Earth System Dynamics* 10.3, pp. 501–523. DOI: [10.5194/esd-10-501-2019](https://doi.org/10.5194/esd-10-501-2019).
- Winkler, A. J. et al. (submitted). "Slow-down of the Greening Trend in Natural Vegetation with Further Rise in Atmospheric CO₂." *Proceedings of the National Academy of Sciences*, pp. 1–14.
- Zalasiewicz, J. et al. (2008). "Are We Now Living in the Anthropocene." *GSA Today* 18.2, p. 4. DOI: [10.1130/gsat01802a.1](https://doi.org/10.1130/gsat01802a.1).
- Zhou, L. et al. (2014). "Widespread Decline of Congo Rainforest Greenness in the Past Decade." *Nature* 509.7498, pp. 86–90. DOI: [10.1038/nature13265](https://doi.org/10.1038/nature13265).
- Zhu, Z. et al. (2013). "Global Data Sets of Vegetation Leaf Area Index (LAI)_{3g} and Fraction of Photosynthetically Active Radiation (FPAR)_{3g} Derived from Global Inventory Modeling and Mapping Studies (GIMMS) Normalized Difference Vegetation Index (NDVI)_{3g} for the Period 1981 to 2011." *Remote Sensing* 5.2, pp. 927–948. DOI: [10.3390/rs5020927](https://doi.org/10.3390/rs5020927).
- Zhu, Z. et al. (2016). "Greening of the Earth and Its Drivers." *Nature Climate Change* 6.8, pp. 791–795. DOI: [10.1038/nclimate3004](https://doi.org/10.1038/nclimate3004).

Part I

THE EFFECTS OF RISING CO₂ ON GLOBAL NATURAL VEGETATION

The attached article has been submitted with some modifications:

Winkler, A. J., R. B. Myneni, A. Hannart, S. Sitch, V. Haverd, D. Lombardozzi, V. K. Arora, J. Pongratz, J. E. M. S. Nabel, D. S. Goll, E. Kato, H. Tian, A. Arneth, P. Friedlingstein, A. K. Jain, S. Zaehle, and V. Brovkin (submitted). "Slow-down of the Greening Trend in Natural Vegetation with Further Rise in Atmospheric CO₂." *Proceedings of the National Academy of Sciences*, pp. 1–14

THE EFFECTS OF RISING CO₂ ON GLOBAL NATURAL VEGETATION

Alexander J. Winkler^{1,2}, Ranga B. Myneni^{1,3},
Alexis Hannart⁴, and Victor Brovkin¹

CONTENTS

1	Introduction	3
2	Data and Methods	6
3	Results and Discussion	13
4	Conclusions	26
	References	28
A	Supplementary Information	34

¹ Max-Planck-Institute for Meteorology, Bundesstrasse 53, 20146 Hamburg, Germany

² International Max-Planck Research School for Earth System Modeling, Bundesstrasse 53, 20146 Hamburg, Germany

³ Department of Earth and Environment, Boston University, Boston MA 02215, USA

⁴ Ouranos, Montreal QC H2L 1K1, Quebec, Canada

Abstract

Long-term satellite data reveal widespread changes of Earth's land surface. Regions dominated by human land-use practices are mostly greening due to direct drivers (i.e. fertilizer application, irrigation, and multiple cropping). Natural vegetation exhibits patterns of greening and browning across all continents. Indirect drivers induced by anthropogenic carbon emissions (i.e. CO₂ fertilization, climatic changes, and episodic disturbances) are hypothesized as being key drivers, however, a biome level attribution integrated into the global picture is lacking. In this study, we analyze the longest satellite-based record of global leaf area observations (1981–2017). We detect and identify clusters of significant rates of increase and decrease of leaf area index (LAI) on a biome level. Based on process-based model simulations (fully-coupled Max Planck Institute Earth System model and 16 standalone land surface models driven with an observed climate), we disentangle the effects of rising CO₂ on LAI. Through the use of Causal Counterfactual Theory, we attribute changes on the biome level to the key drivers in a probabilistic setting. Our analysis unveils a slowing down of greening and a strengthening of browning trends, particularly in the last two decades (2000–2017). Decreases in LAI primarily occurs in regions of high LAI (i.e. tropical forests), whereas increases in LAI are generally confined to low LAI regions (i.e. northern and arid non-forested lands). On the global scale, these opposing trends are driving a convergence of the natural vegetation. We find that many biomes bear the signature of climatic changes through warming (temperature-limited ecosystems) and rainfall anomalies (northern sub-Saharan regions). CO₂ fertilization is the main driver in the temperate forests and biomes in cold and/or arid climatic zones. These results question the previously suggested global prevalence of CO₂ fertilization. Models largely underestimate vegetation browning, especially in tropical and Northern American boreal forests. Persistent leaf area loss in the most productive ecosystems could be an early indicator of a slow-down in the terrestrial carbon sink. Models need to better account this effect on natural vegetation for plausible Earth system projections of the 21st century.

Author Contributions A.J.W. performed the research and drafted the manuscript with inputs from R.B.M. and V.B., A.J.W. and A.H. conducted the attribution analysis. All authors contributed ideas and to the interpretation of the results.

1 INTRODUCTION

Almost four decades of satellite observations reveal widespread changes of the terrestrial vegetation across the globe. These greening and browning trends reflect persistent changes in the abundance of green leaves, and thus, the rate of photosynthesis. Plants modulate pivotal land-atmosphere interactions through the process of photosynthesis. Hence, changes in photosynthetic activity immediately affects the land-atmosphere exchange of energy (Forzieri et al., 2017), water (McPherson, 2007; Ukkola et al., 2016) and carbon (Poulter et al., 2014; Thomas et al., 2016; Winkler et al., 2019a). Several studies reported that the Earth is largely greening across diverse biomes from Arctic tundra to subtropical drylands (Myneni et al., 1997; Nemani et al., 2003; Mao et al., 2016; Zhu et al., 2016; Chen et al., 2019; Winkler et al., 2019a; Winkler et al., 2019b). Others have identified regions of persistent declining trends in leaf area (Goetz et al., 2005; Verbyla, 2011). The drivers underlying these long-term vegetation changes, however, remain unclear.

Anthropogenic vegetation (i.e. agriculturally dominated areas) and natural vegetation should be considered separately due to their distinct origin and properties. A recent study by Chen et al. (2019) reported that anthropogenic vegetation (35% of the global vegetated area) is greening in consequence of human land management. The authors identified artificial irrigation, multiple cropping, and the application of fertilizers and pesticides as the main drivers of leaf area enhancement (direct drivers). These results challenge the conclusions of a preceding study by Zhu et al. (2016) claiming that the global greening trend can be attributed to indirect drivers induced by CO₂ emissions, in particular, CO₂ fertilization (70%).

In the literature, indirect drivers of vegetation changes usually comprise CO₂ fertilization and climate change, both of which are consequences of rising CO₂. The term "CO₂ fertilization" conflates two effects of increased ambient CO₂ on the physiology of plants. Foremost, elevated CO₂ in the interior of leaves stimulate carbon assimilation, which enhances plant productivity and could lead to increased biomass (Leakey et al., 2009; Fatichi et al., 2016). Simultaneously, plant leaves adapt to the CO₂-enriched atmosphere by lowering their stomatal conductance. As a consequence, water loss through plant transpiration decreases and results in an enhanced water-use efficiency (ratio of carbon assimilation to transpiration rate Ukkola et al., 2016; Fatichi et al., 2016). In theory, both effects should result in an expansion of leaf area, especially in environments where plant growth is constrained by water availability (Ukkola et al., 2016; Donohue et al., 2009; Donohue et al., 2013).

The radiative effect of CO₂ induces climatic changes (temperature, precipitation, and radiation), which can affect ecosystems in either way. Temperature-limited biomes are expected to green due to warming and the associated prolongation of the growing season (Park et al., 2016; Winkler et al., 2019a). But long-term drying (Zhou et al., 2014), as well as increased intensity and frequency of disturbances (Seidl et al., 2017) such as droughts (Bonafant et al., 2016) and wildfires (Goetz et al., 2005; Verbyla, 2011), can induce regional vegetation browning trends. Greening and browning patterns can also be associated with insect outbreaks, local deforestation practices, or nitrogen deposition; however, these drivers are considered to be of minor importance on a global scale (Zhu et al., 2016).

Indirect drivers affect both natural and anthropogenic vegetation, whereas direct drivers are confined to the latter. Chen et al. (2019) demonstrated that indirect drivers have either opposing or minor enhancing effects on leaf area of anthropogenic vegetation. In general, the greening of anthropogenic vegetation has a negligible effect on the carbon cycle, because carbon absorbed by agricultural plants almost immediately reenters the atmosphere. On the contrary, natural ecosystems act as a strong carbon sink of anthropogenic emissions ($\sim 12 \text{ Pg CO}_2 \text{ yr}^{-1}$, $\sim 30\%$ of CO₂ emissions; Quéré et al., 2018) and mitigate man-made climate change (Bonan, 2008; Sitch et al., 2015; Winkler et al., 2019a). Thus, a mechanistic understanding of natural vegetation dynamics under rising CO₂ is critical and helps to answer one of the key question in current climate research: *Where does the anthropogenic carbon go* (Marotzke et al., 2017)?

In the light of nearly forty years of continuous satellite observations and new results by Chen et al. (2019), we reassess the driver attribution of global vegetation changes and challenge previous findings (e.g. Zhu et al., 2016). This study focuses on the response of natural vegetation under the influence of the two key indirect drivers, the physiological and radiative effect of rising CO₂. Throughout this paper and in accordance with the literature, the terms "CO₂ fertilization" and "physiological effect of CO₂" are used interchangeably, as are "climate change" and "radiative effect of CO₂".

Here, we analyze a 37-year record of leaf area index (LAI) satellite observations (1982–2017, LAI3g, Data and Methods). The LAI3g product is based on the Advanced Very High Resolution Radiometer (AVHRR) sensors, for which there are a number of shortcomings (no on-board calibration, no correction of orbit loss, minimal correction for atmospheric contamination and limited cloud screening; Zhu et al., 2013; Chen et al., 2019). Despite these limitations, the AVHRR is unique in terms of its temporal coverage, and thereby opens up the opportunity to investigate on the evolution of Earth's vegetation while atmospheric CO₂ concentration increased by 65 ppm (341 to 406 ppm). We define greening and browning as LAI sensitivity to rising CO₂ relative to the baseline period 1982–1984 (Data and Methods). Based on a carefully crafted biome map (Figure A2, Table A1, Data and Methods), we identify spatial clusters of significant vegetation greening and browning in natural vegetation.

We make use of the latest version of the fully-coupled Max Planck Institute Earth system model in ensemble-mode (MPI-ESM, Data and Methods) and a collection of 16 land surface models (LSMs) driven with observed climatic conditions (Quéré et al., 2018, TRENDYv7 ensemble, Data and Methods). As a first step, we analyze historical simulations to examine if these models capture the observed behavior of natural vegetation under rising CO₂. Next, we analyze factorial simulations to disentangle and quantify the effects of rising CO₂ on LAI. Each factorial experiment consists of all historical forcings except one, which is retained at its pre-industrial conditions (Data and Methods).

The conventional approach in the field of Detection and Attribution is the optimal fingerprinting method as applied in Zhu et al. (2016). This framework which considers the observed change to be a linear combination of individual forced signals, is prone to overfitting, and assumes that linear correlation reflects causation (Hannart and Naveau, 2018). To overcome these limitations, we propose to apply the Causal Counterfactual Theory which has recently been introduced into climate science (Data and Methods Pearl,

2009; Hannart et al., 2016; Hannart and Naveau, 2018). The method allows us to test if long-term greening/browning trends can be attributed to the effects of rising CO₂ in a probabilistic setting combining necessary and sufficient causation (Data and Methods).

This is the first study that addresses vegetation browning as well as greening patterns across all biomes, integrated into a global picture. In terms of area fraction, greening is dominant, but browning clusters are intensifying, primarily in the biodiverse tropical forests. We find that CO₂ fertilization is an important driver of greening in some biomes, but it is not globally prevalent as was previously suggested (Zhu et al., 2016). The surge of browning areas is most likely tied to long-term drying and droughts. Overall, our findings suggest that the emerging browning clusters in the high productivity ecosystems might be a precursor of a weakening land carbon sink, which is not captured by current Earth system models.

2 DATA AND METHODS

Satellite observations of LAI: AVHRR LAI3g product. We used an updated version (V₁) of the leaf area index dataset (LAI3g; Chen et al., 2019) based on the methodology developed by Zhu et al. (2013). The data provides global year-round LAI observations at 15-day (bi-monthly) temporal resolution and 1/12 degree spatial resolution. It spans from July 1981 to December 2017 and is currently the only available record of such length. The full time series of LAI3gV₁ was generated using an artificial neural network and the latest version (third generation) of the Global Inventory Modeling and Mapping Studies group (GIMMS) Advanced Very High Resolution Radiometer (AVHRR) normalized difference vegetation index (NDVI) data (NDVI3g). The latter have been corrected for sensor degradation, inter-sensor differences, cloud cover, observational geometry effects due to satellite drift, Rayleigh scattering and stratospheric volcanic aerosols (Pinzon and Tucker, 2014).

The LAI3g datasets prior to 2000 were not evaluated due to a lack of required field data (Zhu et al., 2013; Chen et al., 2019). After 2000, the quality of the LAI3g dataset was assessed through direct comparisons with ground measurements of LAI and indirectly with other satellite-data based LAI products, and also through statistical analysis with climatic variables such as temperature and precipitation variability (Zhu et al., 2013). Various studies used the predecessor LAI3gV₀ and the related dataset of fraction of absorbed photosynthetically active radiation (fapar; Anav et al., 2013; Forkel et al., 2016; Zhu et al., 2016; Mao et al., 2016; Mahowald et al., 2016; Piao et al., 2014; Poulter et al., 2014; Keenan et al., 2016) and its successor LAI3gV₁ (Winkler et al., 2019a; Chen et al., 2019).

Leaf area index is defined as the one-sided green leaf area per unit ground area in broadleaf canopies and as one-half the green needle surface area in needleleaf canopies in both satellite observations and models (ESMs and LSMs). It is expressed in units of m² green leaf area per m² ground area. Missing values in the LAI3gV₁ dataset are filled using the climatology of each 16-day composite during 1982-2017. We use the annual averaged LAI of each pixel in this study.

Characterization of biomes & clusters of significant change. The land cover product of the Moderate Resolution Imaging Spectroradiometer (MODIS) sensors (MCD12C1; MODIS/Terra and Aqua Combined Land Cover Type Climate Modeling Grid (CMG) Yearly Global 0.05 Deg V006, https://lpdaac.usgs.gov/dataset_discovery/modis/modis_products_table/mcd12c1_v006) is the primary source underlying the land cover map used in this study (hereafter MODIS land cover). The classes from the International Geosphere-Biosphere Programme (IGBP) in the MODIS land cover product are aggregated as follows: Tropical Forests include Evergreen Broadleaf Forest (EBF), Temperate Forests include Deciduous Broadleaf Forest (DBF) and Mixed Forest, and Boreal Forests include Evergreen Needleleaf Forest (ENF) and Deciduous Needleleaf Forest (DNF). Savannas include Woody Savannas and Savannas. Shrublands include Closed Shrublands and Open Shrublands. Croplands include Croplands and Croplands / Natural Vegetation Mosaic. The class Others includes Permanent Wetlands, Urban and Built-up Lands, Permanent Snow and Ice, and Barren. The classes Grasslands and Water Bodies remain unchanged. The MODIS land cover product provides estimates for the time period from 2001 to 2017 for each pixel. In

this study we define a representative biome map based on the most frequently occurring land cover type throughout the period of 17 years.

The MODIS land cover classification does not contain the biome tundra, which is why we use in addition the land cover product GLDAS2 / Noah version 3.3 that uses a modified IGBP classification scheme providing the classes Wooded, Mixed or Bare Ground Tundra (<https://ldas.gsfc.nasa.gov/gldas/GLDASvegetation.php>, hereafter GLDAS land cover Rodell et al., 2004). Accordingly, pixels originally of the classes Shrublands, Grasslands, Permanent Wetlands, or Barren, are converted to Tundra, if classified as Wooded, Mixed or Bare Ground Tundra in the GLDAS land cover product. The classes Woody Savannas and Savannas span vast areas across the globe in the MODIS land cover product. We use the GLDAS classification for these pixels, but only for regions where the MODIS and GLDAS land cover products disagree. In doing so, we obtain a more accurate global land cover classification. Table A1 describes in detail how the fusion of the MODIS and GLDAS land cover products is realized.

As a last step, we integrate the MODIS tree cover product MOD44B (MODIS/Terra Vegetation Continuous Fields Yearly L3 Global 250 m SIN Grid V006, https://lpdaac.usgs.gov/dataset_discovery/modis/modis_products_table/mod44b_v006) to account for the underestimation of forested area in the MODIS land cover product. Areas with tree cover exceeding 10% are formally defined as forests (MacDicken et al., 2015). Thus, we set non-forest pixels in the MODIS land cover product above 10% tree cover to Boreal Forest in the high latitudes 50° N/S. For tropical forest (25° S – 25° N), we increase the threshold to 20% tree cover to allow for a realistic areal extent of savannas. The pixels in the bands 25° N/S – 50° N/S remain unchanged, because the MODIS land cover product already realistically represents the forested area in these latitudes. Table A1 provides a detailed overview on the conflation of MODIS land cover product, GLDAS land cover product and the MODIS Tree cover product. The final biome map (originally resolved at 0.05°) is regridded to the different resolutions of the AVHRR sensor and the models simulations (MPI-ESM and TRENDYv7) applying a largest area fraction remapping scheme.

Based on the observational LAI dataset we define various clusters for greening or browning in most biomes: North American Tundra (NAm Tundra), Eurasian Tundra (EA Tundra), North American Boreal Forests (NAm Brl F), Eurasian Boreal Forests (EA Brl F), Temperate Forests (Tmp F), Tropical Forests (Trp F), Central African Tropical Forests (CAf Trp F), Northern African Savannas and Grasslands (NAf Sv Gl), Southern African Savannas and Grasslands (SAf Sv Gl), Cool Grasslands (Cool Gl), and Australian Shrublands (Aus Sl). Some clusters require a more detailed definition of their geographical location and extent: Southern (Northern) African Savannas and Grasslands represent respective vegetation type south (north) of the equator including Madagascar. Central African Tropical Forests represent all tropical forests in Africa. Cool Grasslands refer to grasslands above 30° N.

Max-Planck-Institute Earth System Model. MPI-ESM1.2 is the latest version of the state-of-the-art Max Planck Institute Earth System Model, which participates in the upcoming sixth phase of the Coupled Model Intercomparison Project (CMIP6; Eyring et al., 2016). Mauritsen et al. (2019) describes thoroughly the model developments and advancements with respect to its predecessor, the CMIP5 version (Giorgetta et al., 2013). Here, we use the low resolution (LR) fully coupled carbon/climate configuration (MPI-ESM1.2-LR), which

consists of the atmospheric component ECHAM6.3 with 47 vertical levels and a horizontal resolution of 200 km grid spacing (spectral truncation at T63). The ocean dynamical model MPIOM is set up on a bi-polar grid with an approximate grid-spacing of 150 km (GR1.5) and 40 vertical levels. MPI-ESM1.2-LR includes the latest versions of the land and ocean carbon cycle modules, comprising the ocean biogeochemistry model HAMOCC6 and the land surface scheme JSBACH3.2 (Mauritsen et al., 2019).

Only the LR variant of the MPI-ESM includes all the important processes relevant for longer time-scale changes of the land surface, such as a thoroughly equilibrated global carbon cycle, dynamical vegetation changes, interactive nitrogen cycle, land use transitions, a process-based fire model (SPITFIRE), and an interactive coupling of all sub-models. Furthermore, it is possible to run this model configuration to generate 45-85 model years per real-time day with a modern supercomputer (Mauritsen et al., 2019). This opens up the possibility to conduct a larger number of realizations for each experiment. Specifically, we used the initial CMIP6 release of the MPI-ESM version 1.2.01 (mpiesm-1.2.01-release, revision number 9234). The final CMIP6 version will include further bug fixes, which are expected to only slightly influence long-term sensitivities of simulated land surface processes.

We conducted historical simulations (all forcings) and three factorial experiments (all forcings except one): (a) all historical forcings except the physiological effect of CO₂ (No PE; increasing CO₂ does not affect the biogeochemical processes), (b) all historical forcings except the radiative effect of CO₂ (No RE; increasing CO₂ does not affect climate), and (c) all historical forcings except anthropogenic forcings (No CO₂). All experiments were performed in ensemble-mode (6 realizations per experiment) using the latest CMIP6 forcing data (1850–2013). Individual realizations were initialized from different points in time of a prolongation run of the official MPI-ESM1.2-LR pre-industrial control simulation. In doing so, we account for the influence of climatic modes (e.g. El Niño Southern Oscillation) as a source of uncertainty in simulating long-term changes.

The simulated time series were shifted by four years to maximize the overlap with the observational record of 1982–2017.

Land surface models: TRENDYv7. Land-surface models (LSMs) or dynamic global vegetation models (DGVMs) simulate key physical and biological key processes of the land system in interaction with the atmosphere. LSMs provide a deeper insight into the mechanisms controlling terrestrial energy, hydrological and carbon cycles, as well as the drivers of phenomena ranging from short-term anomalies to long-term changes (Sitch et al., 2015; Bastos et al., 2018). Here, we analyze the most recent TRENDY ensemble (version 7) comprising 16 state-of-the-art LSMs which vary in their representation of ecosystem processes. All models simulate vegetation growth and mortality, deforestation and regrowth, vegetation and soil carbon responses to increasing atmospheric CO₂ levels, climate change and natural variability (Quéré et al., 2018). Some models simulate an explicit nitrogen cycle (allowing for potential nitrogen limitation) and account for atmospheric N deposition (Table A1 in Quéré et al., 2018). Most LSMs include the most important components of land use and land use changes, but they are far from representing all processes resulting from direct human land management (Table A1 in Quéré et al., 2018). A more detailed description of the TRENDYv7 ensemble, model-specific simulation setups and references can be found in Quéré et al. (2018, Table 4 and Table A1).

We use output from five simulations: all forcings (S₃), physiological effect of CO₂ only (S₁), radiative plus physiological effect of CO₂ (S₂), land-use changes only (S₄), and the control run (S₀; no forcings: fixed CO₂ concentration of 276.59 ppm and fixed land use map, loop of mean climate and variability from 1901–1920). The forcing data consist of observed atmospheric CO₂ concentrations, observed temporal patterns of temperature, precipitation, and incoming surface radiation from the CRU-NCEP reanalysis (Quéré et al., 2018; Harris et al., 2014), and human-induced land-cover changes and management from the most recent Land-Use Harmonization (LUH2) dataset (Hurtt et al., 2011; Quéré et al., 2018).

In this study, we only analyze output for the period 1982–2017 (matching the observational record) from models providing spatially gridded data for all five simulations. A few models provide LAI at the level of plant functional types (PFT). We calculate the average value of all LAI values on PFT level multiplied by their land cover fraction for each grid cell. All model outputs were spatially regridded to a common resolution of 1° based on a first-order conservative remapping scheme (Jones, 1999).

The design of factorial simulations in TRENDYv7 and by the MPI-ESM are conceptually different. The MPI-ESM simulations were conducted using the counterfactual approach, i.e. all forcings are present except the driver of interest. TRENDYv7 provides simulations with different combinations of drivers as described above. To obtain comparability, we have to make the assumption that the absence of a specific driver has the same effect, in absolute values, as its sole presence. Thus, we process the output of the simulations S₁, S₂, S₃ and S₄ to obtain the counterfactual setup as described above for MPI-ESM. It has to be noted that these simulations are only to some extent comparable. For instance, in the MPI-ESM we can specifically determine the impact of the radiative effect of CO₂, whereas TRENDYv7 uses observed atmospheric fields including changes induced from other drivers, such as non-CO₂ greenhouse gases.

For certain clusters, some models show unreasonable LAI changes and/or extreme inter-annual variability. To reduce the influence of these extreme models on the overall analysis, we apply a two-step filtering method for each cluster beforehand. Models are excluded from the analysis, if they exceed three times the inter-annual variability of observations and/or show a drastic change (of either sign) of more than 250% between the start and end of the observational period. Further, we apply a weighting scheme based on the performance of the all-forcings run for each cluster. We calculate quartic weights based on the distance between the simulated and observational estimate. These weights are applied when calculating the multi-model average and standard deviations for the factual and counterfactual runs.

Atmospheric CO₂ concentration. Global monthly means of atmospheric CO₂ concentration are taken from the GLOBALVIEW-CO₂ product (for details see <http://dx.doi.org/10.3334/OBSPACK/1002>) provided by the National Oceanic and Atmospheric Administration/Earth System Research Laboratory (NOAA/ESRL).

Processing of the gridded data. Areas of significant change in LAI are estimated using the non-parametric Mann-Kendall test, which detects monotonic trends in time series. In this study, we set the significance level to $p \leq 0.1$. An alternative statistical test for trend detection (Cox-Stuart test Sachs, 1997) yields approximately the same results. The trends

are either calculated for time series on the pixel level or for area-weighted large-scale aggregated time series (e.g. biome level).

We define greening (browning) either as a positive (negative) temporal trend, or for better comparison among models and observations, as a positive (negative) LAI sensitivity to rising atmospheric CO₂ concentration, i.e. change in annual average LAI (m² m⁻²) per change in CO₂ concentration (ppm). To obtain a better global comparison across diverse biomes, we express these sensitivities relative to the initial LAI level at the beginning of the observational record (average state from 1982-1984), denoted as Λ (% ppm⁻¹ CO₂).

The calculation of yearly net changes in leaf area balances the effects from both statistically significant browning and greening grid cells. For each cell, we multiply the estimated trends by the respective grid area. The net change is the sum of all grid cells, where areas of insignificant change are set to zero.

Models fairly accurately reproduce global patterns of vegetation greening, however, the fraction of browning is considerably underrepresented. Yet, we can only consider pixels with significant negative trends in LAI, in observations and models alike, and test models with respect to driver attribution of browning trends. Thus, the attribution of browning trends in this paper exclusively refers to browning pixels only.

Models reveal biases in comparison to observations. To obtain informative results in the attribution analysis, we process the simulations to match the mean and variance of the observational time-series. Assuming additive and multiplicative biases in simulations, we apply the following corrections:

$$b = \frac{\sigma_o}{\sigma_{af}}, \quad (1)$$

$$a = \bar{x}_o + b \times \bar{x}_{af}, \text{ and} \quad (2)$$

$$y_i = a + b * x_i, \quad (3)$$

where \bar{x}_o represents the mean value and σ_o the standard deviation of the observational times series. \bar{x}_{af} and σ_{af} are analogous to the all-forcings simulations. All simulated time series x_i are scaled using equation 3, where $i \in \Omega = \{\text{factual runs, counterfactual runs}\}$. This processing step does not affect the nature of simulated trends.

Causal counterfactual theory. The causal counterfactual approach is anchored in a formal theory of event causation developed in computer science (Pearl, 2009; Marotzke, 2019). Recently, a framework for driver attribution of long-term trends in the context of climate change has been introduced (Hannart et al., 2016; Hannart and Naveau, 2018), and increasingly gains popularity (e.g. Marotzke, 2019). Through the use of this method we can ascertain the likelihood that a certain external forcing has caused an observed change in the Earth system. More precisely, we address the question of interest in a probabilistic

setting, i.e. what is the probability that a given forcing (e.g. radiative effect of CO₂) has caused an observed long-term change in the system (e.g. greening of the Arctic).

In the following, we highlight the key ideas and relevant concepts of causal theory. A detailed description and formal derivations can be found in (Pearl, 2009; Hannart et al., 2016; Hannart and Naveau, 2018). We define the cause event (C) as "presence of a given forcing" (i.e. the factual world that occurred) and the complementary event (\bar{C}) as "absence of a given forcing" (i.e. the counterfactual world that would have existed in the absence of a given forcing; Hannart and Naveau, 2018). Further, we define the effect event (E) as the occurrence of a long-term change (here, greening or browning) and the complementary event (\bar{E}) as the non-occurrence of a long-term change (i.e. no persistent vegetation changes). In making use of numerical models, we can conduct factual runs comprising all forcings (i.e. historical simulations) as well as simulate counterfactual worlds by switching off a forcing of interest (i.e. all forcings except one). Based on an ensemble of simulations, either in a multi-model and/or multi-realizations setup, we derive the so-called factual (p_1) and counterfactual probability (p_0), which read $p_1 = P\{E|\text{do}(C)\}$ and $p_0 = P\{E|\text{do}(\bar{C})\}$, respectively (Hannart and Naveau, 2018). More precisely, p_1 describes the probability of the event E in the real world where forcing C was present, whereas p_0 refers to the probability of the event E in a hypothetical world where forcing C was absent. The notation $\text{do}(\cdot)$ means that an *experimental intervention* is applied to the system to obtain the probabilities (Hannart and Naveau, 2018).

The three distinct facets of causality can be established based on the probabilities p_1 and p_0 :

$$\text{PN} = \max \left\{ 1 - \frac{p_0}{p_1}, 0 \right\}, \quad (4)$$

$$\text{PS} = \max \left\{ 1 - \frac{1 - p_1}{1 - p_0}, 0 \right\}, \text{ and} \quad (5)$$

$$\text{PNS} = \max \{ p_1 - p_0, 0 \}. \quad (6)$$

PN refers to the probability of necessary causation, where the occurrence of E requires that of C but may also require other forcings. PS refers to the probability of sufficient causation, where the occurrence of C drives that of E but may not be required for E to occur. PNS describes the probability of necessary and sufficient causation, where PN and PS both hold (Hannart and Naveau, 2018). In other words, PNS may be considered as the probability that combines necessity and sufficiency. Thus, the main goal is to establish a high PNS that reflects and communicates evidence for the existence of a causal relationship in a simple manner (Hannart and Naveau, 2018).

To obtain PNS, we follow the methodology described in detail in Hannart and Naveau (2018) and derive cumulative distribution functions (CDF) for the factual and counterfactual worlds, denoted D_0 and D_1 , respectively. Assuming a Gaussian distribution, PNS follows as

$$\text{PNS} = \max \{ D_1(\mu_1, \Sigma) - D_0(\mu_0, \Sigma) \}, \quad (7)$$

where μ_1 and μ_0 refer to the mean response of all factual and all counterfactual runs, respectively. Σ denotes the overall uncertainty and is estimated based on all simulations, comprising factual, counterfactual, and centuries-long unforced (pre-industrial) model runs (Hannart and Naveau, 2018, for details see). Finally, the maximum of PNS determines the sought probability of causation (Hannart and Naveau, 2018). We express probabilities using the terminology and framework defined by the IPCC (Mastrandrea et al., 2011; Hannart and Naveau, 2018).

3 RESULTS AND DISCUSSION

Natural vegetation exhibits a net gain of leaf area over the last decades, but the number of browning regions is increasing. More than three decades of satellite observations (1982–2017, Data and Methods) reveal that 40% of Earth’s natural vegetation shows statistically significant positive trends in LAI (Mann-Kendall test, $p < 0.1$; Table 1), for a contemporary increase in atmospheric CO_2 of 65 ppm. However, more and more browning clusters are beginning to emerge across all continents (14%; Table 1). Analyzing three LAI datasets of a shorter time span (1982–2009), Zhu et al. (2016) reported a considerably smaller browning fraction of less than 4% and greening percentages ranging from 25% to 50% considering all global vegetation (i.e. including agriculturally dominated regions). The higher browning estimate found in the extended record analyzed in this study indicates an intensification of leaf area loss in recent years.

Earth’s forests respond diversely to rising CO_2 . A global map of relative change in LAI per unit rise in atmospheric CO_2 ($\% \text{ ppm}^{-1} \text{ CO}_2$, denoted Λ , Data and Methods) for natural vegetation unveils clusters of greening and browning across the globe (Figure 1). Temperate forests ($\Lambda > 0$: 56%) and Eurasian boreal forests ($\Lambda > 0$: 53%) are extensively greening, and thereby, contribute the largest fraction to the enhancement of leaf area on the planet (Table 2). On the contrary, the global belt of tropical forests, albeit showing a net greening ($\Lambda > 0$: 28%), also feature widespread browning areas ($\Lambda < 0$: 16%). In particular, the Central African tropical forests contain large areas of pronounced negative sensitivity to CO_2 ($\Lambda < 0$: 25%). North American boreal forests exhibit the largest fraction of browning vegetation ($\Lambda < 0$: 31%) resulting in an annual net loss of leaf area (Table 1 and 2). The recent development of Earth’s forests as pictured by LAI observations is generally in line with results based on other data resources. For instance, Song et al. (2018) analyzed satellite-based datasets of tree cover and reported a net gain of global forested area, with a net loss in the tropics being compensated by a net gain in the extra-tropics.

Just as in forests, non-forested biomes also indicate divergent vegetation responses to rising CO_2 . Tundra in North America is primarily greening ($\Lambda > 0$: 46% versus $\Lambda < 0$: 7%), whereas in Eurasia, browning is intensifying ($\Lambda > 0$: 35% versus $\Lambda < 0$: 20%), especially so in the northern regions of Scandinavia and on the Taymar Peninsula in Northern Russia. Grasslands in cool arid climates, mainly comprising the Mongolian and Kazakh Steppe, as well as the Australian shrublands, stand out as prominent greening clusters ($\Lambda > 0$: 40% and 49%, respectively). Although these biomes show a strong positive sensitivity to rising CO_2 , they are characterized by an overall low level of LAI. The African continent, which is still dominated by natural vegetation, reveals an eminently distinctive change in leaf area. A greening band of savannas and grasslands in the northern regions of Sub-Saharan Africa and a greening cluster in Southern Africa enclose the browning regions of equatorial Africa (Figure 1). Overall, the response of LAI to rising CO_2 is confined for some biomes (secular widespread browning of the tropical forests and dominant greening of the temperate forests), but divergent for others (tundra and boreal forests show a ‘North America – Eurasia’ asymmetry, interestingly, in that they show changes of reversed sign; Figure 1).

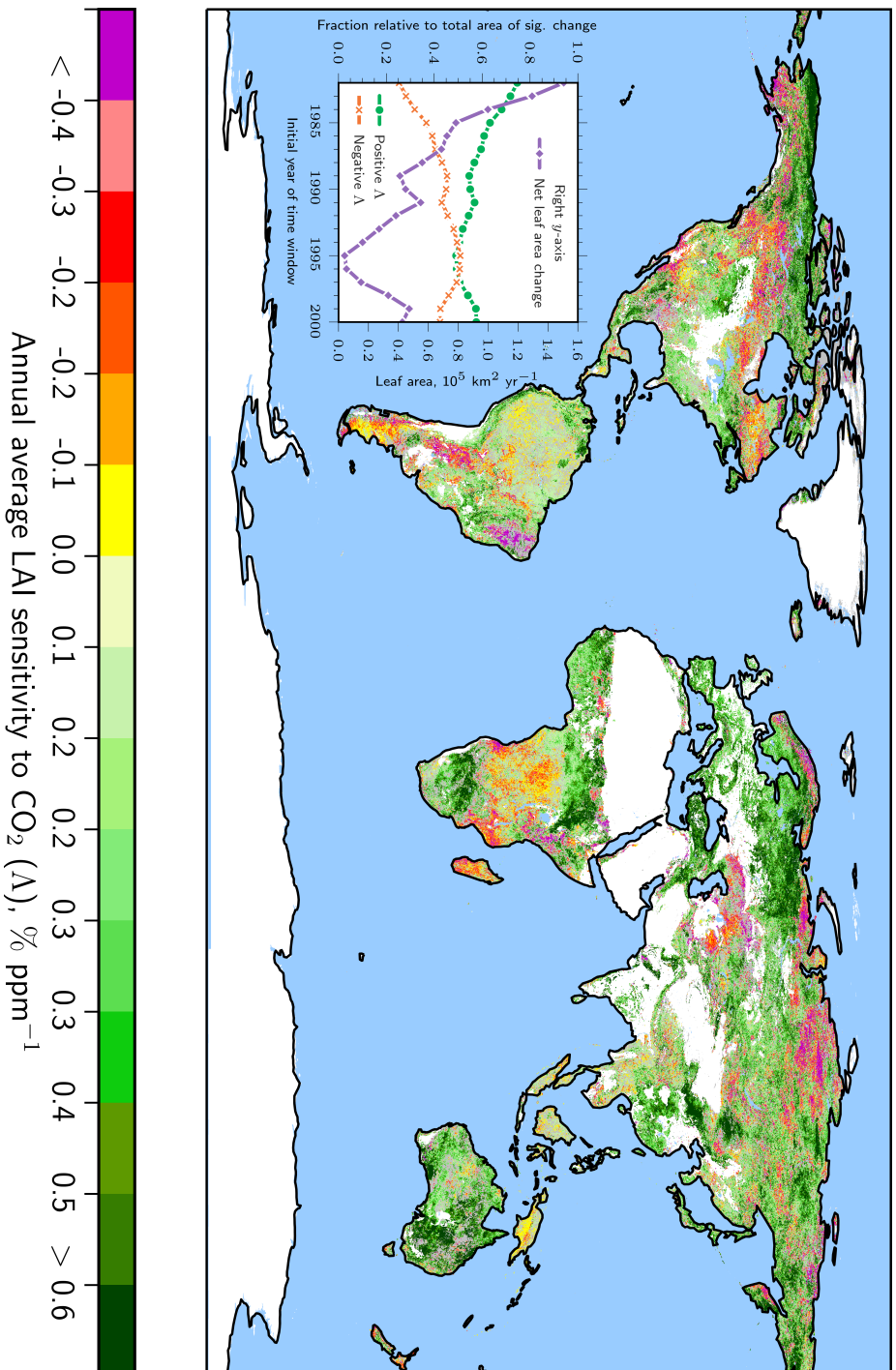


Figure 1 | **Natural vegetation exhibits patterns of opposing long-term LAI sensitivities to rising CO₂.** Global map of statistically significant (Mann-Kendall test, $p < 0.1$) annual average LAI sensitivities to CO₂ (denoted Δ) relative to the average state from 1982–1984 for the entire period 1982–2017 (AVHRR, color-coded). Areas of non-significant change are shown in gray. Anthropogenic vegetation (Data and Methods) is masked in white. Other white areas depict ice sheets or barren land. The inset line plot illustrates the change in fraction of positive (green dots) and negative Δ (orange crosses) relative to the total area of significant change, and net leaf area change (purple squares; right y -axis) for time windows of moving initial year (final year fixed at 2017). The x -axis shows the advancing initial year of the time window.

Net annual gain of leaf area is declining in natural vegetation. Leaf area loss occurs primarily in densely vegetated biomes (i.e. forests), which outweighs leaf area gain in rather sparsely vegetated regions (e.g. grasslands). For instance, the vigorously greening areas of circumpolar tundra result in a leaf area gain of $8.74 \times 10^3 \text{ km}^2 \text{ yr}^{-1}$, which is almost fourfold outbalanced by a leaf area loss of $34.31 \times 10^3 \text{ km}^2 \text{ yr}^{-1}$ of the browning regions in the tropical forests (Table 2). To assess the opposed responses of different biomes to rising CO_2 in more detail, we iteratively calculate statistically significant LAI trends for a time window of advancing initial year (i.e. 1982, 1983, ..., 2000), but fixed final year (2017). Although the estimated trends become less robust with a shortening of the time series, this analysis allows us to test for weakening or strengthening responses to further rising CO_2 . We show that the fraction of significantly browning regions is increasing over time reaching a maximum for a time window starting in 1995. The greening fraction evolves in the opposite direction. The estimates are represented as fractions of the total area of significant change, because the latter inherently decreases as a result of the Mann-Kendall test for shorter time windows. As a consequence, the average annual net leaf area gain of $150.51 \times 10^3 \text{ km}^2 \text{ yr}^{-1}$ for the entire observational period (1982–2017) diminishes with advancing initial year, approaches zero (1995–2017), and finally rebounds to $\sim 40 \times 10^3 \text{ km}^2 \text{ yr}^{-1}$ (2000–2017; purple line in inset in Figure 1). To obtain comparability between different time windows, the net leaf area gain estimates were scaled to the total area of significant change derived for 1982–2017 (unprocessed estimates for period 2000–2017 are listed in Table A2). Chen et al. (2019) reported a global greening proportion of $\sim 33\%$ (AVHRR: 21%; Table A2) and a browning proportion of only 5% (AVHRR: 13%; Table A2) analyzing the MODIS record including anthropogenic vegetation (2000–2017). On a global scale, LAI trends from MODIS and AVHRR agree over 61% of the vegetated area (Chen et al., 2019). Disagreement arises primarily in the tropical regions (absence of browning Central African tropical forests in the MODIS record) and at northern high latitudes (Chen et al., 2019).

High LAI regions are browning, low LAI regions are greening. The intensification of browning during the second half of the observational period (2000–2017) results in a reversal of the sign in terms of net leaf area change in some biomes (e.g. tropical forests, North American boreal forests, and Eurasian tundra; Table A3). Critically, the tropical forests display the sharpest transition from a substantial net gain of $24.11 \times 10^3 \text{ km}^2 \text{ yr}^{-1}$ (Table 2) to a comparably strong net loss of leaf area ($-18.42 \times 10^3 \text{ km}^2 \text{ yr}^{-1}$; Table A3). To address the temporal development of positive and negative Δ in more detail, we calculate time series of area-weighted averages of LAI (Figure 2a). We find that browning of natural vegetation occurs at a considerably higher level of LAI (on average ~ 1.85) than greening (on average ~ 1.32). Throughout the observational period, these two time series of opposite trends converge towards a LAI of 1.6 (Figure 2a). This convergence of greening and browning is not only evident in terms of their LAI level (Figure 2a), but also in their proportions (inset in Figure 1). On the contrary, time series of anthropogenic vegetation, aggregated for positive and negative Δ , are both confined to a comparable low LAI level (on average between 1 and 1.25). We next investigate the global LAI distributions of negative and positive Δ and their development over time. Comparing distributions of the earlier (1982–1984) with those of the more recent years (2015–2017) reveals that browning primarily occurs at a high (5–6) and a medium level of LAI (1–2.5; Figure 2b). Greening, however, is occurring almost entirely at low levels of LAI between 0–1.5. As a consequence, the global

area-weighted averages of the browning and greening regions are approaching one another (dashed versus solid vertical lines in Figure 2b), as also depicted by the time series (Figure 2a). Overall, the above results suggest a homogenization of Earth’s natural vegetation with rising CO₂. This homogenization becomes prominent when we compare the distributions of negative and positive Δ over time using a Q-Q plot (quantile-quantile; Figure 2c). The relationship between the quantiles is skewed to the left at higher LAI (positive Δ on x -axis, negative Δ on y -axis), because browning is prevalent at high LAI regions. Over time, the quantiles of the greening and browning distributions are approaching the 1-1 line (representing identical distributions), emphasizing their convergence.

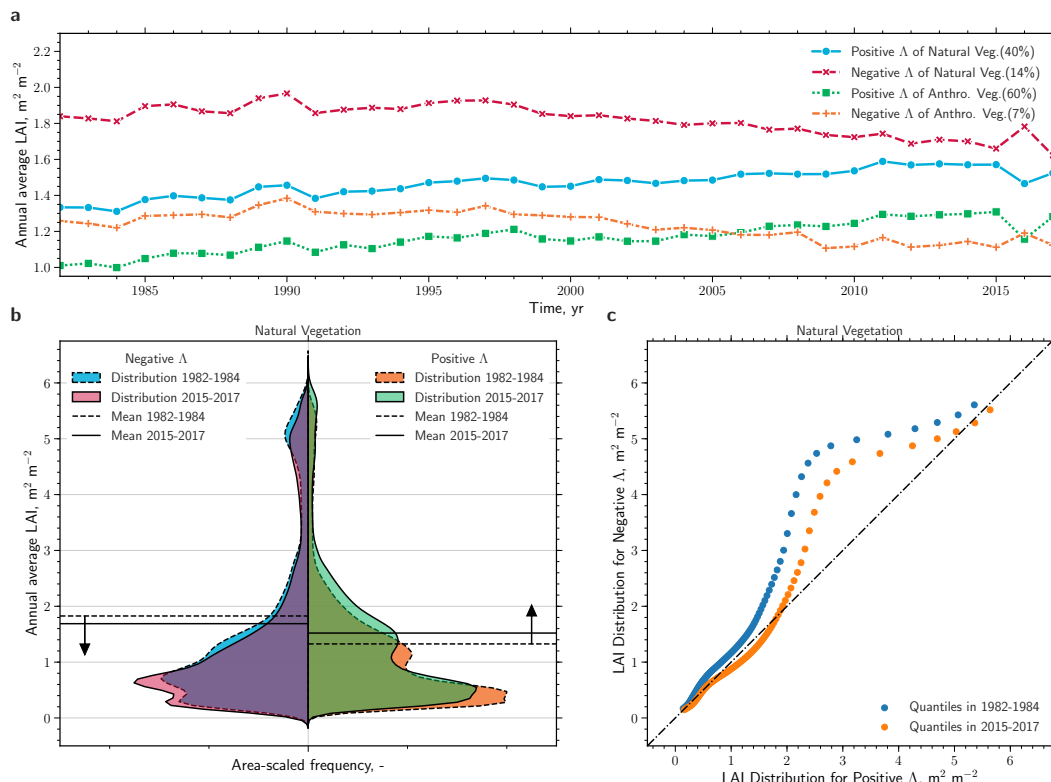


Figure 2 | **Observed homogenization of the global natural vegetation.** **a** Time series of the area-weighted annual average LAI (AVHRR, 1982-2017) of natural and anthropogenic vegetation for regions of positive and negative sensitivity to rising atmospheric CO₂ concentration (Δ). Only regions of significant change are considered (Mann-Kendall significance test, $p < 0.1$). The percentages in brackets in the legend represent the respective proportions with respect to the total area. **b** Violin plot comparison of probability density functions (PDF, Gaussian kernel density estimation; all PDFs scaled to contain the same area) of LAI distributions of natural vegetation for negative (left) and positive Δ (right), and in time, 1982-1984 (dashed) versus 2015-2017 (solid). The horizontal lines represent the mean values for the respective period. **c** Q-Q (quantile-quantile) plot comparing the distributions of LAI for negative (x -axis) and positive Δ (y -axis) and their change over time, 1982-1984 (blue dots) versus 2015-2017 (orange dots).

Table 1 | Greening, browning and non-changing fractions of vegetated area for different biomes and prominent clusters of change for the time period 1982–2017. Significant changes are determined by the means of the Mann-Kendall significance test ($p < 0.1$). The abbreviations used to describe the different clusters are explained in Section 2.

Area	Vegetated Area	Positive Δ Fraction	Negative Δ Fraction	No-Change Fraction
<i>Unit</i>	10^6 km^2	-	-	-
All Vegetation	109.42	0.43	0.13	0.45
Anthro. Vegetation	15.37	0.6	0.07	0.32
Natural Vegetation	94.05	0.4	0.14	0.47
Biomes				
Grasslands	26.77	0.4	0.12	0.48
Tropical Forests	20.32	0.28	0.16	0.55
Boreal Forests	13.69	0.4	0.19	0.41
Temperate Forests	11.2	0.56	0.08	0.36
Shrublands	10.37	0.41	0.1	0.49
Tundra	7.03	0.41	0.14	0.45
Savannas	4.22	0.48	0.13	0.38
Clusters				
Cool Gl	12.32	0.4	0.12	0.48
EA Brl F	8.0	0.53	0.1	0.37
NAm Brl F	5.69	0.23	0.31	0.46
NAf Sv Gl	5.6	0.59	0.06	0.35
CAf Trp F	5.35	0.3	0.25	0.45
SAf Sv Gl	4.6	0.24	0.24	0.52
Aus Sl	4.43	0.49	0.03	0.49
EA Tundra	3.57	0.35	0.2	0.44
NAm Tundra	3.46	0.46	0.07	0.47

The majority of models reproduce the observed convergence of greening and browning trends. Thus far, we have described in depth the diverse long-term changes of natural vegetation across all continents and throughout the entire satellite era. We next investigate the underlying mechanisms driving these greening and browning trends and use the fully-coupled MPI-ESM and the TRENDYv7 ensemble of observation-driven LSMs (Data and Methods). As a first step, we examine if these models capture the observed behavior of natural vegetation under rising CO₂. MPI-ESM reproduces the observed browning of high LAI and the greening of low LAI regions, however, the levels of LAI do not match the observations (Figure A1). Historical simulations of TRENDYv7 (here 13 models) also show pronounced changes in vegetation, but feature a quite diverse behavior among the models (results not shown for brevity). Seven LSMs reproduce observed converging trends of greening and browning, whereas the other six models show divergent trends. All TRENDYv7 models are driven with identical atmospheric forcing fields, hence, these six models most likely lack or incorrectly represent key processes of ecosystem functioning. In general, simulated greening patterns are comparable to observations (Murray-Tortarolo et al., 2013; Sitch et al., 2015; Mahowald et al., 2016), but browning, especially in the North American boreal forests, is underestimated (Sitch et al., 2015).

Models point at the physiological effect of CO₂ as main driver of greening on global scale. Hereafter, we use changes in annual average LAI relative to the baseline period 1982–1984 (Data and Methods). Expressed in this form, we obtain a better comparability among biomes, various simulations and the observed signal. Time series of relative LAI changes from historical simulations (multi-model average for TRENDYv7 and multi-realizations average for MPI-ESM) are comparable to observations on a globally aggregated level (Figure 3a and 3b; temporal correlations are low due to high internal variability of the signal).

We use the framework of Counterfactual Causal Theory (Pearl, 2009; Hannart et al., 2016; Hannart and Naveau, 2018) to attribute changes in LAI to a given driver in a probabilistic setting (Data and Methods). Based on the all-forcings (also termed factual) and factorial runs (also termed counterfactual), we derive probabilities of causation that combines necessity and sufficiency of each factor (PNS). On global scale, the estimates of observed (~ 1.08 % decade⁻¹) and the factual MPI-ESM estimate (~ 1.14 % decade⁻¹) are comparable, whereas the multi-model average of the TRENDYv7 ensemble is overestimated (~ 1.79 % decade⁻¹; Figure 3c). Omitting CO₂-induced climate change (No RE) does not have a strong effect in the MPI-ESM (~ 1.04 % decade⁻¹), i.e. the estimate does not differ considerably from the factual run. The TRENDYv7 models indicate that the positive trend in LAI can be explained by climate change to some extent (~ 1.21 % decade⁻¹). However, PNS are low for the radiative effect of CO₂ (Figure 3d). The opposite is the case, when the physiological effect of CO₂ (No PE) is excluded. Both model setups agree that almost no positive trend in LAI is present in a world without CO₂ fertilization (MPI-ESM: ~ 0.18 % decade⁻¹, TRENDYv7: ~ 0.08 % decade⁻¹; both estimates are lower than internal variability of ~ 0.49 % decade⁻¹). As a consequence, high PNS can be established: The physiological effect of CO₂ has in the case of MPI-ESM *likely* (68%) and in the case of TRENDYv7 *very likely* (91%) caused the positive trend of global LAI in recent decades (Figure 3d). This result is in line with Zhu et al. (2016) who reported that 70% of global greening is attributable to CO₂ fertilization. Removing both effects of CO₂ results in slight negative trends, probably rooted in gradual deforestation practices (Figure 3c).

Table 2 | Leaf area gain, loss, and net change for different biomes and prominent clusters of change for the time period 1982–2017. Significant changes are determined by the means of the Mann-Kendall significance test ($p < 0.1$). The abbreviations used to describe the different clusters are explained in Data and Methods.

Leaf Area	Leaf Area Gain	Leaf Area Loss	Net Leaf Area Change
<i>Unit</i>	$10^3 \text{ km}^2 \text{ yr}^{-1}$	$10^3 \text{ km}^2 \text{ yr}^{-1}$	$10^3 \text{ km}^2 \text{ yr}^{-1}$
All Vegetation	296.87	-85.71	211.16
Anthro. Vegetation	67.12	-6.47	60.65
Natural Vegetation	229.75	-79.24	150.51
Biomes			
Grasslands	48.01	-12.51	35.50
Tropical Forests	58.42	-34.31	24.11
Boreal Forests	32.11	-14.45	17.66
Temperate Forests	53.32	-7.45	45.87
Shrublands	10.9	-2.4	8.50
Tundra	8.74	-3.69	5.05
Savannas	17.99	-4.21	13.78
Clusters			
Cool Gl	15.06	-3.75	11.31
EA Brl F	25.93	-4.26	21.67
NAm Brl F	6.18	-10.18	-4.00
NAf Sv Gl	23.42	-0.98	22.44
CAf Trp F	16.76	-13.76	3.00
SAf Sv Gl	5.51	-6.76	-1.25
Aus Sl	4.48	-0.16	4.32
EA Tundra	3.96	-3.04	0.92
NAm Tundra	4.78	-0.64	4.14

The global signal switches to a minor negative trend in the second half of the observational period. Natural vegetation shows as slight negative trend for the period 2000–2017 (~ -0.4 % decade⁻¹; Figure 3e). This estimate is within the range of internal variability, and thus, should be interpreted with caution. Yet, this result points in the direction of an intensification of vegetation browning and/or weakening of vegetation greening on the global scale. Note, that the net change in leaf area is still positive when considering only significantly changing pixels (inset in Figure 1). Models reproduce this reversal in the sign when the physiological effect of CO₂ is excluded or with a complete absence of CO₂ forcing (Figure 3e). Overall, driver attribution on the global scale, as described above and used in Zhu et al. (2016), neglects the heterogeneity of natural vegetation and the possibility that divergent responses of different biomes might cancel out. To account for this omission, we identify eleven clusters of significant change and derive probabilities of causation for each driver across different vegetation types (Figure 4).

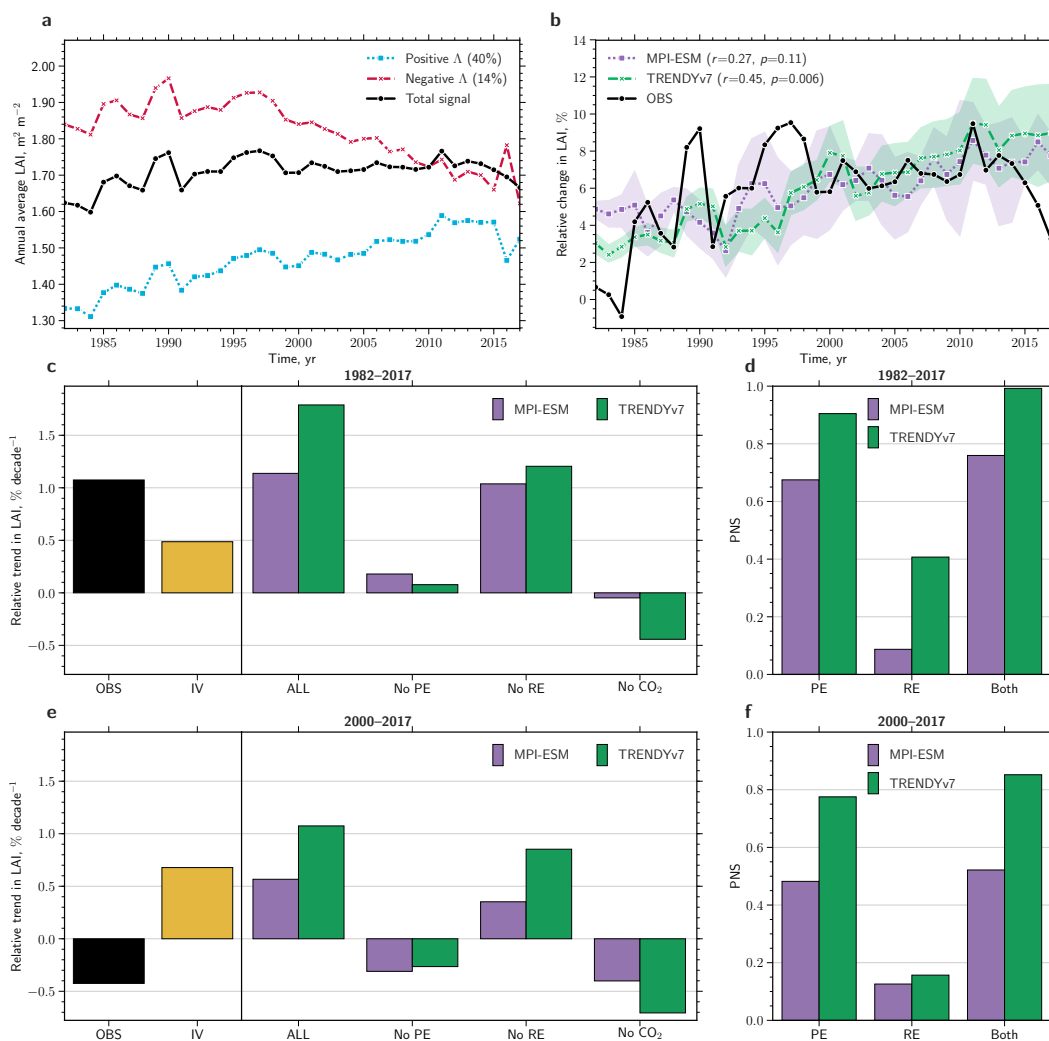


Figure 3 | Figure caption on the following page.

Figure 3 | **Driver attribution of changing natural vegetation for the entire period versus the second half of the observational record.** **a** Time series of the area-weighted annual average LAI (AVHRR, 1982–2017) for regions of positive (blue dotted line) and negative sensitivity (red dashed line) to rising atmospheric CO₂ concentration (Δ) of natural vegetation. Black solid line represents the overall signal of all pixels. The percentages in brackets in the legend represent the greening and browning proportions with respect to the total area. **b** Time series of changes in LAI relative to the average state from 1982–1984, comparing observations (black solid line) with historical simulations, where the green dashed line denotes the ensemble mean of 13 offline-driven land surface models (TRENDYv7, Data and Methods), and the purple dotted line denotes the average of an ensemble of multi-realizations with a fully-coupled Earth system model (MPI-ESM, Data and Methods). The colored shading represents the 95% confidence interval estimated by bootstrapping. The correlation coefficients (including significance level) of the observed and simulated time series are displayed in brackets in the legend. **c** Bar chart showing relative trends in LAI (in % yr⁻¹) of the total observed signal (black) and for factual (all historical forcings; ALL) as well as for counterfactual simulations, i.e. no historical CO₂ forcing (No CO₂), all historical forcings except the physiological effect (No PE) or the radiative effect (No RE) of atmospheric CO₂, as estimated by TRENDYv7 (green) and MPI-ESM (purple). The yellow bar represents internal variability (IV) derived from all simulations (control, factual and counterfactual). **d** Probabilities of necessary and sufficient causation (PNS) of the change in LAI, comparing the physiological (PE) and radiative effect (RE) of CO₂ as well as their combined effect (Both). **e** as in **c** but for the period 2000–2017. **f** as in **d** but for the period 2000–2017.

Temperate forests prosper with rising CO₂, tropical forests are increasingly under pressure. Forests in a temperate climate exhibit a strong positive trend in LAI (~ 2.53 % decade⁻¹), which is also seen in the models, albeit slightly overestimated (MPI-ESM: ~ 3.18 % decade⁻¹, TRENDYv7: ~ 2.69 % decade⁻¹; Figure A3). The physiological effect of CO₂ is the main driver with high PNS (85% for MPI-ESM, 80% for TRENDYv7; Figure 4). The trends are slightly weakened when only analyzing the second half of the observational period, but the overall results do not change. Observed warming might have additionally contributed to enhanced vegetation growth (e.g. growing season extension; Piao et al., 2011; Park et al., 2016), however, it is not identified as an important driver by models. Most temperate forests are located in industrialized countries, and thus, are managed in a sustainable manner for several decades (Currie and Bergen, 2008). It is conceivable, that some of the positive trend in LAI could be attributed to forestry, however, this is not captured by the models (i.e. trends are negative when complete CO₂ forcing is absent; Figure A3).

The response of tropical forests to rising CO₂ is more complex. The signal over the entire observational period is slightly positive (~ 0.3 % decade⁻¹), however, it is within the range of internal variability. Therefore, no robust driver attribution is practicable (Figure 4 and Figure A4). TRENDYv7 models show strongly opposed responses of LAI to the different effects of CO₂: LAI decreases when the physiological effect is omitted, but increases when the radiative effect is omitted. MPI-ESM shows qualitatively the same responses, but less pronounced (Figure A4). For the second half of the satellite record, the observed trend switches sign to a pronounced negative trend (~ -1.4 % decade⁻¹). The models reproduce this tendency, however, the multi-model average of the TRENDYv7 ensemble is still positive. During the same time period, the opposed reactions to CO₂ in the factorial runs are more

strongly marked (Figure A4). These results suggest that browning caused by CO₂-induced climate change is compensated by greening affiliated to CO₂ fertilization on the biome level. Based on these findings we hypothesize that the physiological effect of CO₂ is strong in models and outbalances the negative effect of climate change in the tropical forests (Kolby Smith et al., 2016). As a consequence, the all-forcings simulations fail to reproduce the observed patterns of strengthening vegetation browning in the tropics (Zhou et al., 2014; Song et al., 2018).

Droughts in the Amazon basin, long-term drying of tropical Africa. The Amazonian tropical forests are frequently afflicted by severe droughts. Several studies have shown that most of these droughts, e.g. in 1997 (Williamson et al., 2000), in 2010 (Xu et al., 2011), and 2015 (Jiménez-Muñoz et al., 2016), are strongly modulated by the El Niño Southern Oscillation (ENSO), but not exclusively (e.g. in 2005; Marengo et al., 2008). Heavy droughts have diverse impacts on tropical ecosystems (Bonafant et al., 2016), the most prominent being an increase in wildfires and tree mortality. Recently, perennial legacy effects have been identified which lead to persistent biomass loss in the aftermath of severe droughts (Saatchi et al., 2013; Yang et al., 2018). For instance, some regions were still recovering from the impact of the megadrought of 2005 when the next major drought began in 2010 (Saatchi et al., 2013). Such droughts and associated wildfires are predicted to increase in frequency (Cai et al., 2014) and intensity (Fasullo et al., 2018) as a consequence of the ENSO-related amplification of heat waves. Overall, these recurrent droughts result in long-term browning trends (Xu et al., 2011), inline with our results of intensified browning of Amazonian forests (Figure 1).

In contrast to episodic droughts in the Amazon, African tropical forests have experienced a long-term drying trend since the 1970s (Malhi and Wright, 2004; Asefi-Najafabady and Saatchi, 2013; Zhou et al., 2014). The origin of this pronounced decreasing trend in rainfall is still under debate. Precipitation in equatorial Africa is expected to increase under climate change (Weber et al., 2018), so it is hypothesized that this trend is associated with the Atlantic Multidecadal Oscillation and/or changes in the West African Monsoon system (Asefi-Najafabady and Saatchi, 2013). Long-term drying in rainforests could also be connected to the physiological effect of rising CO₂. Recently, it has been demonstrated that the reduction in stomatal conductance and transpiration induces a drier, warmer, and deeper boundary layer, resulting in a decline in local rainfall (Langenbrunner et al., 2019). Regardless of what the origins may be, this long-term water deficit has led to pronounced vegetation browning in recent decades (~ -2.3 % decade⁻¹ for 2000–2017; Zhou et al., 2014), which is not captured by models (Figure A5). Accordingly, no robust attribution is possible with this set of models. Interestingly, the MODIS record does not reflect this pronounced browning cluster (Chen et al., 2019), though it has been reported in other independent observational datasets (Zhou et al., 2014). Also the latest atmospheric CO₂ inversions have identified negative trends of carbon uptake for this region (Fernández-Martínez et al., 2019).

Deforestation practices can explain some part of the observed gradual browning in African tropical forests (Mayaux et al., 2013; Tyukavina et al., 2018) and in the Amazon (Song et al., 2015). In South-Asia, however, deforestation plays a crucial role in the browning of the pristine tropical forests. Significant negative trends align strongly with patterns of drastic deforestation during recent decades, described in detail by Stibig et al. (2014).

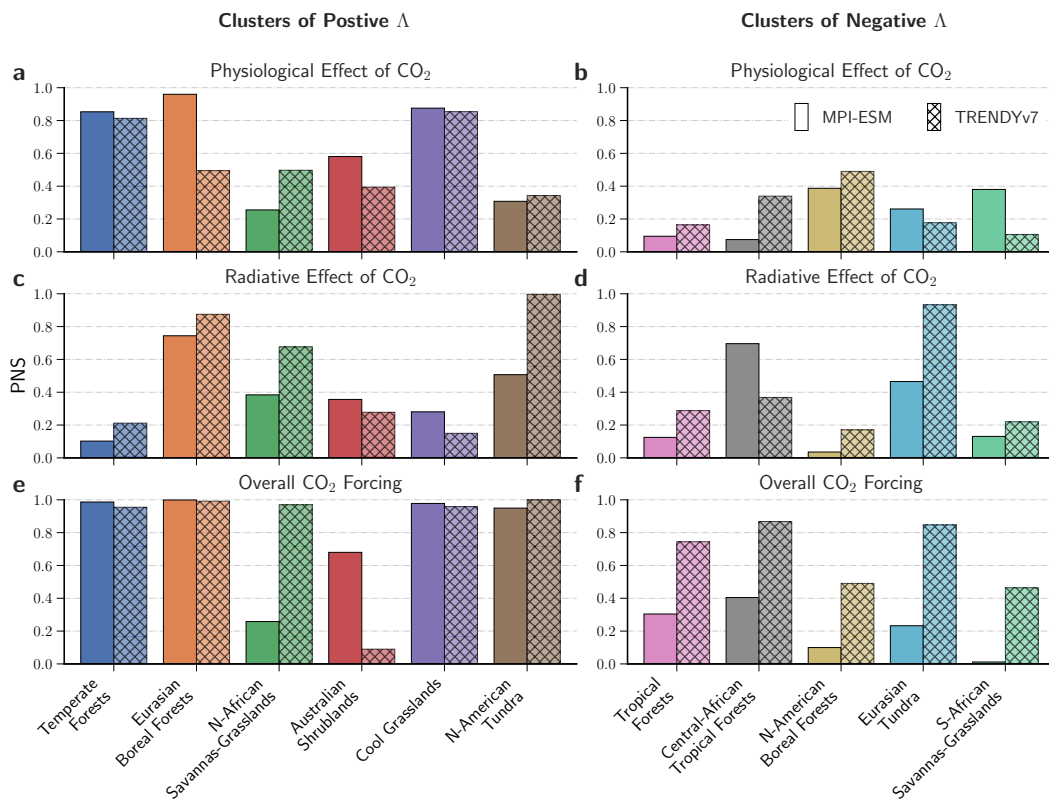


Figure 4 | **Probabilities of sufficient and necessary causation (PNS) of LAI changes in response to CO₂ for eleven clusters.** Bar charts represent PNS of LAI changes in response to the physiological effect (a, b), radiative effect of CO₂ (c, d) and all anthropogenic forcings (e, f). Different colors represent the identified clusters of substantial change in LAI. Panels on the left comprise clusters that show consistent greening, panels on the right represent emerging browning clusters (observed net leaf area loss in the period 2000–2017; attribution is conducted only for significant decreasing trends, Data and Methods). The two types of bar illustrate the two different ensembles of model simulations (left: MPI-ESM, right: TRENDYv7).

Climate change drives an asymmetrical development of North American and Eurasian ecosystems. The boreal forests show pronounced positive trends in Eurasia (Observations: ~ 2.69 % decade⁻¹, MPI-ESM: ~ 3.48 % decade⁻¹, and TRENDYv7: ~ 2.08 % decade⁻¹), which can mostly be attributed to amplified warming of the temperature-limited northern high latitudes (PNS = 71% for TRENDYv7, PNS = 44% for MPI-ESM; Figure A6). North American boreal forests exhibit a negative response to rising CO₂, which has amplified over the last two decades (~ -0.95 % decade⁻¹, 2000–2017). Models do not reproduce the dominant browning (Figure A7), which is most likely connected to the inadequate representation of disturbances (Sitch et al., 2015). Several studies have proposed that browning has occurred as consequence of droughts, wildfire, and insect outbreaks in the North American boreal forests (Goetz et al., 2005; Sitch et al., 2015; Beck and Goetz, 2011). Macias Fauria and Johnson (2008) showed that the frequency of wildfires is strongly related to the dynamics of

large-scale climatic patterns (Pacific Decadal Oscillation, El Niño Southern Oscillation, and Arctic Oscillation) and thus, cannot be tied conclusively to anthropogenic climate change. However, there is also evidence that the residing tree species suffer from drought stress induced by higher evaporative demands as the temperature rises (Verbyla, 2011). Moreover, models lack a representation of the asymmetry in tree species distribution between North America and Eurasia, which could explain their divergent reactions to changes in key environmental variables (Abis and Brovkin, 2017). Further observational evidence for the browning of North American boreal forests and the associated decline in net ecosystem productivity can also be inferred from CO₂ inversion products (Fernández-Martínez et al., 2019; Bastos et al., 2019).

Tundra ecosystems also reveal a dipole-type development between North America and Eurasia, however with a reversed sign. Hence, North American tundra is strongly greening (Observations: ~ 4.23 % decade⁻¹, MPI-ESM: ~ 4 % decade⁻¹, and TRENDYv7: ~ 4.51 % decade⁻¹), which is *virtually certain* (PNS = 99% for TRENDYv7) and *about likely as not* (PNS = 51% for MPI-ESM) caused by warming (Figure A8). The trend decreases for the period 2000–2017, which could be linked to the warming hiatus in the years 1998–2012 (Bhatt et al., 2013; Ballantyne et al., 2017; Hedemann et al., 2017). This is in line with the observed slow down in tundra greening due to short-term cooling after volcanic eruptions (Lucht et al., 2002).

Eurasian tundra show a positive trend for the years 1982–2017, but a reversal in trend sign for the years 2000–2017 (Figure A9). Models exhibit some evidence of a strengthening browning signal, but fail to capture the full extent of the emerging browning clusters seen in observations. If we only consider the grid cells that show significant browning in observations and models, we are able to conduct a robust driver attribution. According to the TRENDYv7 ensemble, the browning cluster in Eurasian tundra can *very likely* be attributed to CO₂ induced climate change (PNS = 93%, PNS = 47% for MPI-ESM). These results are in line with studies showing that tundra ecosystems are susceptible to warm spells during growing season (Phoenix and Bjerke, 2016) and exposed to frequent droughts (Beck and Goetz, 2011). The asymmetry between Eurasia and North America can be explained by changes in large-scale circulation. Eurasia is cooling through increased summer cloud cover, whereas North America is warming through more cloudless skies (Bhatt et al., 2013; Bhatt et al., 2014). Also linkages between regional Arctic sea ice retreat, subsequent increasing ice-free waters, and regional Arctic vegetation dynamics have been described (Bhatt et al., 2014).

Vegetation in arid climates is greening, except in South America. Non-forested greening clusters beyond the high northern latitudes coincide with semi-arid to arid climates (Park et al., 2018). The Northern Sub-Saharan African savannas and grasslands greened extensively in recent decades (~ 4.63 % decade⁻¹; Figure A10), which is reproduced by the observation-driven TRENDYv7 models (~ 4.55 % decade⁻¹), and is *likely* caused by climatic changes (PNS = 68%). No robust attribution is feasible based on the MPI-ESM simulations. However, it is noteworthy, that the fully-coupled Earth system model points to climate change having a negative effect in these regions, thus, not reproducing the increase in rainfall observed (Figure A10). This provides evidence for the hypothesis that African precipitation anomalies are not induced by rising CO₂, but rather follow a multidecadal internal climatic mode (Asefi-Najafabady and Saatchi, 2013).

Internal variability in LAI changes is strong in the Southern African grasslands and savannas, and thus, no robust long-term change can be identified (Figure A11). It has been shown that shrublands in more southern regions are greening as response to increased rainfall (Fensholt and Rasmussen, 2011). In general, the literature suggests that greening and browning patterns in arid climates are mainly driven by precipitation anomalies (Fensholt and Rasmussen, 2011; Fensholt et al., 2012; Gu et al., 2016; Adler et al., 2017). Close resemblance arises when comparing the spatial patterns of precipitation trends throughout the satellite era (Adler et al., 2017) with significant changes in vegetation in arid environments, especially so on the African continent. Decreased rainfall in arid South America coincides with strong browning clusters (Fensholt et al., 2012). This is in disagreement with the expected strong manifestation of CO₂ fertilization in water-limited environments (Ukkola et al., 2016).

Australian Shrublands show a persistent positive LAI trend (~ 3.84 % decade⁻¹), intermittently perturbed by climatic extreme events (e.g. strong anomalous rainfall with subsequent extensive vegetation greening in 2011 (Poulter et al., 2014, Figure A12). Models reproduce the steady greening of Australia, but no robust driver attribution is feasible due to strong internal variability. However, both model setups point at the physiological effect of CO₂ as the dominant driver (Figure A12). These results are in line with recent studies (Donohue et al., 2009; Ukkola et al., 2016) showing that CO₂ fertilization enhanced vegetation growth by lowering the water limitation threshold.

Grasslands in the cool arid climates exhibit persistent positive trends (~ 2.03 % decade⁻¹, Figure A13). Simulated estimates are in the range of the observations (MPI-ESM: ~ 2.33 % decade⁻¹ and TRENDYv7: ~ 1.81 % decade⁻¹). Our analysis suggests that the positive response of cool arid grasslands to rising CO₂ can be explained by the physiological effect of CO₂ (PNS = 85% for TRENDYv7, PNS = 88% for MPI-ESM). These ecosystems are dominated by C₃-type plants (Still et al., 2003), which are susceptible to CO₂ fertilization (Sage et al., 2012), thus, consistent with our results. In the warm arid areas, C₄-type grasses dominate (Still et al., 2003), which are less sensitive to the physiological effects of CO₂ (Sage et al., 2012). As discussed above, vegetation changes there are mostly driven by precipitation anomalies, although CO₂ fertilization might also contribute to a limited degree (Sage et al., 2012).

4 CONCLUSIONS

In this paper, we examine almost four decades of global LAI observations under rising atmospheric CO₂ concentration. We find that the Earth's greening trend is weakening and clusters of browning are beginning to emerge, and critically, expanded during the last two decades. Leaf area is primarily decreasing in the pan-tropical green belt of dense vegetation. Leaf area gain occurs mostly in sparsely vegetated regions in cold and/or arid climatic zones, and in the temperate forests. Taken together, vegetation greening occurs mainly in regions of low LAI, whereas browning happens primarily in regions of high LAI. As a consequence, the time series of the aggregated greening and browning signals are approaching another and induce a convergence of Earth's natural vegetation.

We identify clusters of greening and browning across all continents and conduct a regional driver attribution based on factorial model simulations. Our results suggest that the physiological effect of CO₂ (i.e. CO₂ fertilization) is the dominant driver of increasing leaf area only in the temperate forests, cool arid grasslands and likely the Australian shrublands, and might only make a small contribution in other biomes. This finding questions the study by Zhu et al. (2016) identifying CO₂ fertilization as prevalent driver of the Earth's greening trend. We find that many clusters of greening and browning bear the signature of climatic changes. The greening of Sub-Saharan grasslands and savannas can be explained by increased rainfall, however, a robust attribution remains inconclusive. Climatic changes, primarily warming and drying, determine the patterns of vegetation changes in the northern ecosystems, i.e. greening of Eurasian boreal forests and North American tundra, but also emerging browning in Eurasian tundra. Models fail to capture the browning of the North American boreal forests. In the tropics, models suggest that rising CO₂ has compensatory effects on LAI. Climatic changes induce browning, which is outweighed by greening due to a strong physiological effect in the models. Hence, if we neglect the physiological effect of CO₂, models simulate emerging browning in the tropics comparable to observations. This lends support to previous findings on the browning of tropical forests caused by climatic changes, covering recurrent droughts in the Amazon as well as long-term drying trends in Africa.

Models represent a simplified view of the real world reduced to its essential processes. Some of these processes are underrepresented or lacking in the current generation of land surface models. Whether they are driven with observed climatic conditions or operate in a fully-coupled Earth System model, they fail to capture the full extent of negative effects of rising CO₂ in natural ecosystems. Especially, the deficiency of reproducing the observed leaf area loss in North American boreal and tropical forests – biomes which account for a large part of the photosynthetic carbon fixation – has considerable implications on future climate projections. Hence, model development should concentrate on not only a better representation of disturbances such as droughts and wildfires, but also on revising the implementation of processes associated with the physiological effect of CO₂, which currently offsets browning induced by climatic changes.

Another vital issue for future research is the impact of large-scale climatic patterns on vegetation. All three major clusters of browning are hypothesized to be associated with temperature or precipitation anomalies modulated by climatic modes. Various heavy

droughts in the Amazon were attributed to El Niño events (Bonal et al., 2016), the long-term drying trend in tropical Africa is possibly connected to the Atlantic Multidecadal Oscillation (Asefi-Najafabady and Saatchi, 2013), and disturbances in North American boreal forests are likely controlled by an interplay of large-scale climatic patterns (Pacific Decadal Oscillation, El Niño Southern Oscillation, and Arctic Oscillation; Macias Fauria and Johnson, 2008). Little is known about how these large-scale pattern might change in a warming climate. Current Earth system models struggle in simulating these climatic modes and related precipitation patterns, which is likely rooted in their coarse spatial resolution. New tools, such as high resolution simulations or large ensembles, open up new possibilities to study these phenomena.

Finally, we point out that the impacts of leaf area changes are not comparable between biomes. Regarding biodiversity, the consequences of leaf area loss in the tropical forests, harboring the most diverse flora and fauna of the planet, are not compensated for by leaf area gain in the temperate and arctic ecosystems. This discrepancy also holds for the carbon cycle perspective, e.g. an additional leaf in the tundra does not offset the reduction in primary productivity of a leaf lost in the tropical rain forest. Thus, our results indicating a substantial loss of tropical leaf area every year are of concern. A recent study suggested that the tropical forests have already switched to being a net source of carbon (Baccini et al., 2017). The uncertainty in future projections is large, ranging from a stable CO₂ fertilization-driven carbon sink to a collapse of the system at a certain CO₂ concentration (Cox et al., 2000). Altogether, the tropical forests have the potential to crucially influence the evolution of climate throughout the 21st century and should be a vital issue for future research.

REFERENCES

- Abis, B. and V. Brovkin (2017). "Environmental Conditions for Alternative Tree-Cover States in High Latitudes." *Biogeosciences* 14.3, pp. 511–527. DOI: [10.5194/bg-14-511-2017](https://doi.org/10.5194/bg-14-511-2017).
- Adler, R. F., G. Gu, M. Sapiano, J.-J. Wang, and G. J. Huffman (2017). "Global Precipitation: Means, Variations and Trends During the Satellite Era (1979–2014)." *Surveys in Geophysics* 38.4, pp. 679–699. DOI: [10.1007/S10712-017-9416-4](https://doi.org/10.1007/S10712-017-9416-4).
- Anav, A. et al. (2013). "Evaluating the Land and Ocean Components of the Global Carbon Cycle in the CMIP5 Earth System Models." *Journal of Climate* 26.18, pp. 6801–6843. DOI: [10.1175/JCLI-D-12-00417.1](https://doi.org/10.1175/JCLI-D-12-00417.1).
- Asefi-Najafabady, S. and S. Saatchi (2013). "Response of African Humid Tropical Forests to Recent Rainfall Anomalies." *Philosophical Transactions of the Royal Society B: Biological Sciences* 368.1625, p. 20120306. DOI: [10.1098/RSTB.2012.0306](https://doi.org/10.1098/RSTB.2012.0306).
- Baccini, A. et al. (2017). "Tropical Forests Are a Net Carbon Source Based on Aboveground Measurements of Gain and Loss." *Science*, eaam5962. DOI: [10.1126/science.aam5962](https://doi.org/10.1126/science.aam5962).
- Ballantyne, A. et al. (2017). "Accelerating Net Terrestrial Carbon Uptake during the Warming Hiatus Due to Reduced Respiration." *Nature Climate Change* 7.2, pp. 148–152. DOI: [10.1038/nclimate3204](https://doi.org/10.1038/nclimate3204).
- Bastos, A. et al. (2018). "Impact of the 2015/2016 El Niño on the Terrestrial Carbon Cycle Constrained by Bottom-up and Top-down Approaches." *Phil. Trans. R. Soc. B* 373.1760, p. 20170304. DOI: [10.1098/rstb.2017.0304](https://doi.org/10.1098/rstb.2017.0304).
- Bastos, A. et al. (2019). "Contrasting Effects of CO₂ Fertilisation, Land-Use Change and Warming on Seasonal Amplitude of Northern Hemisphere CO₂ Exchange." *Atmospheric Chemistry and Physics Discussions*, pp. 1–22. DOI: [10.5194/ACP-2019-252](https://doi.org/10.5194/ACP-2019-252).
- Beck, P. S. A. and S. J. Goetz (2011). "Satellite Observations of High Northern Latitude Vegetation Productivity Changes between 1982 and 2008: Ecological Variability and Regional Differences." *Environmental Research Letters* 6.4, p. 045501. DOI: [10.1088/1748-9326/6/4/045501](https://doi.org/10.1088/1748-9326/6/4/045501).
- Bhatt, U. S. et al. (2013). "Recent Declines in Warming and Vegetation Greening Trends over Pan-Arctic Tundra." *Remote Sensing* 5.9, pp. 4229–4254. DOI: [10.3390/rs5094229](https://doi.org/10.3390/rs5094229).
- Bhatt, U. S. et al. (2014). "Implications of Arctic Sea Ice Decline for the Earth System." *Annual Review of Environment and Resources* 39.1, pp. 57–89. DOI: [10.1146/annurev-environ-122012-094357](https://doi.org/10.1146/annurev-environ-122012-094357).
- Bonal, D., B. Burban, C. Stahl, F. Wagner, and B. Hérault (2016). "The Response of Tropical Rainforests to Drought—Lessons from Recent Research and Future Prospects." *Annals of Forest Science* 73, pp. 27–44. DOI: [10.1007/S13595-015-0522-5](https://doi.org/10.1007/S13595-015-0522-5).
- Bonan, G. B. (2008). "Forests and Climate Change: Forcings, Feedbacks, and the Climate Benefits of Forests." *Science* 320.5882, pp. 1444–1449. DOI: [10.1126/science.1155121](https://doi.org/10.1126/science.1155121).
- Cai, W. et al. (2014). "Increasing Frequency of Extreme El Niño Events Due to Greenhouse Warming." *Nature Climate Change* 4.2, pp. 111–116. DOI: [10.1038/NCLIMATE2100](https://doi.org/10.1038/NCLIMATE2100).
- Chen, C. et al. (2019). "China and India Lead in Greening of the World through Land-Use Management." *Nature Sustainability* 2.2, p. 122. DOI: [10.1038/s41893-019-0220-7](https://doi.org/10.1038/s41893-019-0220-7).
- Cox, P. M., R. A. Betts, C. D. Jones, S. A. Spall, and I. J. Totterdell (2000). "Acceleration of Global Warming Due to Carbon-Cycle Feedbacks in a Coupled Climate Model." *Nature* 408.6809, p. 184. DOI: [10.1038/35041539](https://doi.org/10.1038/35041539).

- Currie, W. S. and K. M. Bergen (2008). "Temperate Forest." In: *Encyclopedia of Ecology*. Ed. by S. E. Jørgensen and B. D. Fath. Oxford, UK: Academic Press, pp. 3494–3503. ISBN: 978-0-08-045405-4. DOI: [10.1016/B978-008045405-4.00704-7](https://doi.org/10.1016/B978-008045405-4.00704-7).
- Donohue, R. J., T. R. McVicar, and M. L. Roderick (2009). "Climate-Related Trends in Australian Vegetation Cover as Inferred from Satellite Observations, 1981–2006." *Global Change Biology* 15.4, pp. 1025–1039. DOI: [10.1111/J.1365-2486.2008.01746.X](https://doi.org/10.1111/J.1365-2486.2008.01746.X).
- Donohue, R. J., M. L. Roderick, T. R. McVicar, and G. D. Farquhar (2013). "Impact of CO₂ Fertilization on Maximum Foliage Cover across the Globe's Warm, Arid Environments." *Geophysical Research Letters* 40.12, pp. 3031–3035. DOI: [10.1002/GRL.50563](https://doi.org/10.1002/GRL.50563).
- Eyring, V. et al. (2016). "Overview of the Coupled Model Intercomparison Project Phase 6 (CMIP6) Experimental Design and Organization." *Geosci. Model Dev.* 9.5, pp. 1937–1958. DOI: [10.5194/gmd-9-1937-2016](https://doi.org/10.5194/gmd-9-1937-2016).
- Fasullo, J. T., B. L. Otto-Bliesner, and S. Stevenson (2018). "ENSO's Changing Influence on Temperature, Precipitation, and Wildfire in a Warming Climate." *Geophysical Research Letters* 45.17, pp. 9216–9225. DOI: [10.1029/2018GL079022](https://doi.org/10.1029/2018GL079022).
- Fatichi, S. et al. (2016). "Partitioning Direct and Indirect Effects Reveals the Response of Water-Limited Ecosystems to Elevated CO₂." *Proceedings of the National Academy of Sciences* 113.45, pp. 12757–12762. DOI: [10.1073/pnas.1605036113](https://doi.org/10.1073/pnas.1605036113).
- Fensholt, R. and K. Rasmussen (2011). "Analysis of Trends in the Sahelian 'Rain-Use Efficiency' Using GIMMS NDVI, RFE and GPCP Rainfall Data." *Remote Sensing of Environment* 115.2, pp. 438–451. DOI: [10.1016/J.RSE.2010.09.014](https://doi.org/10.1016/J.RSE.2010.09.014).
- Fensholt, R. et al. (2012). "Greenness in Semi-Arid Areas across the Globe 1981–2007 — an Earth Observing Satellite Based Analysis of Trends and Drivers." *Remote Sensing of Environment* 121, pp. 144–158. DOI: [10.1016/j.rse.2012.01.017](https://doi.org/10.1016/j.rse.2012.01.017).
- Fernández-Martínez, M. et al. (2019). "Global Trends in Carbon Sinks and Their Relationships with CO₂ and Temperature." *Nature Climate Change* 9.1, p. 73. DOI: [10.1038/s41558-018-0367-7](https://doi.org/10.1038/s41558-018-0367-7).
- Forkel, M. et al. (2016). "Enhanced Seasonal CO₂ Exchange Caused by Amplified Plant Productivity in Northern Ecosystems." *Science* 351.6274, pp. 696–699. DOI: [10.1126/science.aac4971](https://doi.org/10.1126/science.aac4971).
- Forzieri, G., R. Alkama, D. G. Miralles, and A. Cescatti (2017). "Satellites Reveal Contrasting Responses of Regional Climate to the Widespread Greening of Earth." *Science* 356.6343, pp. 1180–1184. DOI: [10.1126/science.aal1727](https://doi.org/10.1126/science.aal1727).
- Giorgetta, M. A. et al. (2013). "Climate and Carbon Cycle Changes from 1850 to 2100 in MPI-ESM Simulations for the Coupled Model Intercomparison Project Phase 5." *Journal of Advances in Modeling Earth Systems* 5.3, pp. 572–597. DOI: [10.1002/jame.20038](https://doi.org/10.1002/jame.20038).
- Goetz, S. J., A. G. Bunn, G. J. Fiske, and R. A. Houghton (2005). "Satellite-Observed Photosynthetic Trends across Boreal North America Associated with Climate and Fire Disturbance." *Proceedings of the National Academy of Sciences of the United States of America* 102.38, pp. 13521–13525. DOI: [10.1073/pnas.0506179102](https://doi.org/10.1073/pnas.0506179102).
- Gu, G., R. F. Adler, and G. J. Huffman (2016). "Long-Term Changes/Trends in Surface Temperature and Precipitation during the Satellite Era (1979–2012)." *Climate Dynamics* 46.3, pp. 1091–1105. DOI: [10.1007/S00382-015-2634-X](https://doi.org/10.1007/S00382-015-2634-X).
- Hannart, A., J. Pearl, F. E. L. Otto, P. Naveau, and M. Ghil (2016). "Causal Counterfactual Theory for the Attribution of Weather and Climate-Related Events." *Bulletin of the American Meteorological Society* 97.1, pp. 99–110. DOI: [10.1175/BAMS-D-14-00034.1](https://doi.org/10.1175/BAMS-D-14-00034.1).

- Hannart, A. and P. Naveau (2018). "Probabilities of Causation of Climate Changes." *Journal of Climate* 31.14, pp. 5507–5524. DOI: [10.1175/JCLI-D-17-0304.1](https://doi.org/10.1175/JCLI-D-17-0304.1).
- Harris, I., P. D. Jones, T. J. Osborn, and D. H. Lister (2014). "Updated High-Resolution Grids of Monthly Climatic Observations – the CRU TS_{3.10} Dataset." *International Journal of Climatology* 34.3, pp. 623–642. DOI: [10.1002/joc.3711](https://doi.org/10.1002/joc.3711).
- Hedemann, C., T. Mauritsen, J. Jungclaus, and J. Marotzke (2017). "The Subtle Origins of Surface-Warming Hiatuses." *Nature Climate Change* 7.5, pp. 336–339. DOI: [10.1038/nclimate3274](https://doi.org/10.1038/nclimate3274).
- Hurtt, G. C. et al. (2011). "Harmonization of Land-Use Scenarios for the Period 1500–2100: 600 Years of Global Gridded Annual Land-Use Transitions, Wood Harvest, and Resulting Secondary Lands." *Climatic Change* 109.1, p. 117. DOI: [10.1007/S10584-011-0153-2](https://doi.org/10.1007/S10584-011-0153-2).
- Jiménez-Muñoz, J. C. et al. (2016). "Record-Breaking Warming and Extreme Drought in the Amazon Rainforest during the Course of El Niño 2015–2016." *Scientific Reports* 6, p. 33130. DOI: [10.1038/SREP33130](https://doi.org/10.1038/SREP33130).
- Jones, P. W. (1999). "First- and Second-Order Conservative Remapping Schemes for Grids in Spherical Coordinates." *Monthly Weather Review* 127.9, pp. 2204–2210. DOI: [10.1175/1520-0493\(1999\)127<2204:FASOCR>2.0.CO;2](https://doi.org/10.1175/1520-0493(1999)127<2204:FASOCR>2.0.CO;2).
- Keenan, T. F. et al. (2016). "Recent Pause in the Growth Rate of Atmospheric CO₂ Due to Enhanced Terrestrial Carbon Uptake." *Nature Communications* 7, p. 13428. DOI: [10.1038/ncomms13428](https://doi.org/10.1038/ncomms13428).
- Kolby Smith, W. et al. (2016). "Large Divergence of Satellite and Earth System Model Estimates of Global Terrestrial CO₂ Fertilization." *Nature Climate Change* 6.3, pp. 306–310. DOI: [10.1038/nclimate2879](https://doi.org/10.1038/nclimate2879).
- Langenbrunner, B., M. Pritchard, G. Kooperman, and J. Randerson (2019). "Why Does Amazon Precipitation Decrease When Tropical Forests Respond to Increasing CO₂?" *Earth's Future* 0 (ja). DOI: [10.1029/2018EF001026](https://doi.org/10.1029/2018EF001026).
- Leakey, A. D. B. et al. (2009). "Elevated CO₂ Effects on Plant Carbon, Nitrogen, and Water Relations: Six Important Lessons from FACE." *Journal of Experimental Botany* 60.10, pp. 2859–2876. DOI: [10.1093/jxb/erp096](https://doi.org/10.1093/jxb/erp096).
- Lucht, W. et al. (2002). "Climatic Control of the High-Latitude Vegetation Greening Trend and Pinatubo Effect." *Science* 296.5573, p. 1687. DOI: [10.1126/science.1071828](https://doi.org/10.1126/science.1071828).
- MacDicken, K. et al. (2015). *Global Forest Resources Assessment 2015: How Are the World's Forests Changing?* Rome: Food and Agriculture Organization of the United Nations. 44 pp.
- Macias Fauria, M. and E. Johnson (2008). "Climate and Wildfires in the North American Boreal Forest." *Philosophical Transactions of the Royal Society B: Biological Sciences* 363.1501, pp. 2317–2329. DOI: [10.1098/RSTB.2007.2202](https://doi.org/10.1098/RSTB.2007.2202).
- Mahowald, N. et al. (2016). "Projections of Leaf Area Index in Earth System Models." *Earth Syst. Dynam.* 7.1, pp. 211–229. DOI: [10.5194/esd-7-211-2016](https://doi.org/10.5194/esd-7-211-2016).
- Malhi, Y. and J. Wright (2004). "Spatial Patterns and Recent Trends in the Climate of Tropical Rainforest Regions." *Philosophical Transactions of the Royal Society of London. Series B: Biological Sciences* 359.1443, pp. 311–329. DOI: [10.1098/RSTB.2003.1433](https://doi.org/10.1098/RSTB.2003.1433).
- Mao, J. et al. (2016). "Human-Induced Greening of the Northern Extratropical Land Surface." *Nature Climate Change* 6.10, pp. 959–963. DOI: [10.1038/nclimate3056](https://doi.org/10.1038/nclimate3056).
- Marengo, J. A. et al. (2008). "The Drought of Amazonia in 2005." *Journal of Climate* 21.3, pp. 495–516. DOI: [10.1175/2007JCLI1600.1](https://doi.org/10.1175/2007JCLI1600.1).
- Marotzke, J. (2019). "Quantifying the Irreducible Uncertainty in Near-term Climate Projections." *Wiley Interdisciplinary Reviews: Climate Change* 10.1, e563. DOI: [10.1002/wcc.563](https://doi.org/10.1002/wcc.563).

- Marotzke, J. et al. (2017). "Climate Research Must Sharpen Its View." *Nature Climate Change* 7, pp. 89–91. DOI: [10.1038/nclimate3206](https://doi.org/10.1038/nclimate3206).
- Mastrandrea, M. D. et al. (2011). "The IPCC AR5 Guidance Note on Consistent Treatment of Uncertainties: A Common Approach across the Working Groups." *Climatic Change* 108.4, p. 675. DOI: [10.1007/S10584-011-0178-6](https://doi.org/10.1007/S10584-011-0178-6).
- Mauritsen, T. et al. (2019). "Developments in the MPI-M Earth System Model Version 1.2 (MPI-ESM1.2) and Its Response to Increasing CO₂." *Journal of Advances in Modeling Earth Systems* 11.4, pp. 998–1038. DOI: [10.1029/2018MS001400](https://doi.org/10.1029/2018MS001400).
- Mayaux, P. et al. (2013). "State and Evolution of the African Rainforests between 1990 and 2010." *Philosophical Transactions of the Royal Society B: Biological Sciences* 368.1625, p. 20120300. DOI: [10.1098/rstb.2012.0300](https://doi.org/10.1098/rstb.2012.0300).
- McPherson, R. A. (2007). "A Review of Vegetation—Atmosphere Interactions and Their Influences on Mesoscale Phenomena." *Progress in Physical Geography: Earth and Environment* 31.3, pp. 261–285. DOI: [10.1177/0309133307079055](https://doi.org/10.1177/0309133307079055).
- Murray-Tortarolo, G. et al. (2013). "Evaluation of Land Surface Models in Reproducing Satellite-Derived LAI over the High-Latitude Northern Hemisphere. Part I: Uncoupled DGVMs." *Remote Sensing* 5.10, pp. 4819–4838. DOI: [10.3390/RS5104819](https://doi.org/10.3390/RS5104819).
- Myneni, R. B., C. D. Keeling, C. J. Tucker, G. Asrar, and R. R. Nemani (1997). "Increased Plant Growth in the Northern High Latitudes from 1981 to 1991." *Nature* 386, pp. 698–702. DOI: [10.1038/386698a0](https://doi.org/10.1038/386698a0).
- Nemani, R. R. et al. (2003). "Climate-Driven Increases in Global Terrestrial Net Primary Production from 1982 to 1999." *Science* 300.5625, pp. 1560–1563. DOI: [10.1126/science.1082750](https://doi.org/10.1126/science.1082750).
- Park, C.-E. et al. (2018). "Keeping Global Warming within 1.5 °C Constrains Emergence of Aridification." *Nature Climate Change* 8.1, p. 70. DOI: [10.1038/S41558-017-0034-4](https://doi.org/10.1038/S41558-017-0034-4).
- Park, T. et al. (2016). "Changes in Growing Season Duration and Productivity of Northern Vegetation Inferred from Long-Term Remote Sensing Data." *Environmental Research Letters* 11.8, p. 084001. DOI: [10.1088/1748-9326/11/8/084001](https://doi.org/10.1088/1748-9326/11/8/084001).
- Pearl, J. (2009). *Causality: Models, Reasoning and Inference*. 2nd ed. Cambridge: Cambridge University Press. ISBN: 978-0-521-89560-6. DOI: [10.1017/CB09780511803161](https://doi.org/10.1017/CB09780511803161).
- Phoenix, G. K. and J. W. Bjerke (2016). "Arctic Browning: Extreme Events and Trends Reversing Arctic Greening." *Global Change Biology* 22.9, pp. 2960–2962. DOI: [10.1111/GCB.13261](https://doi.org/10.1111/GCB.13261).
- Piao, S. et al. (2011). "Changes in Satellite-Derived Vegetation Growth Trend in Temperate and Boreal Eurasia from 1982 to 2006." *Global Change Biology* 17.10, pp. 3228–3239. DOI: [10.1111/J.1365-2486.2011.02419.X](https://doi.org/10.1111/J.1365-2486.2011.02419.X).
- Piao, S. et al. (2014). "Evidence for a Weakening Relationship between Interannual Temperature Variability and Northern Vegetation Activity." *Nature Communications* 5, p. 5018. DOI: [10.1038/ncomms6018](https://doi.org/10.1038/ncomms6018).
- Pinzon, J. E. and C. J. Tucker (2014). "A Non-Stationary 1981–2012 AVHRR NDVI3g Time Series." *Remote Sensing* 6.8, pp. 6929–6960. DOI: [10.3390/rs6086929](https://doi.org/10.3390/rs6086929).
- Poulter, B. et al. (2014). "Contribution of Semi-Arid Ecosystems to Interannual Variability of the Global Carbon Cycle." *Nature* 509.7502, pp. 600–603. DOI: [10.1038/nature13376](https://doi.org/10.1038/nature13376).
- Quéré, C. L. et al. (2018). "Global Carbon Budget 2018." *Earth System Science Data* 10.4, pp. 2141–2194. DOI: [10.5194/ESSD-10-2141-2018](https://doi.org/10.5194/ESSD-10-2141-2018).
- Rodell, M. et al. (2004). "The Global Land Data Assimilation System." *Bulletin of the American Meteorological Society* 85.3, pp. 381–394. DOI: [10.1175/BAMS-85-3-381](https://doi.org/10.1175/BAMS-85-3-381).

- Saatchi, S. et al. (2013). "Persistent Effects of a Severe Drought on Amazonian Forest Canopy." *Proceedings of the National Academy of Sciences* 110.2, pp. 565–570. DOI: [10.1073/PNAS.1204651110](https://doi.org/10.1073/PNAS.1204651110).
- Sachs, L. (1997). *Angewandte Statistik*. Springer Berlin Heidelberg. DOI: [10.1007/978-3-662-05746-9](https://doi.org/10.1007/978-3-662-05746-9).
- Sage, R. F., T. L. Sage, and F. Ocarina (2012). "Photorespiration and the Evolution of C₄ Photosynthesis." *Annual Review of Plant Biology* 63.1, pp. 19–47. DOI: [10.1146/ANNUREV-ARPLANT-042811-105511](https://doi.org/10.1146/ANNUREV-ARPLANT-042811-105511).
- Seidl, R. et al. (2017). "Forest Disturbances under Climate Change." *Nature Climate Change* 7.6, pp. 395–402. DOI: [10.1038/NCLIMATE3303](https://doi.org/10.1038/NCLIMATE3303).
- Sitch, S. et al. (2015). "Recent Trends and Drivers of Regional Sources and Sinks of Carbon Dioxide." *Biogeosciences* 12.3, pp. 653–679. DOI: [10.5194/BG-12-653-2015](https://doi.org/10.5194/BG-12-653-2015).
- Song, X.-P., C. Huang, S. S. Saatchi, M. C. Hansen, and J. R. Townshend (2015). "Annual Carbon Emissions from Deforestation in the Amazon Basin between 2000 and 2010." *PLOS ONE* 10.5, e0126754. DOI: [10.1371/JOURNAL.PONE.0126754](https://doi.org/10.1371/JOURNAL.PONE.0126754).
- Song, X.-P. et al. (2018). "Global Land Change from 1982 to 2016." *Nature*, p. 1. DOI: [10.1038/s41586-018-0411-9](https://doi.org/10.1038/s41586-018-0411-9).
- Stibig, H.-J., F. Achard, S. Carboni, R. Raši, and J. Miettinen (2014). "Change in Tropical Forest Cover of Southeast Asia from 1990 to 2010." *Biogeosciences* 11.2, pp. 247–258. DOI: [10.5194/BG-11-247-2014](https://doi.org/10.5194/BG-11-247-2014).
- Still, C. J., J. A. Berry, G. J. Collatz, and R. S. DeFries (2003). "Global Distribution of C₃ and C₄ Vegetation: Carbon Cycle Implications." *Global Biogeochemical Cycles* 17.1, pp. 6–16–14. DOI: [10.1029/2001GB001807](https://doi.org/10.1029/2001GB001807).
- Thomas, R. T. et al. (2016). "Increased Light-Use Efficiency in Northern Terrestrial Ecosystems Indicated by CO₂ and Greening Observations." *Geophysical Research Letters* 43.21, pp. 11,339–11,349. DOI: [10.1002/2016GL070710](https://doi.org/10.1002/2016GL070710).
- Tyukavina, A. et al. (2018). "Congo Basin Forest Loss Dominated by Increasing Smallholder Clearing." *Science Advances* 4.11, eaat2993. DOI: [10.1126/SCIADV.AAT2993](https://doi.org/10.1126/SCIADV.AAT2993).
- Ukkola, A. M. et al. (2016). "Reduced Streamflow in Water-Stressed Climates Consistent with CO₂ Effects on Vegetation." *Nature Climate Change* 6.1, pp. 75–78. DOI: [10.1038/nclimate2831](https://doi.org/10.1038/nclimate2831).
- Verbyla, D. (2011). "Browning Boreal Forests of Western North America." *Environmental Research Letters* 6.4, p. 041003. DOI: [10.1088/1748-9326/6/4/041003](https://doi.org/10.1088/1748-9326/6/4/041003).
- Weber, T. et al. (2018). "Analyzing Regional Climate Change in Africa in a 1.5, 2, and 3 °C Global Warming World." *Earth's Future* 6.4, pp. 643–655. DOI: [10.1002/2017EF000714](https://doi.org/10.1002/2017EF000714).
- Williamson, G. B. et al. (2000). "Amazonian Tree Mortality during the 1997 El Niño Drought." *Conservation Biology* 14.5, pp. 1538–1542. DOI: [10.1046/J.1523-1739.2000.99298.X](https://doi.org/10.1046/J.1523-1739.2000.99298.X).
- Winkler, A. J., R. B. Myneni, G. A. Alexandrov, and V. Brovkin (2019a). "Earth System Models Underestimate Carbon Fixation by Plants in the High Latitudes." *Nature Communications* 10.1, p. 885. DOI: [10.1038/S41467-019-08633-Z](https://doi.org/10.1038/S41467-019-08633-Z).
- Winkler, A. J., R. B. Myneni, and V. Brovkin (2019b). "Investigating the Applicability of Emergent Constraints." *Earth System Dynamics* 10.3, pp. 501–523. DOI: [10.5194/esd-10-501-2019](https://doi.org/10.5194/esd-10-501-2019).
- Xu, L. et al. (2011). "Widespread Decline in Greenness of Amazonian Vegetation Due to the 2010 Drought." *Geophysical Research Letters* 38.7. DOI: [10.1029/2011GL046824](https://doi.org/10.1029/2011GL046824).

- Yang, Y. et al. (2018). "Post-Drought Decline of the Amazon Carbon Sink." *Nature Communications* 9.1, p. 3172. DOI: [10.1038/S41467-018-05668-6](https://doi.org/10.1038/S41467-018-05668-6).
- Zhou, L. et al. (2014). "Widespread Decline of Congo Rainforest Greenness in the Past Decade." *Nature* 509.7498, pp. 86–90. DOI: [10.1038/nature13265](https://doi.org/10.1038/nature13265).
- Zhu, Z. et al. (2013). "Global Data Sets of Vegetation Leaf Area Index (LAI)_{3g} and Fraction of Photosynthetically Active Radiation (FPAR)_{3g} Derived from Global Inventory Modeling and Mapping Studies (GIMMS) Normalized Difference Vegetation Index (NDVI)_{3g} for the Period 1981 to 2011." *Remote Sensing* 5.2, pp. 927–948. DOI: [10.3390/rs5020927](https://doi.org/10.3390/rs5020927).
- Zhu, Z. et al. (2016). "Greening of the Earth and Its Drivers." *Nature Climate Change* 6.8, pp. 791–795. DOI: [10.1038/nclimate3004](https://doi.org/10.1038/nclimate3004).

Acknowledgements We thankfully acknowledge Taejin Park and Chi Chen for their help with remote sensing data. We thank Stephen Sitch, Pierre Friedlingstein and the TRENDY modelers for providing the TRENDYv7 ensemble model output. A.J.W. wishes to thank Thomas Raddatz and Veronika Gayler for their support in working with the MPI-M Earth system model. We gratefully acknowledge Thomas Riddick for his review and valuable comments on the manuscript.

Author Information The Authors declare no conflict of interests. Correspondence and requests for materials should be addressed to A.J.W. (alexander.winkler@pimmet.mpg.de).

A SUPPLEMENTARY INFORMATION

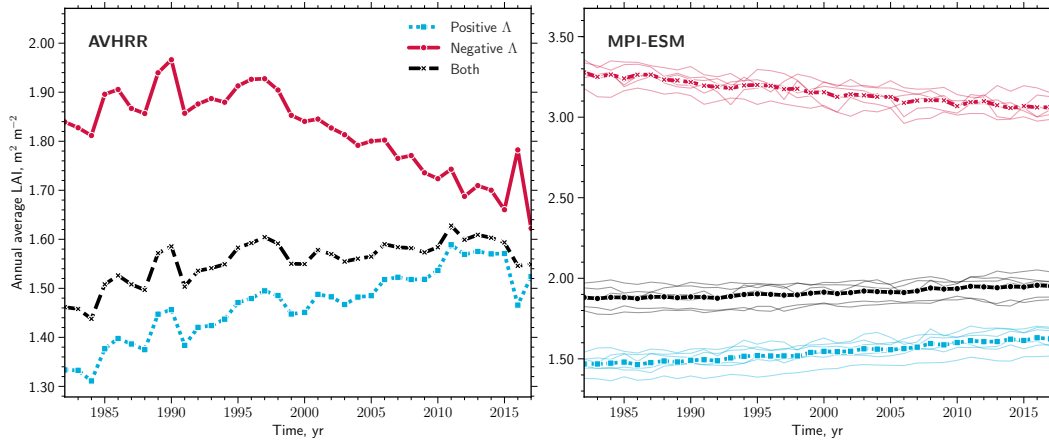


Figure A1 | **Observations versus MPI-ESM.** Time series of area-weighted annual average LAI (left: AVHRR, right: MPI-ESM) for regions of positive (blue line) and negative sensitivity (red line) to rising atmospheric CO₂ concentration (Δ) of natural vegetation. Black line represent the overall signal of all pixels.

Table A1 | Scheme for mapping land covers used in this study from the International Geosphere-Biosphere Programme (IGBP) classes provided by MODIS (https://lpdaac.usgs.gov/dataset_discovery/modis/modis_products_table/mcd12c1_v006) and classes from Global Land Data Assimilation System (GLDAS, (Rodell et al., 2004)). MODIS tree cover product (https://lpdaac.usgs.gov/dataset_discovery/modis/modis_products_table/mod44b_v006) was used to account for the underestimated forested area in MODIS land cover product. Further details are depicted in Data and Methods section of the main paper.

Table A1 | Table caption on the previous page.

IGBP Land Cover Type	Land Cover This Study
Evergreen Needleleaf Forests (ENF)	Boreal Forest
Evergreen Broadleaf Forests (EBF)	Tropical Forest
Deciduous Needleleaf Forests (DNF)	Boreal Forest
Deciduous Broadleaf Forests (DBF)	Temperate Forest
Mixed Forests (MF)	Temperate Forest
Closed Shrublands	Shrublands Tropical Forests for tree cover > 20% and 25° S – 25° N Boreal Forests for tree cover > 10% and > 50° N/S
Open Shrublands	Shrublands Tundra for Wooded, Mixed or Bare Ground Tundra in GLDAS Tropical Forests for tree cover > 20% and 25° S – 25° N Boreal Forests for tree cover > 10% and > 50° N/S
Woody Savannas	1. Step: Tropical Forests for 25° S – 25° N 2. Step: Temperate Forests for DBF or MF in GLDAS Boreal Forests for ENF or DNF in GLDAS 3. Step: Temperate Forests for 25° N/S – 50° N/S Boreal Forests for > 50° N/S
Savannas	Savannas Croplands for Croplands in GLDAS Grasslands for Grasslands in GLDAS Shrublands for Open or Closed Shrublands in GLDAS Tropical Forests for tree cover > 20% and 25° S – 25° N Boreal Forests for tree cover > 10% and > 50° N/S
Grasslands	Grasslands Tundra for Wooded, Mixed or Bare Ground Tundra in GLDAS Tropical Forests for tree cover > 20% and 25° S – 25° N Boreal Forests for tree cover > 10% and > 50° N/S
Permanent Wetlands	Others Tundra for Wooded, Mixed or Bare Ground Tundra in GLDAS
Croplands	Croplands
Urban and Built-up Lands	Others
Cropland/Natural Vegetation Mosaics	Croplands
Permanent Snow and Ice	Others
Barren	Others Tundra for Wooded, Mixed or Bare Ground Tundra in GLDAS
Water Bodies	Water

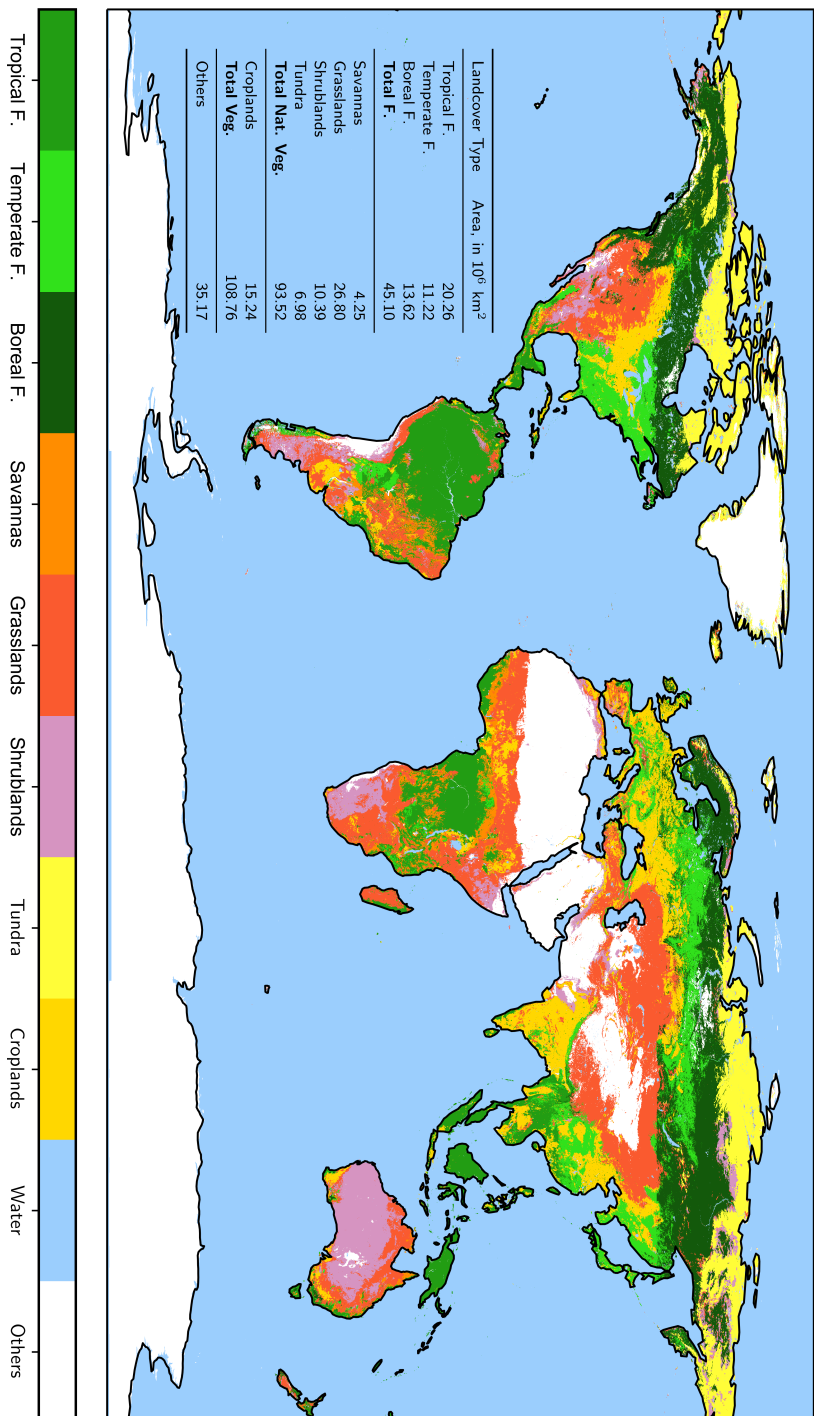


Figure A2 | **Land cover map for broad vegetation classes.** Global map of the distribution of broad land cover types based on the International Geosphere-Biosphere Programme (IGBP) classification, aggregated in anthropogenic (Croplands) and seven natural vegetation classes (Tropical, Temperate, and Boreal Forests, Savannas, Grasslands, Shrublands, and Tundra). The inset table shows the areal extent of each land cover type. Supplementary Table 1 provides a detailed overview on the conflation of the three land and forest cover products used to develop this map. Further details are depicted in the Data and Methods section of the main paper.

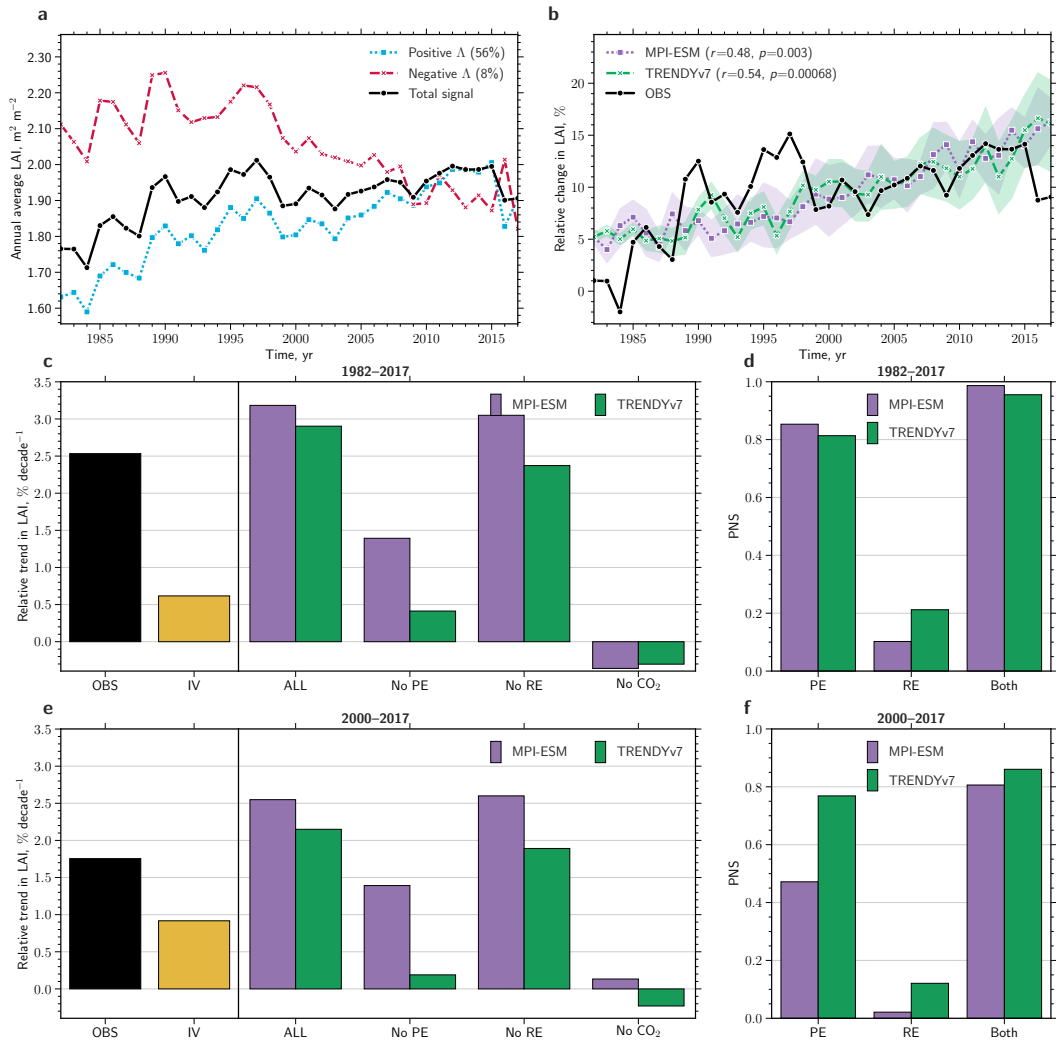


Figure A3 | Figure caption on the following page.

Figure A3 | **Temperate Forests: Driver attribution of changing vegetation for the entire period versus the second half of the observational record.** **a** Time series of the area-weighted annual average LAI (AVHRR, 1982–2017) for regions of positive (blue dotted line) and negative sensitivity (red dashed line) to rising atmospheric CO₂ concentration (Δ) of natural vegetation. Black solid line represent the overall signal of all pixels. The percentages in brackets in the legend represent the greening and browning proportions with respect to the total area. **b** Time series of changes in LAI relative to the average state from 1982–1984, comparing observations (black solid line) with historical simulations, where the green dashed line denotes the ensemble mean of 13 offline-driven land surface models (TRENDYv7, Data and Methods), and the purple dotted line denotes the average of an ensemble of multi-realizations with a fully-coupled Earth system model (MPI-ESM, Data and Methods). The colored shading represents the 95% confidence interval estimated by bootstrapping. The correlation coefficients (including significance level) of the observed and simulated time series are displayed in brackets in the legend. **c** Bar chart showing relative trends in LAI (in % yr⁻¹) of the total observed signal (black) and for factual (all historical forcings; ALL) as well as for counterfactual simulations, i.e. no historical CO₂ forcing (No CO₂), all historical forcings except the physiological effect (No PE) or the radiative effect (No RE) of atmospheric CO₂, as estimated by TRENDYv7 (green) and MPI-ESM (purple). The yellow bar represents internal variability (IV) derived from all simulations (control, factual and counterfactual). **d** Probabilities of necessary and sufficient causation (PNS) of the change in LAI, comparing the physiological (PE) and radiative effect (RE) of CO₂ as well as their combined effect (Both). **e** as in c but for the period 2000–2017. **f** as in d but for the period 2000–2017.

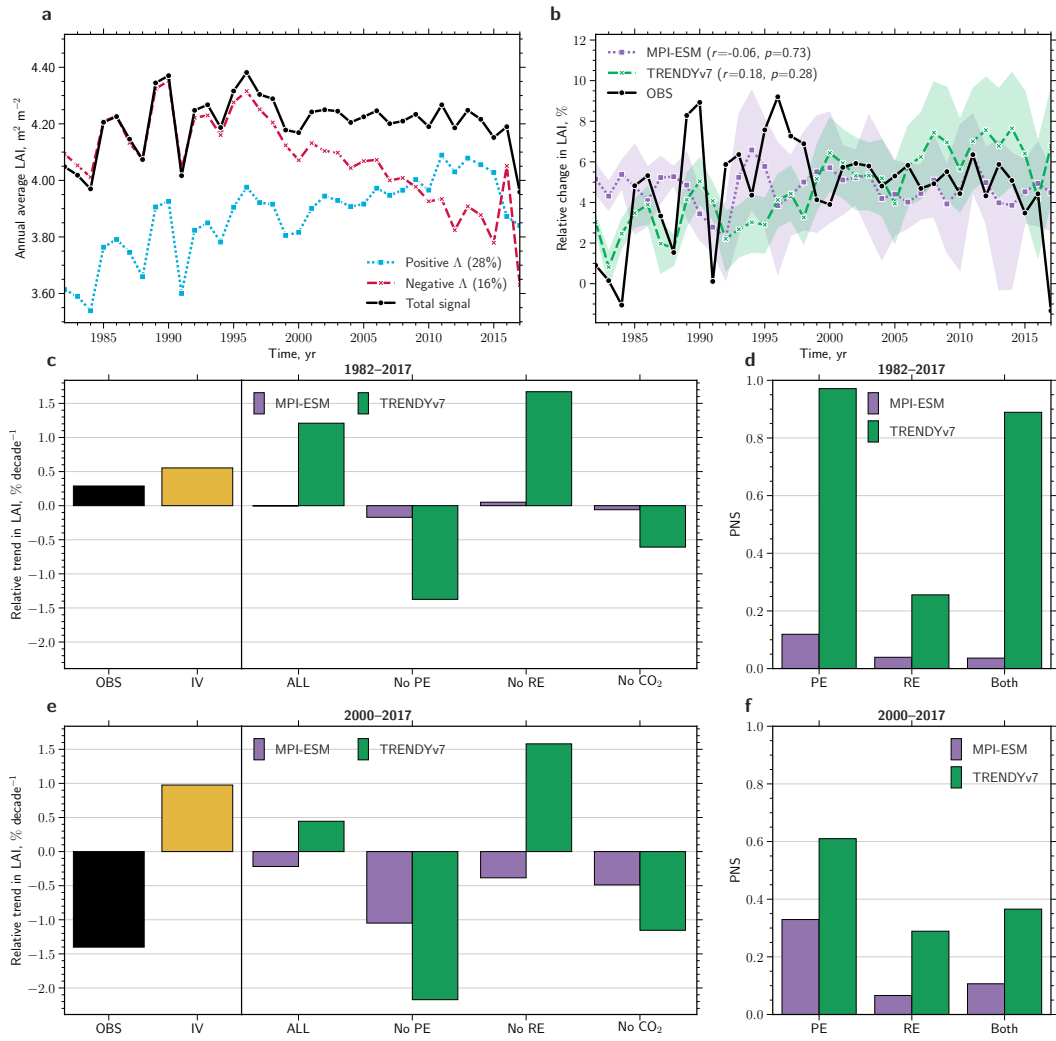


Figure A4 | Tropical Forests – caption analogous to Figure A3.

THE EFFECTS OF RISING CO₂ ON GLOBAL NATURAL VEGETATION

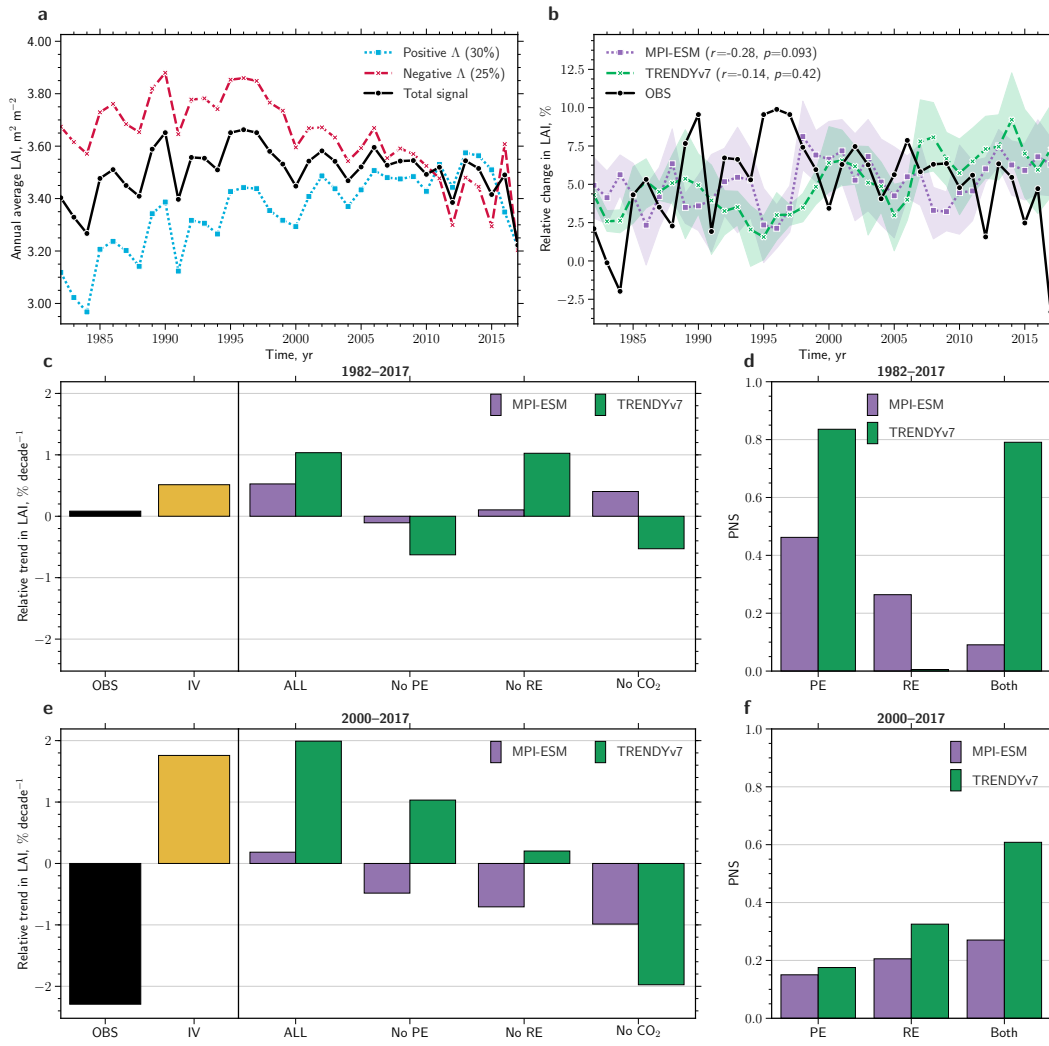


Figure A5 | Central African Tropical Forests – caption analogous to Figure A3.

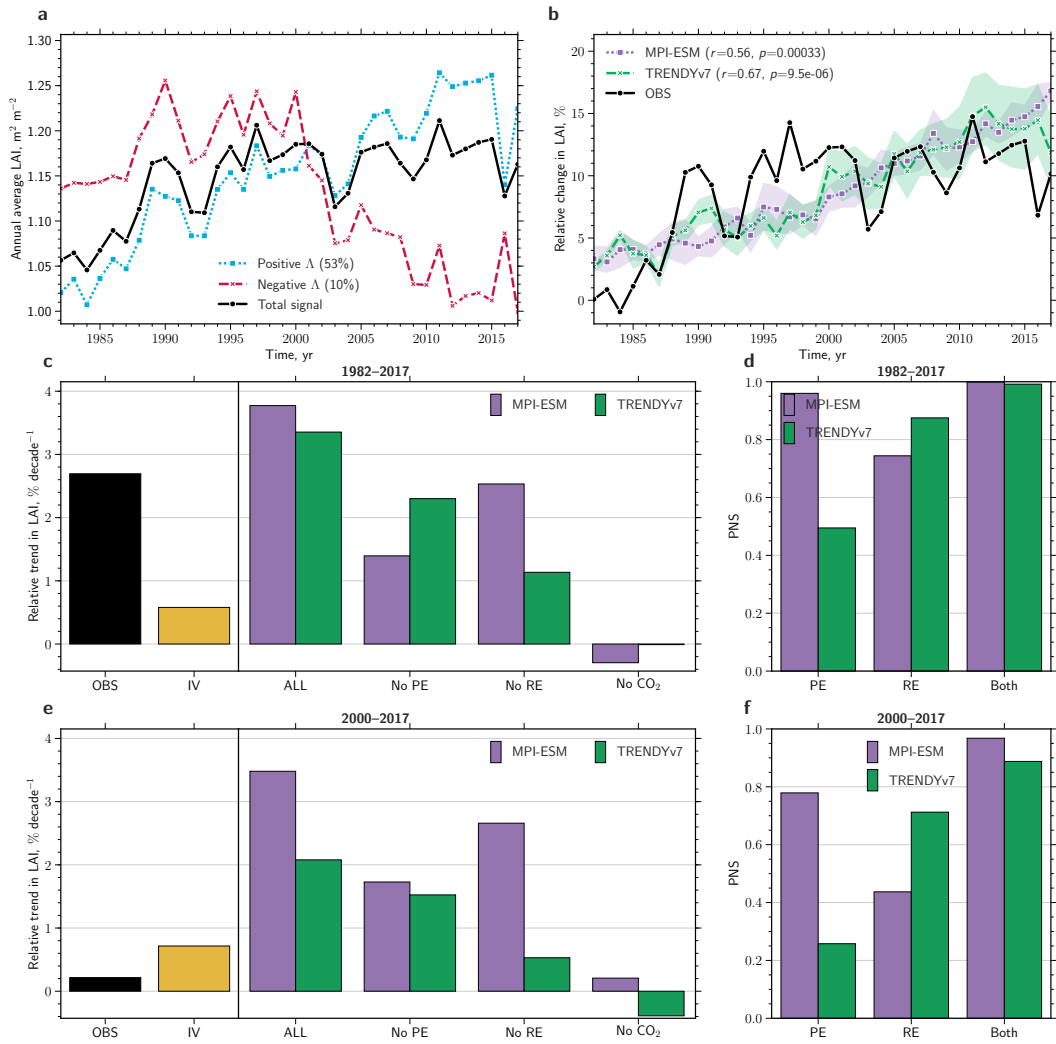


Figure A6 | Eurasian Boreal Forests – caption analogous to Figure A3.

THE EFFECTS OF RISING CO₂ ON GLOBAL NATURAL VEGETATION

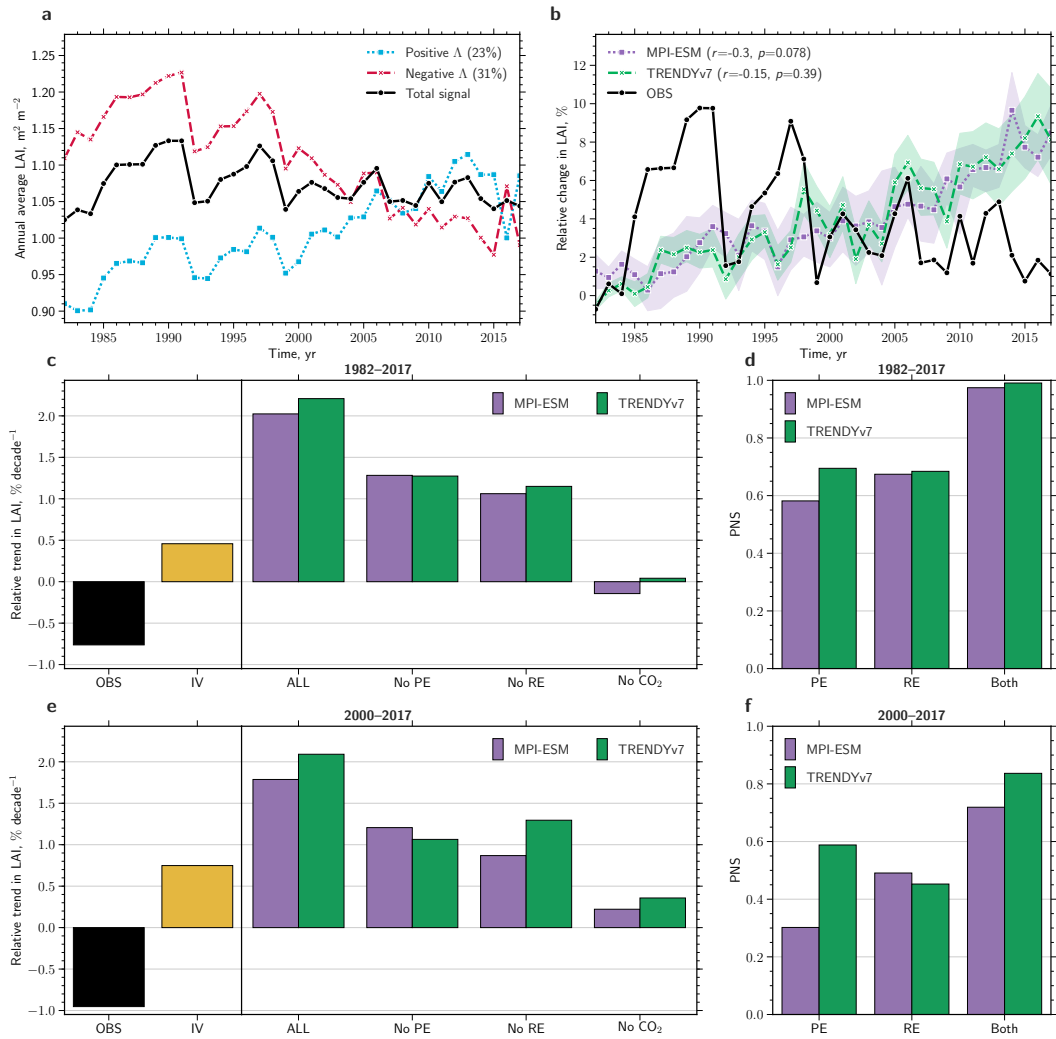


Figure A7 | North American Boreal Forests – caption analogous to Figure A3.

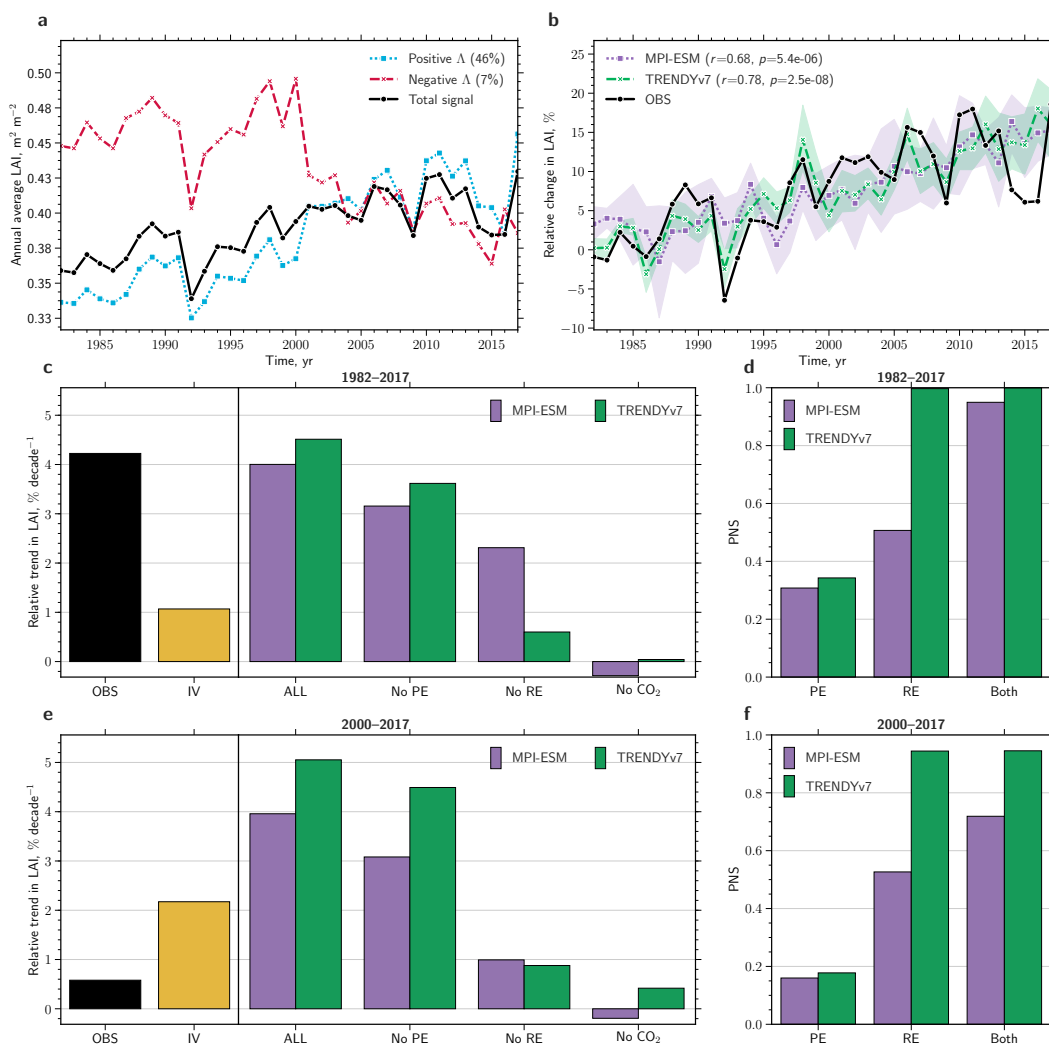


Figure A8 | North American Tundra – caption analogous to Figure A3.

THE EFFECTS OF RISING CO₂ ON GLOBAL NATURAL VEGETATION

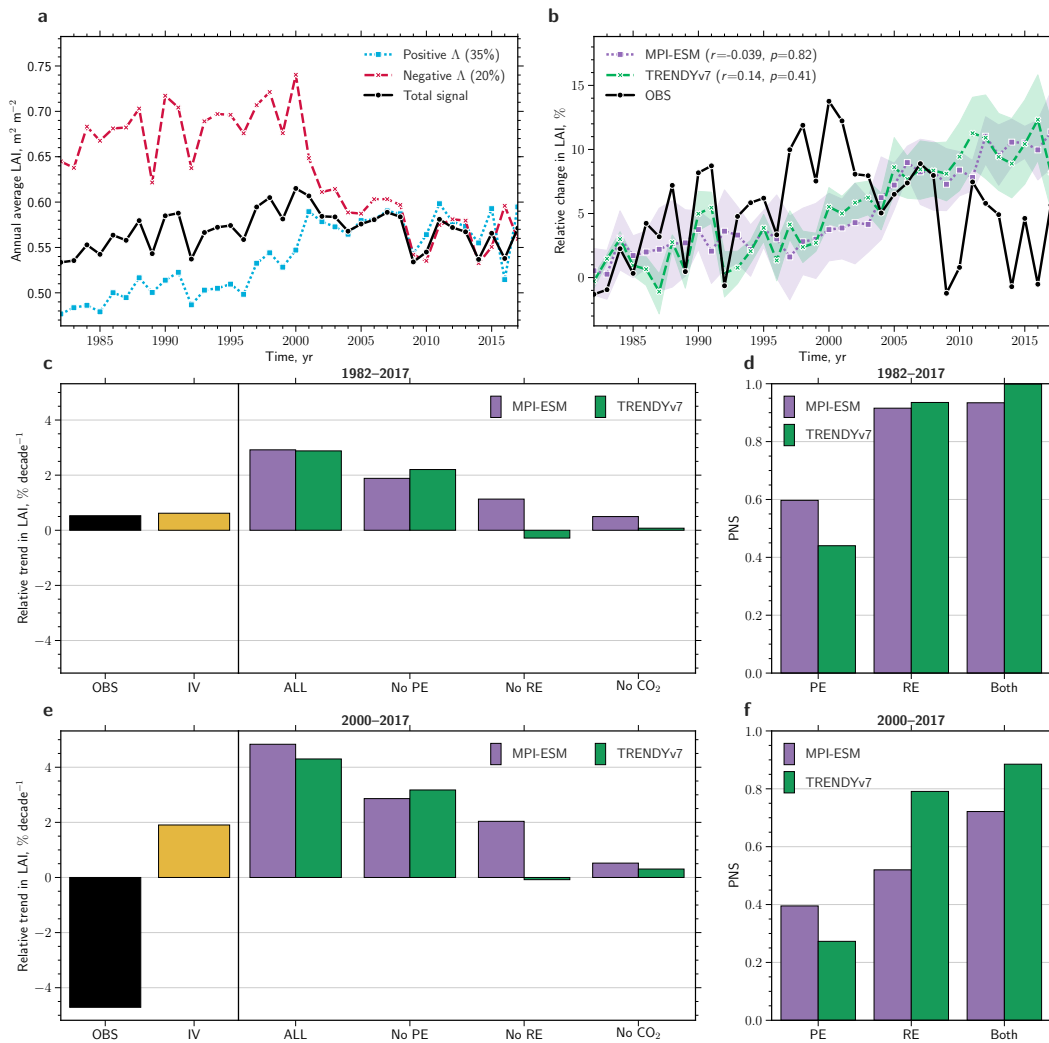


Figure A9 | Eurasian Tundra – caption analogous to Figure A3.

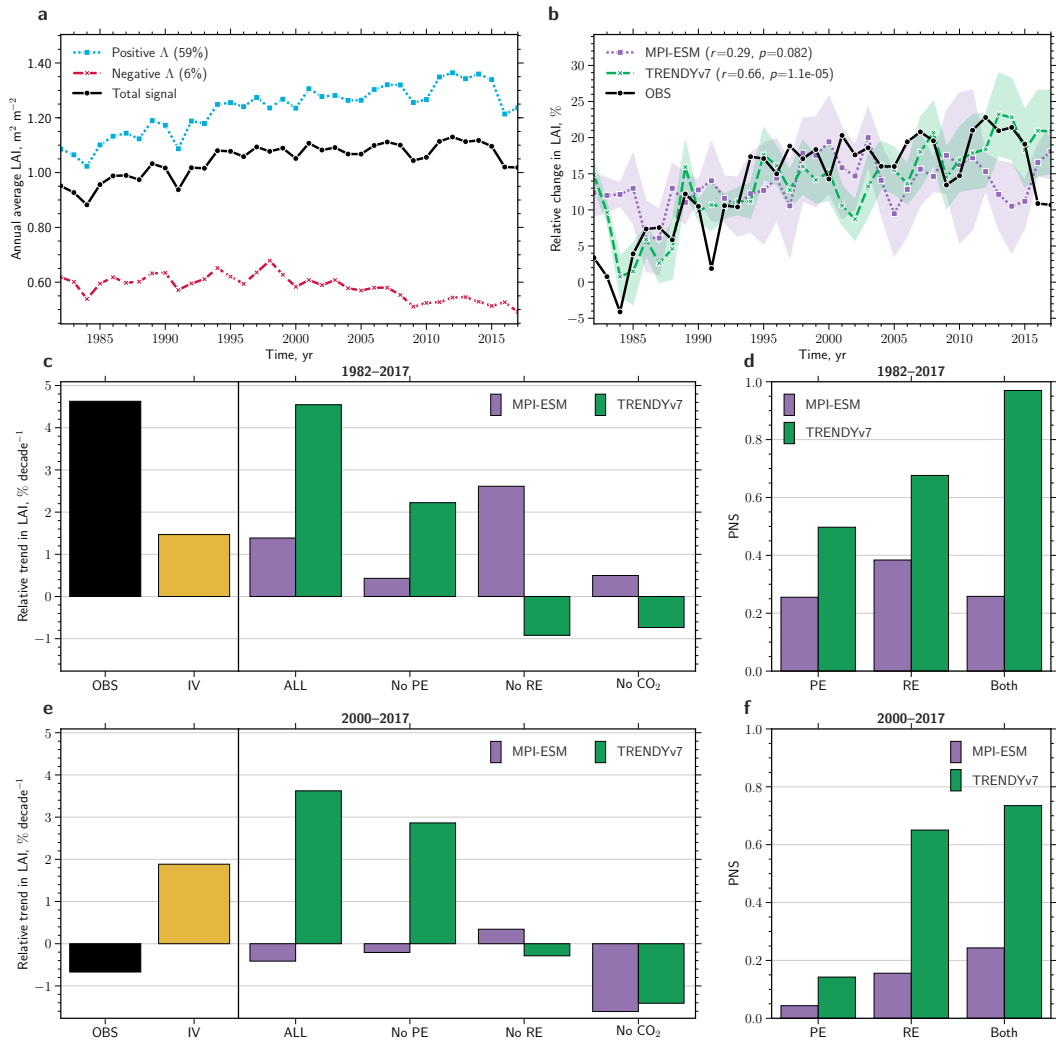


Figure A10 | Northern African Savannas Grasslands – caption analogous to Figure A3.

THE EFFECTS OF RISING CO₂ ON GLOBAL NATURAL VEGETATION

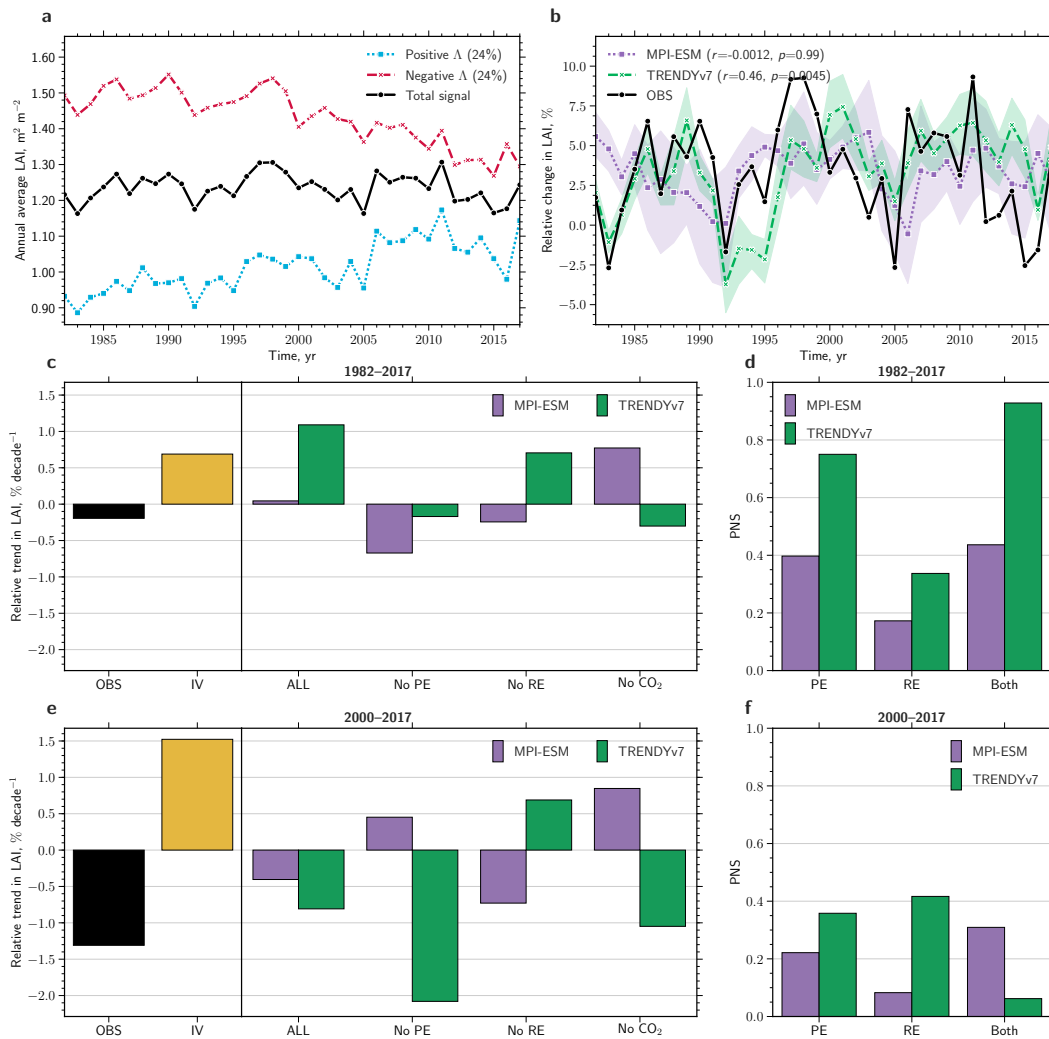


Figure A11 | Southern African Savannas Grasslands – caption analogous to Figure A3.

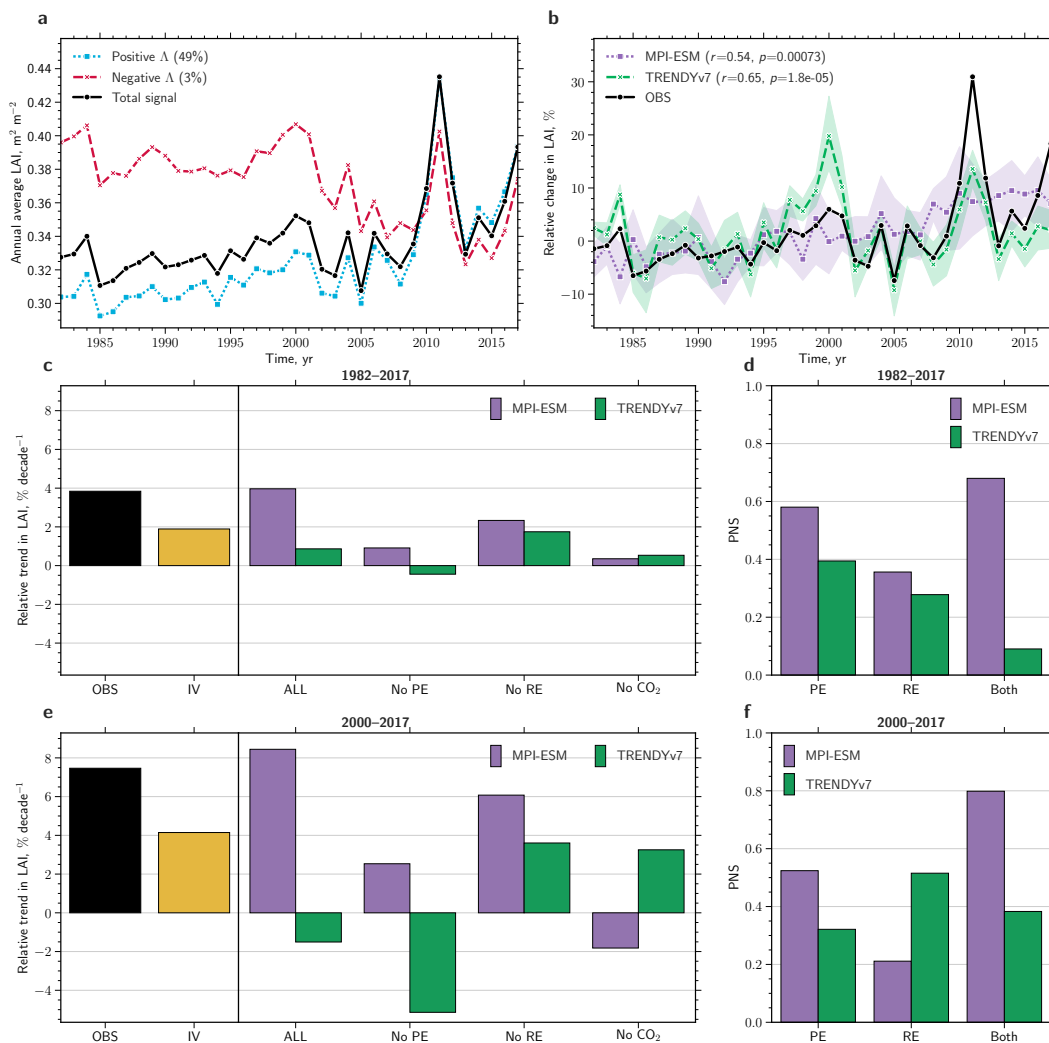


Figure A12 | Australian Shrublands – caption analogous to Figure A3.

THE EFFECTS OF RISING CO₂ ON GLOBAL NATURAL VEGETATION

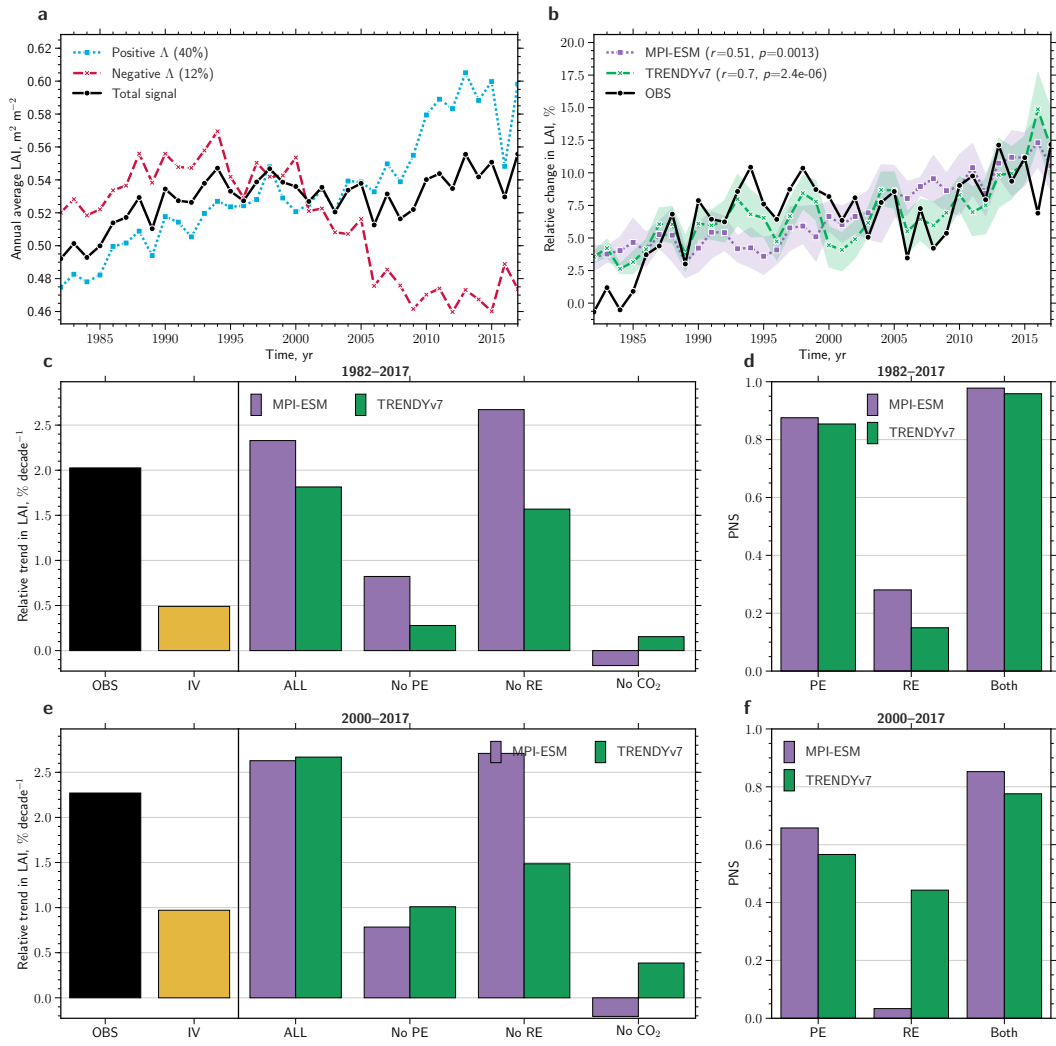


Figure A13 | Cool Grasslands – caption analogous to Figure A3.

Table A2 | Greening, browning and non-changing fractions of vegetated area for different biomes and prominent clusters of change for the time period 2000–2017. Significant changes are determined by the means of the Mann-Kendall significance test ($p < 0.1$). The abbreviations used to describe the different clusters are explained in Data and Methods.

Area	Vegetated Area	Positive Λ Fraction	Negative Λ Fraction	No-Change Fraction
<i>Unit</i>	10^6 km^2	-	-	-
All Vegetation	109.42	0.21	0.13	0.66
Anthro. Vegetation	15.37	0.33	0.09	0.58
Natural Vegetation	94.05	0.19	0.14	0.68
Biomes				
Grasslands	26.77	0.22	0.12	0.66
Tropical F.	20.32	0.11	0.19	0.7
Boreal F.	13.69	0.19	0.18	0.63
Temperate F.	11.2	0.26	0.07	0.67
Shrublands	10.37	0.21	0.09	0.69
Tundra	7.03	0.14	0.14	0.72
Savannas	4.22	0.17	0.11	0.72
Clusters				
Cool Gl	12.32	0.26	0.12	0.62
EA Brl F	8.0	0.23	0.14	0.63
NAm Brl F	5.69	0.14	0.23	0.63
NAf Sv Gl	5.6	0.18	0.1	0.72
CAf Trp F	5.35	0.09	0.23	0.69
SAf Sv Gl	4.6	0.07	0.19	0.74
Aus Sl	4.43	0.29	0.02	0.69
EA Tundra	3.57	0.13	0.2	0.67
NAm Tundra	3.46	0.15	0.08	0.77

Table A3 | Leaf area gain, loss, and net change for different biomes and prominent clusters of change for the time period 2000–2017. Significant changes are determined by the means of the Mann-Kendall significance test ($p < 0.1$). The abbreviations used to describe the different clusters are explained in Data and Methods.

Leaf Area	Leaf Area Gain	Leaf Area Loss	Net Leaf Area Change
<i>Unit</i>	$10^3 \text{ km}^2 \text{ yr}^{-1}$	$10^3 \text{ km}^2 \text{ yr}^{-1}$	$10^3 \text{ km}^2 \text{ yr}^{-1}$
All Vegetation	140.25	-79.68	60.57
Anthro.Vegetation	40.69	-5.9	34.78
Natural Vegetation	99.56	-73.78	25.79
Biomes			
Grasslands	25.12	-11.65	13.47
Tropical F.	18.85	-37.27	-18.42
Boreal F.	15.02	-11.13	3.88
Temperate F.	26.29	-5.43	20.86
Shrublands	5.77	-1.85	3.91
Tundra	2.39	-2.68	-0.28
Savannas	5.97	-3.57	2.41
Clusters			
Cool Gl	10.23	-3.0	7.24
EA Brl F	11.82	-4.24	7.58
NAm Brl F	3.2	-6.9	-3.69
NAf Sv Gl	6.26	-1.25	5.01
CAf Trp F	3.5	-13.16	-9.66
SAf Sv Gl	1.52	-5.19	-3.67
Aus Sl	3.15	-0.12	3.02
EA Tundra	0.97	-2.23	-1.26
NAm Tundra	1.43	-0.45	0.97

Part II

EARTH SYSTEM MODELS UNDERESTIMATE CARBON FIXATION BY PLANTS IN THE HIGH LATITUDES

The attached article has been published as:

Winkler, A. J., R. B. Myneni, G. A. Alexandrov, and V. Brovkin (2019a). "Earth System Models Underestimate Carbon Fixation by Plants in the High Latitudes." *Nature Communications* 10.1, p. 885. DOI: [10.1038/s41467-019-08633-z](https://doi.org/10.1038/s41467-019-08633-z)

The comprehensive peer review process was partly published in a separate document (not included here) and can be obtained via <https://www.nature.com/articles/s41467-019-08633-z>

EARTH SYSTEM MODELS UNDERESTIMATE CARBON FIXATION BY PLANTS IN THE HIGH LATITUDES

ALEXANDER J. WINKLER^{1,2}, RANGA B. MYNENI^{1,3},
GEORGII A. ALEXANDROV⁴, AND VICTOR BROVKIN¹

CONTENTS

1	Introduction	3
2	Results	5
3	Discussion	9
4	Methods	10
	References	17
A	Supplementary Information	21

¹ Max-Planck-Institute for Meteorology, Bundesstrasse 53, 20146 Hamburg, Germany

² International Max-Planck Research School for Earth System Modeling, Bundesstrasse 53, 20146 Hamburg, Germany

³ Department of Earth and Environment, Boston University, Boston MA 02215, USA

⁴ A.M. Obukhov Institute of Atmospheric Physics, Pyzhyovskiy pereulok 3, Moscow, Russia

Abstract

Most Earth system models agree that land will continue to store carbon due to the physiological effects of rising CO₂ concentration and climatic changes favoring plant growth in temperature-limited regions. But they largely disagree on the amount of carbon uptake. The historical CO₂ increase has resulted in enhanced photosynthetic carbon fixation (Gross Primary Production, GPP), as can be evidenced from atmospheric CO₂ concentration and satellite Leaf Area Index (LAI) measurements. Here, we use leaf area sensitivity to ambient CO₂ from the past 36 years of satellite measurements to obtain an Emergent Constraint (EC) estimate of GPP enhancement in the northern high latitudes at two-times the pre-industrial CO₂ concentration (3.4 ± 0.2 Pg C yr⁻¹). To imbue confidence, we derive three independent comparable estimates from CO₂ measurements and atmospheric inversions. Our EC estimate is 60% larger than the conventionally used multi-model average (44% higher at the global scale). This suggests that most models largely underestimate photosynthetic carbon fixation and therefore likely overestimate future atmospheric CO₂ abundance and ensuing climate change, though not proportionately.

Author Contributions A.J.W. performed the research. All authors contributed ideas and to the interpretation of the results. R.B.M. and A.J.W. drafted the manuscript with inputs from G.A.A. and V.B.

1 INTRODUCTION

Predicting climate change requires knowing how much of the emitted CO₂ (currently ~40 Pg CO₂ yr⁻¹) will remain in the atmosphere (~46%) and how much will be stored in the oceans (~24%) and lands (~30%; Quéré et al., 2018). Earth system models (ESM) show a large spread in projected increase of terrestrial photosynthetic carbon fixation (GPP; Ciais et al., 2013; Zhao and Zeng, 2014; Friedlingstein et al., 2013; Anav et al., 2013; Arora et al., 2013) and are thought to overestimate current estimates (Anav et al., 2013; Kolby Smith et al., 2016), although the latter is also subject of debate (Anav et al., 2013; De Kauwe et al., 2016; Campbell et al., 2017; Welp et al., 2011; Koffi et al., 2012). Historical increase of atmospheric CO₂ concentration, from 280 to current 400 ppm, has resulted in enhanced GPP due to its radiative (Nemani et al., 2003) and physiological effects (Leakey et al., 2009; Thomas et al., 2016), which is indirectly evident in amplified seasonal swings of atmospheric CO₂ concentration (Forkel et al., 2016; Keeling et al., 1996; Graven et al., 2013) and large scale increase in summer time green leaf area (Myneni et al., 1997; Zhu et al., 2016; Mao et al., 2016). Thus, these observables, expressed as sensitivities to ambient CO₂ concentration, might serve as predictors of changes in GPP (Cox et al., 2013; Wenzel et al., 2014; Wenzel et al., 2016; Mystakidis et al., 2016) and help to reduce uncertainty in multi-model projections of terrestrial carbon cycle entities.

This study is focused on the northern high latitudes (NHL, north of 60° N) where significant and linked changes in climate (Screen and Simmonds, 2010) and vegetation (Forkel et al., 2016) have been observed in the past three to four decades: 52% of the vegetated lands show statistically significant greening trends over the 36-year record of satellite observations (1981 to 2016, Methods; Zhu et al., 2013), while only 12% show browning trends, mostly in the North American boreal forests due to disturbances (Figure 1; Goetz et al., 2005). We therefore hypothesize that the greening sensitivity (i.e. LAI changes in response to changes in the driver variables) inferred from the historical period of CO₂ increase can be used to obtain a constrained estimate (Wenzel et al., 2016) of future GPP enhancement from both the radiative and physiological effects (Figure A1).

State-of-the-art fully coupled carbon-climate ESMs vary in their representation of many key processes, e.g. vegetation dynamics, carbon-nitrogen interactions, physiological effects of CO₂ increase, climate sensitivity, etc. This results in divergent trajectories of evolution of the 21st century carbon cycle (Friedlingstein et al., 2013; Anav et al., 2013; Arora et al., 2013). To capture this variation, we use two sets of simulations (Taylor et al., 2012) available from seven ESMs (Wenzel et al., 2016) from the Coupled Model Intercomparison Project Phase 5 (CMIP5) - one with historical forcings including anthropogenic CO₂ emissions for the period 1850–2005 and the second with idealized forcing (1% CO₂ increase per year, compounded annually, starting from a preindustrial value of 284 ppm until quadrupling). In our analyses, the magnitude of the physiological effect is represented by the CO₂ concentration and the radiative effect by growing degree days (GDD₀, > 0° C, Methods) as plant growth in NHL is principally limited by the growing season temperature (Nemani et al., 2003). Leaf area changes can be represented either by changes in annual maximum LAI (LAI_{max} Cook and Pau, 2013) or growing season average LAI – we use the former because of its ease and unambiguity, as the latter requires quantifying the start- and

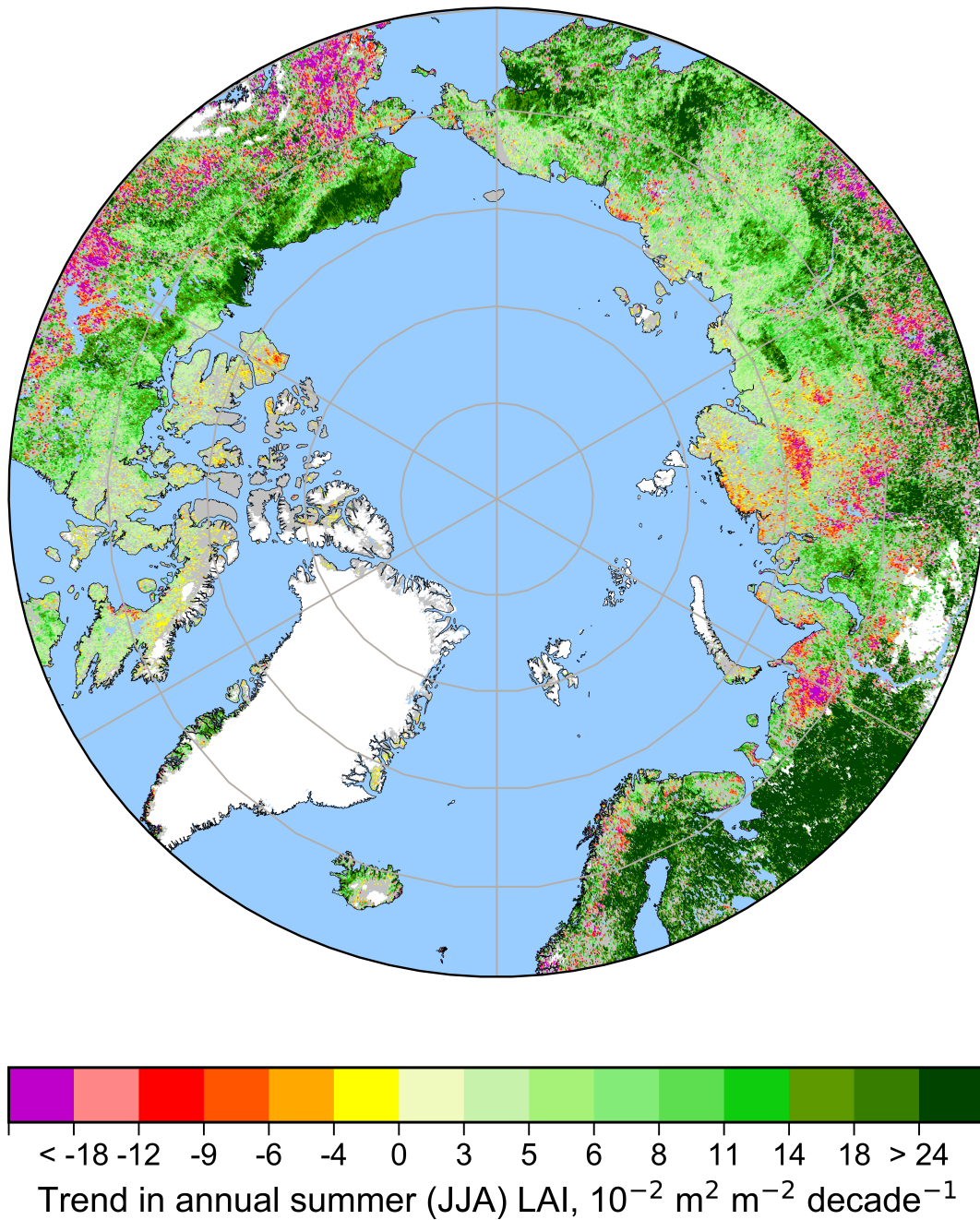


Figure 1 | **Greening (LAI increase) and browning trends during 1981 to 2016 in the northern high latitudes.** Statistically significant (Mann-Kendall test, $p < 0.1$) trends in summer (June to August) average LAI are color coded. Non-significant changes are shown in grey. White areas depict ice sheets or barren land. Details of the LAI data set are provided in Methods. The figure was created using the cartographic python library Cartopy (Release: 0.16.0).

end-dates of the growing season, something that is difficult to do accurately in NHL (Park et al., 2016) with the low-resolution model data.

Here, we apply the concept of Emergent Constraints to reduce uncertainty in multi-model projections of GPP using historical simulations and satellite observations of LAI focusing on NHL. We find that the EC estimate is 60% larger than the commonly accepted multi-model mean value, in line with a recent study that assessed the impact of physiological effects of higher CO₂ concentration on GPP of northern hemispheric extra-tropical vegetation (Wenzel et al., 2016). Detailed independent analyses of *in-situ* CO₂ measurements and atmospheric inversions imbue confidence in our conclusions. Our central finding is, the effect of ambient CO₂ concentration on terrestrial photosynthesis is larger than previously thought, and thus, has important implications for future carbon cycle and climate.

2 RESULTS

Large inter-model spread in greening sensitivity. The enhancement in NHL greenness throughout the observational period relates linearly to both increasing quantities, GDDo and CO₂ concentration, in general agreement between models and observations (Forkel et al., 2016; Zhu et al., 2016; Mahowald et al., 2016). To avoid redundancy from co-linearity between the two driver variables, but retain their underlying time-trend and interannual variability (Table A1), we use the dominant mode from a principal component analysis of CO₂ and GDDo as the proxy driver (denoted ω) in subsequent analysis (Methods). Expressed in this compact form, greenness level (Figure 2a) as well as greening sensitivity to (hereafter greening sensitivity, Figure 2b) span a wide range across the multi-model ensemble. All models with low greenness levels ($\text{LAI}_{\text{max}} < 0.75 \text{ m}^2 \text{ m}^{-2}$) tend to simulate low greening sensitivities ($< 0.015 \text{ m}^2 \text{ m}^{-2} \text{ LAI}_{\text{max}}$ per 1 unit ω), relative to observations. These models (NorESM1-ME, CESM1-BGC, and CanESM2) lack a representation of dynamic vegetation, i.e. do not allow plant functional type shifts in response to changing simulated climate, and/or show overly strong nitrogen limitations on plant growth and thus fail to capture GPP enhancement and its re-investment in green leaf area (Table A2). The other four models behave randomly – some reproduce observed greenness levels ($\text{LAI}_{\text{max}} \sim 1.7 \text{ m}^2 \text{ m}^{-2}$) but not the greening sensitivities ($\sim 0.045 \text{ m}^2 \text{ m}^{-2} \text{ LAI}_{\text{max}}$ per 1 unit ω) and the others vice versa. Whether this is because these four models in common lack carbon-nitrogen interactions, or are missing some other key processes, is not known (Mahowald et al., 2016), but the end result is a large range in model simulated greening sensitivity (hereafter LAI_{max} sensitivity), during the historical period ($0.022 - 0.075 \text{ m}^2 \text{ m}^{-2} \text{ LAI}_{\text{max}}$ per 1 unit ω).

Emergent Constraint on projected increase of GPP. What is known, however, is the strong linear relationship between modelled contemporaneous changes in LAI_{max} and GPP arising from the combined radiative and physiological effects of CO₂ enrichment in the range $1 \times \text{CO}_2$ to $2 \times \text{CO}_2$ (Figures A2 and A3). As a result, models with low LAI_{max} sensitivity (Figure 2b) project lower ΔGPP for a given increment of CO₂ concentration, and vice versa. Thus, the large variation in modelled historical LAI_{max} sensitivities (Figure 2b) linearly maps to variation in ΔGPP at $2 \times \text{CO}_2$ (Figure 2c; $r = 0.98$, $P = 0.0001$), with the consequence that the uncertainty of the multi-model mean ΔGPP is large enough to undermine its value

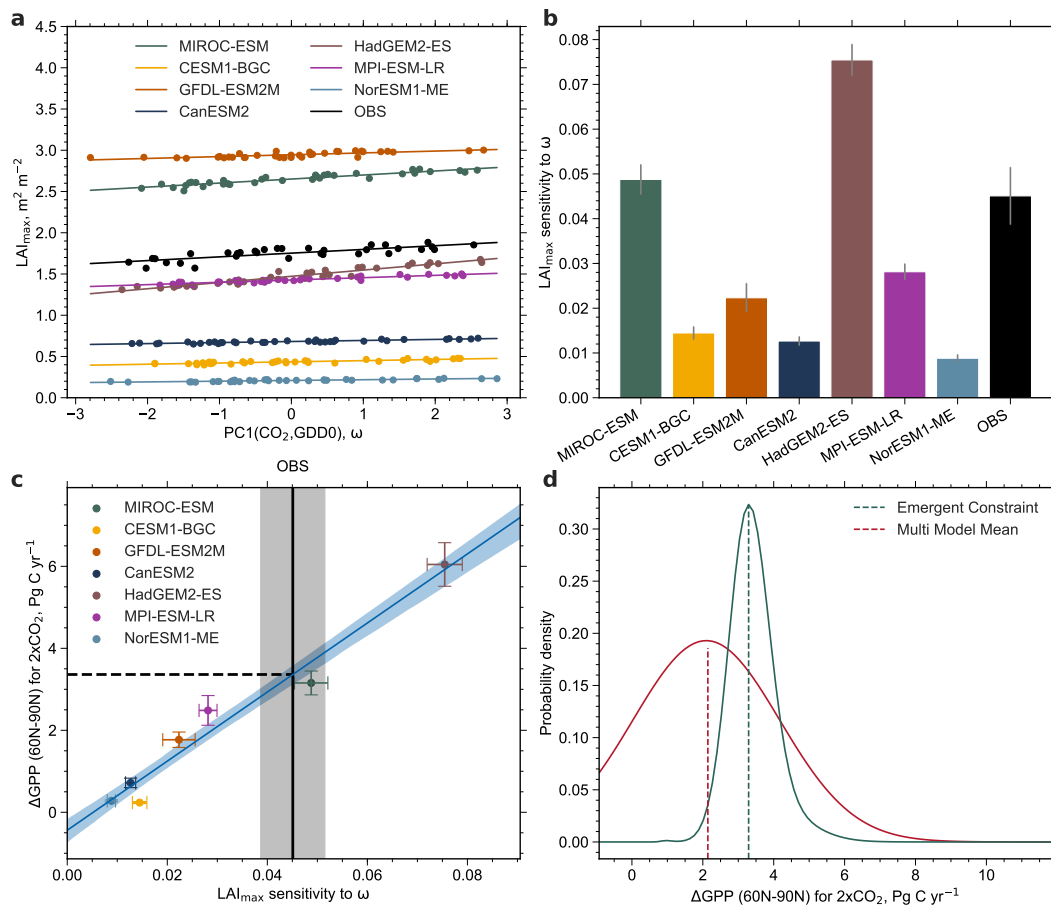


Figure 2 | **CMIP5 ensemble mean considerably underestimates absolute increase of GPP for a doubling of pre-industrial atmospheric CO₂ concentration (2×CO₂).** **a**, Observations (black) and CMIP5 historical simulations (colors) of the first principal component of annual mean atmospheric CO₂ and annual growing degree days above 0 °C (ω) versus the annual LAI_{max}. All quantities are area weighted and spatially averaged for NHL (60°N - 90°N). **b**, Bar chart showing the corresponding slopes of the best linear fits, where the grey bar at the top indicates the standard error. Linear trends are derived for the period 1982-2016 for observations and 1971-2005 for model simulations, maximizing the overlap and sample size. **c**, Linear relationship between the sensitivity of annual LAI_{max} to ω (x axis) and the absolute increase of high-latitude GPP at 2×CO₂. Each model is represented by an individually colored marker with error bars indicating one standard deviation (y axis) and standard error (x axis). The black solid line shows observed sensitivity, where the grey shading indicates the respective standard error. The blue line shows the best linear fit across the CMIP5 ensemble including the 68% confidence interval estimated by bootstrapping (blue shading; Methods). The intersection of the blue and black line gives the Emergent Constraint on Δ GPP at 2×CO₂ (dashed black line). **d**, Probability density functions resulting from Emergent Constraint (blue) and CMIP5 ensemble mean estimates (red, assuming Gaussian distribution). Details in Methods.

– e.g. $2.1 \pm 1.91 \text{ Pg C yr}^{-1}$ for $2\times\text{CO}_2$ in NHL. This linear relation in inter-model variation between ΔGPP at $2\times\text{CO}_2$ and historical LAI_{max} sensitivities allows using the observed sensitivity as an Emergent Constraint (EC) on GPP estimation at $2\times\text{CO}_2$. Moreover, the probability contours about the best linear fit together with the uncertainty of observed sensitivity (blue and grey shadings in Figure 2c) allow a robust characterization of the constrained estimate (Wenzel et al., 2016), namely $3.4 \pm 0.2 \text{ Pg C yr}^{-1}$ for $2\times\text{CO}_2$ in NHL (Figure 2d). This EC estimate is 60% larger than the multi-model mean value. Wenzel et al. (2016) reported a similar result for NHL ($37\% \pm 9\%$ vs. $20\% - 25\%$ for relative GPP increase at $2\times\text{CO}_2$) and a somewhat smaller number for the extra-tropical vegetation in the northern hemisphere, both for the physiological effect only (Figure A4 shows that the radiative and physiological effects each contribute about half of the total GPP enhancement). Together, these results indicate that most models are largely underestimating photosynthetic carbon fixation, which is in contrast to previous studies (Anav et al., 2013; Kolby Smith et al., 2016) that suggested an over-sensitivity of ESMs to atmospheric CO_2 . Below, we provide three independent lines of evidence, i.e. not using LAI_{max} but atmospheric CO_2 measurements, to buttress our EC estimate.

Independent lines of evidence. First, the seasonal cycle of CO_2 concentration in the NHL, which shows a winter maximum due to respiratory processes and a late-summer minimum due to photosynthetic drawdown, may be considered as a proxy for NHL carbon exchange with the atmosphere (Forkel et al., 2016; Keeling et al., 1996; Graven et al., 2013). Analyses of long-term measurements at NHL stations, Point Barrow (BRW, Alaska) and Alert Nunavut (ALT, Canada), reveal that this seasonal cycle has changed over time, dominated by a decreasing trend in the annual CO_2 minimum (Figure 3a, b). Nearly all of this change can be attributed to the land, as the trend in the abutting Arctic ocean flux is ~ 15 times smaller (Figure 3d; Methods). This strengthening of the seasonal swings of CO_2 concentration relates to photosynthesis rather than respiration changes (Forkel et al., 2016; Keeling et al., 1996; Graven et al., 2013) and thus features changes in GPP. So, if the EC estimate is closer to the true value of ΔGPP at $2\times\text{CO}_2$, then, models matching the EC estimate (e.g. MIROC-ESM) must also better simulate the changing CO_2 seasonal cycle measured at the NHL stations, in comparison to models that over- (e.g. HadGEM2-ES) or underestimate (e.g. CESM1-BGC). Indeed, the MIROC-ESM best reproduces the average observed seasonal cycle, and critically, the change in summertime minimum over time at both stations, in comparison to the other models (Figure 3a, b). None of the models reproduce the observed phase of the seasonal cycle, which suggests a recurring problem among models in their representation of vegetation phenology (Anav et al., 2013). Nevertheless, the model that projects ΔGPP matching the LAI_{max} based EC estimate is also the one that best captures the changes in observed seasonal cycle suggesting that the EC estimate, rather than the corresponding multi-model mean, best represents the true value of ΔGPP at $2\times\text{CO}_2$. Thus, the multi-model mean is a large underestimate.

Second, measured changes in the amplitude of CO_2 seasonal cycle can be regarded as a metric of changes in NHL GPP (Forkel et al., 2016; Keeling et al., 1996; Graven et al., 2013; Wenzel et al., 2016). This is not necessarily the case in ESMs, because uncertainty in wintertime carbon release processes influences considerably the annual CO_2 maximum and hence the amplitude – variations unrelated to photosynthetic activity (Graven et al., 2013). To better isolate the effect of photosynthetic carbon fixation in the seasonal CO_2 signal, we use the slope of summertime drawdown instead of its amplitude. With the observed

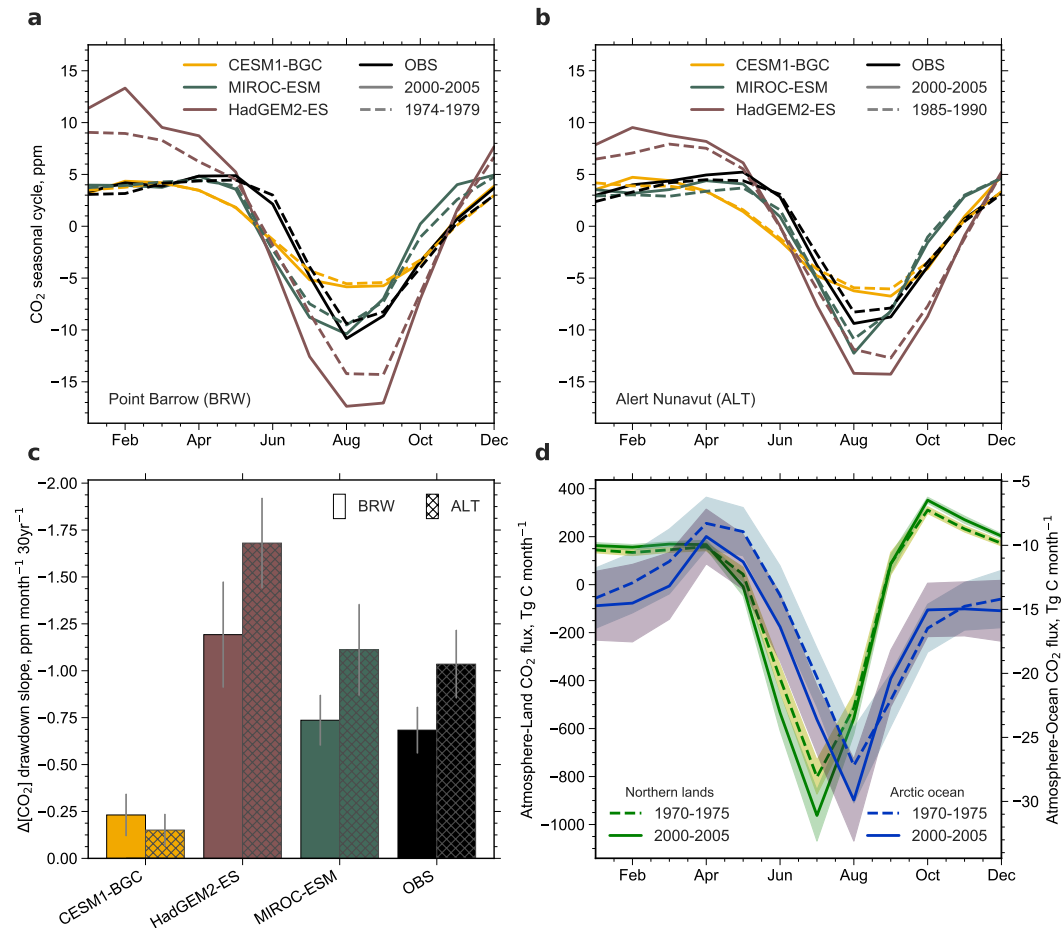


Figure 3 | Lines of evidence in support of the Emergent Constraint estimate of NHL GPP. **a**, Detrended seasonal cycle of Point Barrow (71.3° N, 203.4° E) CO₂ concentration at two time periods, 1974–79 (dashed) and 2000–2005 (solid), from observations (black) and selected CMIP5 models (colored) spanning the full range of LAI_{max} sensitivity (low-end: CESM1-BGC, closest-to-observations: MIROC-ESM, and high-end: HadGEM2-ES). **b**, As in **a**, but showing the detrended seasonal cycle of Alert Nunavut (82.5° N, 297.7° E) CO₂ concentration at the two time periods, 1985–90 (dashed) and 2000–2005 (solid). **c**, Changes in the slope of summertime drawdown of CO₂ concentration over a 30-year period in representative models and observations at both stations (Methods). Grey bars denote one standard deviation. **d**, Seasonal cycle of CO₂ fluxes into NHL land (green, 60° N - 90° N, historical simulation, average of 3 realizations, MPI-ESM-LR) and Arctic Ocean (blue, 65° N, historical simulation, average of 10 realizations, MPI-ESM-HR), for two time periods, 1970–75 (dashed) and 2000–2005 (solid). Shading indicates one standard deviation.

lengthening of the growing season (Park et al., 2016) and general enhancement of GPP, the CO₂ concentration is increasingly tugged downward relative to the steady increasing trend. At both stations, the drawdown slope decreased over a period of 30 years (ALT: -1.04 ± 0.18 ppm month⁻¹ 30yr⁻¹ and BRW: $(-0.68 \pm 0.12$ ppm month⁻¹ 30yr⁻¹; Figure 3c; Methods). The models also show a decreasing slope but disagree on the magnitude (Figure 3c). Again, we note that the MIROC-ESM best reproduces the observed change in drawdown slope at both stations. Likewise, HadGEM2-ES considerably overestimates and CESM1-BGC underestimates the decline of the drawdown slope. According to the hypothesized EC approach (Figure A1), this is rooted in MIROC-ESM correctly capturing the sensitivity of an observable (LAI_{max} in Figure 2b or BRW and ALT drawdown slope in Figure 3c) to CO₂ concentration. Consequently, this agreement in changes in CO₂ drawdown slope between long-term measurements and the closest-to-observations model in terms of greening sensitivity provides further support for the EC estimate of Δ GPP at $2 \times$ CO₂ and suggests that the multi-model mean is a large underestimate.

Third, the available longest records of carbon exchange between the land/ocean and atmosphere (1980-2015) indicate that NHL lands changed from being a small carbon source in the early 1980s to a strong sink in the mid-2010s (Figure A5) meaning that the net biome production (NBP) increased – Jena CarboScope (JENA; Rödenbeck et al., 2003) Δ NBP: 0.31 ± 0.09 Pg C yr⁻¹ and the Copernicus Atmosphere Monitoring Service (CAMS; Chevallier et al., 2010) Δ NBP: 0.78 ± 0.04 Pg C yr⁻¹. NBP fluxes include emissions from disturbances, such as fire, and heterotrophic respiration, which may have increased due to warming over the period of record. Accordingly, the derived changes in NBP from the CO₂ inversion products can be considered as conservative estimates of NPP enhancement. The EC estimate using greening observations translates to a land net primary production (NPP) enhancement of about 0.32 ± 0.02 Pg C yr⁻¹, when adjusted for CO₂ concentration increase over the period of the atmospheric CO₂ inversion datasets (Methods). This estimate better agrees with the JENA estimate than the multi-model mean (0.19 ± 0.18 Pg C yr⁻¹). All three, however, do not overlap with the CAMS estimate. Hence, the available evidence from inversion studies of atmospheric CO₂ measurements indicates NPP changes in NHL comparable to or larger than our EC estimate, and therefore the multi-model mean to be an underestimate.

3 DISCUSSION

The causes for model underestimation can perhaps be traced to representation of carbon-nitrogen interactions and vegetation dynamics. Models that strongly underestimate (CESM1-BGC, NorESM-ME, and CanESM2) show excessive nitrogen limitation (in CanESM2, the CO₂ fertilization effect is down-regulated based on ambient and elevated CO₂ experiments; Arora et al., 2013). These models also lack simulation of vegetation cover dynamics, and thus, do not reproduce the observed northward shift of vascular plants and the associated higher productivity of shrubs and trees (Arora et al., 2013). On the other hand, models that overestimate (HadGEM2-ES) show overly strong CO₂ fertilization effect and consequently excessive greening, presumably due to a lack of nitrogen limitation (Wenzel et al., 2016; Anav et al., 2015). The model MIROC-ESM, which is closest to the EC estimate, stands out in its implementation of photosynthetic response to CO₂. Unlike the

biogeochemical approach in other models, MIROC-ESM uses an empirical approach that implicitly includes nutrient limitation (Arora et al., 2013; Ito and Oikawa, 2002).

Although the Arctic represents only a small fraction of the terrestrial biosphere, the rapid climatic changes in NHL and uncertainties associated with the net carbon balance emphasize the need for further detailed analysis. The tendency for GPP underestimation in NHL by models reported here is also seen at the global scale (Figure A6). This, together with another recent study (Wenzel et al., 2016), suggests that most models are underestimating photosynthetic carbon fixation by plants and thus possibly overestimating atmospheric CO₂ and ensuing climatic changes (Ciais et al., 2013; Friedlingstein et al., 2013; Arora et al., 2013).

4 METHODS

Observational LAI product (LAI3gV1). The new version (V1) of the leaf area index data set is an update of the widely used LAI3g data set (Zhu et al., 2013). It was generated using an artificial neural network (ANN) and the latest version (third generation) of the Global Inventory Modeling and Mapping Studies group (GIMMS) Advanced Very High Resolution Radiometer (AVHRR) normalized difference vegetation index (NDVI) data (NDVI3g). The latter have been corrected for sensor degradation, intersensor differences, cloud cover, solar zenith angle, viewing angle effects due to satellite drift, Rayleigh scattering and stratospheric volcanic aerosols (Pinzon and Tucker, 2014). The ANN model was trained with overlapping data of NDVI3g and Collection 6 Terra MODIS LAI product (Yan et al., 2016a; Yan et al., 2016b), and then applied to the full NDVI3g time series to generate the LAI3gV1 data set. This data set provides global and year-round LAI observations at 15-day (bi-monthly) temporal resolution and 1/12 degree spatial resolution from July 1981 to December 2016. Currently, it is the only data set that spans this long period.

The quality of the previous version (Vo) of the GIMMS LAI3g data set was evaluated through direct comparisons with ground based measurements of LAI, indirectly with other estimates from similar satellite-data products, and also through statistical analysis with climatic variables, such as temperature and precipitation variability (Zhu et al., 2013). The LAI3gVo data set (and related fraction vegetation-absorbed photosynthetically active radiation data set) has been widely used in various studies (Anav et al., 2013; Forkel et al., 2016; Zhu et al., 2016; Mao et al., 2016; Mahowald et al., 2016; Piao et al., 2014; Poulter et al., 2014; Keenan et al., 2016). The new version LAI3gV1 used in our study is an update of that earlier version.

For both, observational and CMIP5 data, LAI is defined as the one-sided green leaf area per unit ground area in broadleaf canopies and as one-half the green needle surface area in needleleaf canopies. It is expressed in units of m² green leaf area per m² ground area. In this study, we use the annual maximum value of LAI, LAI_{max}, to quantify the greenness level of a surface. LAI_{max} is less influenced by cloudiness and noise; accordingly, it is most useful in investigations of long-term greening and browning trends. The drawback of LAI_{max} is the saturation effect at high LAI values (Myneni et al., 2002). However, this is less of a problem in high latitudinal ecosystems which are mostly sparsely vegetated, with LAI_{max} values typically in the range of 2 to 3.

The bi-monthly GIMMS LAI_{3gV1} data are merged to a monthly temporal resolution by averaging the two composites in the same month. Then, for model and observational data alike, the two-dimensional global fields are cropped to the northern high latitudinal band defined as 60° N to 90° N, averaged in space and temporally reduced to the annual maximum value.

Although the AVHRR data underlying the LAI data in this study have corrections for various deleterious effects (Pinzon and Tucker, 2014), the data may still contain residual non-vegetation related effects. Therefore, we sought confirmation of the greening trend (Zhu et al., 2016), on which the current study relies, from a more reliable but shorter record from the MODIS sensors (Yan et al., 2016a; Yan et al., 2016b). These data are well calibrated, cloud-screened and corrected for atmospheric effects, especially tropospheric aerosols. The sensor-platforms are regularly adjusted to maintain precise orbits. All algorithms, including the LAI algorithm, are physics-based, well-tested and currently producing the sixth generation data sets. The results, not shown here for brevity, illustrate global scale greening, across all latitudinal zones and broad vegetation classes. Zhang et al. (2017) also reported matching greening trends between the latest (Version 6) MODIS and AVHRR (Version 3) vegetation index data sets.

We also found that the LAI_{max} sensitivity derived with MODIS LAI data matched well with that obtained from the AVHRR LAI data (results not shown for brevity). Whether this indicates that the 17-year MODIS record from the period 2000 to 2016 captures information similar to the longer AVHRR record (1981 to 2016), or is simply a fortuitous occurrence, is not known, and deserves further study. In the present context, however, this adds confidence to the AVHRR LAI data used in our study.

Temperature data from ECMWF ERA-Interim. Estimates of surface air temperature at 2 m height are from the widely used global atmospheric reanalysis product ERA-Interim by ECMWF (Dee et al., 2011, for details see: <https://www.ecmwf.int/en/research/climate-reanalysis/era-interim>). The global temperature fields were retrieved at a resolution of 0.5° × 0.5° for monthly mean estimates derived from daily means. Other reanalysis products with similar specifications (NCEP/NCAR reanalysis, University of Delaware Air Temperature & Precipitation, and GHCN/CAMS reanalysis product) were also investigated. The differences among the various products were found to be minor.

CMIP5 models used in this study. In this study, we analyze a set of the most recent climate-carbon simulations of seven ESMs participating in the fifth phase of the Coupled Model Intercomparison Project, CMIP5 (Taylor et al., 2012). The model data were obtained from the Earth System Grid Federation, ESGF (<https://esgf-data.dkrz.de/projects/esgf-dkrz/>). Seven ESMs provided output for the variables of interest for simulations esmHistorical, 1pctCO₂, esmFixClim, and esmFdbk.

The esmHistorical simulation spans the period 1850 to 2005 and was driven by observed conditions such as solar forcing, emissions or concentrations of short-lived species and natural and anthropogenic aerosols or their precursors, land use, anthropogenic as well as volcanic influences on atmospheric composition. The models are forced by prescribed anthropogenic CO₂ emissions, rather than atmospheric CO₂ concentrations.

1pctCO₂ is an idealized fully coupled carbon/climate simulation initialized from steady state of the preindustrial control run and atmospheric CO₂ concentration prescribed to

increase $1\% \text{ yr}^{-1}$ until quadrupling of the preindustrial level. The simulations `esmFixClim` and `esmFdbk` and are set up as the `1pctCO2` with the difference, that in `esmFixClim` (`esmFdbk`) only the radiative effect from increasing CO_2 concentration is included, while the carbon cycle sees the preindustrial CO_2 level (*vice versa*; Taylor et al., 2012; Taylor et al., 2009).

Historical simulation with MPI-ESM higher-resolution setup. MPI-ESM-HR is the coupled high-resolution setup of the latest version of the Max-Planck-Institute Earth System Model MPI-ESM1.2, which is the baseline for the upcoming Coupled Model Intercomparison Project Phase 6 (CMIP6). Here, the atmospheric component ECHAM6.3 has 95 vertical levels and twice the horizontal resolution ($\sim 100\text{km}$) than the CMIP5 version. The ocean component MPIOM is set up on a tripolar grid at nominal 0.4° horizontal resolution (TPo4) and 40 vertical levels. MPI-ESM1.2 includes the latest versions of the land and ocean carbon cycle modules, comprising the ocean biogeochemistry model HAMOCC and the land surface scheme JSBACH. The forcing components for the historical simulation are chosen from CMIP5 (Methods) as at the time the simulations were conducted CMIP6 forcing was not available (Müller et al., 2018).

Atmospheric CO_2 concentration data. Monthly means of atmospheric CO_2 concentration at Point Barrow (71.3° N , 203.4° E) and Alert Nunavut (82.5° N , 297.7° E) are taken from the Global Monitoring Division measurement datasets (`co2_brw_surface-insitu_1_ccgg_MonthlyData` respectively `co2_alt_surface-flask_1_ccgg_month`) provided by the National Oceanic and Atmospheric Administration / Earth System Research Laboratory (NOAA / ESRL). Global monthly means of atmospheric CO_2 concentration are taken from the GLOBALVIEW- CO_2 product (for details see <http://dx.doi.org/10.15138/G3259Z>) also available at NOAA / ESRL.

Atmospheric CO_2 inversion products. Atmospheric CO_2 inversions estimate surface-atmosphere net carbon exchange fluxes by utilizing CO_2 concentration measurements, a transport model and prior information on anthropogenic carbon emissions as well as carbon exchange between atmosphere and land respectively ocean (Peylin et al., 2013). We choose two products, which cover the longest time period (1980-2015) and are regularly updated, the Jena CarboScope (JENA; Rödenbeck et al., 2003, version `s81_v3.8`, for details see http://www.bgc-jena.mpg.de/CarboScope/s/s81_v3.8.html), and the Copernicus Atmosphere Monitoring Service (CAMS; Chevallier et al., 2010, version `v15r2`, for details see <http://atmosphere.copernicus.eu/documentation-supplementary-products#greengas-fluxes>) inversion systems. Both products provide monthly mean net flux estimates on a spatial resolution of 3.75° latitude and 5° longitude (JENA) and 1.875° latitude and 3.75° longitude (CAMS).

Calculation of growing degree days above 0° C (GDDo). The global temperature fields from the reanalysis and model data are cropped to the northern high latitudinal band and averaged in space. The resulting one-dimensional time-series is converted to growing degree days above 0° C by multiplying the days of each month with the respective monthly mean estimate if it is above 0° C . Thus, we not only capture the warming signal, but also the prolongation of the growing season.

Dimension reduction using Principal Component Analysis. The drivers GDDo and atmospheric CO_2 concentration vary co-linearly due to the radiative effect of increasing

CO₂ concentration in the NHL. Thus, it is problematic to conduct an accurate factor separation in terms of their respective contribution to increase in LAI_{max}. However, the co-linearity suggests that a large amount of the signal is shared. Therefore, we conduct a principal component analysis (PCA) to apply dimension reduction (Hannachi et al., 2007).

The aim of the PCA is to find a linear combination of the driver variables that represents the one-dimensional projection with the largest possible variance. First, each driver time series x_i is normalized by centering on its mean (subtracting \bar{x}_i) and scaling to unit variance (divide by one standard deviation σ_i). Thus,

$$\mathbf{X} = x'_i = \frac{x_i - \bar{x}_i}{\sigma_i} \quad (1)$$

The matrix \mathbf{X} contains the scaled time series x'_i as columns. Next, we compute the covariance matrix $\mathbf{C}^{\mathbf{X}}$,

$$\mathbf{C}^{\mathbf{X}} = \frac{1}{n} \mathbf{X}^{\text{T}} \mathbf{X} \quad (2)$$

where n is the length of each time series. The eigenvector \mathbf{u}_k is obtained by solving the eigenvalue problem,

$$\mathbf{C}^{\mathbf{X}} \mathbf{u}_k = \lambda_k \mathbf{u}_k \quad (3)$$

The eigenvectors \mathbf{u}_k are sorted according to the ordering of their associated eigenvalues λ_k . Projecting the initial driver matrix \mathbf{X} onto the eigenvector \mathbf{u}_1 with the highest associated eigenvalue we arrive at the one-dimensional vector, the first principal component (PC),

$$\omega = (\mathbf{X} \mathbf{u}_1)^{\text{T}}. \quad (4)$$

Transposed to a row vector, ω denotes the time-series of the first PC, which explains the maximum variance of the two driver time series, atmospheric CO₂ concentration and GDDo.

Estimation of historical LAI_{max} sensitivity. We derive the historical LAI_{max} sensitivity applying a standard linear regression model (f_n)

$$f_n = a + bx_n \quad (5)$$

where x_n denotes the driver time series, a the intercept and b the gradient. We obtain the best-fit line by minimizing the squared error (s^2)

$$s^2 = \frac{1}{N-2} \sum_{n=1}^N (y_n - f_n)^2 \quad (6)$$

where y_n is the predictand time series and N is the number of data points of each time series. The resulting best-fit gradient b' represents the sought sensitivity. The standard error of b and a are given by

$$\sigma_b = \frac{s}{\sigma_x \sqrt{N}} \quad (7)$$

and

$$\sigma_a = s \sqrt{\frac{1}{N} + \frac{\bar{x}^2}{\sigma_x^2 N}} \quad (8)$$

respectively, for σ_x being the standard deviation and \bar{x} being the mean value of x_n .

Derivation of changes in NHL CO₂ drawdown slope. Graven et al. (2013) showed that NHL CO₂ drawdown mostly happens in June and July. ESMs, however, disagree on the phase, mainly due to a premature start of the growing season (Figure 3a, b). As a consequence, the CO₂ drawdown in models peaks earlier in the season. To obtain comparability for changes in CO₂ drawdown strength, we calculate the first derivative of the CO₂ concentration time series for the observational sites and each model individually. The annual minimum of the derivative in each time series reflects the months where the increase in photosynthetic CO₂ fixation is strongest (CO₂ drawdown slope). This procedure does not require a detrending of the atmospheric CO₂ signal.

For the BRW record, the 30 years of continuous overlap with the CMIP5 historical simulations were used to calculate the drawdown slopes (1974 - 2005). Due to the shorter overlap in the ALT record, 30 years of data from 1985 (start of measuring campaign) to 2015 were used for comparison with models. This is legitimate, because the CO₂ concentration rate of increment for both periods are just about the same. Model time series are obtained from the near-surface CO₂ concentration using the grid box in close proximity to each site. All yearly time series are slightly smoothed with a two-year moving window. Changes are calculated from five year averages at the beginning and end of the record. Here, we only present a low-end, high-end and the closest-to-observation model from the greening EC analysis, because Wenzel et al. (2016) already reported the behavior of the entire CMIP5 ensemble in terms of simulating the NHL CO₂ seasonal cycle.

Scaling of NPP estimates. We scale and convert the Emergent Constraint (EC) estimate for changes in the GPP flux $\Delta F_{GPP,EC}$ for a doubling of the preindustrial CO₂ level ($[\text{CO}_2]_{pi}$) to a NPP flux ($\Delta F_{NPP,EC}$) to obtain a comparable estimate to the atmospheric CO₂ inversion datasets using

$$\Delta F_{NPP,EC} = b \frac{\Delta [\text{CO}_2]_{1980-2015}}{[\text{CO}_2]_{pi}} \times \Delta F_{GPP,EC} \quad (9)$$

where $\Delta [\text{CO}_2]_{1980-2015}$ denotes the change in atmospheric CO₂ concentration over the observational period from 1980 to 2015 and b the standard GPP to NPP conversion factor of 0.5 (assuming uncertainty of 10%; Prentice et al., 2001; Zhang et al., 2009).

Comparison of atmospheric carbon fluxes between Arctic Ocean and NHL land. We require the use of a fully coupled Earth system model to separate between land and ocean in terms of the sign, magnitude and seasonal cycle of the respective net carbon exchange fluxes with the atmosphere. We have access to a spatially-high resolved historical run (10 realizations) of the MPI-ESM which has the ability to reproduce seasonality in the Arctic Ocean (Methods). The terrestrial carbon pools have not been brought into equilibrium due to computational limitations in these high resolution simulations. Thus, we use simulations from the same model but at low spatial resolution (3 realizations), the CMIP5 esmHistorical simulation, to address land carbon exchange fluxes (Methods).

The NHL land sink is approximately 2.5 times larger than the Arctic Ocean sink, on an annual basis. However, in terms of the change in carbon sink between the mid-1970s and early-2000s, the increase in CO₂ uptake by the land is about 15 times larger than the ocean. Accordingly, the Arctic Ocean can be ignored when trying to explain changes during the recent past, i.e. BRW period of CO₂ concentration measurements.

During the months from May to September (may-to-sep) when photosynthetic CO₂ drawdown is happening, the change in land sink is about 0.4 Pg C on an annual basis. Especially between May and July, the CO₂ concentration is rapidly declining, i.e. photosynthesis prevails CO₂ release processes. Thus, nearly the entire increase of 0.4 Pg C can be attributed to increasing NPP. The Emergent Constraint analysis shows that the MPI-ESM model is rather close to observations but generally underestimating greening sensitivity and thus also the GPP enhancement. These results are not provided as further proof of the EC estimate, although they are not contradictory, they are provided to compare the strength of NHL land and Arctic Ocean carbon sinks and why the ocean component can be neglected.

Bootstrapping for probability estimation. We apply bootstrapping to estimate the 68% confidence of the emergent linear relationship due to the small sample size of the CMIP5 ensemble. First, we randomly resample the data with replacement, where the size of the resample is equal to the size of the original sample N . Second, we compute the least-squares linear best fit for the resampled data. Third, we repeat this procedure times (minimum $m = 100$) until the difference between the median best fit line $m - 1$ of and m computed regressions approaches zero (the actual threshold was set to a difference less than 1%). We derive the 68% confidence contours of equal probability based on the set of m random regression lines.

Calculation of probability density functions . We derive a probability density function (PDF) for the observed sensitivity b' (associated standard error σ_b , Methods)

$$P(b) = \frac{1}{\sqrt{2\pi\sigma_b^2}} \exp \left\{ -\frac{(b - b')^2}{2\sigma_b^2} \right\} \quad (10)$$

assuming Gaussian distribution. The probability density function of for given

$$P(y|x) = \frac{1}{\sqrt{2\pi\sigma_f^2}} \exp \left\{ -\frac{(y - f(x))^2}{2\sigma_f^2} \right\}, \quad (11)$$

represent the contours of equal probability density around the best-fit linear regression, where denotes the 68% confidence contours estimated by bootstrapping (Methods). As shown in Cox et al. (2013), for a given observation-based PDF $P(b)$ and a model-based PDF $P(y|x)$, the PDF of the Emergent Constraint on y is

$$P(y) = \int_{-\infty}^{\infty} P\{x|y\}P(x)dx. \quad (12)$$

The PDF of the CMIP5 unweighted multi model mean is configured assuming Gaussian distribution.

Code availability The code used in this study is available from the corresponding author upon request.

Data availability All data used in this study are available from public databases or literature, which can be found with the references provided in respective Methods section. Processed data is available from the corresponding author upon request.

REFERENCES

- Anav, A. et al. (2013). "Evaluating the Land and Ocean Components of the Global Carbon Cycle in the CMIP5 Earth System Models." *Journal of Climate* 26.18, pp. 6801–6843. DOI: [10.1175/JCLI-D-12-00417.1](https://doi.org/10.1175/JCLI-D-12-00417.1).
- Anav, A. et al. (2015). "Spatiotemporal Patterns of Terrestrial Gross Primary Production: A Review." *Reviews of Geophysics* 53, pp. 785–818. DOI: [10.1002/2015RG000483](https://doi.org/10.1002/2015RG000483).
- Arora, V. K. et al. (2011). "Carbon Emission Limits Required to Satisfy Future Representative Concentration Pathways of Greenhouse Gases." *Geophysical Research Letters* 38.5, p. L05805. DOI: [10.1029/2010GL046270](https://doi.org/10.1029/2010GL046270).
- Arora, V. K. et al. (2013). "Carbon–Concentration and Carbon–Climate Feedbacks in CMIP5 Earth System Models." *Journal of Climate* 26.15, pp. 5289–5314. DOI: [10.1175/JCLI-D-12-00494.1](https://doi.org/10.1175/JCLI-D-12-00494.1).
- Bentsen, M. et al. (2013). "The Norwegian Earth System Model, NorESM1-M – Part 1: Description and Basic Evaluation of the Physical Climate." *Geosci. Model Dev.* 6.3, pp. 687–720. DOI: [10.5194/gmd-6-687-2013](https://doi.org/10.5194/gmd-6-687-2013).
- Campbell, J. E. et al. (2017). "Large Historical Growth in Global Terrestrial Gross Primary Production." *Nature* 544.7648, pp. 84–87. DOI: [10.1038/nature22030](https://doi.org/10.1038/nature22030).
- Chevallier, F. et al. (2010). "CO₂ Surface Fluxes at Grid Point Scale Estimated from a Global 21 Year Reanalysis of Atmospheric Measurements." *Journal of Geophysical Research: Atmospheres* 115.D21, p. D21307. DOI: [10.1029/2010JD013887](https://doi.org/10.1029/2010JD013887).
- Ciais, P. et al. (2013). "Carbon and Other Biogeochemical Cycles." In: *Climate Change 2013: The Physical Science Basis. Contribution of Working Group I to the Fifth Assessment Report of the Intergovernmental Panel on Climate Change*. Ed. by T. Stocker et al. Cambridge, United Kingdom and New York, NY, USA: Cambridge University Press, pp. 465–570. ISBN: ISBN 978-1-107-66182-0.
- Collins, W. J. et al. (2011). "Development and Evaluation of an Earth-System Model – HadGEM2." *Geoscientific Model Development* 4.4, pp. 1051–1075. DOI: [10.5194/gmd-4-1051-2011](https://doi.org/10.5194/gmd-4-1051-2011).
- Cook, B. I. and S. Pau (2013). "A Global Assessment of Long-Term Greening and Browning Trends in Pasture Lands Using the GIMMS LAI3g Dataset." *Remote Sensing* 5.5, pp. 2492–2512. DOI: [10.3390/rs5052492](https://doi.org/10.3390/rs5052492).
- Cox, P. M. et al. (2013). "Sensitivity of Tropical Carbon to Climate Change Constrained by Carbon Dioxide Variability." *Nature* 494.7437, pp. 341–344. DOI: [10.1038/nature11882](https://doi.org/10.1038/nature11882).
- De Kauwe, M. G., T. F. Keenan, B. E. Medlyn, I. C. Prentice, and C. Terrer (2016). "Satellite Based Estimates Underestimate the Effect of CO₂ Fertilization on Net Primary Productivity." *Nature Climate Change* 6.10, pp. 892–893. DOI: [10.1038/nclimate3105](https://doi.org/10.1038/nclimate3105).
- Dee, D. P. et al. (2011). "The ERA-Interim Reanalysis: Configuration and Performance of the Data Assimilation System." *Quarterly Journal of the Royal Meteorological Society* 137.656, pp. 553–597. DOI: [10.1002/qj.828](https://doi.org/10.1002/qj.828).
- Dunne, J. P. et al. (2012a). "GFDL's ESM2 Global Coupled Climate–Carbon Earth System Models. Part I: Physical Formulation and Baseline Simulation Characteristics." *Journal of Climate* 25.19, pp. 6646–6665. DOI: [10.1175/JCLI-D-11-00560.1](https://doi.org/10.1175/JCLI-D-11-00560.1).
- Dunne, J. P. et al. (2012b). "GFDL's ESM2 Global Coupled Climate–Carbon Earth System Models. Part II: Carbon System Formulation and Baseline Simulation Characteristics." *Journal of Climate* 26.7, pp. 2247–2267. DOI: [10.1175/JCLI-D-12-00150.1](https://doi.org/10.1175/JCLI-D-12-00150.1).

- Forkel, M. et al. (2016). "Enhanced Seasonal CO₂ Exchange Caused by Amplified Plant Productivity in Northern Ecosystems." *Science* 351.6274, pp. 696–699. DOI: [10.1126/science.aac4971](https://doi.org/10.1126/science.aac4971).
- Friedlingstein, P. et al. (2013). "Uncertainties in CMIP5 Climate Projections Due to Carbon Cycle Feedbacks." *Journal of Climate* 27.2, pp. 511–526. DOI: [10.1175/JCLI-D-12-00579.1](https://doi.org/10.1175/JCLI-D-12-00579.1).
- Goetz, S. J., A. G. Bunn, G. J. Fiske, and R. A. Houghton (2005). "Satellite-Observed Photosynthetic Trends across Boreal North America Associated with Climate and Fire Disturbance." *Proceedings of the National Academy of Sciences of the United States of America* 102.38, pp. 13521–13525. DOI: [10.1073/pnas.0506179102](https://doi.org/10.1073/pnas.0506179102).
- Graven, H. D. et al. (2013). "Enhanced Seasonal Exchange of CO₂ by Northern Ecosystems Since 1960." *Science* 341.6150, pp. 1085–1089. DOI: [10.1126/science.1239207](https://doi.org/10.1126/science.1239207).
- Hannachi, A., I. T. Jolliffe, and D. B. Stephenson (2007). "Empirical Orthogonal Functions and Related Techniques in Atmospheric Science: A Review." *International Journal of Climatology* 27.9, pp. 1119–1152. DOI: [10.1002/joc.1499](https://doi.org/10.1002/joc.1499).
- Ito, A. and T. Oikawa (2002). "A Simulation Model of the Carbon Cycle in Land Ecosystems (Sim-CYCLE): A Description Based on Dry-Matter Production Theory and Plot-Scale Validation." *Ecological Modelling* 151.2, pp. 143–176. DOI: [10.1016/S0304-3880\(01\)00473-2](https://doi.org/10.1016/S0304-3880(01)00473-2).
- Keeling, C. D., J. F. S. Chin, and T. P. Whorf (1996). "Increased Activity of Northern Vegetation Inferred from Atmospheric CO₂ Measurements." *Nature* 382.6587, pp. 146–149. DOI: [10.1038/382146a0](https://doi.org/10.1038/382146a0).
- Keenan, T. F. et al. (2016). "Recent Pause in the Growth Rate of Atmospheric CO₂ Due to Enhanced Terrestrial Carbon Uptake." *Nature Communications* 7, p. 13428. DOI: [10.1038/ncomms13428](https://doi.org/10.1038/ncomms13428).
- Koffi, E. N., P. J. Rayner, M. Scholze, and C. Beer (2012). "Atmospheric Constraints on Gross Primary Productivity and Net Ecosystem Productivity: Results from a Carbon-Cycle Data Assimilation System." *Global Biogeochemical Cycles* 26.1, GB1024. DOI: [10.1029/2010GB003900](https://doi.org/10.1029/2010GB003900).
- Kolby Smith, W. et al. (2016). "Large Divergence of Satellite and Earth System Model Estimates of Global Terrestrial CO₂ Fertilization." *Nature Climate Change* 6.3, pp. 306–310. DOI: [10.1038/nclimate2879](https://doi.org/10.1038/nclimate2879).
- Leakey, A. D. B. et al. (2009). "Elevated CO₂ Effects on Plant Carbon, Nitrogen, and Water Relations: Six Important Lessons from FACE." *Journal of Experimental Botany* 60.10, pp. 2859–2876. DOI: [10.1093/jxb/erp096](https://doi.org/10.1093/jxb/erp096).
- Lindsay, K. et al. (2014). "Preindustrial-Control and Twentieth-Century Carbon Cycle Experiments with the Earth System Model CESM1(BGC)." *Journal of Climate* 27.24, pp. 8981–9005. DOI: [10.1175/JCLI-D-12-00565.1](https://doi.org/10.1175/JCLI-D-12-00565.1).
- Mahowald, N. et al. (2016). "Projections of Leaf Area Index in Earth System Models." *Earth Syst. Dynam.* 7.1, pp. 211–229. DOI: [10.5194/esd-7-211-2016](https://doi.org/10.5194/esd-7-211-2016).
- Mao, J. et al. (2016). "Human-Induced Greening of the Northern Extratropical Land Surface." *Nature Climate Change* 6.10, pp. 959–963. DOI: [10.1038/nclimate3056](https://doi.org/10.1038/nclimate3056).
- Müller, W. A. et al. (2018). "A Higher-Resolution Version of the Max Planck Institute Earth System Model (MPI-ESM1.2-HR)." *Journal of Advances in Modeling Earth Systems* 10.7, pp. 1383–1413. DOI: [10.1029/2017MS001217](https://doi.org/10.1029/2017MS001217).
- Myneni, R. B. et al. (2002). "Global Products of Vegetation Leaf Area and Fraction Absorbed PAR from Year One of MODIS Data." *Remote Sensing of Environment*. The Moderate

- Resolution Imaging Spectroradiometer (MODIS): A New Generation of Land Surface Monitoring 83.1–2, pp. 214–231. DOI: [10.1016/S0034-4257\(02\)00074-3](https://doi.org/10.1016/S0034-4257(02)00074-3).
- Myneni, R. B., C. D. Keeling, C. J. Tucker, G. Asrar, and R. R. Nemani (1997). “Increased Plant Growth in the Northern High Latitudes from 1981 to 1991.” *Nature* 386, pp. 698–702. DOI: [10.1038/386698a0](https://doi.org/10.1038/386698a0).
- Mystakidis, S., E. L. Davin, N. Gruber, and S. I. Seneviratne (2016). “Constraining Future Terrestrial Carbon Cycle Projections Using Observation-Based Water and Carbon Flux Estimates.” *Global Change Biology* 22.6, pp. 2198–2215. DOI: [10.1111/gcb.13217](https://doi.org/10.1111/gcb.13217).
- Nemani, R. R. et al. (2003). “Climate-Driven Increases in Global Terrestrial Net Primary Production from 1982 to 1999.” *Science* 300.5625, pp. 1560–1563. DOI: [10.1126/science.1082750](https://doi.org/10.1126/science.1082750).
- Park, T. et al. (2016). “Changes in Growing Season Duration and Productivity of Northern Vegetation Inferred from Long-Term Remote Sensing Data.” *Environmental Research Letters* 11.8, p. 084001. DOI: [10.1088/1748-9326/11/8/084001](https://doi.org/10.1088/1748-9326/11/8/084001).
- Peylin, P. et al. (2013). “Global Atmospheric Carbon Budget: Results from an Ensemble of Atmospheric CO₂ Inversions.” *Biogeosciences* 10.10, pp. 6699–6720. DOI: [10.5194/bg-10-6699-2013](https://doi.org/10.5194/bg-10-6699-2013).
- Piao, S. et al. (2014). “Evidence for a Weakening Relationship between Interannual Temperature Variability and Northern Vegetation Activity.” *Nature Communications* 5, p. 5018. DOI: [10.1038/ncomms6018](https://doi.org/10.1038/ncomms6018).
- Pinzon, J. E. and C. J. Tucker (2014). “A Non-Stationary 1981–2012 AVHRR NDVI3g Time Series.” *Remote Sensing* 6.8, pp. 6929–6960. DOI: [10.3390/rs6086929](https://doi.org/10.3390/rs6086929).
- Poulter, B. et al. (2014). “Contribution of Semi-Arid Ecosystems to Interannual Variability of the Global Carbon Cycle.” *Nature* 509.7502, pp. 600–603. DOI: [10.1038/nature13376](https://doi.org/10.1038/nature13376).
- Prentice, I. C. et al. (2001). “The Carbon Cycle and Atmospheric Carbon Dioxide.” In: *Climate Change 2001: The Scientific Basis. Contributions of Working Group I to the Third Assessment Report of the Intergovernmental Panel on Climate Change*. Ed. by J. T. Houghton et al. Cambridge, UK: Cambridge University Press, pp. 185–237.
- Quére, C. L. et al. (2018). “Global Carbon Budget 2017.” *Earth System Science Data* 10.1, pp. 405–448. DOI: [10.5194/essd-10-405-2018](https://doi.org/10.5194/essd-10-405-2018).
- Raddatz, T. J. et al. (2007). “Will the Tropical Land Biosphere Dominate the Climate–Carbon Cycle Feedback during the Twenty-First Century?” *Climate Dynamics* 29.6, pp. 565–574. DOI: [10.1007/s00382-007-0247-8](https://doi.org/10.1007/s00382-007-0247-8).
- Reick, C. H., T. Raddatz, V. Brovkin, and V. Gayler (2013). “Representation of Natural and Anthropogenic Land Cover Change in MPI-ESM.” *Journal of Advances in Modeling Earth Systems* 5.3, pp. 459–482. DOI: [10.1002/jame.20022](https://doi.org/10.1002/jame.20022).
- Rödenbeck, C., S. Houweling, M. Gloor, and M. Heimann (2003). “CO₂ Flux History 1982–2001 Inferred from Atmospheric Data Using a Global Inversion of Atmospheric Transport.” *Atmos. Chem. Phys.* 3.6, pp. 1919–1964. DOI: [10.5194/acp-3-1919-2003](https://doi.org/10.5194/acp-3-1919-2003).
- Screen, J. A. and I. Simmonds (2010). “The Central Role of Diminishing Sea Ice in Recent Arctic Temperature Amplification.” *Nature* 464.7293, pp. 1334–1337. DOI: [10.1038/nature09051](https://doi.org/10.1038/nature09051).
- Taylor, K. E., R. J. Stouffer, and G. A. Meehl (2009). “A Summary of the CMIP5 Experiment Design.” *PCDMI Rep.* P. 33.
- (2012). “An Overview of Cmpip5 and the Experiment Design.” *Bulletin of the American Meteorological Society* 93.4, pp. 485–498. DOI: [10.1175/BAMS-D-11-00094.1](https://doi.org/10.1175/BAMS-D-11-00094.1).

- Thomas, R. T. et al. (2016). "Increased Light-Use Efficiency in Northern Terrestrial Ecosystems Indicated by CO₂ and Greening Observations." *Geophysical Research Letters* 43.21, pp. 11,339–11,349. DOI: [10.1002/2016GL070710](https://doi.org/10.1002/2016GL070710).
- Watanabe, S. et al. (2011). "MIROC-ESM 2010: Model Description and Basic Results of CMIP5-20c3m Experiments." *Geosci. Model Dev.* 4.4, pp. 845–872. DOI: [10.5194/gmd-4-845-2011](https://doi.org/10.5194/gmd-4-845-2011).
- Welp, L. R. et al. (2011). "Interannual Variability in the Oxygen Isotopes of Atmospheric CO₂ Driven by El Niño." *Nature* 477.7366, pp. 579–582. DOI: [10.1038/nature10421](https://doi.org/10.1038/nature10421).
- Wenzel, S., P. M. Cox, V. Eyring, and P. Friedlingstein (2014). "Emergent Constraints on Climate-Carbon Cycle Feedbacks in the CMIP5 Earth System Models." *Journal of Geophysical Research: Biogeosciences* 119.5, pp. 794–807. DOI: [10.1002/2013JG002591](https://doi.org/10.1002/2013JG002591).
- (2016). "Projected Land Photosynthesis Constrained by Changes in the Seasonal Cycle of Atmospheric CO₂." *Nature* 538.7626, pp. 499–501. DOI: [10.1038/nature19772](https://doi.org/10.1038/nature19772).
- Yan, K. et al. (2016a). "Evaluation of MODIS LAI/FPAR Product Collection 6. Part 1: Consistency and Improvements." *Remote Sensing* 8.5, p. 359. DOI: [10.3390/rs8050359](https://doi.org/10.3390/rs8050359).
- Yan, K. et al. (2016b). "Evaluation of MODIS LAI/FPAR Product Collection 6. Part 2: Validation and Intercomparison." *Remote Sensing* 8.6, p. 460. DOI: [10.3390/rs8060460](https://doi.org/10.3390/rs8060460).
- Zhang, Y., M. Xu, H. Chen, and J. Adams (2009). "Global Pattern of NPP to GPP Ratio Derived from MODIS Data: Effects of Ecosystem Type, Geographical Location and Climate." *Global Ecology and Biogeography* 18.3, pp. 280–290. DOI: [10.1111/j.1466-8238.2008.00442.x](https://doi.org/10.1111/j.1466-8238.2008.00442.x).
- Zhang, Y., C. Song, L. E. Band, G. Sun, and J. Li (2017). "Reanalysis of Global Terrestrial Vegetation Trends from MODIS Products: Browning or Greening?" *Remote Sensing of Environment* 191, pp. 145–155. DOI: [10.1016/j.rse.2016.12.018](https://doi.org/10.1016/j.rse.2016.12.018).
- Zhao, F. and N. Zeng (2014). "Continued Increase in Atmospheric CO₂ Seasonal Amplitude in the 21st Century Projected by the CMIP5 Earth System Models." *Earth Syst. Dynam.* 5.2, pp. 423–439. DOI: [10.5194/esd-5-423-2014](https://doi.org/10.5194/esd-5-423-2014).
- Zhu, Z. et al. (2013). "Global Data Sets of Vegetation Leaf Area Index (LAI)_{3g} and Fraction of Photosynthetically Active Radiation (FPAR)_{3g} Derived from Global Inventory Modeling and Mapping Studies (GIMMS) Normalized Difference Vegetation Index (NDVI)_{3g} for the Period 1981 to 2011." *Remote Sensing* 5.2, pp. 927–948. DOI: [10.3390/rs5020927](https://doi.org/10.3390/rs5020927).
- Zhu, Z. et al. (2016). "Greening of the Earth and Its Drivers." *Nature Climate Change* 6.8, pp. 791–795. DOI: [10.1038/nclimate3004](https://doi.org/10.1038/nclimate3004).

Acknowledgements We acknowledge T. Park and C. Chen for their help with remote sensing data. We thank W. Müller, H. Li and T. Ilyina for providing the high-resolution MPI-ESM simulations. Further, we thank H. Graven for assistance with the Point Barrow CO₂ data, R. Keeling for advice on the seasonal cycle of CO₂, M. Heimann, C. Rödenbeck and P. Ciais for advice on atmospheric CO₂ inversion, and G. Lasslop for reviewing the manuscript. R.B.M. acknowledges funding by the NASA Earth Science Directorate and the Alexander von Humboldt Foundation. This work contributes to the H2020 project CRESCENDO, which receives funding from the European Union's Horizon 2020 research and innovation program under grant agreement no. 641816.

Author Information Reprints and permissions information is available at www.nature.com/reprints. The Authors declare no conflict of interests. Readers are welcome to comment on the online version of the paper. Correspondence and requests for materials should be addressed to A.J.W. (alexander.winkler@mpimet.mpg.de).

A SUPPLEMENTARY INFORMATION

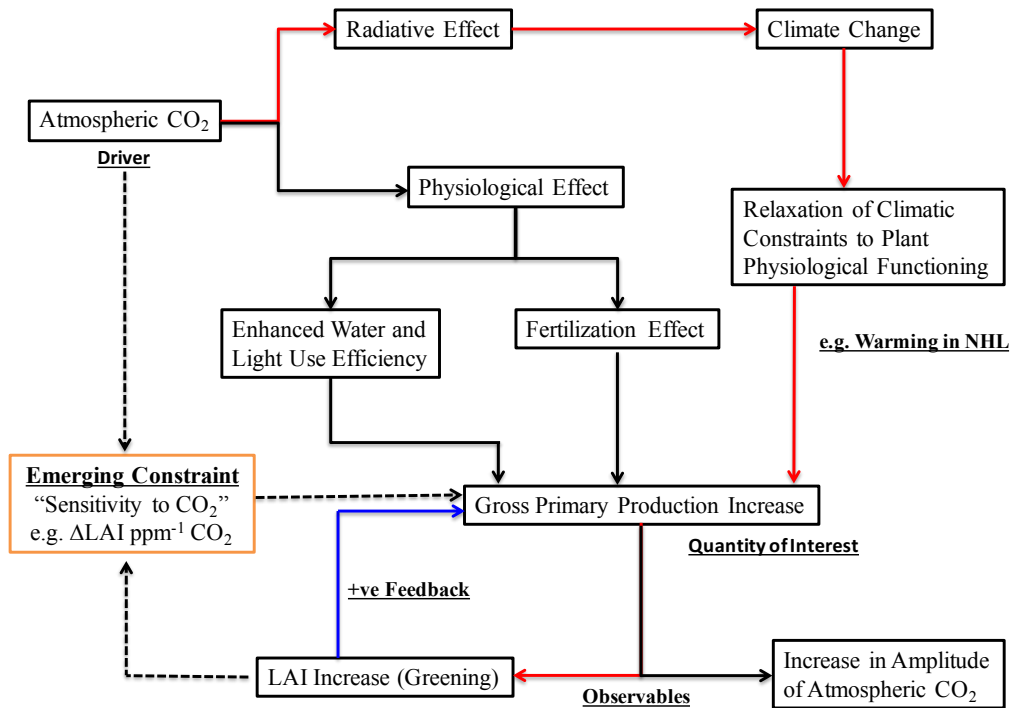


Figure A1 | **Schematic of the Emergent Constraint concept.** The radiative and physiological effects of increasing atmospheric CO₂ concentration, in the range 280 to 560 ppm, are thought to increase GPP (Ciais et al., 2013; Zhao and Zeng, 2014; Nemani et al., 2003; Leakey et al., 2009; Thomas et al., 2016). This is indirectly observed as changes in LAI (Myneni et al., 1997; Zhu et al., 2016) or the amplitude of the seasonal cycle of atmospheric CO₂ (Keeling et al., 1996; Graven et al., 2013; Wenzel et al., 2016). The sensitivity of changes in observables to historical increase in CO₂ concentration (e.g., 280 to 400 ppm) can be thought of as an Emergent Constraint on model-projected changes in carbon cycle quantities (e.g., ΔGPP for CO₂ change from 280 to 560 ppm), if the inter-model variation of projections is linear, or nearly so, with respect to modeled historical sensitivities (Wenzel et al., 2016). GPP enhancement due to the radiative effect (red arrows) was not included in Wenzel et al. (2016) because their focus was on obtaining a constrained estimate for the physiological effect only. GPP enhancement from the positive feedback effect (blue arrow) is thought to be small (Keenan et al., 2016) relative to the physiological and radiative effects, and included in our study.

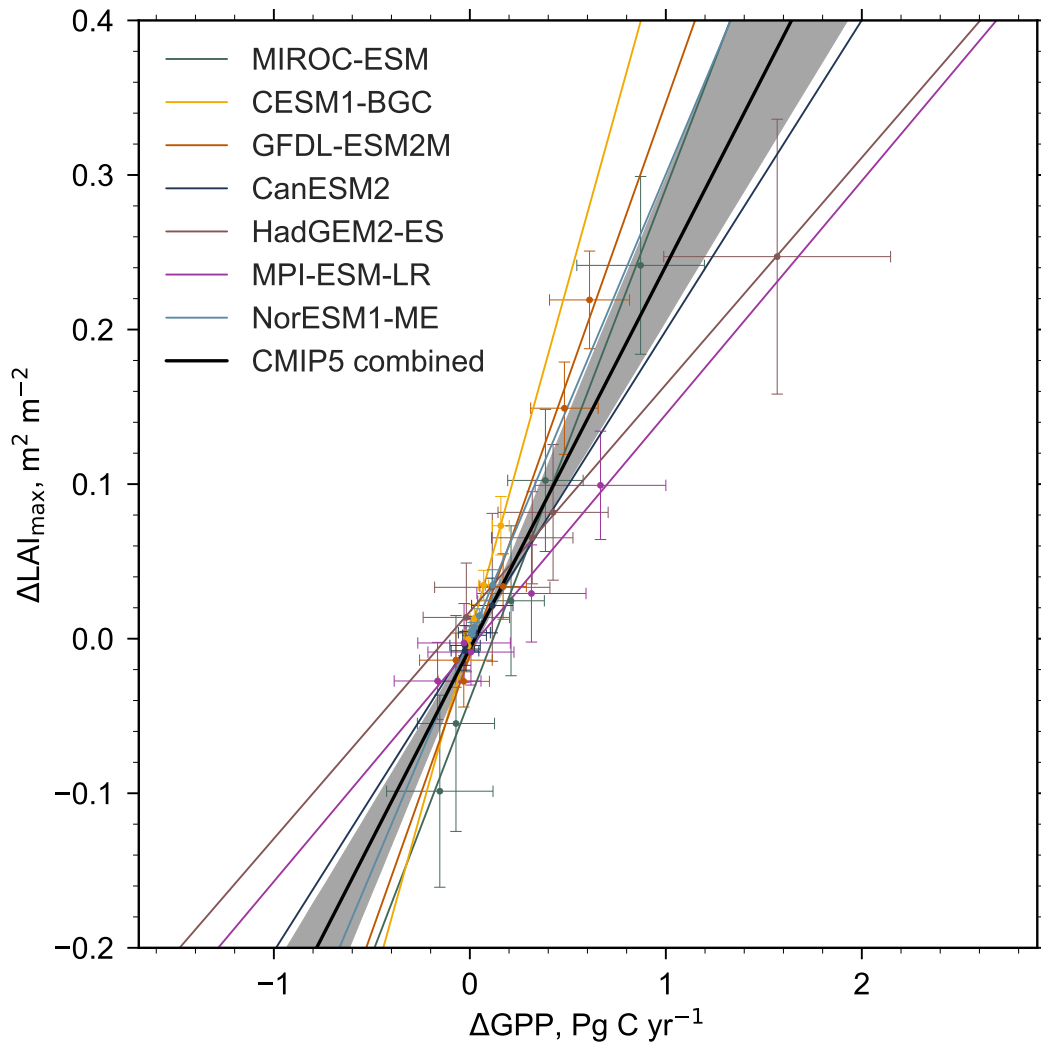


Figure A2 | **Linear relationship between concurrent changes in LAI_{max} and annual mean GPP.** Comparison of changes in LAI_{max} and annual mean GPP for the historical period (1860 to 2005) for the NHL (60° N – 90° N) in the CMIP5 ensemble. The colored dots show values for 30 year chunks of the total time series (error bars denote one standard deviation). The colored lines represent the best linear fit for each model, while the black line indicates the best linear fit for all models. The 68% confidence interval estimated by bootstrapping is shown by the grey shading.

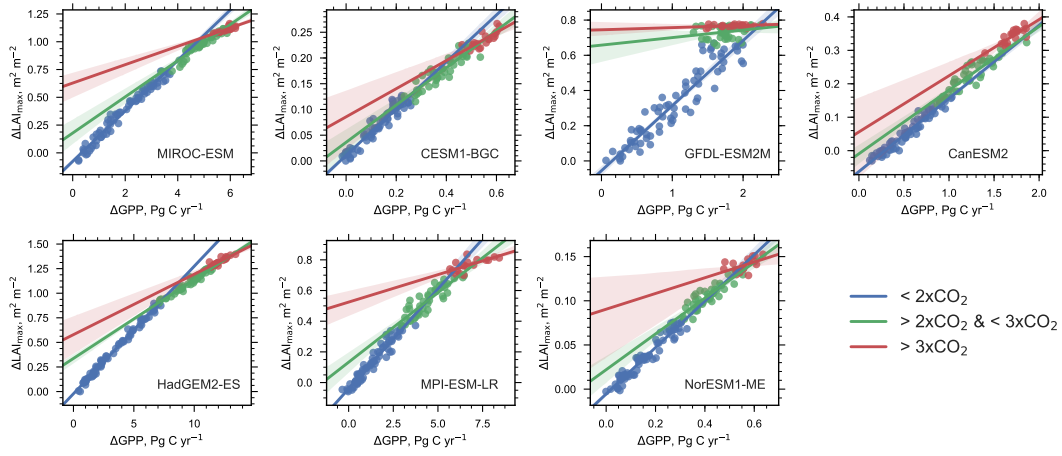


Figure A3 | Relationship between $\Delta\text{LAI}_{\text{max}}$ and ΔGPP with increasing CO_2 forcing, starting from a pre-industrial concentration of 280 ppm ($1 \times \text{CO}_2$) to $4 \times \text{CO}_2$. Blue colored dots represent the relation for concentration below $2 \times \text{CO}_2$. Green colored dots between $2 \times \text{CO}_2$ and $3 \times \text{CO}_2$. Red colored dots between $3 \times \text{CO}_2$ and $4 \times \text{CO}_2$ (Table A3). The respective colored lines are the regressions through those dots and the shading represents the 95% confidence interval.

Table A1 | Summary data for Principal Component Analysis, LAI_{max} sensitivity estimation and GPP increase.

Model	Explained variance by ω	Offset to initial LAI_{max} (m^{-2})	Initial LAI_{max} (m^2)	LAI_{max} sensitivity to ω , ($\text{m}^2 \text{ m}^{-2}$ unit ω)	Correlation coefficient	ΔGPP for $2 \times \text{CO}_2$ ($\text{Pg C} / \text{yr}^{-1}$)
MIROC-ESM	0.89	$2.7 \pm 0.7\text{e-}3$	1.0 ± 0.1	$0.049 \pm 3.3\text{e-}3$	0.93	3.2 ± 0.29
CESM1-BGC	0.83	$0.44 \pm 0.3\text{e-}3$	1.0 ± 0.1	$0.014 \pm 1.4\text{e-}3$	0.86	0.24 ± 0.025
GFDL-ESM2M	0.64	$2.9 \pm 0.6\text{e-}3$	1.0 ± 0.1	$0.022 \pm 3.2\text{e-}3$	0.76	1.8 ± 0.19
CanESM2	0.91	$0.68 \pm 0.2\text{e-}3$	1.0 ± 0.1	$0.013 \pm 1.0\text{e-}3$	0.91	0.72 ± 0.12
HadGEM2-ES	0.94	$1.5 \pm 0.8\text{e-}3$	1.0 ± 0.1	$0.075 \pm 3.5\text{e-}3$	0.97	6 ± 0.53
MPI-ESM-LR	0.77	$1.4 \pm 0.4\text{e-}3$	1.0 ± 0.1	$0.028 \pm 1.8\text{e-}3$	0.94	2.5 ± 0.36
NorESM1-ME	0.84	$0.21 \pm 0.2\text{e-}3$	1.0 ± 0.1	$0.0088 \pm 0.8\text{e-}3$	0.88	0.28 ± 0.022
Observations	0.9	$1.8 \pm 1.5\text{e-}3$	1.0 ± 0.1	$0.045 \pm 6.4\text{e-}3$	0.78	-

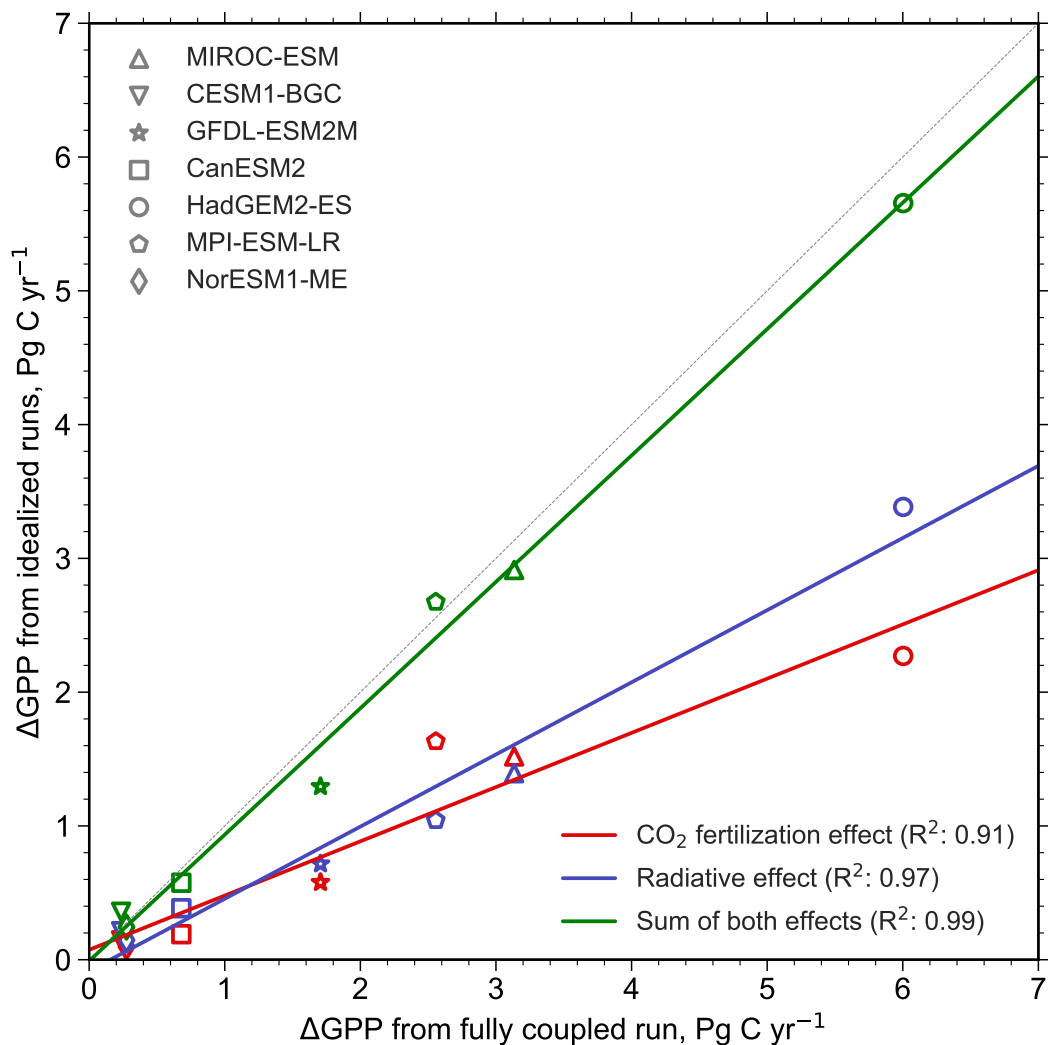


Figure A4 | **Radiative and fertilization effects on NHL photosynthesis.** Changes in annual mean GPP for doubling of pre-industrial CO_2 concentration from $1\% \text{CO}_2$ (CO_2 concentration increased by $1\% \text{ yr}^{-1}$ from preindustrial level) fully coupled (radiative plus fertilization) CMIP5 model runs (x -axis) plotted against idealized simulations (y -axis) with only the radiative (CMIP5's *esmFdbk*; Arora et al., 2013) or the fertilization (CMIP5's *esmFixClim*; Arora et al., 2013) effect included runs. The markers show the corresponding model values from these runs. The colored lines are best fits to the respective markers (red for fertilization effect only, blue for radiative effect only). The green line represents the best fit to the sum of quantities from the idealized runs and the fully coupled run. Wenzel et al. (2016) provided a constrained estimate for GPP projection considering the fertilization effect only. Including the radiative effect would at least double their estimate.

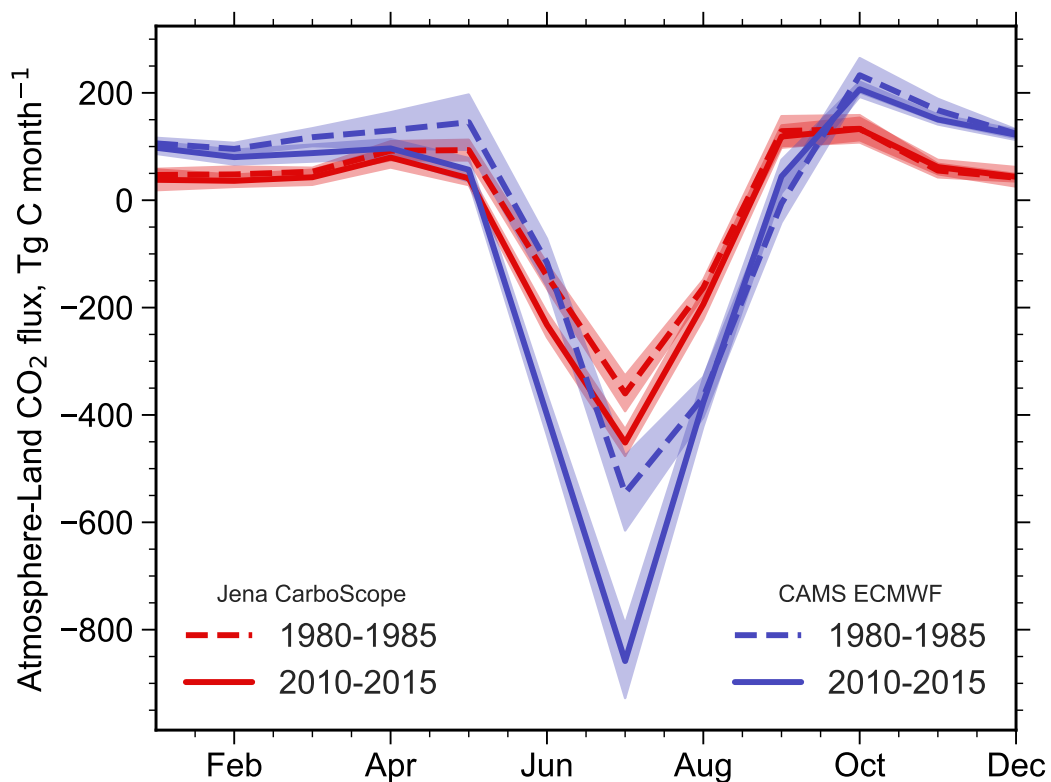


Figure A5 | **Atmospheric CO₂ inversions suggest strong increase of NHL land carbon sink.** Seasonal cycle of land-atmospheric CO₂ exchange estimated by two inversion procedures, Jena CarboScope (red) and CAMS ECMWF (blue), for two time periods 1980-1985 (dashed) and 2010-2015 (solid). Shading indicates one standard deviation.

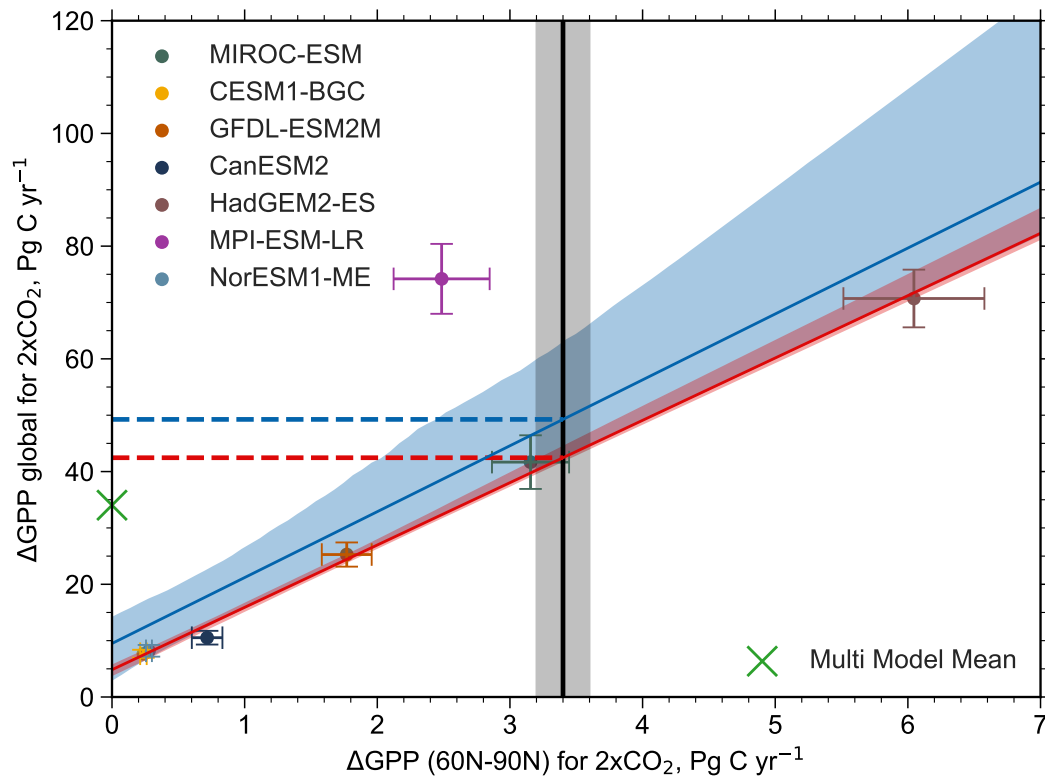


Figure A6 | **Strong linear relationship between global and NHL GPP increase in the CMIP5 ensemble.** Comparison of NHL (x -axis) and global (y -axis) estimates of changes in annual mean GPP for doubling of pre-industrial CO_2 concentration. The markers show the individual model including error bars for one standard deviation. The black vertical line shows the observation-based Emergent Constraint estimate of NHL GPP increase with the gray shading indicating uncertainty (Methods). The blue line represents the best linear fit across the entire CMIP5 ensemble (blue shading denotes the 68% confidence interval), whereas the red line shows the best fit excluding the outlier MPI-ESM-LR (purple, the MPI-ESM-LR CMIP5 version is overly productive in the tropics due to almost absent water limitation). The dashed horizontal lines indicate the respective constraints on global GPP increase. Based on this result, also on global scale a substantial underestimation of photosynthetic carbon fixation is present – constrained estimate is 44% higher than multi-model mean indicated by green cross (56% excluding outlier).

Table A2 | Overview of CMIP5 models included in this study.

Models	No. of PFTs	Land model	Land resolution
MPI-ESM-LR	12	JSBACH	$1.9^\circ \times 1.9^\circ$
CanESM2	9	CTEM	$2.8^\circ \times 2.8^\circ$
MIROC-ESM	13	SEIB-DGVM	$2.8^\circ \times 2.8^\circ$
NorESM1-ME	16	CLM4	$2.5^\circ \times 1.9^\circ$
CESM1-BGC	16	CLM4	$0.9^\circ \times 1.2^\circ$
GFDL-ESM2M	5	LM3	$2.5^\circ \times 2.5^\circ$
HadGEM2-ES	5	TRIFFID	$1.9^\circ \times 1.2^\circ$

Table A2 | Overview of CMIP5 models included in this study (*continued*).

Models	Dynamic vegetation	Explicit nitrogen cycle	Reference
MPI-ESM-LR	Yes	No	Raddatz et al. (2007) and Reick et al. (2013)
CanESM2	No	No	Arora et al. (2011)
MIROC-ESM	Yes	No	Watanabe et al. (2011)
NorESM1-ME	No	Yes	Bentsen et al. (2013)
CESM1-BGC	No	Yes	Lindsay et al. (2014)
GFDL-ESM2M	Yes	No	Dunne et al. (2012a) and Dunne et al. (2012b)
HadGEM2-ES	Yes	No	Collins et al. (2011)

Table A3 | Correlation coefficients for the relations shown in Figure A3.

Models	MPI-ESM-LR	CanESM2	MIROC-ESM	NorESM1-ME	CESM1-BGC	GFDL-ESM2M	HadGEM2-ES
$< 2 \times \text{CO}_2$	0.94	0.95	0.97	0.94	0.93	0.89	0.99
$> 2 \times \text{CO}_2$ & $< 3 \times \text{CO}_2$	0.78	0.83	0.89	0.77	0.82	0.067	0.96
$> 3 \times \text{CO}_2$	0.51	0.67	0.63	0.27	0.62	0.12	0.78

Part III

INVESTIGATING THE APPLICABILITY OF EMERGENT CONSTRAINTS

The attached article has been published as:

Winkler, A. J., R. B. Myneni, and V. Brovkin (2019b). "Investigating the Applicability of Emergent Constraints." *Earth System Dynamics* 10.3, pp. 501–523. DOI: [10.5194/esd-10-501-2019](https://doi.org/10.5194/esd-10-501-2019)

INVESTIGATING THE APPLICABILITY OF EMERGENT CONSTRAINTS

ALEXANDER J. WINKLER^{1,2}, RANGA B. MYNENI^{1,3},
AND VICTOR BROVKIN¹

CONTENTS

1	Introduction	3
2	Data and Methods	7
2.1	Remotely sensed leaf area index	7
2.2	Environmental driver variables	8
2.3	Earth system model simulations	8
2.4	Estimation of greening sensitivities	9
3	Results and Discussion	10
3.1	Uncertainty in Observed Predictor Due to Data Source	10
3.2	Uncertainty Due to Spatial Aggregation	11
3.3	Uncertainty Due to Temporal Variations	14
3.4	Level and Time Rate of CO ₂ Forcing	15
3.5	Effects of CO ₂ Forcing	21
3.6	Uncertainties in the Multi-Model Ensemble	22
4	Conclusions	22
	References	27
A	Supplementary Information	31

¹ Max-Planck-Institute for Meteorology, Bundesstrasse 53, 20146 Hamburg, Germany

² International Max-Planck Research School for Earth System Modeling, Bundesstrasse 53, 20146 Hamburg, Germany

³ Department of Earth and Environment, Boston University, Boston MA 02215, USA

Abstract

Recent research on Emergent Constraints (EC) has delivered promising results in narrowing down uncertainty in climate predictions. The method utilizes a measurable variable (predictor) from the recent historical past to obtain a constrained estimate of change in an entity of interest (predictand) at a potential future CO₂ concentration (forcing) from multi-model projections. This procedure critically depends on, first, accurate estimation of the predictor from observations and models, and second, on a robust relationship between inter-model variations in the predictor-predictand space. Here, we investigate issues related to these two themes in a carbon cycle case study using observed vegetation greening sensitivity to CO₂ forcing as a predictor of change in photosynthesis (Gross Primary Productivity, GPP) for a doubling of pre-industrial CO₂ concentration. Greening sensitivity is defined as changes in annual maximum of green leaf area index (LAI_{max}) per unit CO₂ forcing realized through its radiative and fertilization effects. We first address the question of how to realistically characterize the predictor of a large area (e.g. greening sensitivity in the northern high latitudes region) from pixel-level data. This requires an investigation into uncertainties in the observational data source and an evaluation of the spatial and temporal variability in the predictor in both the data and model simulations. Second, the predictor-predictand relationship across the model ensemble depends on a strong coupling between the two variables, i.e. simultaneous changes in GPP and LAI_{max}. This coupling depends in a complex manner on the magnitude (level), time-rate of application (scenarios) and effects (radiative and/or fertilization) of CO₂ forcing. We investigate how each one of these three aspects of forcing can affect the EC estimate of the predictand (Δ GPP). Our results show that uncertainties in the EC method primarily originate from a lack of predictor comparability between observations and models, the observational data source, and temporal variability of the predictor. The disagreement between models on the mechanistic behavior of the system under intensifying forcing limits the EC applicability. The discussed limitations and sources of uncertainty in the EC method go beyond carbon cycle research and are generally applicable in Earth system sciences.

Author Contributions A.J.W. performed the research. All authors contributed ideas and to the interpretation of the results. A.J.W. and R.B.M. drafted the manuscript with inputs from V.B.

1 INTRODUCTION

Earth system models (ESMs) are powerful tools to predict responses to a variety of forcings such as increasing atmospheric concentration of greenhouse gases and other agents of radiative forcing (Klein and Hall, 2015). Still, longterm ESM projections of climate change have substantial uncertainties. This can be due to poorly understood processes in some cases, and in others, to missing or simplified representations called parameterizations (Flato et al., 2013; Klein and Hall, 2015; Knutti et al., 2017). Certain important processes, especially in the atmosphere, happen at spatial scales finer than can be possibly represented in current ESMs. Consequently, various phenomena in the system ranging from local extreme precipitation events to large-scale climate modes, can be poorly simulated (Flato et al., 2013). Errors propagate and can be amplified through feedbacks among interacting components in the Earth system, resulting in biases whose origins can be difficult to identify (Flato et al., 2013). Furthermore, an inherent component of the Earth climatic system, its internal natural variability, is complicated to represent and simulate in models (Flato et al., 2013; Klein and Hall, 2015).

Model Intercomparison Projects explore these uncertainties by coordinating a wide range of simulation setups focusing on internal variability, boundary conditions, parameterizations, etc. (Taylor et al., 2012; Flato et al., 2013; Eyring et al., 2016; Knutti et al., 2017). Models developed at various institutions are driven with the same forcing information (e.g. historical forcing) or with identical idealized boundary conditions. However, each modeling group decides which of the processes to consider and implement in their ESM. The conventional approach of handling these multi-model ensembles is to use unweighted ensemble averages (Knutti, 2010; Knutti et al., 2017). This assumes that the models are independent of one another and equally good at simulating the climate system (Flato et al., 2013; Knutti et al., 2017). The large spread between model projections suggests that this assumption is not valid. Therefore, alternate methods have been developed to extract results more accurate than multi-model averages (e.g. model weighting scheme based on performance and interdependence, Knutti et al., 2017). The concept of *Emergent Constraints* arises in this context, namely, as a method to reduce uncertainty in ESM projections relying on historical simulations and observations (Hall and Qu, 2006; Boé et al., 2009; Cox et al., 2013; Klein and Hall, 2015; Cox et al., 2018).

The two key parts of an Emergent Constraint (EC) based method are a linear relationship arising from the collective behavior of a multi-model ensemble and an observational estimate for imposing the said constraint (Fig. 1). The linear relationship is a physically (or physiologically) based correlation between inter-model variations in an observable entity of the contemporary climate system (*predictor*) and a projected variable (*predictand*) that is difficult to observe or not observable at all. Combining the emergent linear relationship with observations of the predictor sets a constraint on the predictand (Cox et al., 2013; Flato et al., 2013; Klein and Hall, 2015; Knutti et al., 2017). Many such ECs have been identified and reported, as briefly summarized below.

Hall and Qu (2006) proposed a constraint on projections of snow-albedo feedback based on the correlation between large inter-model variations in feedback strength of the current seasonal cycle. The EC was first established for the CMIP3 ensemble and confirmed for phase five of the Coupled Model Intercomparison Project (CMIP5; Flato et al., 2013;

Qu and Hall, 2014). Several EC studies followed with the goal of reducing uncertainty in projections of the cloud feedback under global warming, as reviewed by Klein and Hall (2015). It is thought that erroneous representation of low-cloud feedback in ESMs contributes essentially to the large uncertainty in equilibrium climate sensitivity (ECS, 1.5 to 5 K), i.e. warming for a doubling of pre-industrial atmospheric CO₂ concentration (2×CO₂; Sherwood et al., 2014; Klein and Hall, 2015). Recently, Cox et al. (2018) presented a different approach to constrain ECS based on its relationship to variability of global temperatures during the recent historical warming period. They reported a constrained ECS estimate of 2.8 K for 2×CO₂ (66% confidence limits of 2.2 – 3.4 K).

The concept of EC also found its way into the field of carbon cycle projections. A series of studies analyzed the extent to which inter-annual atmospheric CO₂ variability can serve as a predictor of longterm temperature sensitivity of terrestrial tropical carbon storage. Cox et al. (2013) and Wenzel et al. (2014) reported an emergent linear relationship, although with different slopes for CMIP3 and CMIP5 ensembles, resulting in slightly divergent constrained estimates (CMIP3: -53 ± 17 Pg C K⁻¹, CMIP5: -44 ± 14 Pg C K⁻¹). Wang et al. (2014) however were unable to detect a similar relationship between the proposed predictor and predictand. Recently, Lian et al. (2018) presented an EC estimate of the global ratio of transpiration to total terrestrial evapotranspiration (T/ET), which is substantially higher (0.62 ± 0.06) than the unconstrained value (0.41 ± 0.11). For the marine tropical carbon cycle, Kwiatkowski et al. (2017) identified an emergent relationship between the longterm sensitivity of tropical ocean net primary production (NPP) to rising sea surface temperature (SST) in the equatorial zone and the interannual sensitivity of NPP to El Niño/Southern Oscillation driven SST anomalies. Tropical NPP is projected to decrease by $3 \pm 1\%$ for 1 K increase in equatorial SST according to the observational constraint.

Similar results were reported for modeled extra-tropical terrestrial carbon fixation in a 2×CO₂ world. Plant productivity is expected to increase due to the fertilizing and radiative effects of rising atmospheric CO₂ concentration. Wenzel et al. (2016) focused on constraining the CO₂ fertilization effect on plant productivity in the northern high latitudes (60° N – 90° N, NHL) and the entire extra-tropical area in the northern hemisphere (30° N – 90° N) using the seasonal amplitude of longterm CO₂ measurements at different latitudes. They presented a linear relationship between the sensitivity of CO₂ amplitude to rising atmospheric CO₂ concentration and the relative increase in zonally averaged gross primary production (GPP) for 2×CO₂. The observed CO₂ amplitude sensitivities at respective stations provide a constraint on the increase of GPP due to the CO₂ fertilization effect, namely $37\% \pm 9\%$ and $32\% \pm 9\%$ for 2×CO₂ in the NHL and the extra-tropical region, respectively.

Focusing on the NHL, Winkler et al. (2019) investigated how both effects of CO₂ enhance plant productivity while assessing the feasibility of vegetation greenness changes as a constraint. Enhanced GPP due to the physiological effect and ensuing climate warming is indirectly evident in large-scale increase in summer time green leaf area (Myneni et al., 1997b; Zhu et al., 2016). Historical CMIP5 simulations show that the maximum annual leaf area index (LAI_{max}, leaf area per ground area) increases linearly with both CO₂ concentration and temperature in NHL. In all ESMs, these changes in LAI_{max} strongly correlate to changes in GPP arising from the combined radiative and physiological effects of CO₂ enrichment. Thus, the large variation in modeled historical LAI_{max} responses to the

effects of CO₂ linearly maps to variation in Δ GPP at $2\times$ CO₂ in the CMIP5 ensemble. This linear relationship in inter-model variations enables the usage of the observed longterm change in LAI_{max} as an EC on Δ GPP at $2\times$ CO₂ in NHL (3.4 ± 0.2 Pg C yr⁻¹ for $2\times$ CO₂; Winkler et al., 2019).

The robustness of these EC estimates is debated, mainly because the EC approach is susceptible to methodological inconsistencies. For example, Cox et al. (2013), Wang et al. (2014) and Wenzel et al. (2015) investigated on constraining future terrestrial tropical carbon storage using the same set of models and data. However, they arrived at different EC estimates and divergent conclusions. Some reasons for failure and essential criteria of the EC approach were described previously (Bracegirdle and Stephenson, 2012b; Klein and Hall, 2015), but this list is far from complete. To account for this gap in the literature, a detailed investigation and description of the EC method in terms of its potential sources of uncertainty and the range of applicability are needed.

Here, we revisit the study of Winkler et al. (2019) and elaborate on key issues concerning the robustness of the EC method. Uncertainty of the constrained estimate depends on (a) observed predictor and (b) modeled relationship, aside from the goodness-of-fit of the latter (green shading in Fig. 1). As for (a), the source of observations is an obvious first line of inquiry (Sect. 3.1). Spatial aggregation of data and model simulations introduces uncertainties, as the EC method is applied on large areal values of predictor and predictand. This is the subject of Sect. 3.2. The observed and modeled predictors are from the historical period. The representativeness, duration and match between data and models all introduce an uncertainty related to variations in the temporal domain – these are explored in Sect. 3.3. The yellow shading in Fig. 1 represents the total uncertainty on observed predictor from these three fronts. Regarding (b), the modeled linear relation varies (grey shading in Fig. 1) depending on three attributes of the forcing, i.e. CO₂ concentration change, its magnitude, rate and effect (Sect. 3.4 and 3.5). Lessons learned from analyses along these lines are presented in the conclusion section at the end.

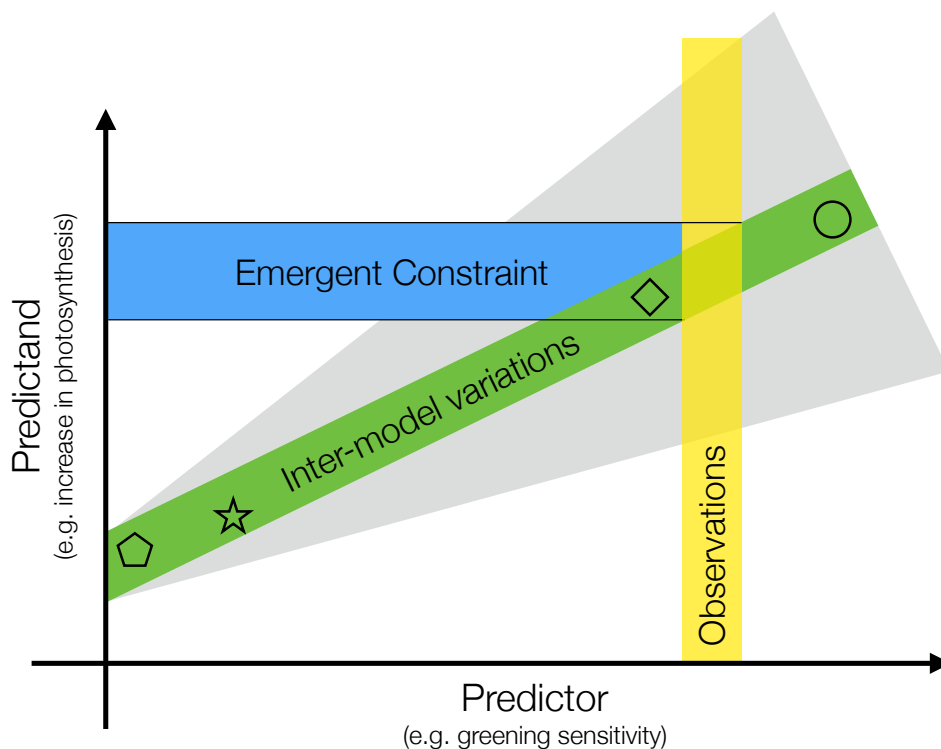


Figure 1 | Schematic depiction of the Emergent Constraint (EC) method and factors affecting the uncertainty of the constrained estimate. The predictor (x axis) is change in annual maximum of green leaf area index (LAI_{max}) due to unit forcing (CO_2 increase and associated climatic changes) during a representative historical period. It is termed greening sensitivity in this study. The predictand (y axis) is projected changes in Gross Primary Productivity (GPP) in response to rising CO_2 concentration (e.g. for a doubling of the pre-industrial level). Both the predictor and predictand refer to large area values, in this case, the entire Northern High Latitudes (NHL). Inter-model variations (each symbol represents a model) in matching pairs of predictor and predictand result in a linear relationship between the two (green band), i.e. the ratio (predictand/predictor) is approximately constant across the model ensemble. The slope depends on forcing attributes (gray shading), such as its level (CO_2 concentration, Sect. 3.4), time rate of application (scenarios such as various RCPs, Sect. 3.4) and different effects (i.e. fertilization, radiative, etc., Sect. 3.5). The observed sensitivity (yellow vertical bar) is used to find the constrained estimate of the predictand (i.e. change in GPP). The ability to accurately estimate the predictor depends on the source of observational data (Sect. 3.1), and its spatial (Sect. 3.2) and temporal variability (Sect. 3.3). Observed (yellow bar) and modeled predictor values (x coordinate of symbols) must be obtained from matching time periods, i.e. at the same level of historical forcing, to ensure comparability (Sect. 3.3 and 3.4). All these factors, together with the goodness-of-fit of inter-model variations (width of green shading), finally define the uncertainty of the derived constrained estimate (blue horizontal bar with black solid lines depicting the upper and lower bound of uncertainty).

2 DATA AND METHODS

2.1 Remotely sensed leaf area index

We used the recently updated version (V_1) of the leaf area index dataset (LAI_{3g}) developed by (Zhu et al., 2013). It was generated using an artificial neural network (ANN) and the latest version (third generation) of the Global Inventory Modeling and Mapping Studies group (GIMMS) Advanced Very High Resolution Radiometer (AVHRR) normalized difference vegetation index (NDVI) data (NDVI_{3g}). The latter have been corrected for sensor degradation, inter-sensor differences, cloud cover, observational geometry effects due to satellite drift, Rayleigh scattering and stratospheric volcanic aerosols (Pinzon and Tucker, 2014). This dataset provides global and year-round LAI observations at 15-day (bi-monthly) temporal resolution and 1/12 degree spatial resolution from July 1981 to December 2016. Currently, this is the only available record of such length.

The quality of previous version (V_0) of LAI_{3g} dataset was evaluated through direct comparisons with ground measurements of LAI and indirectly with other satellite-data based LAI products, and also through statistical analysis with climatic variables, such as temperature and precipitation variability (Zhu et al., 2013). The LAI_{3g} V_0 dataset (and related fraction vegetation-absorbed photosynthetically active radiation dataset) has been widely used in various studies (Anav et al., 2013; Piao et al., 2014; Poulter et al., 2014; Forkel et al., 2016; Zhu et al., 2016; Mao et al., 2016; Mahowald et al., 2016; Keenan et al., 2016). The new version, LAI_{3g} V_1 , used in our study is an update of that earlier version.

We also utilized a more reliable but shorter dataset from the Moderate Resolution Imaging Spectroradiometer (MODIS) aboard the NASA's Terra satellite (Yan et al., 2016a; Yan et al., 2016b). These data are well calibrated, cloud-screened and corrected for atmospheric effects, especially tropospheric aerosols. The sensor-platform is regularly adjusted to maintain a precise orbit. All algorithms, including the LAI algorithm, are physics-based, well-tested and currently producing sixth generation datasets. The dataset provides global and year-round LAI observations at 16-day (bi-monthly) temporal resolution and 1/20 degree spatial resolution from 2000 to 2016.

Leaf area index is defined as the one-sided green leaf area per unit ground area in broadleaf canopies and as one-half the green needle surface area in needleleaf canopies in both observational and CMIP5 simulation datasets. It is expressed in units of m^2 green leaf area per m^2 ground area. Leaf area changes can be represented either by changes in annual maximum LAI (LAI_{max}; Cook and Pau, 2013), or growing season average LAI. In this study, we use the former because of its ease and unambiguity, as the latter requires quantifying the start- and end-dates of the growing season, something that is difficult to do accurately in NHL (Park et al., 2016) with the low resolution model data. Further, LAI_{max}, is less influenced by cloudiness and noise; accordingly, it is most useful in investigations of long-term greening and browning trends. The drawback of LAI_{max}, is the saturation effect at high LAI values (Myneni et al., 2002). However, this is less of a problem in high latitudinal ecosystems which are less-densely vegetated compared to tropical regions, with LAI_{max}, values typically in the range of 2 to 3.

The bi-monthly satellite datasets were merged to a monthly temporal resolution by averaging the two composites in the same month and bi-linearly remapped to the resolution of the applied reanalysis product ($0.5^\circ \times 0.5^\circ$, CRU TS4.01).

2.2 *Environmental driver variables*

We use time series of temperature and CO₂ to derive the observed historical forcing (Sect. 2.4) and climatologies of precipitation and temperature to calculate climatic regimes (Fig. 2). Monthly averages of near-surface air temperature and precipitation are from the latest version of the Climatic Research Unit Timeseries dataset (CRU TS4.01). The global data are gridded to $0.5^\circ \times 0.5^\circ$ resolution (Harris et al., 2014). Global monthly means of atmospheric CO₂ concentration are from the GLOBALVIEW-CO₂ product ([obspack_co2_1_GLOBALVIEWplus_v2.1_2016_09_02](https://doi.org/10.25925/20190520); for details see <https://doi.org/10.25925/20190520>) provided by the National Oceanic and Atmospheric Administration / Earth System Research Laboratory (NOAA / ESRL).

2.3 *Earth system model simulations*

We analyzed recent climate-carbon simulations of seven ESMs participating in the fifth phase of the Coupled Model Intercomparison Project, CMIP (Taylor et al., 2012). The model simulated data were obtained from the Earth System Grid Federation, ESGF (<https://esgf-data.dkrz.de/projects/esgf-dkrz/>). Seven ESMs provide output for the variables of interest (GPP, CO₂, LAI, and near-surface air temperature) for simulations titled esmHistorical, RCP4.5, RCP8.5, 1pctCO₂, esmFixClim1, and esmFdbk1. It is the same set of models analyzed in Wenzel et al. (2016) and Winkler et al. (2019). The individual model setups and components are illustrated in more detail in various studies, such as Arora et al., 2013; Wenzel et al., 2014; Mahowald et al., 2016; Winkler et al., 2019.

The esmHistorical simulation spanned the period 1850 to 2005 and was driven by observed conditions such as solar forcing, emissions or concentrations of short-lived species and natural and anthropogenic aerosols or their precursors, land use, anthropogenic as well as volcanic influences on atmospheric composition. The models are forced by prescribed anthropogenic CO₂ emissions, rather than atmospheric CO₂ concentrations.

Several Representative Concentration Pathways (RCPs) have been formulated describing different trajectories of greenhouse gas emissions, air pollutant production and land use changes for the 21st century. These scenarios have been designed based on projections of human population growth, technological advancement and societal responses (Vuuren et al., 2011; Taylor et al., 2012). We analyzed simulations forced with specified concentrations of a high emissions scenario (RCP8.5) and a medium mitigation scenario (RCP4.5) reaching a radiative forcing level of 8.5 and 4.5 W m⁻² at the end of the century, respectively. These simulations were initialized with the final state at the end of the historical runs and spanned the period 2006 to 2100.

1pctCO₂ is an idealized fully coupled carbon-climate simulation initialized from a steady state of the pre-industrial control run and atmospheric CO₂ concentration prescribed to

increase $1\% \text{ yr}^{-1}$ until quadrupling of the pre-industrial level. The simulations `esmFixClim` and `esmFdbk` aim to disentangle the two carbon cycle feedbacks in response to rising CO_2 analogous to the `1pctCO2` setup: In `esmFixClim` CO_2 -induced climate change is suppressed (i.e. radiation transfer model sees constant pre-industrial CO_2 level), while the carbon cycle responds to increasing CO_2 concentration (*vice versa* for `esmFdbk`; Taylor et al., 2009; Taylor et al., 2012; Arora et al., 2013).

2.4 Estimation of greening sensitivities

We largely follow the methodology detailed in Winkler et al. (2019). For both model and observational data, the two-dimensional global fields of LAI and the driver variables are cropped according to different classification schemes (namely, climatic regimes, latitudinal bands and vegetation classes; Olson et al., 2001; Fritz et al., 2015). The aggregated values are area-weighted, averaged in space, and temporally reduced to annual estimates dependent on the variable: annual maximum LAI, annual average atmospheric CO_2 concentration, and growing degree days (GDDo, yearly accumulated temperature of days where near-surface air temperature $> 0^\circ \text{ C}$).

We use a standard linear regression model to derive the historical greening sensitivities in models and observations alike (for details see the Methods section *Estimation of historical LAI_{max} sensitivity* in Winkler et al., 2019). On the global scale, LAI_{max} is assumed to be a linear function of atmospheric CO_2 concentration. For the temperature-limited high northern latitudes, we also have to account for warming and include temperature as an additional driver. We do this using GDDo. Through a principal component analysis (PCA) of CO_2 and GDDo we avoid redundancy from co-linearity between the two driver variables, but retain their underlying time-trend and interannual variability (for details see the Methods section *Dimension reduction using principal component analysis* in Winkler et al., 2019). In particular, the PCA is performed on large-scale aggregated values as well as on pixel level to investigate on spatial variations. We only retain the first principal component (denoted ω), which explains a large fraction of the variance in models and observations (for more details see Supplementary Table 1 in Winkler et al., 2019). Figure A1 depicts the temporal development of CO_2 and GDDo as well as their principal component ω for observations. For the NHL, LAI_{max} is then formulated as a linear function of the proxy driver time series ω (Winkler et al., 2019). The best-fit gradients and associated standard errors of the linear regression model represent the LAI_{max} sensitivities, or greening sensitivities, and their uncertainty estimates, respectively.

3 RESULTS AND DISCUSSION

There are two parts to the EC methodology (Fig. 1) – a statistically robust relationship between modeled matching pairs of predictor-predictand values and an observed value of the predictor. The predictors are from a representative historical period. The predictands are modeled changes in a variable of interest at another forcing state of the system (e.g. potential future). The projection of the observed predictor on the modeled relation yields a constrained value of the predictand. A causal basis has to buttress the predictor-predictand relationship, else the EC method may be spurious. For example, meaningful coupling between concurrent changes in GPP and LAI_{max} with increasing atmospheric CO_2 concentration underpins our specific case study in the NHL, i.e. some of the enhanced GPP due to rising CO_2 concentration is invested in additional green leaves by plants (Myneni et al., 1997b; Forkel et al., 2016; Zhu et al., 2016; Mao et al., 2016; Winkler et al., 2019). Supplementary Figure 1 in Winkler et al. (2019) illustrates the specifics of the causal link underlying this predictor-predictand relationship. This tight coupling assures an approximately constant ratio of predictand to predictor across the models within the ensemble, thus setting up the potential for deriving an EC estimate. Uncertainty in the constrained estimate depends on the observed predictor and modeled relationship, aside from the goodness-of-fit of the latter (Fig. 1). These are detailed below.

3.1 *Uncertainty in Observed Predictor Due to Data Source*

We investigate observational uncertainty using LAI data from two different sources, AVHRR (1/12 degree) and MODIS (1/20 degree), and spatially aggregating these over broad vegetation classes, latitudinal bands and climatic regimes. The observed large-scale LAI_{max} sensitivities to CO_2 forcing are always positive (greening), irrespective of the source data and the method of aggregation (Fig. 2, Tab. 1). Overall, MODIS based estimates have higher uncertainty because of the shorter length of the data record (17 years). The failure to reliably estimate sensitivities in tropical forests (also in the latitudinal band $30^\circ S - 30^\circ N$, and in hot, wet and humid climatic regimes, see Tab. 1 and Fig. 2) is due to saturation of optical remote sensing data over dense vegetation ($LAI_{max} > 5$) and problems associated with high aerosol content and ubiquitous cloudiness. In other regions, the estimated sensitivities are comparable across sensors and aggregation schemes, in particular in the high latitudinal band ($> 60^\circ N/S$; AVHRR: $[3.4 \pm 0.5] \times 10^{-3}$, MODIS: $[3.6 \pm 0.9] \times 10^{-3} m^2 m^{-2} ppm^{-1} CO_2$). This aligns with previous studies reporting a net increase in green leaf area across the high latitudes during the observational period (Myneni et al., 1997a; Zhu et al., 2016; Forkel et al., 2016).

This analysis illustrates the applicability and limitations of using observed greening sensitivities to CO_2 forcing as a constraint on photosynthetic production. For example, data from both AVHRR and MODIS sensors provide a comparable estimate of greening sensitivity in the colder high latitudes (boreal forests and tundra vegetation classes; Winkler et al., 2019). In the lower latitudes, however, the discrepancies among the two sensors indicate a considerable observational uncertainty and thus no robust estimation of the observed predictor is possible.

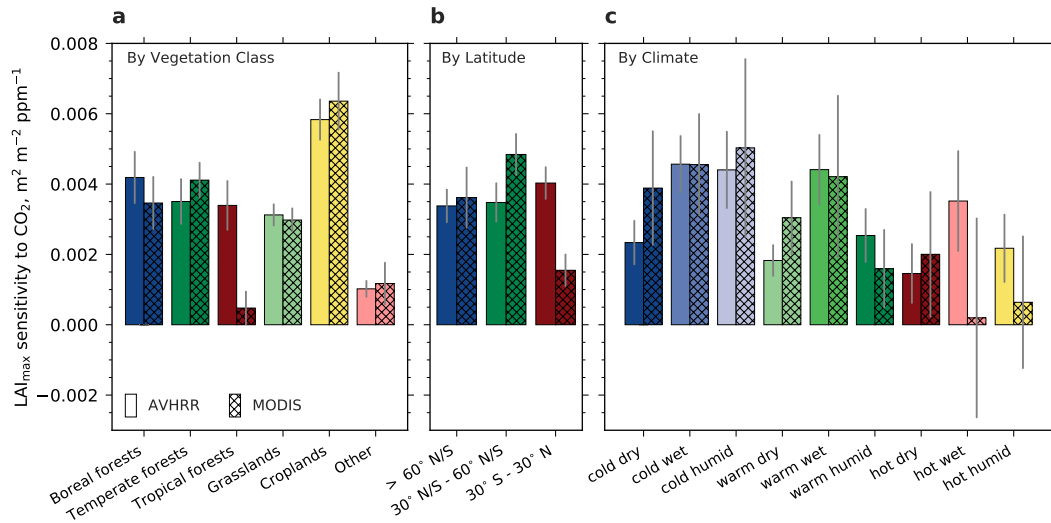


Figure 2 | Bar charts showing regression slopes of LAI_{max} against atmospheric CO₂ concentration for broad vegetation classes (a; Olson et al., 2001; Fritz et al., 2015), latitudinal bands (b) and climate regimes (c). The class "Other" includes deserts, mangroves, barren and urban land, snow and ice, and permanent wetlands. The climatic boundaries are defined as follows - cold: < 10°C; warm: > 10°C & < 25°C; hot: > 25°C; dry: < 500 mm a⁻¹; wet: > 500 mm a⁻¹ & < 1000 mm a⁻¹; humid: > 1000 mm a⁻¹. Sensitivities evaluated from data from two satellite-borne sensors are shown, AVHRR (1982 – 2016; Pinzon and Tucker, 2014) and MODIS (2000 – 2016; Yan et al., 2016a; Yan et al., 2016b). Grey bars indicate the standard error of the best linear fit.

3.2 Uncertainty Due to Spatial Aggregation

We focus further analyses on the NHL region (> 60° N; Fig. 2b), because of two reasons. First, the direct human impact (i.e. land management) can be neglected in the high latitudes, thus, we can assume that the observed changes reflect the response of natural ecosystems. Second, the observational evidence of an increased plant productivity in the recent decades is well established (e.g. Keeling et al., 1996; Myneni et al., 1997b; Graven et al., 2013; Forkel et al., 2016; Wenzel et al., 2016, and Sect. 3.1) – an important requisite in defining a robust predictor.

In addition to the physiological effect of CO₂, warming also plays a key role in controlling plant productivity of the NHL temperature-limited ecosystems, and thus, vegetation greenness. To avoid redundancy from co-linearity between CO₂ and GDDo, we reduce dimensionality by performing a principal component analysis of the two driver variables (Sect. 2.4). The resulting first principal component explains most of the variance and retains the trend and year-to-year fluctuations in both CO₂ and GDDo. Therefore, we obtain a proxy driver (hereafter denoted ω) that represents the overall forcing signal causing observed vegetation greenness changes in NHL (Fig. A1). Accordingly, greening sensitivity for the entire NHL area is derived as response to ω , the combined forcing signal of rising CO₂ and warming. This procedure also enables a better comparability between

observations and models because varying strengths of physiological and radiative effects of CO₂ among models are taken into account (Sect. 3.3 – 3.5).

The vegetated landscape in the NHL region is heterogeneous, with boreal forests in the south, vast tundra grasslands to the north and shrublands in-between. The species within each of these broad vegetation classes respond differently to changes in key environmental factors. Even within a species, such responses might vary due to different boundary conditions, such as topography, soil fertility, micrometeorological conditions, etc. How this fine scale variation in greening sensitivity impacts the aggregated value is assessed below.

The distribution of greening sensitivities from all NHL pixels is slightly skewed towards the positive (blue histogram). The mean value of this distribution (blue dashed line) is comparable to the sensitivity estimate derived from the spatially-averaged NHL time series (yellow dashed line; Fig. 3). Based on the Mann-Kendall test ($p > 0.1$), nearly over half the pixels (54%) show positive statistically significant trends (greening), while about 10% show browning trends (possibly due to disturbances; Goetz et al., 2005). The distribution of these statistically significant sensitivities (red histogram) therefore has two modes, a weak browning and a dominant greening mode, resulting in a substantially higher mean value (red dashed line) in comparison to the spatially-averaged estimate (yellow dashed line; Fig. 3). Thus, by taking into account the remaining 36% of non-significantly changing pixels (as in the NHL spatially-averaged estimate), an additional source of uncertainty is possibly introduced. The mean sensitivity value is, of course, higher when only pixels showing a greening trend are considered in the analysis (green dashed line; Fig. 3). These are the only areas in NHL that actually show a large increase in plant productivity and consequently significant changes in leaf area.

Model output of several ESMs (CMIP5) reveal similar pixel-level variation in both the predictor (LAI_{max} to ω , historical simulation; Sect. 2.3) and associated changes in the predictand (GPP, 1pctCO₂; Sect. 2.3), although ESMs operate on much coarser resolution (Fig. A2; see also Anav et al., 2013; Anav et al., 2015). Due to the coupling of the predictor and predictand, the distribution of pixels with significant changes is approximately the same for the two variables (Fig. A2). Accordingly, averaging the equally distributed estimates likely does not affect the predictor-predictand relationship in the model ensemble (Fig. 1). Consequently, if all spatial gridded data arrays are consistently processed to spatially-aggregated estimates, each predictand and predictor (observed and modeled) estimate contain a coherent component of spatial variations. In other words, considering browning and non-significant pixels results in a lower overall LAI_{max} sensitivity in NHL, which in turn leads to a lower constrained estimate of Δ GPP in NHL. This is consistent with the underlying relationship between predictor and predictand. On a related note, Bracegirdle and Stephenson (2012a) suggest that this source of error is not significantly dependent on the spatial resolution when comparing model subsets from high to low resolution.

The above analysis informs that spatially-averaged estimates are approximations containing a random error component due to inclusion of data from insignificantly changing pixels and a systematic bias component from pixels of reversed sign. This uncertainty is relevant to the EC method, where the observed sensitivity decisively determines the constrained estimate from the ensemble of ESM projections (Kwiatkowski et al., 2017; Winkler et al., 2019). However, if spatial variations are treated consistently as an inherent component

Table 1 | Coefficients of determination (R^2) of LAI_{max} sensitivity to CO_2 for different large-scale aggregated regions. Data are from two optical remote sensors of different time length, AVHRR (1982 – 2016) and MODIS (2000 – 2016). Asterisks denote non-significant values: ** $p > 0.1$; * $p > 0.05$.

Correlation coefficient R^2	AVHRR	MODIS
Biomes		
Boreal forests	0.49	0.58
Temperate forests	0.47	0.81
Tropical forests	0.41	0.06**
Graslands	0.75	0.83
Croplands	0.75	0.8
Other	0.35	0.2*
Latitudinal Bands		
> 60° N/S	0.51	0.61
30° N/S – 60° N/S	0.67	0.83
30° S – 30° N	0.65	0.26
Climate Space		
cold dry	0.29	0.27
cold wet	0.49	0.4
cold humid	0.33	0.21*
warm dry	0.33	0.36
warm wet	0.37	0.18*
warm humid	0.25	0.12**
hot dry	0.08*	0.08**
hot wet	0.15	0.00**
hot humid	0.13	0.01**

of observations and models, the EC method is only slightly susceptible to this source of uncertainty.

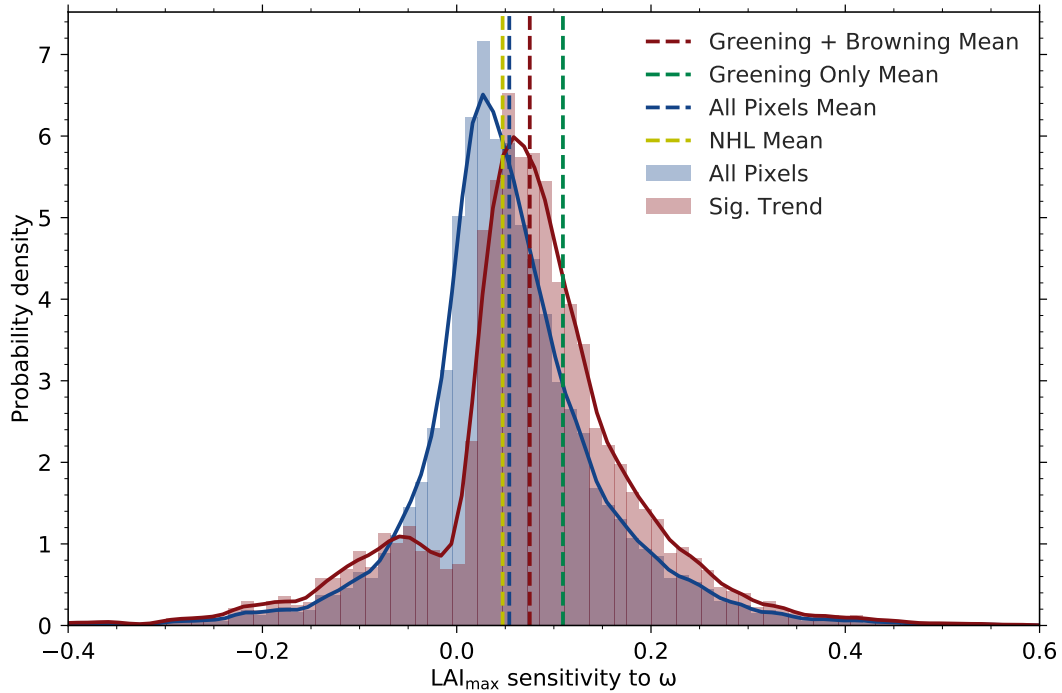


Figure 3 | Histograms and associated probability density functions (Gaussian kernel density estimation) of observed LAI_{max} sensitivity to ω at pixel scale for the northern high latitudinal band (> 60° N, data from AVHRR sensor). Blue color depicts the distribution of LAI_{max} sensitivities of all pixels and the red color for pixels with statistically significant (Mann-Kendall test, $p < 0.1$) greening or browning trends (the dashed lines denote the respective mean value). The green dashed line shows the mean value of ‘greening’ pixels only, whereas the yellow dashed line shows the LAI_{max} sensitivity to ω for the entire northern high latitudinal belt.

3.3 Uncertainty Due to Temporal Variations

We seek recourse to longterm CMIP5 ESM simulations covering the historical period 1850 to 2005 (Sect. 2.3) to assess temporal variation in the predictor variable, because of the shortness of observational record. Three representative models (CESM1-BGC, MIROC-ESM, and HadGEM2-ES) spanning the full range of NHL greening sensitivities in the CMIP5 ensemble (Winkler et al., 2019) are selected for this analysis. For each model, LAI_{max} sensitivity to ω in moving windows of different lengths are evaluated (15, 30, and 45 years; Fig. 4 and A3). The analysis reveals two crucial aspects that highlight how temporal variations impair comparability of the predictor variable between models and observations – an essential component of the EC approach.

First, window locations of modeled and observed predictor variable have to match. If the forcing in the simulations is low, for example, as in the second half of the 19th century when CO₂ concentration was increasing slowly, inter-annual variability dominates and LAI_{max} sensitivity cannot be accurately estimated irrespective of the window length (Fig. 4 and A3). With increasing forcing over time (rising yearly rate of CO₂ emissions, and consequently, the concentration), the signal-to-noise ratio increases and LAI_{max} sensitivity to ω estimation stabilizes, for example, as in the second half of the 20th century. Therefore, LAI_{max} sensitivities estimated at different temporal locations result in non-comparable values and eventually a false constrained estimate (details in Sect. 3.4). As an example, modeled sensitivities based on a 30-year window centered on year 1900, when CO₂ level increased by 10 ppm, and observed sensitivity estimated from a 30-year window centered on year 2000, when CO₂ level increased by 55 ppm, describe different states of the system and therefore should not be contrasted in the EC method.

Second, in addition to temporal location, also window lengths have to match between observations and models. For all three models, sensitivities estimated from 15-year chunks show high variability and thus, a 15-year record is perhaps too short to obtain robust estimates. The LAI_{max} sensitivity estimation becomes more stable with strengthening forcing and increasing window length (Fig. 4 and A3). As a consequence, using short-term observed sensitivity as a constraint on long-term model projections results in an incorrect EC estimate. Hence, the MODIS sensor record is, on the one hand, too short and does not, on the other hand, overlap temporally with the historical CMIP5 forcing. Therefore, it does not provide a robust predictor in this EC study.

3.4 Level and Time Rate of CO₂ Forcing

The EC method raises an obvious question – does it not implicitly assume that the key operative mechanisms underpinning the EC relation remain unchanged because a future system state is being predicted based on its past behavior? To be specific, we are attempting to predict GPP at a future point in time based on greening sensitivity inferred from the past. Does this not require the assumption that the key underlying relationship which makes this prediction possible, namely, a robust coupling between contemporaneous changes in GPP and LAI_{max} remains unchanged from the past to the future? To address this question, we resort to the CMIP5 idealized simulation (1pctCO₂), where atmospheric CO₂ concentration increases 1% annually, starting from a pre-industrial level of 284 ppm until a quadruple of this value is reached (Sect. 2.3). We limit the analysis to the three models (CESM1-BGC, MIROC-ESM, and HadGEM2-ES) which bracket the full range of GPP enhancement and LAI_{max} sensitivity in the original seven ESM ensemble (Winkler et al., 2019).

The relationship between simultaneous changes in GPP and LAI_{max} remains linear for all CMIP5 models in the range 1×CO₂ to 2×CO₂ (Fig. 5 and A4, Tab. 2). With concentration increasing beyond 2×CO₂, all models show weakening correlation (R^2 , Tab. 2) and decreasing slope (b , Tab. 2) of this relationship (Fig. 5 and A4), suggesting a saturating rate of allocation of additional GPP to new leaves at higher levels of CO₂. Consequently, LAI_{max} sensitivity to increasing CO₂ and associated warming decreases. At and over 4×CO₂ (1140 ppm), a level unlikely to be seen in the near future, there appears to be no relationship between Δ GPP and Δ LAI_{max} in some models. This raises the question as

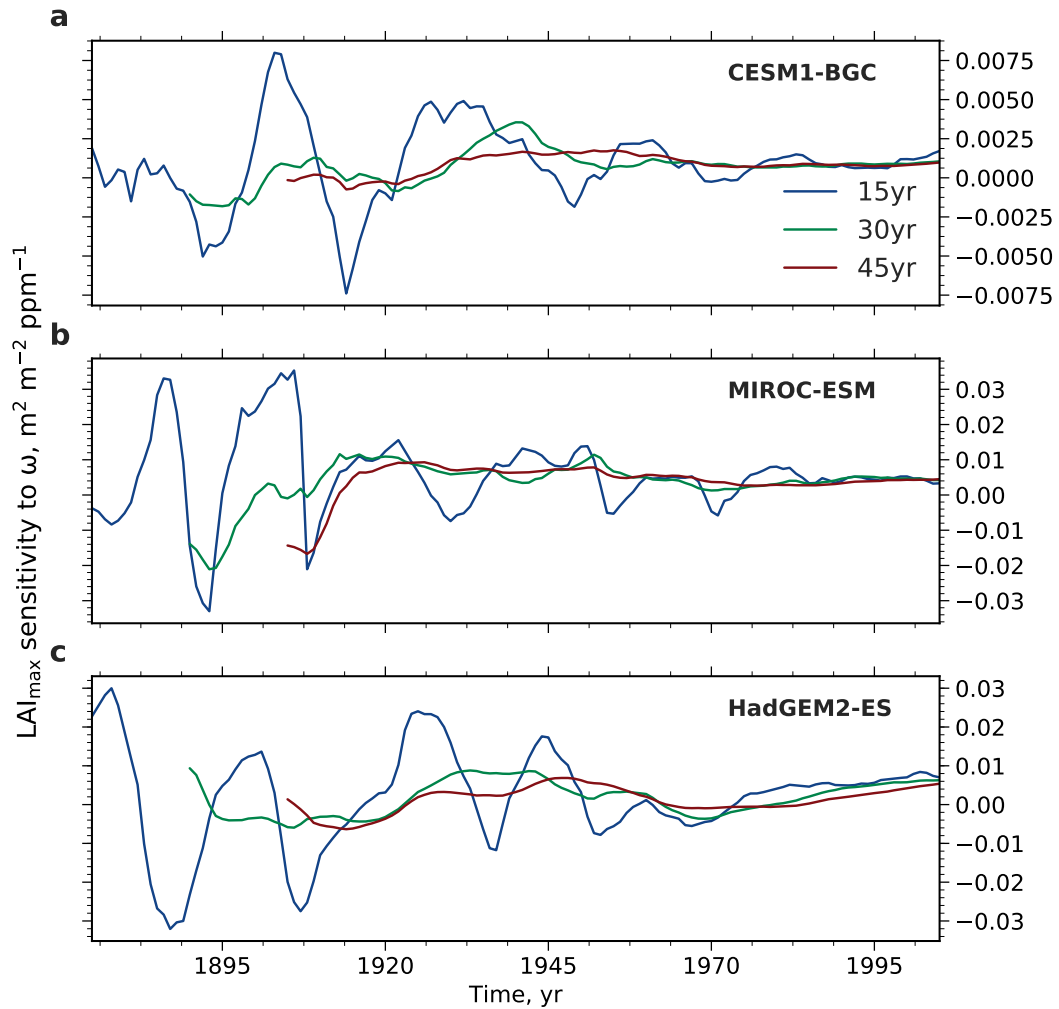


Figure 4 | Temporal variation of LAI_{max} sensitivity to ω in three selected CMIP5 models spanning the full range from low (CESM1-BGC, a), to closest-to-observations (MIROC-ESM, b), to high-end (HadGEM2-ES, c). The colored lines show LAI_{max} sensitivity variations for moving windows of varying length of 15 (blue), 30 (green), and 45 (red) years over the historical period from 1860 to 2005.

to what extent does the weakening of the relationship between the predictor and predictand in each model at higher CO₂ concentrations affect the EC analysis (Fig. 1). To shed light on this matter, we perform the following thought experiment.

Understanding the relationship and interplay between forcing (increasing CO₂ concentration), predictor (LAI_{max} sensitivity), and the predictand (Δ GPP) is key to evaluating the EC method. We conceive four possible scenarios of how the system might behave with increasing forcing. For simplicity, we assume linearly increasing CO₂ concentration, LAI represents LAI_{max}, and GPP refers to its annual value below (Fig. 6). The four scenarios are: *All linear*, *all non-linear* (saturation), and two *mixed linear / non-linear* cases (Tab. A1). We emulate a multi-model ensemble by applying different random parameterizations for the linear and saturation (the hyperbolic tangent function) responses of GPP to CO₂ and of LAI to GPP. One of these realizations is assumed to represent pseudo-observations (dashed lines, Fig. 6). We discuss one case in detail for illustrative purposes (No. 3, Tab. A1).

In scenario 3, Δ GPP increases linearly with increasing CO₂ (Fig. 6a), while Δ LAI/ Δ GPP saturates (Fig. 6b). The LAI sensitivity to CO₂ weakens with increasing forcing (Fig. 6c) as a response to saturation of GPP allocation to leaf area. We derive LAI sensitivities to CO₂ for three different periods ('past periods' in Fig. 6c) to constrain Δ GPP at a much higher CO₂ level ('projected period' in Fig. 6a). Next, we apply the EC method on these pseudo-projections of Δ GPP relying on LAI sensitivities derived from the three past periods (Fig. 6d). The EC method is applicable even at a low forcing level (past period 1) in this simplified scenario because we neglect stochastic internal variability of the system. The slope of emergent linear relationship increases (Fig. 6d) as modeled LAI sensitivities decrease with rising CO₂ concentration (Fig. 6c). The observational constraint on future Δ GPP, however, remains nearly the same, because pseudo-observed LAI sensitivity also weakens at higher CO₂ levels (dashed lines, Fig. 6c, d). Thus, the three EC estimates of Δ GPP are approximately identical (Fig. 6d) and independent of the forcing level during past periods. With intensified forcing, the relationship between predictor and predictand remains linear within the model ensemble, although their relationship becomes non-linear within each model and, crucially, in reality as well. In other words, as long as the models agree on the occurrence and strength of saturation for given forcing, i.e. the dynamics of the system, the inter-model variations of predictor and predictand relate linearly within the ensemble (Fig. 6). The same behavior is also seen in the other three scenarios (Tab. A1; Fig. A5, A6).

Nevertheless, with ever increasing forcing and associated steepening of the emergent linear relationship, the LAI sensitivity loses its explanatory power at some point because the linear relationship eventually lies within the observational uncertainty and no meaningful constraint can be derived. This and disagreement between models on system dynamics are ultimate limits of the EC method. Interestingly, we find that all CMIP5 models agree on the occurrence of saturation, but slightly disagree on the strength of saturation for given CO₂ forcing (Fig. 5, A4, and Tab. 2). Further, we find that the 'all non-linear' scenario best describes the dynamics of the system in the forcing range from 1 \times CO₂ to 4 \times CO₂. However, the saturation of LAI to GPP happens at a lower CO₂ level than saturation of GPP to CO₂. Still, inferences from interpretation of Case 3 (Fig. 6) are equally applicable.

Results from the above thought experiment also highlight the importance of matching window locations and lengths between models and observations, as discussed earlier (Sect.

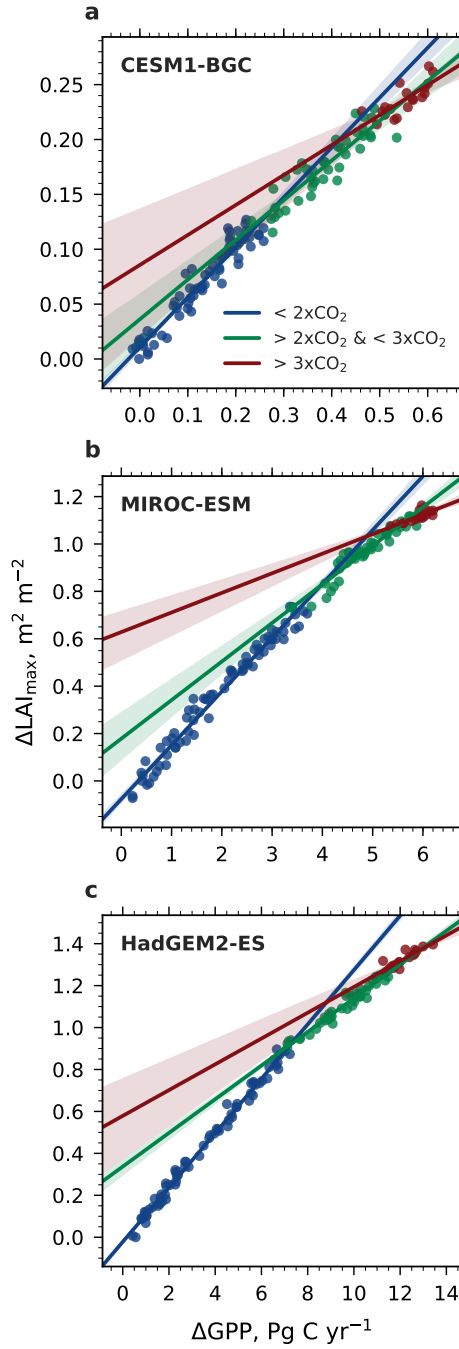


Figure 5 | Correlation of $\Delta\text{LAI}_{\text{max}}$ and ΔGPP with increasing CO₂ forcing, starting from a pre-industrial concentration of 280 ppm ($1\times\text{CO}_2$) to $4\times\text{CO}_2$ (CMIP5 1pctCO₂ simulations). Results are shown for three selected CMIP5 models spanning the full range of LAI_{max} sensitivity to ω , low-end: CESM1-BGC (a), closest-to-observations: MIROC-ESM (b), and high-end: HadGEM2-ES (c). Blue colored dots show the relation between $1\times\text{CO}_2$ and $2\times\text{CO}_2$, green colored dots between $2\times\text{CO}_2$ and $3\times\text{CO}_2$, and red colored dots between $3\times\text{CO}_2$ and $4\times\text{CO}_2$. The respective colored lines represent the best linear fit through those dots and the shading represents the 95% confidence interval.

3.3). For instance, taking LAI sensitivity from past period 2 (green dashed line, Fig. 6d) as an observational constraint on the multi-model linear relationship based on past period 3 (red solid line, Fig. 6d), results in a significant overestimation of constrained Δ GPP (intersection of the two lines, Fig. 6d).

The above analysis informs that the constrained GPP estimate at one future period (e.g. $2\times\text{CO}_2$) is nearly independent of the past periods from when the observational sensitivities are derived. Now, we evaluate the EC method where sensitivity from one past period is used to obtain constrained GPP estimates at different periods in a potential future, i.e. progressively farther down the time-line of a CO₂-enriched world. We utilize the greening sensitivity derived from 35 years of observed LAI_{max} data (AVHRR, Sect. 2.1) and apply the EC method to CMIP5 1pctCO₂ simulations. The sensitivities in this case are due to forcing from both CO₂ increase and associated warming during the observational period (Sect. 2.4). We seek constrained GPP estimates for the NHL at different CO₂ levels ($2\times\text{CO}_2$, $3\times\text{CO}_2$, and $4\times\text{CO}_2$).

Table 2 | Slopes (b) and coefficients of determination (R^2) for regression between changes of LAI_{max} against changes in annual mean GPP for the NHL at different atmospheric CO₂ levels in all available CMIP5 models (1pctCO₂ simulation). Asterisks denote non-significant values: ** $p > 0.1$; * $p > 0.05$.

Correlation details	< $2\times\text{CO}_2$		> $2\times\text{CO}_2$ & < $3\times\text{CO}_2$		> $3\times\text{CO}_2$	
	b	R^2	b	R^2	b	R^2
MIROC-ESM	0.23	0.97	0.16	0.89	0.08	0.63
CESM1-BGC	0.45	0.93	0.36	0.82	0.27	0.62
GFDL-ESM2M	0.37	0.89	0.04	0.07**	0.01	0.12**
CanESM2	0.22	0.95	0.19	0.83	0.17	0.67
HadGEM2-ES	0.13	0.99	0.08	0.96	0.06	0.78
MPI-ESM-LR	0.13	0.94	0.09	0.78	0.04	0.51
NorESM1-ME	0.26	0.94	0.2	0.77	0.09	0.27

Winkler et al. (2019) previously reported a strong linear relationship between modeled contemporaneous changes in LAI_{max} and GPP arising from the combined radiative and physiological effects of CO₂ enrichment until $2\times\text{CO}_2$ in the CMIP5 ensemble. As a result, models with low LAI_{max} sensitivity to ω project lower Δ GPP for a given increment of CO₂ concentration, and *vice versa*. Thus, the large variation in modeled historical LAI_{max} sensitivities linearly maps to variation in Δ GPP at $2\times\text{CO}_2$ (Winkler et al., 2019, blue line, Fig. 7a). At higher levels, such as $3\times\text{CO}_2$ (green line, $R^2 = 0.93$) and $4\times\text{CO}_2$ (red line, $R^2 = 0.88$), this linear relationship within the model ensemble, while still present, weakens (Fig. 7a; Tab. 3). This is because the CMIP5 models do not agree on the strength of the saturation effect at higher CO₂ levels (Fig. 5 and A4). The increment in constrained GPP estimates for successive equal increments of CO₂ decreases due to the saturation effect in all CMIP5 models (dashed horizontal lines, Fig. 7a). For example, the change in GPP

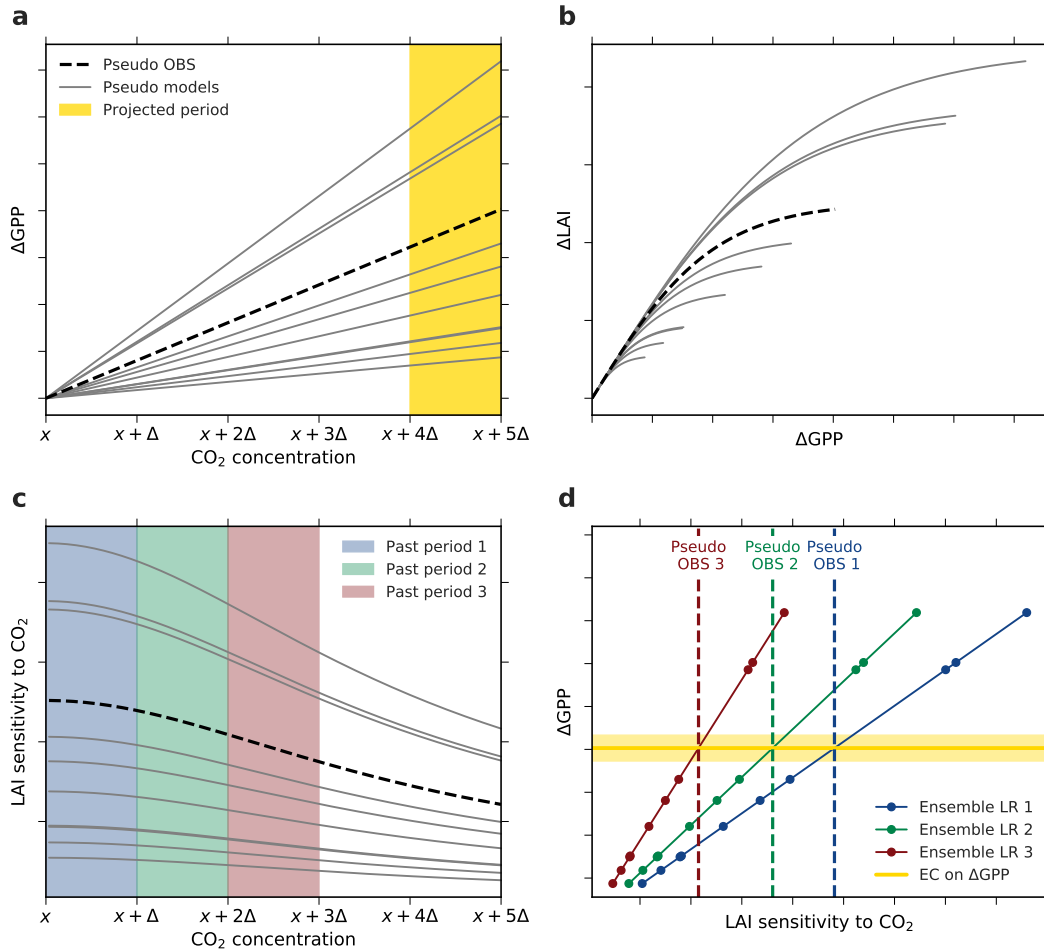


Figure 6 | Thought experiment to examine the applicability of EC analysis under the assumption of an idealized linear / non-linear behavior of the system (Case 3, Table A1). **a**, Changes in GPP relate linearly to changes in CO_2 concentration. The yellow band marks the projection period of interest, i.e. the period of CO_2 concentration from $x + 4\Delta$ to $x + 5\Delta$. **b**, The increment in LAI with increasing GPP is assumed to decrease with rising CO_2 concentration (described by a hyperbolic tangent function). The parameterization in the linear and non-linear functions for pseudo observations (dashed black line) as well as models (solid grey lines) are determined randomly for each model. **c**, The diagnostic variable, LAI sensitivity to CO_2 , is decreasing with increasing CO_2 as a consequence of the non-linear relation between ΔGPP and ΔLAI . The colored bands indicate three 'past' periods from x to $x + \Delta$ (blue), $x + \Delta$ to $x + 2\Delta$ (green), and $x + 2\Delta$ to $x + 3\Delta$ (red). **d**, Linear relationships among the pseudo model ensembles (Ensemble LR, colored lines) between LAI sensitivities to CO_2 of the three past periods and ΔGPP from the projected period. Colored dots mark different models and the dashed lines represent associated pseudo observations for the respective historical period. Yellow solid line depicts the constant EC on projected ΔGPP irrespective of the past period.

between $3\times\text{CO}_2$ and $4\times\text{CO}_2$ ($\Delta\text{GPP} \sim 1.06 \text{ Pg C yr}^{-1}$, Tab. 3) is much lower than between $2\times\text{CO}_2$ and $3\times\text{CO}_2$ ($\Delta\text{GPP} \sim 2.34 \text{ Pg C yr}^{-1}$, Tab. 3).

We have thus far focused on the magnitude of CO₂ concentration change and not on the time rate of this change. For example, a given amount of change in CO₂ concentration, say 200 ppm, can be realized over different time periods, say over a 100 or 150 years. The problem of varying rates of CO₂ concentration change is implicitly encountered when ESMs are executed under different forcing scenarios, such as RCPs (Sect. 2.3). A question then arises whether the constrained predictand estimate is independent of the time rate of CO₂ concentration change and dependent only on the magnitude of CO₂ concentration change. To investigate this aspect of forcing, we extract GPP estimates at the same CO₂ concentration (535 ppm; final concentration in RCP4.5) from three simulations of different forcing rates and calculate the difference relative to a common initial CO₂ concentration (380 ppm; initial concentration of RCP scenarios). Hence, the magnitude of the forcing is the same but applied over different durations (RCP4.5: $\sim 90\text{yr}$, RCP8.5: $\sim 45\text{yr}$, and 1pctCO₂: $\sim 30\text{yr}$). A clear majority of the CMIP5 models show substantial differences in ΔGPP between the different pathways of CO₂ forcing. In general, GPP changes are higher for lower time rates of CO₂ forcing, i.e. forcing over longer time periods. As a consequence, the EC estimates of ΔGPP for the same increase in CO₂ concentration are scenario-dependent (Fig. 7b; Tab. 3) – a counter-intuitive result. For instance, in the RCP4.5 scenario (which is characterized by a lower rate of CO₂ increase) an increment of 155 ppm CO₂ yields a GPP enhancement of $\sim 2.84 \text{ Pg C yr}^{-1}$ (see Tab. 3). This GPP enhancement is $\sim 39\%$ and $\sim 20\%$ larger than in the 1pctCO₂ run ($\sim 2.05 \text{ Pg C yr}^{-1}$, Tab. 3) and the RCP8.5 ($\sim 2.38 \text{ Pg C yr}^{-1}$, Tab. 3) scenario, respectively, for the same total increase in CO₂ concentration. Both these scenarios are characterized by a faster rate of CO₂ increase than RCP4.5. This analysis suggests that the vegetation response to rising CO₂ is pathway dependent, at least in the NHL. One of the reasons for this could be species compositional changes in scenarios of low forcing rates, i.e. over longer time frames. This novel result, however, requires a separate in-depth study.

3.5 Effects of CO₂ Forcing

Higher concentration of CO₂ in the atmosphere stimulates plant productivity through the fertilization and radiative effects (Nemani et al., 2003; Leakey et al., 2009; Arora et al., 2011; Goll et al., 2017). The two effects can be disentangled in the model world by conducting simulations in a ‘CO₂ fertilization effect only’ (esmFixClim1) and a ‘radiative effect only’ (esmFdbk1) setup (Sect. 2.3). These are termed below as idealized model simulations. We investigate here whether historical runs and observations, which include both effects, can be used to constrain GPP changes in idealized CMIP5 simulations (e.g. as in Wenzel et al., 2016).

We find strong linear relationships between historical LAI_{max} sensitivity and ΔGPP for $2\times\text{CO}_2$ in both idealized setups (esmFixClim1: $R^2 = 0.92$, esmFdbk1: $R^2 = 0.98$, Tab. 3, Fig. 7c). Consequently, this linear relationship is also pronounced for calculated sums of both effects for each model (esmFixClim1 + esmFdbk1: $R^2 = 0.95$, Tab. 3, Fig. 7c). This suggests that the two effects act additively on plant productivity and, thus, each effect can be simply expressed in terms of a scaling factor of the total GPP enhancement. Hence, the

application of the EC method on idealized simulations using real world observations is conceptually feasible.

Interestingly, the two effects contribute about the same to the general increase in GPP at $2\times\text{CO}_2$ (esmFixClim1: $\Delta\text{GPP} \sim 1.35 \text{ Pg C yr}^{-1}$, esmFdbk1: $\Delta\text{GPP} \sim 1.38 \text{ Pg C yr}^{-1}$, Tab. 3, Fig. 7c). At higher concentrations, such as $3\times\text{CO}_2$ and $4\times\text{CO}_2$, the enhancement in GPP saturates in both idealized setups. However, the radiative effect becomes dominant relative to the CO_2 fertilization effect when CO_2 concentration exceeds $2\times\text{CO}_2$ (e.g. at $4\times\text{CO}_2$ esmFixClim1: $\Delta\text{GPP} \sim 2.42 \text{ Pg C yr}^{-1}$, esmFdbk1: $\Delta\text{GPP} \sim 3.06 \text{ Pg C yr}^{-1}$, Tab. 3). Therefore, we can expect that at some point in the future, NHL photosynthetic carbon fixation will benefit more from climate change (e.g. warming) than from the fertilizing effect of CO_2 .

3.6 Uncertainties in the Multi-Model Ensemble

Besides methodological sources of uncertainty discussed above, the estimate of an EC may also be deficient due to inaccurate assumptions about the model ensemble. First, possible common systematic errors in a multi-model ensemble (i.e. the entire ensemble misses an unknown process, which plays a key role in a high CO_2 world) are implicitly omitted in the EC approach, however, could cause a general over- or underestimation of the constrained value (Bracegirdle and Stephenson, 2012b; Stephenson et al., 2012). Second, the set of forcing variables for historical simulations may be incomplete (i.e. not yet identified drivers of observed changes) and thus the comparability of observations and model simulations is limited (Flato et al., 2013). Third, the EC method can be overly sensitive to individual models of the ensemble, which has a bearing on the robustness of the constrained value (Bracegirdle and Stephenson, 2012b). Bracegirdle and Stephenson (2012b) proposed a diagnostic metric (Cook's distance) to test an ensemble for influential models. Fourth, the predictand-predictor relationship not only has to rely on a physical, but also on a logical connection within the model ensemble. For instance, Wenzel et al. (2016) established a linear relationship between relative changes in the predictand taking the initial state into account (changes in GPP for doubling of CO_2 relative to the initial pre-industrial state), and a predictor neglecting the initial state (historical sensitivity of CO_2 amplitude to rising CO_2). This statistical relationship can be spurious, because the model skill of simulating an accurate initial state and a plausible sensitivity to a forcing are not connected. These issues are to be contemplated when establishing an EC estimate and evaluating its robustness.

4 CONCLUSIONS

An in-depth analysis of the EC method is illustrated in this article through its application to projections of change in NHL photosynthesis under conditions of rising atmospheric CO_2 concentration. Key conclusions highlighting the functionality of the EC method are presented below.

The importance of how the observational predictor is obtained cannot be emphasized enough because the EC method is particularly sensitive to observational uncertainty. The single observational estimate essentially determines the EC, whereas the emergent linear

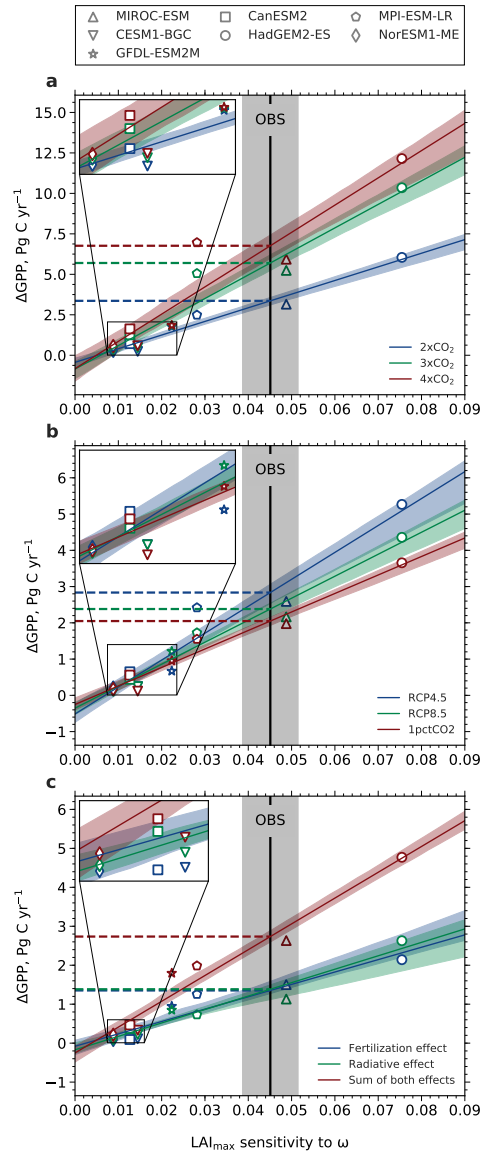


Figure 7 | Linear relationships between historical sensitivity of LAI_{max} to ω and absolute increase of GPP at different levels (a), different time-rates (b) as well as effects of rising CO₂ (c). The black solid line depicts the observational sensitivity including the standard error (grey shading). Each CMIP5 model is represented by a distinct marker (legend at the top). The colored lines show the best linear fits including the 68% confidence interval estimated by bootstrapping across the model ensemble. The colored dashed lines indicate the derived constraints on ΔGPP. a, Absolute changes in GPP at different levels of CO₂: 2×CO₂ (blue), 3×CO₂ (green), and 4×CO₂ (red). b, Absolute changes in GPP for rising CO₂ concentration from 380 to 535 ppm at different time-rates: RCP4.5 (90 yr, blue), RCP8.5 (45 yr, green), and 1pctCO₂ (30 yr, red). c, Absolute changes in GPP due to the two disentangled effects of CO₂ at 2×CO₂ in idealized simulations: Fertilization effect (esmFixClim1, blue), radiative effect (esmFdbk1, green), and the sum of both effects (red).

Table 3 | Coefficients of determination (R^2) of the emergent linear relationships in Figure 7 (asterisks denote non-significant values: ** $p > 0.1$; * $p > 0.05$). ECs on Δ GPP (upper and lower bound of uncertainty in square brackets) for different atmospheric CO_2 levels and fully-coupled as well as idealized setups. The rightmost column shows the increase of Δ GPP for an increment of $1 \times \text{CO}_2$. The lowermost section compares EC estimates of Δ GPP for equivalent changes in CO_2 concentration (CO_2 rises from 380 to 535 ppm), but for different time-rates.

	R^2	EC Δ GPP estimate (Pg C yr^{-1})	EC Δ GPP for $\Delta 1 \times \text{CO}_2$ (Pg C yr^{-1})
2xCO₂			
Fully coupled (1pctCO ₂)	0.96	3.36 [3.15, 3.56]	-
CO ₂ fertilization only (esmFixClim1)	0.88	1.35 [1.29, 1.62]	-
Radiative effect only (esmFdbk1)	0.94	1.38 [1.13, 1.51]	-
Sum of both effects (esmFixClim1 + esmFdbk1)	0.95	2.74 [2.6, 2.9]	-
3xCO₂			
Fully coupled (1pctCO ₂)	0.93	5.7 [5.26, 6.16]	2.34
CO ₂ fertilization only (esmFixClim1)	0.92	2.15 [2.02, 2.37]	0.79
Radiative effect only (esmFdbk1)	0.98	2.53 [2.3, 2.66]	1.15
Sum of both effects (esmFixClim1 + esmFdbk1)	0.96	4.68 [4.38, 4.97]	1.94
4xCO₂			
Fully coupled (1pctCO ₂)	0.88	6.76 [6.08, 7.53]	1.06
CO ₂ fertilization only (esmFixClim1)	0.88	2.42 [2.23, 2.74]	0.28
Radiative effect only (esmFdbk1)	0.97	3.06 [2.83, 3.2]	0.53
Sum of both effects (esmFixClim1 + esmFdbk1)	0.95	5.49 [5.09, 5.85]	0.81
380 – 535 ppm CO₂			
Slow increase in CO ₂ (RCP4.5)	0.93	2.84 [2.54, 3.08]	-
Medium-fast increase in CO ₂ (RCP8.5)	0.96	2.38 [2.18, 2.55]	-
Rapid increase in CO ₂ (1pctCO ₂)	0.96	2.05 [1.94, 2.16]	-

relationship is established based on a collection of multi-model estimates (each model gets 'one vote', however, some models might be more influential than others; Bracegirdle and Stephenson, 2012b). Hence, the observational uncertainty has a much larger bearing on the EC than the uncertainty of each individual model. To overcome this source of uncertainty, various meaningful observations should be taken into consideration when establishing the observed predictor.

Spatially aggregating observations and model output of different resolutions in the EC method constitutes another source of uncertainty. Predictors and predictands expressed as regional estimates (e.g. area-weighted mean of the NHL) are approximations of complex fine-scale processes. Aggregation will inevitably introduce a random error component due to inclusion of estimates from areas where the predictor is not changing or a systematic bias from areas where the predictor has a reversed sign. Thus, the spatially-aggregated variables are meaningful only if most of the region is in agreement about the response to CO₂ forcing (e.g. more than half of the NHL is greening with rising CO₂). However, we find that the source of uncertainty related to spatial aggregation is of minor importance as long as spatial variations in observations and models simulations are treated consistently.

A large source of uncertainty is associated with temporal variability of the predictor variable when comparing models and observations. Establishing a robust predictor requires evaluating temporal window lengths of sufficient duration (approximately 30 years) and their locations along the forcing time line. Both window length and location should match between models and observations in the EC method. For example, the analysis in Wenzel et al. (2016) might have yielded different results and conclusions if model and observational predictor sensitivities were temporally matched. We find that the relevance of window length decreases with increasing and accelerating forcing, depending on the magnitude of natural/internal variability (signal-to-noise ratio) of the predictor variable.

The level, effect and time-rate of applied CO₂ forcing can have a bearing on the linear relationship between the predictand and predictor variables (Fig. 1). In our case study, the relationship underpinning the EC method, namely, that between concurrent Δ GPP and Δ LAI_{max} changes non-linearly with increasing forcing level (i.e. saturation with rising CO₂ concentration). The EC method can still be applied, because the CMIP5 models agree on the non-linear behavior of the system. However, at very high CO₂ concentrations the models diverge and this relation breaks down, at which point the EC method fails. The two dominant effects of rising CO₂ concentration on vegetation, namely, the fertilization and radiative effects, appear to be approximately additive in terms of GPP enhancement to CO₂ forcing in the NHL. Therefore, the EC method can be applied to constrain estimates of GPP due to one or the other, or both the effects. The models, however, document a higher radiative effect than fertilization at concentrations exceeding $2\times$ CO₂. Another intriguing conclusion from our analysis is that the time-rate of forcing has an effect on GPP changes, that is, the projected GPP enhancement to CO₂ forcing seems to be dependent on how the forcing is applied over time, as in different scenarios or RCPs. This aspect is presently not well understood and requires further study.

The EC framework is widely promoted as observation-based evaluation tool for climate projections, especially in the context of the nascent CMIP6 ensemble (Eyring et al., 2019; Hall et al., 2019). Previous EC studies, however, exclusively focused on predictor-predictand combinations which exhibit so-called existent ECs (Hall et al., 2019), i.e. predictor and

predictand are found to relate linearly across the ensemble. In the context of ESM evaluation, non-existent ECs, i.e. predictor and predictand are found to be unrelated in the ensemble, are equally important. Since predictor and predictand variables are premised on our mechanistic process understanding, non-existent ECs reveal a fundamental disagreement on the system dynamics among the models. This study encourages to scrutinize these system dynamics in the predictor-predictand space and also report such non-existent, yet expected, ECs in order to advance model development and evaluation.

Across different disciplines each EC and its set of predictor and predictand are unique to some extent and require an individual detailed examination. In this article, we addressed general potential sources of uncertainty and limitations in the EC method by the means of a case study in carbon cycle research. Thus, the illustrated results are qualitatively transmissible to other sets of predictors and predictands and are generally relevant in Earth system sciences.

Code availability The code used in this study is available from the corresponding author upon request.

Data availability All data used in this study are available from public databases or literature, which can be found with the references provided in respective Methods section. Processed data is available from the corresponding author upon request.

REFERENCES

- Anav, A. et al. (2013). "Evaluating the Land and Ocean Components of the Global Carbon Cycle in the CMIP5 Earth System Models." *Journal of Climate* 26.18, pp. 6801–6843. DOI: [10.1175/JCLI-D-12-00417.1](https://doi.org/10.1175/JCLI-D-12-00417.1).
- Anav, A. et al. (2015). "Spatiotemporal Patterns of Terrestrial Gross Primary Production: A Review." *Reviews of Geophysics* 53, pp. 785–818. DOI: [10.1002/2015RG000483](https://doi.org/10.1002/2015RG000483).
- Arora, V. K. et al. (2011). "Carbon Emission Limits Required to Satisfy Future Representative Concentration Pathways of Greenhouse Gases." *Geophysical Research Letters* 38.5, p. L05805. DOI: [10.1029/2010GL046270](https://doi.org/10.1029/2010GL046270).
- Arora, V. K. et al. (2013). "Carbon–Concentration and Carbon–Climate Feedbacks in CMIP5 Earth System Models." *Journal of Climate* 26.15, pp. 5289–5314. DOI: [10.1175/JCLI-D-12-00494.1](https://doi.org/10.1175/JCLI-D-12-00494.1).
- Boé, J., A. Hall, and X. Qu (2009). "September Sea-Ice Cover in the Arctic Ocean Projected to Vanish by 2100." *Nature Geoscience* 2.5, pp. 341–343. DOI: [10.1038/ngeo467](https://doi.org/10.1038/ngeo467).
- Bracegirdle, T. J. and D. B. Stephenson (2012a). "Higher Precision Estimates of Regional Polar Warming by Ensemble Regression of Climate Model Projections." *Climate Dynamics* 39.12, pp. 2805–2821. DOI: [10.1007/s00382-012-1330-3](https://doi.org/10.1007/s00382-012-1330-3).
- (2012b). "On the Robustness of Emergent Constraints Used in Multimodel Climate Change Projections of Arctic Warming." *Journal of Climate* 26.2, pp. 669–678. DOI: [10.1175/JCLI-D-12-00537.1](https://doi.org/10.1175/JCLI-D-12-00537.1).
- Cook, B. I. and S. Pau (2013). "A Global Assessment of Long-Term Greening and Browning Trends in Pasture Lands Using the GIMMS LAI3g Dataset." *Remote Sensing* 5.5, pp. 2492–2512. DOI: [10.3390/rs5052492](https://doi.org/10.3390/rs5052492).
- Cox, P. M. et al. (2013). "Sensitivity of Tropical Carbon to Climate Change Constrained by Carbon Dioxide Variability." *Nature* 494.7437, pp. 341–344. DOI: [10.1038/nature11882](https://doi.org/10.1038/nature11882).
- Cox, P. M., C. Huntingford, and M. S. Williamson (2018). "Emergent Constraint on Equilibrium Climate Sensitivity from Global Temperature Variability." *Nature* 553.7688, pp. 319–322. DOI: [10.1038/nature25450](https://doi.org/10.1038/nature25450).
- Eyring, V. et al. (2016). "Overview of the Coupled Model Intercomparison Project Phase 6 (CMIP6) Experimental Design and Organization." *Geosci. Model Dev.* 9.5, pp. 1937–1958. DOI: [10.5194/gmd-9-1937-2016](https://doi.org/10.5194/gmd-9-1937-2016).
- Eyring, V. et al. (2019). "Taking Climate Model Evaluation to the next Level." *Nature Climate Change* 9.2, pp. 102–110. DOI: [10.1038/s41558-018-0355-y](https://doi.org/10.1038/s41558-018-0355-y).
- Flato, G. et al. (2013). "Evaluation of Climate Models." In: *Climate Change 2013: The Physical Science Basis. Contribution of Working Group I to the Fifth Assessment Report of the Intergovernmental Panel on Climate Change*. Ed. by T. Stocker et al. Cambridge, United Kingdom and New York, NY, USA: Cambridge University Press, pp. 741–866. ISBN: ISBN 978-1-107-66182-0.
- Forkel, M. et al. (2016). "Enhanced Seasonal CO₂ Exchange Caused by Amplified Plant Productivity in Northern Ecosystems." *Science* 351.6274, pp. 696–699. DOI: [10.1126/science.aac4971](https://doi.org/10.1126/science.aac4971).
- Fritz, S. et al. (2015). "Mapping Global Cropland and Field Size." *Global Change Biology* 21.5, pp. 1980–1992. DOI: [10.1111/GCB.12838](https://doi.org/10.1111/GCB.12838).
- Goetz, S. J., A. G. Bunn, G. J. Fiske, and R. A. Houghton (2005). "Satellite-Observed Photosynthetic Trends across Boreal North America Associated with Climate and Fire

- Disturbance." *Proceedings of the National Academy of Sciences of the United States of America* 102.38, pp. 13521–13525. DOI: [10.1073/pnas.0506179102](https://doi.org/10.1073/pnas.0506179102).
- Goll, D. S. et al. (2017). "Carbon–Nitrogen Interactions in Idealized Simulations with JSBACH (Version 3.10)." *Geosci. Model Dev.* 10.5, pp. 2009–2030. DOI: [10.5194/gmd-10-2009-2017](https://doi.org/10.5194/gmd-10-2009-2017).
- Graven, H. D. et al. (2013). "Enhanced Seasonal Exchange of CO₂ by Northern Ecosystems Since 1960." *Science* 341.6150, pp. 1085–1089. DOI: [10.1126/science.1239207](https://doi.org/10.1126/science.1239207).
- Hall, A. and X. Qu (2006). "Using the Current Seasonal Cycle to Constrain Snow Albedo Feedback in Future Climate Change." *Geophysical Research Letters* 33.3, p. L03502. DOI: [10.1029/2005GL025127](https://doi.org/10.1029/2005GL025127).
- Hall, A., P. Cox, C. Huntingford, and S. Klein (2019). "Progressing Emergent Constraints on Future Climate Change." *Nature Climate Change* 9.4, pp. 269–278. DOI: [10.1038/s41558-019-0436-6](https://doi.org/10.1038/s41558-019-0436-6).
- Harris, I., P. D. Jones, T. J. Osborn, and D. H. Lister (2014). "Updated High-Resolution Grids of Monthly Climatic Observations – the CRU TS_{3.10} Dataset." *International Journal of Climatology* 34.3, pp. 623–642. DOI: [10.1002/joc.3711](https://doi.org/10.1002/joc.3711).
- Keeling, C. D., J. F. S. Chin, and T. P. Whorf (1996). "Increased Activity of Northern Vegetation Inferred from Atmospheric CO₂ Measurements." *Nature* 382.6587, pp. 146–149. DOI: [10.1038/382146a0](https://doi.org/10.1038/382146a0).
- Keenan, T. F. et al. (2016). "Recent Pause in the Growth Rate of Atmospheric CO₂ Due to Enhanced Terrestrial Carbon Uptake." *Nature Communications* 7, p. 13428. DOI: [10.1038/ncomms13428](https://doi.org/10.1038/ncomms13428).
- Klein, S. A. and A. Hall (2015). "Emergent Constraints for Cloud Feedbacks." *Current Climate Change Reports* 1.4, pp. 276–287. DOI: [10.1007/s40641-015-0027-1](https://doi.org/10.1007/s40641-015-0027-1).
- Knutti, R. (2010). "The End of Model Democracy?" *Climatic Change* 102.3-4, pp. 395–404. DOI: [10.1007/s10584-010-9800-2](https://doi.org/10.1007/s10584-010-9800-2).
- Knutti, R. et al. (2017). "A Climate Model Projection Weighting Scheme Accounting for Performance and Interdependence." *Geophysical Research Letters* 44.4, pp. 1909–1918. DOI: [10.1002/2016GL072012](https://doi.org/10.1002/2016GL072012).
- Kwiatkowski, L. et al. (2017). "Emergent Constraints on Projections of Declining Primary Production in the Tropical Oceans." *Nature Climate Change* 7.5, pp. 355–358. DOI: [10.1038/nclimate3265](https://doi.org/10.1038/nclimate3265).
- Leakey, A. D. B. et al. (2009). "Elevated CO₂ Effects on Plant Carbon, Nitrogen, and Water Relations: Six Important Lessons from FACE." *Journal of Experimental Botany* 60.10, pp. 2859–2876. DOI: [10.1093/jxb/erp096](https://doi.org/10.1093/jxb/erp096).
- Lian, X. et al. (2018). "Partitioning Global Land Evapotranspiration Using CMIP5 Models Constrained by Observations." *Nature Climate Change* 8.7, pp. 640–646. DOI: [10.1038/s41558-018-0207-9](https://doi.org/10.1038/s41558-018-0207-9).
- Mahowald, N. et al. (2016). "Projections of Leaf Area Index in Earth System Models." *Earth Syst. Dynam.* 7.1, pp. 211–229. DOI: [10.5194/esd-7-211-2016](https://doi.org/10.5194/esd-7-211-2016).
- Mao, J. et al. (2016). "Human-Induced Greening of the Northern Extratropical Land Surface." *Nature Climate Change* 6.10, pp. 959–963. DOI: [10.1038/nclimate3056](https://doi.org/10.1038/nclimate3056).
- Myneni, R. B. et al. (2002). "Global Products of Vegetation Leaf Area and Fraction Absorbed PAR from Year One of MODIS Data." *Remote Sensing of Environment*. The Moderate Resolution Imaging Spectroradiometer (MODIS): A New Generation of Land Surface Monitoring 83.1–2, pp. 214–231. DOI: [10.1016/S0034-4257\(02\)00074-3](https://doi.org/10.1016/S0034-4257(02)00074-3).

- Myneni, R. B., R. Ramakrishna, R. Nemani, and S. Running (1997a). "Estimation of Global Leaf Area Index and Absorbed Par Using Radiative Transfer Models." *IEEE Transactions on Geoscience and Remote Sensing* 35.6, pp. 1380–1393. DOI: [10.1109/36.649788](https://doi.org/10.1109/36.649788).
- Myneni, R. B., C. D. Keeling, C. J. Tucker, G. Asrar, and R. R. Nemani (1997b). "Increased Plant Growth in the Northern High Latitudes from 1981 to 1991." *Nature* 386, pp. 698–702. DOI: [10.1038/386698a0](https://doi.org/10.1038/386698a0).
- Nemani, R. R. et al. (2003). "Climate-Driven Increases in Global Terrestrial Net Primary Production from 1982 to 1999." *Science* 300.5625, pp. 1560–1563. DOI: [10.1126/science.1082750](https://doi.org/10.1126/science.1082750).
- Olson, D. M. et al. (2001). "Terrestrial Ecoregions of the World: A New Map of Life on Earth." *BioScience* 51.11, pp. 933–938. DOI: [10.1641/0006-3568\(2001\)051\[0933:TEOTWA\]2.0.CO;2](https://doi.org/10.1641/0006-3568(2001)051[0933:TEOTWA]2.0.CO;2).
- Park, T. et al. (2016). "Changes in Growing Season Duration and Productivity of Northern Vegetation Inferred from Long-Term Remote Sensing Data." *Environmental Research Letters* 11.8, p. 084001. DOI: [10.1088/1748-9326/11/8/084001](https://doi.org/10.1088/1748-9326/11/8/084001).
- Piao, S. et al. (2014). "Evidence for a Weakening Relationship between Interannual Temperature Variability and Northern Vegetation Activity." *Nature Communications* 5, p. 5018. DOI: [10.1038/ncomms6018](https://doi.org/10.1038/ncomms6018).
- Pinzon, J. E. and C. J. Tucker (2014). "A Non-Stationary 1981–2012 AVHRR NDVI3g Time Series." *Remote Sensing* 6.8, pp. 6929–6960. DOI: [10.3390/rs6086929](https://doi.org/10.3390/rs6086929).
- Poulter, B. et al. (2014). "Contribution of Semi-Arid Ecosystems to Interannual Variability of the Global Carbon Cycle." *Nature* 509.7502, pp. 600–603. DOI: [10.1038/nature13376](https://doi.org/10.1038/nature13376).
- Qu, X. and A. Hall (2014). "On the Persistent Spread in Snow-Albedo Feedback." *Climate Dynamics* 42.1-2, pp. 69–81. DOI: [10.1007/s00382-013-1774-0](https://doi.org/10.1007/s00382-013-1774-0).
- Sherwood, S. C., S. Bony, and J.-L. Dufresne (2014). "Spread in Model Climate Sensitivity Traced to Atmospheric Convective Mixing." *Nature* 505.7481, pp. 37–42. DOI: [10.1038/nature12829](https://doi.org/10.1038/nature12829).
- Stephenson, D. B., M. Collins, J. C. Rougier, and R. E. Chandler (2012). "Statistical Problems in the Probabilistic Prediction of Climate Change." *Environmetrics* 23.5, pp. 364–372. DOI: [10.1002/env.2153](https://doi.org/10.1002/env.2153).
- Taylor, K. E., R. J. Stouffer, and G. A. Meehl (2009). "A Summary of the CMIP5 Experiment Design." *PCDMI Rep.* P. 33.
- (2012). "An Overview of Cmpip5 and the Experiment Design." *Bulletin of the American Meteorological Society* 93.4, pp. 485–498. DOI: [10.1175/BAMS-D-11-00094.1](https://doi.org/10.1175/BAMS-D-11-00094.1).
- Vuuren, D. P. van et al. (2011). "The Representative Concentration Pathways: An Overview." *Climatic Change* 109.1-2, pp. 5–31. DOI: [10.1007/s10584-011-0148-z](https://doi.org/10.1007/s10584-011-0148-z).
- Wang, J., N. Zeng, Y. Liu, and Q. Bao (2014). "To What Extent Can Interannual CO₂ Variability Constrain Carbon Cycle Sensitivity to Climate Change in CMIP5 Earth System Models?" *Geophysical Research Letters* 41.10, pp. 3535–3544. DOI: [10.1002/2014GL060004](https://doi.org/10.1002/2014GL060004).
- Wenzel, S., P. M. Cox, V. Eyring, and P. Friedlingstein (2014). "Emergent Constraints on Climate-Carbon Cycle Feedbacks in the CMIP5 Earth System Models." *Journal of Geophysical Research: Biogeosciences* 119.5, pp. 794–807. DOI: [10.1002/2013JG002591](https://doi.org/10.1002/2013JG002591).
- Wenzel, S., V. Eyring, E. P. Gerber, and A. Y. Karpechko (2015). "Constraining Future Summer Austral Jet Stream Positions in the CMIP5 Ensemble by Process-Oriented Multiple Diagnostic Regression." *Journal of Climate* 29.2, pp. 673–687. DOI: [10.1175/JCLI-D-15-0412.1](https://doi.org/10.1175/JCLI-D-15-0412.1).

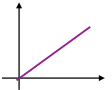
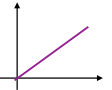
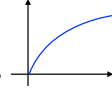
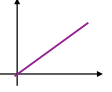
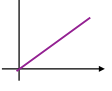
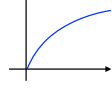
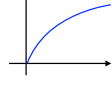
- Wenzel, S., P. M. Cox, V. Eyring, and P. Friedlingstein (2016). "Projected Land Photosynthesis Constrained by Changes in the Seasonal Cycle of Atmospheric CO₂." *Nature* 538.7626, pp. 499–501. DOI: [10.1038/nature19772](https://doi.org/10.1038/nature19772).
- Winkler, A. J., R. B. Myneni, G. A. Alexandrov, and V. Brovkin (2019). "Earth System Models Underestimate Carbon Fixation by Plants in the High Latitudes." *Nature Communications* 10.1, p. 885. DOI: [10.1038/S41467-019-08633-Z](https://doi.org/10.1038/S41467-019-08633-Z).
- Yan, K. et al. (2016a). "Evaluation of MODIS LAI/FPAR Product Collection 6. Part 1: Consistency and Improvements." *Remote Sensing* 8.5, p. 359. DOI: [10.3390/rs8050359](https://doi.org/10.3390/rs8050359).
- Yan, K. et al. (2016b). "Evaluation of MODIS LAI/FPAR Product Collection 6. Part 2: Validation and Intercomparison." *Remote Sensing* 8.6, p. 460. DOI: [10.3390/rs8060460](https://doi.org/10.3390/rs8060460).
- Zhu, Z. et al. (2013). "Global Data Sets of Vegetation Leaf Area Index (LAI)_{3g} and Fraction of Photosynthetically Active Radiation (FPAR)_{3g} Derived from Global Inventory Modeling and Mapping Studies (GIMMS) Normalized Difference Vegetation Index (NDVI)_{3g} for the Period 1981 to 2011." *Remote Sensing* 5.2, pp. 927–948. DOI: [10.3390/rs5020927](https://doi.org/10.3390/rs5020927).
- Zhu, Z. et al. (2016). "Greening of the Earth and Its Drivers." *Nature Climate Change* 6.8, pp. 791–795. DOI: [10.1038/nclimate3004](https://doi.org/10.1038/nclimate3004).

Acknowledgements We thankfully acknowledge T. Park and C. Chen for their help with remote sensing data. We thank G. Lasslop for reviewing the manuscript. R.B.M. thanks Alexander von Humboldt Foundation and NASA's Earth Science Division for funding support that made his participation possible in this research. Finally, we thank three anonymous reviewers and Vivek Arora whose comments helped to substantially improve the manuscript.

Author Information The Authors declare no conflict of interests. Readers are welcome to comment on the online version of the paper. Correspondence and requests for materials should be addressed to A.J.W. (alexander.winkler@pimmet.mpg.de).

A SUPPLEMENTARY INFORMATION

Table A1 | Overview of four possible cases of interaction between forcing, non-observable (predictand) and observable (predictor) identified in the thought experiment: All linear, all non-linear, and two mixed cases.

Different assumptions	$\frac{d[\text{non-observable}]}{d[\text{forcing}]}$, e.g. $\frac{d[\text{GPP}]}{d[\text{CO}_2]}$	$\frac{d[\text{observable}]}{d[\text{non-observable}]}$, e.g. $\frac{d[\text{LAI}]}{d[\text{GPP}]}$
1	linear 	linear 
2	non-linear 	linear 
3	linear 	non-linear 
4	non-linear 	non-linear 

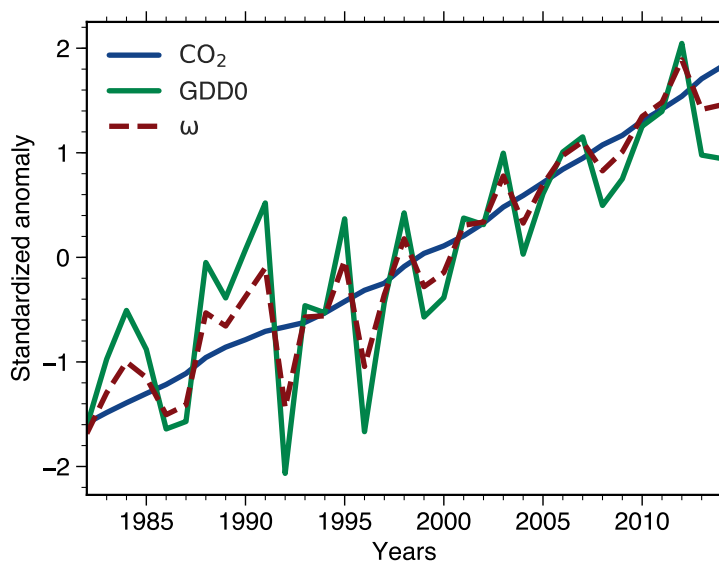


Figure A1 | Standardized temporal anomalies of annual averaged atmospheric CO₂ concentration (blue solid line), area-weighted averaged GDDo for NHL (green solid line), and their leading principal component ω (red dashed line) in observations.

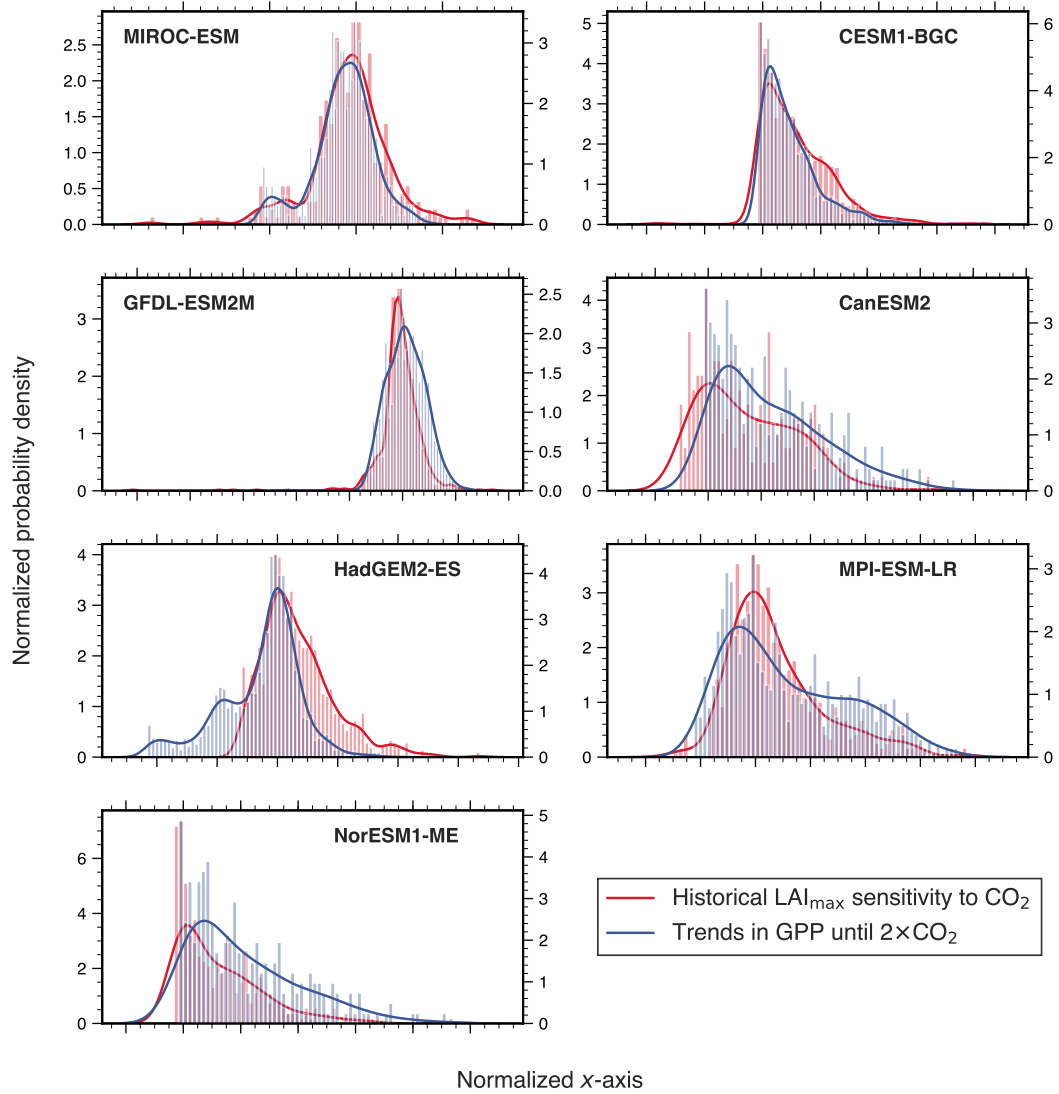


Figure A2 | Similar pixel distribution of predictor and predictand in each model, except HadGEM2-ES. Histograms and associated probability density functions (Gaussian kernel density estimation) of LAI sensitivity to ω (red, left y -axis, historical simulations) and temporal trends in GPP (blue, right y -axis, 1pctCO₂, until 2×CO₂) for NHL are shown for all CMIP5 models. Only significant pixels are included (Mann-Kendall test, $p < 0.1$). To obtain comparability between the distributions, the x -axis was normalized and has only qualitative meaning.

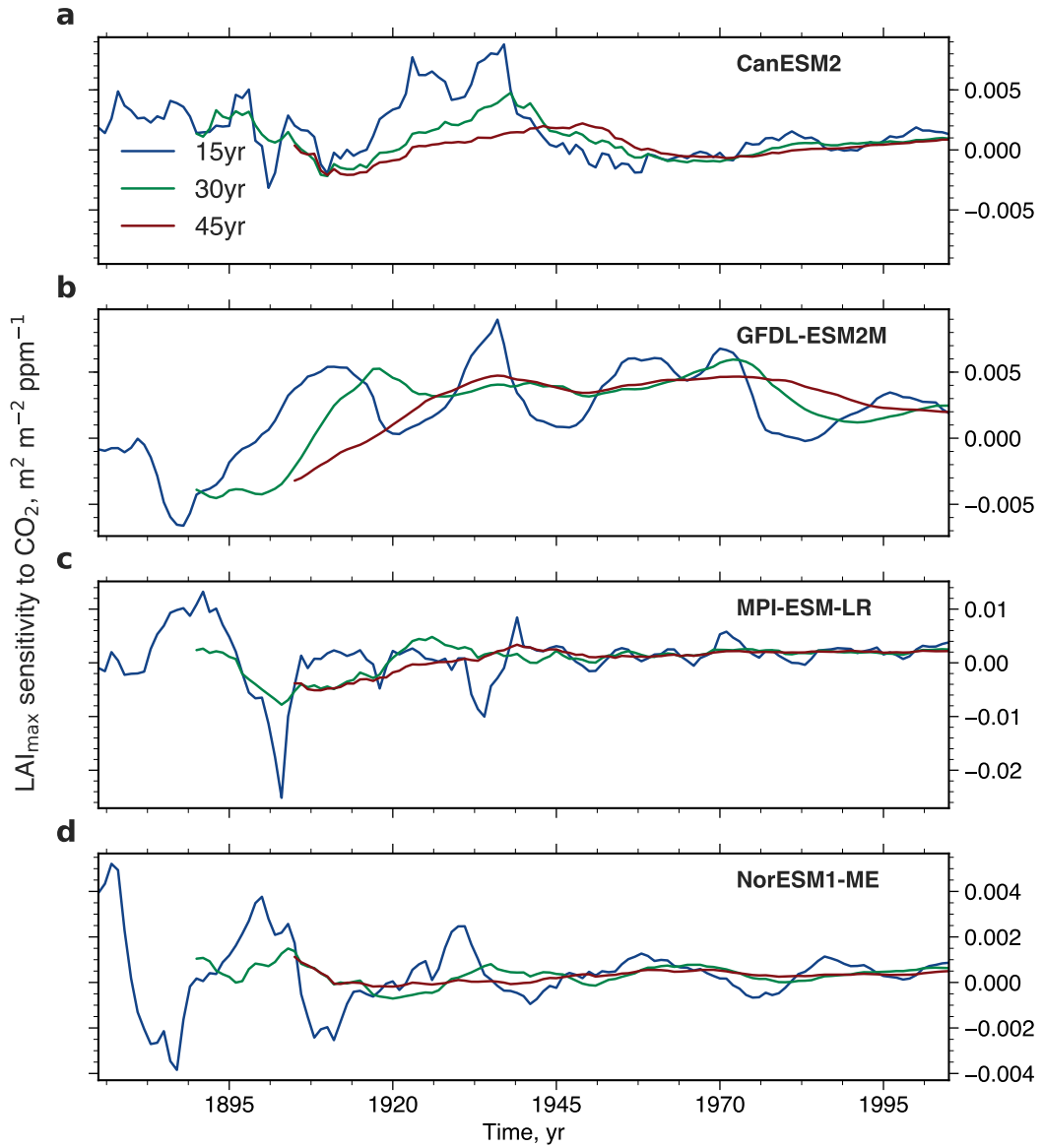


Figure A3 | Temporal variation of LAI_{max} sensitivity to ω in four CMIP5 models analogous to Fig. 4. The colored lines show LAI_{max} sensitivity variations for moving windows of varying length of 15 (blue), 30 (green), and 45 (red) years over the historical period from 1860 to 2005.

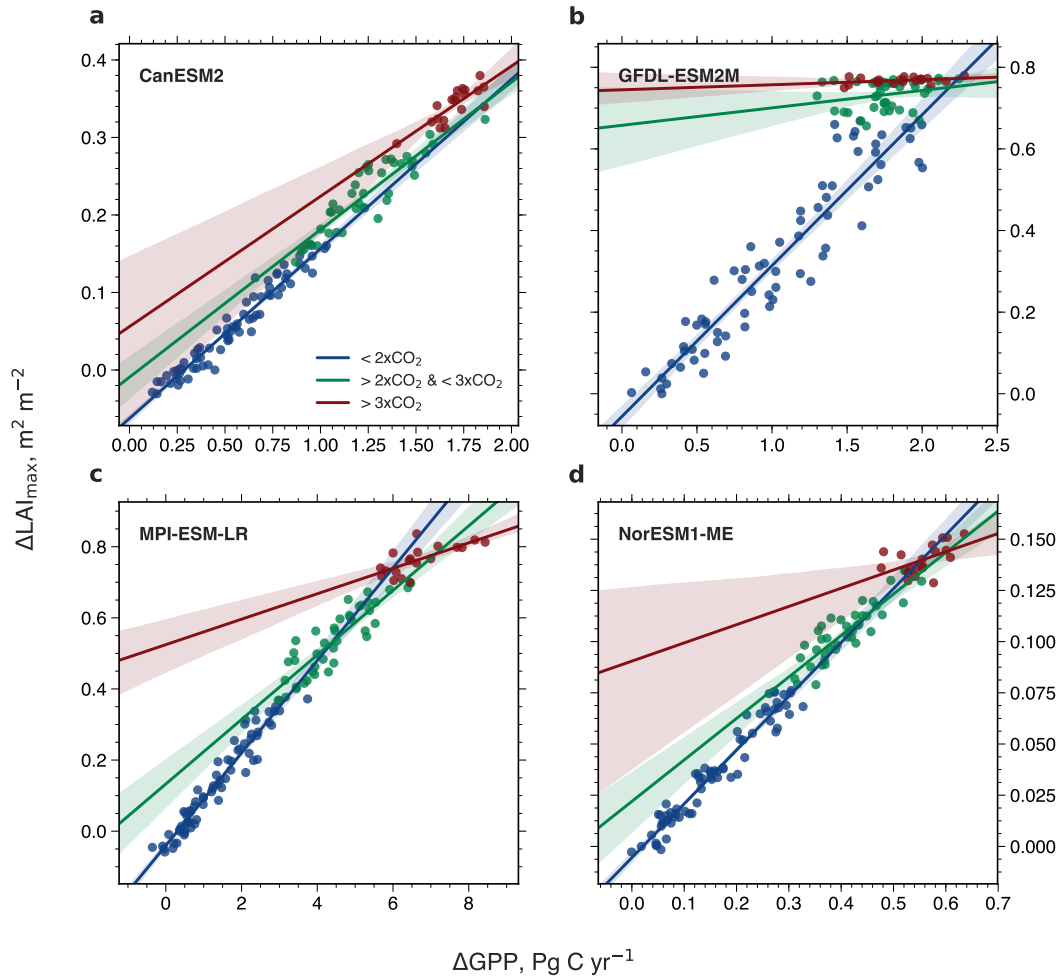


Figure A4 | Correlation of ΔLAI_{max} and ΔGPP with increasing CO₂ forcing, starting from a pre-industrial concentration of 280 ppm (1xCO₂) to 4xCO₂ (CMIP5 1pctCO₂ simulations). Results are shown for four CMIP5 models analogous to Fig. 5. Blue colored dots show the relation between 1xCO₂ and 2xCO₂, green colored dots between 2xCO₂ and 3xCO₂, and red colored dots between 3xCO₂ and 4xCO₂. The respective colored lines represent the best linear fit through those dots and the shading represents the 95% confidence interval.

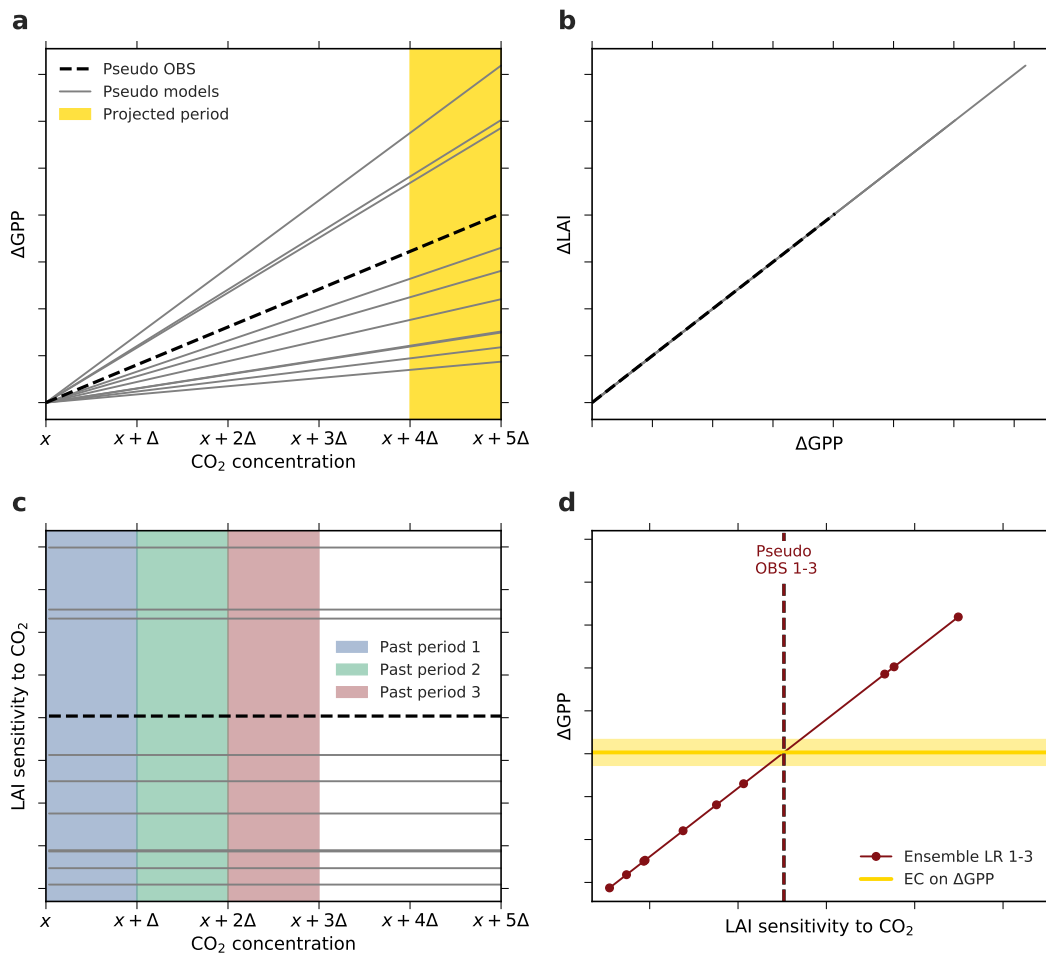


Figure A5 | Thought experiment to examine the applicability of the EC analysis assuming an idealized linear / linear behavior of the system (Case 1, Table A1). **a**, Changes in GPP relate linearly to changes in CO_2 concentration. The yellow band marks the projection period of interest, i.e. the period of CO_2 concentration from $x + 4\Delta$ to $x + 5\Delta$. **b**, Changes in LAI relate linearly to changes in GPP. The parameterization in the linear functions for pseudo observations (dashed black line) as well as models (solid grey lines) are determined randomly for each model. **c**, The diagnostic variable, LAI sensitivity to CO_2 , remains constant with increasing CO_2 as a consequence of the overall linear characteristics of the system. The colored bands indicate three ‘past’ periods from x to $x + \Delta$ (blue), $x + \Delta$ to $x + 2\Delta$ (green), and $x + 2\Delta$ to $x + 3\Delta$ (red). **d**, Linear relationships among the pseudo model ensembles (Ensemble LR 1-3 on top of each other, red) between LAI sensitivity to CO_2 of the three past periods and ΔGPP from the projected period. Red dots mark different models and the dashed line represents associated pseudo observations for all three historical periods. Yellow solid line depicts the constant EC on projected ΔGPP irrespective of the past period.

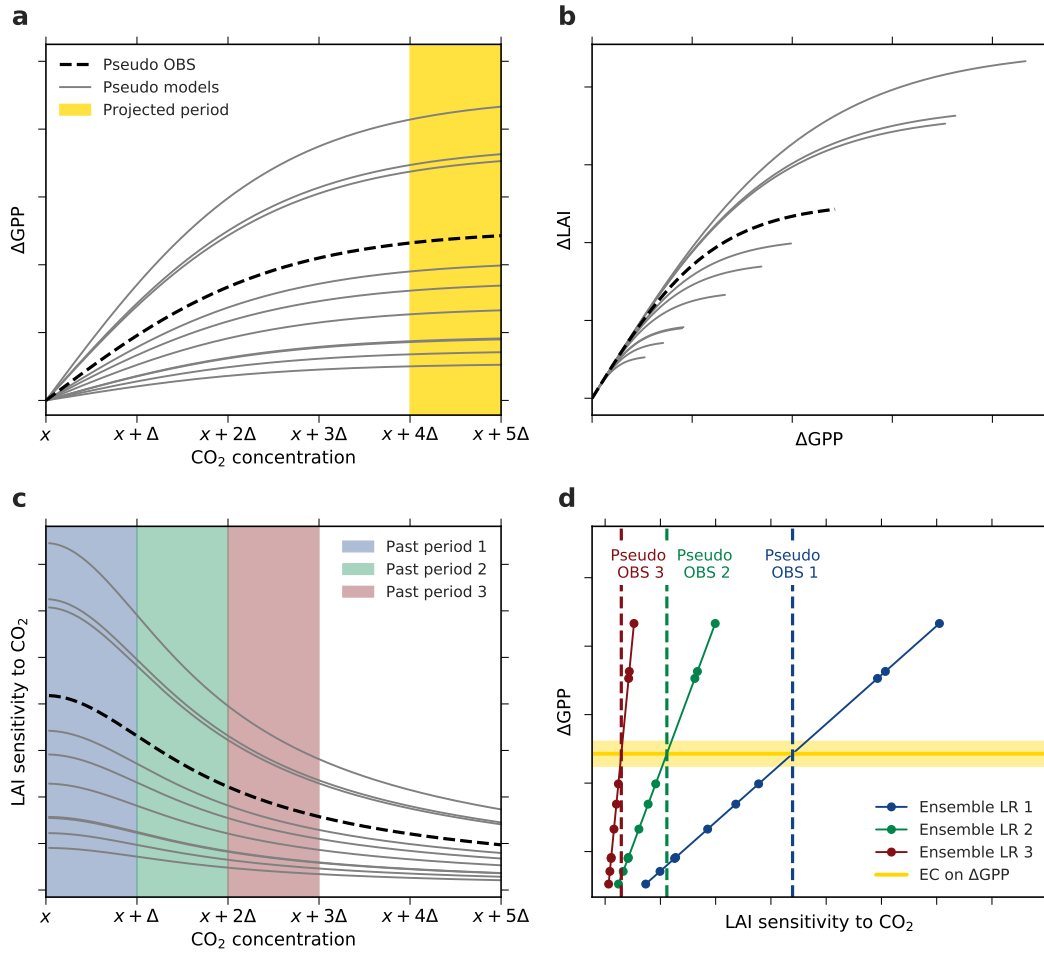


Figure A6 | Thought experiment to examine the applicability of the EC analysis assuming an idealized non-linear / non-linear behavior of the system (Case 4, Table A1). **a**, ΔGPP decreases with increasing CO_2 concentration (described by a hyperbolic tangent function). The yellow band marks the projected period of interest, i.e. the period of CO_2 concentration from $x + 4\Delta$ to $x + 5\Delta$. **b**, Also ΔLAI decreases with increasing GPP (described by a hyperbolic tangent function). The parameterization in the hyperbolic tangent functions for pseudo observations (dashed black line) as well as models (solid grey lines) are determined randomly for each model. **c**, The diagnostic variable, LAI sensitivity to CO_2 , is decreasing with increasing CO_2 as a consequence of the overall saturating characteristics of the system. The colored bands indicate three ‘past’ periods from x to $x + \Delta$ (blue), $x + \Delta$ to $x + 2\Delta$ (green), and $x + 2\Delta$ to $x + 3\Delta$ (red). **d**, Linear relationships among the pseudo model ensembles (Ensemble LR, colored lines) between LAI sensitivity to CO_2 of the three past periods and ΔGPP from the projected period. Colored dots mark different models and the dashed lines represent associated pseudo observations for respective historical period. Yellow solid line depicts the constant EC on projected ΔGPP irrespective of the past period.

ACKNOWLEDGMENTS

Writing this dissertation was only possible thanks to the continuous and invaluable support of others.

Five years ago Victor Brovkin hired me as a student assistant in his group. Since then, he has guided me to become an independent researcher. Victor, I am very grateful for giving me this opportunity and for being such a great supervisor and mentor. I thank Martin Claußen and Lars Kutzbach for their valuable suggestions and critical questions about my research projects during our advisory panel meetings. A very special thanks goes to Ranga Myneni for investing so much time and energy in my research, for inviting me to Boston University and NASA Ames, and for introducing me to so many interesting people. Ranga, many thanks for your brilliant advice along the way and for your motivating words during the lengthy peer review of our publications.

Many thanks to my co-authors Georgii Alexandrov and Alexis Hannart for their valuable contributions and enriching discussions. I also would like to thank Chi Chen and the Taejin Park for their support in handling the remote sensing data and for introducing me to culinary delights during my visit to the USA. A very big thanks goes to Jeremy Caves Rugenstein, Leonard Borchert, Thomas Riddick, Christopher Hedemann, Gitta Lasslop and Veit Lüschof for proof-reading parts of this thesis. I am also very grateful to the IMPRS office, namely Antje Weitz, Cornelia Kampmann and Michaela Born, for making my life as a doctoral student as easy as possible. I thank Veronika Gayler, Reiner Schnur and Thomas Raddatz for their excellent technical support in handling the MPI models. Special thanks also goes to Thomas Raddatz for stimulating discussions about the universe. Many thanks to my office colleagues, especially to Vivienne Groner, Sabine Egerer, Zoé Rehder, Johannes Winckler, Guilherme Mendonça and István Dunkl for creating such a wonderful and interesting working environment.

Last but not least, for so many reasons, I am deeply grateful to my family, Koni, my brothers Samuel and Johannes, and especially to my mother Theresa – I truly admire you. And, of course, Lena*, I couldn't have done it without you – thank you so very much.

Many thanks to André Miede and Ivo Pletikosić, the authors of the CLASSICTHESIS template, which was used to typeset this document (available at: <https://bitbucket.org/amiede/classicthesis/>).

AFFIRMATION ON OATH

Eidesstattliche Erklärung

Hiermit versichere ich an Eides statt, dass ich die vorliegende Dissertation mit dem Titel: "The Response of Global Terrestrial Photosynthesis to Rising CO₂ – A Synthesis of Models and Observations" selbstständig verfasst und keine anderen als die angegebenen Hilfsmittel – insbesondere keine im Quellenverzeichnis nicht benannten Internet-Quellen – benutzt habe. Alle Stellen, die wörtlich oder sinngemäß aus Veröffentlichungen entnommen wurden, sind als solche kenntlich gemacht. Ich versichere weiterhin, dass ich die Dissertation oder Teile davon vorher weder im In- noch im Ausland in einem anderen Prüfungsverfahren eingereicht habe und die eingereichte schriftliche Fassung der auf dem elektronischen Speichermedium entspricht.

Hamburg, 30 April 2019

Alexander Josef Winkler

Hinweis / Reference

Die gesamten Veröffentlichungen in der Publikationsreihe des MPI-M
„Berichte zur Erdsystemforschung / Reports on Earth System Science“,
ISSN 1614-1199

sind über die Internetseiten des Max-Planck-Instituts für Meteorologie erhältlich:
<http://www.mpimet.mpg.de/wissenschaft/publikationen.html>

*All the publications in the series of the MPI -M
„Berichte zur Erdsystemforschung / Reports on Earth System Science“,
ISSN 1614-1199*

*are available on the website of the Max Planck Institute for Meteorology:
<http://www.mpimet.mpg.de/wissenschaft/publikationen.html>*

